Complete biotic and sedimentary records of the Permian-Triassic transition from Meishan section, South China: ecologically assessing mass extinction and its aftermath

Zhong-Qiang Chen[a,*], Hao Yang[a], Mao Luo[b], Michael J. Benton[c], Kunio Kaiho[d], Laishi Zhao[e], Yuangeng Huang[a], Kexing Zhang[a], Yuheng Fang[a], Haishui Jiang[a], Huan Qiu[e], Yang Li[e], Chengyi Tu[a], Lei Shi[a], Lei Zhang[e], Xueqian Feng[a], Long Chen[a]

[a] *State Key Laboratory of Biogeology and Environmental Geology, China University of Geosciences (Wuhan), Wuhan 430074, China*

[b] *School of Earth and Environment, The University of Western Australia, Crawley, WA 3009, Australia*

[c] *School of Earth Sciences, University of Bristol, Bristol, BS8 1RJ, UK;*

[d] *Institute of Geology and Paleontology, Tohoku University, Sendai 980-8578, Japan;*

[e] *State Key Laboratory of Geological Processes and Mineral Resources, China University of Geosciences (Wuhan), Wuhan 430074, China*

* Corresponding author (Z.Q. Chen). *E-mail address:* zhong.qiang.chen@cug.edu.cn

ABSTRACT

The Meishan section, South China is the Global Stratotype Section and Point (GSSP) for the Permian-Triassic boundary (PTB), and also is well known for the best record demonstrating the Permian-Triassic mass extinction (PTME) all over the world. This section has also been studied using multidisciplinary approaches to reveal the possible causes for the greatest Phanerozoic biocrisis of life on Earth; many important scenarios interpreting the great dying have been proposed on the basis of data from Meishan. Nevertheless, debates on biotic extinction patterns and possible killers still continue. This paper reviews all fossil and sedimentary records from the Permo-Triassic (P-Tr) transition, based on previously published data and our newly obtained data from Meishan, and assesses ecologically the PTME and its aftermath to determine the biotic response to climatic and environmental extremes associated with the biocrisis. Eight updated conodont zones: *C. yini, C. meishanensis*, *H. changxingensis*, *C. taylorae*, *H. parvus*, *I. staeschei*, *I. isarcica*, and *C. planate* Zones are proposed for the PTB beds at Meishan.

Major turnover in fossil fragment contents and ichnodiversity occurs across the boundary between Bed 24e-5 and Bed 24e-6, suggesting an extinction horizon in thin section. The irregular surface in the middle of Bed 27 is re-interpreted as a firmground of *Glossifungites* ichnofacies rather than the previously proposed submarine dissolution surface or hardground surface. Both fossil fragment contents and ichnodiversity underwent dramatic declines in Beds 25–26a, coinciding with metazoan mass extinction. Fossil fragment content, ichnodiversity and all ichnofabric proxies (including burrow size, tiering level, bioturbation level) indicate that the P-Tr ecologic crisis comprises two discrete stages, coinciding with the first and second phases of the PTME in Meishan. Ecologic crisis lagged behind biodiversity decline during the PTME. Pyrite framboid size variations suggest that depositional redox condition was anoxic to euxinic in the latest Changhsingian, became euxinic in Beds 25–26a, turned dysoxic in Bed 27, then varied from euxinic to anoxic through most of the Griesbachian. The ~9 °C increase in seawater surface temperature from Bed 24e to Bed 27 at Meishan seems to result in dramatic declines in biodiversity and fossil fragment contents in Beds 25–26a, but had little effect on all ecologic proxies. Both metazoans and infauna seem not to be affected by the pre-extinction anoxic-euxinic condition. The anoxic event associated with the PTME

may have occurred in a much shorter period than previously thought and is only recorded in Beds 25–26a at Meishan. Fossil fragment contents, ichnofaunas, ichnofabrics and pyrite framboid size all show that no signs of oceanic acidification and anoxia existed in Bed 27. The early Griesbachian anoxia may have resulted in rarity of ichnofauna and metazoans in the lower Yinkeng Formation, in which the ichnofauna is characterized by small, simple horizontal burrows of *Planolites*, and metazoan faunas are characterized by low diversity, high abundance, opportunist-dominated communities. The rapid increase of ~9 °C in sea-surface temperature and a short anoxia or acidification coincided with the first-pulse biocrisis, while a prolonged and widespread anoxia probably due to a long period of high seawater temperate condition may be crucial in morality of most organisms in the second-pulse PTME. Marine ecosystems started to recover, coupled with environmental amelioration, in the late Griesbachian.

Keywords: mass extinction, Permian-Triassic, fossil fragment, trace fossils, redox condition, Meishan section

69 **Contents**

1. Introduction

As the greatest biocrisis of life on Earth (Sepkoski, 1981), the Permian-Triassic mass extinction (PTME) changed Earth's ecosystems fundamentally (Benton and Twitchett, 2003; Erwin, 2006). After they had recovered, the marine ecosystems after the PTME gave rise to the forerunners of modern-day ecosystems, both the Triassic and modern ecosystems being comparable to each other in composition of functioning groups and trophic structure (Chen and Benton, 2012). However, the causes of this enigmatic biocrisis have long been disputed despite intense study, and the same is true of the profoundly delayed recovery following the PTME (Erwin, 2001). Thus, studies of these issues have enjoyed a surge in scientific interest in the past 30 years that shows no sign of abating (Chen et al., 2014a).

Although this era-boundary crisis has been widely recognized in Permian–Triassic boundary (PTB) sections around the world, many important hypotheses have been proposed based on paleontological and experimental data sampled from the Meishan section of Changhsing County, Zhejiang Province, east China (Fig. 1A; Renne et al., 1995; Bowring et al., 1998; Jin et al., 2000; Yin et al., 2001, 2012; Kaiho et

al., 2001, 2006a, b; Mundil et al., 2001, 2004; Grice et al., 2005; Xie et al., 2005, 2007; Riccardi et al., 2007; Wang and Visscher, 2007; Cao et al., 2009; Chen et al., 2009, 2010a; Song et al., 2009, 2013a, b; Shen et al., 2011b; Huang et al., 2011; Wu et al., 2013; Wang et al., 2014; Burgess et al., 2014; Fig. 1A). This section is the Global Stratotype Section and Point (GSSP) for the PTB (Yin et al., 2001; Fig. 1C) and also well known for the best record of both biotic and geochemical signals demonstrating the PTME all over the world. Here, the exposures of the PTB beds are spectacular, extending about 2 km laterally along the Meishan hill (Fig. 1E). The PTME has been well demonstrated by Jin et al. (2000), whose study based on paleontological data from Meishan reveals that this extinction event was abrupt and dramatic, with most Permian organisms being wiped out within a very short interval, which was precisely calibrated to the base of Bed 25, a white clay bed, in Meishan (Fig. 1B, D), while the PTB is placed at the middle of Bed 27, about 16-20 cm above the base of Bed 25 in the same section (Yin et al., 2001; Fig. 1C). As such, the biocrisis clearly pre-dated the PTB (Fig. 1D). The P-Tr ecologic crisis is also marked by a pronounced negative carbon isotopic excursion (Xu and Yan, 1993; Jin et al., 2000; Kaiho et al., 2001; Cao et al., 2002; Xie et al., 2005, 2007; Fig. 2) and is also associated with an end-Permian sulfur event (Kaiho et al., 2006; Riccardi et al., 2006).

After Jin et al.'s (2000) influential study, which was largely based on fossil data obtained in 1980s (i.e., Zhao et al., 1981; Sheng et al., 1984; Liao, 1984; Sheng et al., 1987; Shi and Wang, 1987), abundant brachiopod and foraminifer faunas have been detected from Beds 25–27, immediately above the PTME horizon in Meishan (Chen et al., 2005a, 2006b; Song et al., 2007, 2009). Quantitative analysis of the updated foraminifer data from Meishan revealed a two-stage extinction pattern near the P-Tr boundary (Song et al., 2009), which agrees well with two distinct peaks of cyanobacteria, detected by biomarker analysis from the same section, suggesting two extinction events corresponding to Beds 25 and 28 (Xie et al., 2005). The two-stage extinction pattern is also strengthened by extremely abundant benthic fossils obtained from a shallow platform facies of the PTB section at Huangzhishan, about 40 km from Meishan (Chen et al., 2009). However, Shen et al. (2011b) clarified an abrupt biotic decline in a short interval equivalent to Beds 25-28 of Meishan based on quantitative analysis of fossil records from Meishan and other PTB sections in South China. In contrast, Song et al. (2013a) demonstrated nicely a two-stage extinction pattern for the P-Tr crisis based on quantitative analysis of paleontological data derived from Meishan and a further six PTB sections in South China. Thus, debate on whether the PTME was either a single crisis or

episodic extinctions still continues (Shen et al., 2011b; Song et al., 2013a; Wang et al., 2014). Regardless of whether the extinction was single or a two-phase pattern, an increasing number of faunas have been found in Beds 25-28 of Meishan and its counterparts across all of South China, although this interval may just last 60 kyr (Burgess et al., 2014).

In addition, a further extinction event resulting in depletion of Permian reefs in South China was calibrated to the base of Bed 24e at Meishan (Yang et al., 1993). Yin et al. (2007) re-documented biotic and geochemical signal changes across this horizon, which is reinforced by several lines of evidence, including reduction in conodont sizes (Luo et al., 2006), possible extinction of radiolarians in deep habitats and a negative shift in organic carbon isotope values (Cao et al., 2009). To sum up, biotic variations based on sound paleontology over the P-Tr transition have been far less studied in comparison with the intense geochemical studies of this catastrophe in most PTB sections. Current, updated fossil records from extensive PTB sections are crucial to reveal the true biotic responses to these environmental crises.

As briefly summarized above, there have been great advances in research on the PTME at Meishan in recent years. Multiple scenarios interpreting the causes of the P-Tr

biocrisis have been proposed based on experimental data sampled from this section. Nevertheless, any reasonable models interpreting the P-Tr crisis need to be tested by analysis of precise biotic extinction patterns and physiological reactions of victims and survivors (Knoll et al., 2007). As a result, we herein document the updated, complete fossil and sedimentary records, including microfacies, microfossils, body and trace fossils, and pyrite framboids, throughout the P-Tr transition and attempt to test biotic responses to various environmental and climatic catastrophes from the GSSP Meishan.

2. Biochronostratigraphy: an update

2.1. Biostratigraphy and correlations

After Yin et al.'s (2001) placement of the PTB at the base of Bed 27c, marked by the first appearance datum (FAD) of the conodont *Hindeodus parvus*, Jiang et al. (2007) established gondolellid and hindeodid conodont zones across the PTB in Meishan. The former include the *Clarkina yini*, *C. meishanensis* and *C. taylorae* Zones, while the latter comprise the *Hindeodus latidentatus*, *H. praeparvus*, *H. changxingensis*, *H. parvus*,

195 *Isarcicella staeschei*, and *I. isarcica* Zones (Jiang et al., 2007, fig. 2). Later, Zhang et al.

196 (2009) integrated them as one conodont zonation series: *C. yini* Zone (Bed 24), *C.*

197 *meishanensis* Zone (Bed 25), *H. changxingensis* Zone (Beds 26-27b), *H. parvus* Zone

198 (Bed 27c), *I. staechei* Zone (Beds 27d-28), *I. isarcica* Zone (Beds 29-51), and *C.*

199 *tulongensis-C. planata* Zone (Beds 52-72, top of the Yinkeng Formation).

200 Given that *C. taylorae* is confined to Bed 27a-28 in Meishan (Jiang et al., 2007;

201 Zhang et al., 2009) and has also been widely reported from PTB beds around the world

202 (Orchard et al., 1994; Orchard and Krystn, 1998; Nicoll et al., 2002; Algeo et al., 2012;

203 Zhao et al., 2013b), the *C. taylorae* Zone is regarded as a discrete zone beneath the *H.*

204 *parvus* Zone and retained for Bed 27a-b (Fig. 2). In addition, we have also re-examined

205 stratigraphic distributions of some key conodont species based on previously published

206 data and newly extracted specimens from Meishan. An updated conodont zonation is

207 proposed for the P-Tr succession of the GSSP Meishan (Fig. 2). The new conodont zones,

208 with their stratigraphic ranges in brackets, include *C. changxingensis* Zone (Beds 22-23),

209 *C. yini* Zone (Bed 24), *C. meishanensis* Zone (Bed 25), *H. changxingensis* Zone (Bed 26),

210 *C. taylorae* Zone (Bed 27a-b), *H. parvus* Zone (Bed 27c-d), *I. staeschei* Zone (Beds

211 28-29a), *I. isarcica* Zone (Bed 29b), *C. planata* Zone (Beds 30-54), and *Neoclarkina*

212 *discreta* Zone (Bed 35 and above) (Fig. 2).

213 It is noteworthy that Yuan et al. (2014) confined the *C. changxingensis* Zone to
214 mid-Bed 10 to mid-Bed 22, *C. yini* Zone to mid-Bed 22 to Bed 24d, and *C. meishanensis*
215 Zone to Bed 24e to Bed 25. The fist occurrence of the nominal species of these conodont
216 zones seems to be lower than they occurred in our samples. In particular, *C. meishanensis*
217 occurs in the so-called 'white boundary clay' bed and above strata in most PTB sections
218 in South China (Zhang et al., 2007; Jiang et al., 2007, 2011, Zhao et al., 2013b) and is
219 rarely present in the Permian bioclastic limestone. The *C. meishanensis* Zone is also
220 associated with a pronounced negative shifting excursion of carbon isotopes in most of
221 the PTB sections in South China. Accordingly, the bases of these Changhsingian
222 conodont zones remain tentative and need to be confirmed when additional conodont
223 samples are processed in future.

224 Other important findings from the PTB beds include restriction of *Isarcicella*
225 *peculiaris* to Bed 28 and the first occurrences of *Hindeodus eurypyge* and *Isarcicella*
226 *lobata* at the bases of Bed 27a and Bed 28, respectively (Jiang et al. 2007; fig. 2). These
227 species also have the potential to serve as key elements marking the PTB beds (Jiang et al.,
228 2007, 2011, 2014). Of these, *I. lobata*, confined to Beds 28-29 in Meishan, was proposed

as a distinct zone between the *H. parvus* and *I. staeschei* Zones in the southern Alps (Perri and Farabegoli, 2003, 2012; Fig. 2). This species therefore occurred slightly earlier in the southern Alps than in the GSSP Meishan. In the new conodont zonation, the *I. isarcica* Zone is retained for Bed 29b, and thus has a much narrower stratigraphic range than before. The *C. planata* Zone is newly proposed for Beds 30-54 and the *Neoclarkina discreta* Zone for Bed 55 and higher strata in Meishan (Fig. 2) based on re-examination of their stratigraphic distributions (Zhang et al., 2007, 2009).

The updated conodont zonation enables the PTB beds of Meishan to be correlated precisely with their counterparts recorded elsewhere in the Tethys region, such as North Italy, Iran, Germanic basin, and Spiti of Himalaya region (Fig. 2). The *H. parvus*, *I. staeschei* and *I. isarcica* Zones have also been recognized in both Spiti and North Italy (Fig. 2). Both *H. parvus* and *I. isarcica* Zones occur in the Abdadeh region, Iran (Korte et al., 2004). Korte et al. (2004) also argued that there might be a hiatus between Beds 24e and 25 because both the *C. iranica* and *C. hauschkei* Zones, between the *C. yini-C. zhangi* and *C. meishanensis-H. praeparvus* Zones, are absent in Meishan. *C. hauschkei* does occur in Meishan, but shares the same stratigraphic range with both *C. yini* and *C. zhangi* in Bed 24 (Jiang et al., 2007, 2011). More importantly, no sedimentary gap has been

found in this interval in the GSSP Meishan (see below). The last occurrence of both *C. yini* and *C. zhangi* has been calibrated to the top of Bed 24e (Yin et al., 2001; Zhang et al., 2007; Jiang et al., 2007). The depositional succession between the *C. meishanensis* and *C. yini* Zones shows no sign of a hiatus. Thus, both *C. hauschkei* and *C. iranica* either can be recognized from the upper part of the *N. yini* Zone in the future, or do not occur due to different biofacies controls (Korte et al., 2004).

Recognition and correlations of PTB beds in conodont-barren sections have long remained problematic. Chen et al. (2009) established the bivalves *Claraia huzhouensis-C.* cf. *bioni* and *Eumorphotis venetiana-Towapteria scythica-Pteria ussurica variablilis* Assemblages from the PTB beds of both the Meishan and adjacent Huangzhishan sections. The former is coeval with the *C. meishanensis* and *H. changxingensis* Zones of the GSSP Meishan (Chen et al., 2009). The small, weakly costated *Claraia*-like species "*Peribositra*" *baoqingensis* from Bed 26 of Meishan (Zhao et al., 1981) has been re-assigned to *Claraia* (Chen, 2004). These primitive *Claraia* species from Meishan are diagnostic of the *C. huzhouensis-C.* cf. *bioni* Assemblage and locate the PTME in the shallow-water, conodont-barren PTB sections in South China (Chen et al., 2009). The latter bivalve assemblage is contemporaneous with the *H. parvus* Zone in the

263 Huangzhishan section, pointing to an age of earliest Triassic (Chen et al., 2009). Both
264 *Claraia wangi* and *C. griesbachi* are also abundant in Beds 29b-54 in Meishan, and thus
265 form the *C. wangi-C. griesbachi* Assemblage (Chen et al., 2010a), which is coeval with
266 the *I. isarcica* and *C. planata* Zones (Fig. 2). The ammonoids *Rotodiscoceras*,
267 *Hypophiceras*, *Ophiceras*, and *Lytophiceras* characterize the assemblages from Beds
268 22-24, Beds 25-26, Beds 27-50, and Beds 51-55, respectively in Meishan (Fig. 2; Zhao et
269 al., 1984; Sheng et al., 1984; Yin et al., 2001; Chen et al., 2010a). Brachiopods are also
270 reasonably abundant in Beds 25-26, Bed 27 and Beds 51-55 of Meishan (Chen et al.,
271 2002, 2006b, 2007). They are assignable to the *Tethyochonetes liaoi* Assemblage (Beds
272 25-26), *Paryphella triquetra* Assemblage (Bed 27), and *Meishanorhynchia meishanensis*
273 Assemblage (Beds 51-55) (Chen et al., 2010a). Song et al. (2007, 2009) also reported
274 diverse foraminifers from the Changhsing and lowest Yinkeng Formations in Meishan,
275 but did not establish biozones. A palynological *Lundbladispora-Taeniaesporites-*
276 *Equisetosporites* Assemblage was established from Beds 33-53 of the Yinkeng
277 Formation (Zhang et al., 2007), which, therefore, correlates collectively with the
278 conodont *C. planata* Zone (Fig. 2).
279

280 *2.2. Geochronology*

281

282 In Meishan, volcanic ash beds are well exposed and conspicuous in the
283 uppermost Permian to Lower Triassic successions. In particular, Beds 25 and 28 near the
284 PTB have been dated by multiple research groups using various techniques (Table 1). The
285 most updated radiometric ages for Beds 25 and 28 are 251.941 ± 0.037 Ma and 251.880 ±
286 0.031 Ma, respectively (Burgess et al., 2014), which constrain the duration between those
287 two phases of the PTME (Song et al., 2013a) or the duration of the PTME (Shen et al.,
288 2011b; Wang et al., 2014) as 60 ka (Burgess et al., 2014). Burgess et al. (2014) have also
289 given updated estimates for sediment accumulation rates through the P-Tr transition,
290 which show that sedimentation rates of the Changhsing Formation decline towards the
291 end of the Permian, reach the lowest value during the time of extinction (Beds 25-28), and
292 then increase gently in the early Griesbachian (Beds 28-37) and steeply in the
293 early-middle Griesbachian (Beds 37-48) in Meishan (Burgess et al., 2014). In addition,
294 these authors estimated that the abrupt decline in $\delta^{13}C_{carb}$ in Bed 24e took place at
295 251.950 ± 0.042 Mya, while the FAD of *H. parvus* at the GSSP Meishan is at 251.902 ±
296 0.024 Mya (Burgess et al., 2014).

297

298 *2.3. Duration of key conodont zones across the P-Tr boundary*

299

300 At Meishan, intense high-precision dating of volcanic ash beds (Table 1) and
301 high resolution conodont zones (Fig. 2) allow reasonable estimates of the duration of
302 each conodont zone. The widespread *H. parvus* Zone is estimated to have lasted 16 ka
303 (Table 2), while the *C. meishanensis* Zone, the PTME marker, lasted 8 ka, which is much
304 shorter than previously thought. The last conodont zone prior to the PTME, the *C. yini*
305 Zone, may have lasted 28 ka (Table 2).

306

307 **3. Microstratigraphy, fossil fragment contents and paleoenvironmental analysis of**
308 **the P-Tr transition**

309

310 At Meishan, the P-Tr succession comprises the Changhsing and Yinkeng
311 Formations below and above. The former unit is a 41-m-thick carbonate succession
312 consisting of medium- to thin-bedded limestone, while the Yinkeng Formation is about
313 15 m thick and dominated by mudstone and muddy limestone in the lower part and

314 characterized by thin-bedded limestone in the upper part (Fig. 3). These two formations
315 have been frequently described (Zhao et al., 1981; Sheng et al., 1984, 1987; Yang et al.,
316 1987; Yin et al., 1996, 2001; Zhang et al., 2005). Cao and Zheng (2007) re-described the
317 Changhsing Formation (Beds 1-24) and recognized 247 natural, single layers, each 2 to
318 37 cm in thickness. Chen et al. (2007) gave an updated description for the Yinkeng
319 Formation (Beds 25-59), in which 183 natural layers are recognizable. In addition, Cao
320 and Shang (1998) conducted the first cm-scale stratigraphy, also termed
321 microstratigraphy, of the P-Tr boundary beds in Meishan. Since then, microstratigraphy
322 of the Beds 24-29 of the Meishan section has been intensely studied (Cao and Zheng,
323 2009; Zhao and Tong, 2010; Zheng et al., 2013).

324 The top two beds of the Changhsing Formation, Beds 23-24, record important
325 sedimentary and paleontological information just prior to the PTME, while most parts of
326 the Yinkeng Formation record the severe biotic extinction and its consequences. Thus,
327 microstratigraphy of the uppermost Changhsing Formation to Yinkeng Formation
328 succession (Beds 23-59) is summarized here in view of the previously published data and
329 our new observations in petrologic thin sections. These thin sections were sampled
330 almost continuously in Beds 24e to 29 and in a 20-cm-interval in Beds 22 to 24d of the

331 Changhsing Formation. The sampling interval is 0.5 m throughout Bed 30 to Bed 59 of
332 the Yinkeng Formation in the GSSP Meishan.
333 Point counting is a relatively quick method that quantifies the occurrence of skeletal
334 fragments of major fossil groups in different horizons under the microscope (Flugel, 1984;
335 Payne et al., 2006). However, care must be taken when using the point-counting method
336 because large shell fragments of some clades may bias counting results (Jacobsen et al.,
337 2011). As an alternative, Jacobsen et al. (2011) proposed the equal area approach to
338 quantify the occurrence of skeletal fragments in thin section. In order to eliminate biases
339 of counting areas, it is suggested that at least eight equal area fields of view ought to be
340 counted per thin section sample (Jacobsen et al., 2011). Similar to the equal area approach,
341 fragment percentage data of various clades from each thin section are estimated based on
342 the observation of 300 to 350 views under a magnification of × 50 in one sample,
343 collected for microfacies analysis of the PTB beds. Then, percentages of various skeletal
344 components, micrite, cavities and undertermined particles (i.e., pyrites and other minerals)
345 from samples throughout Bed 22 to Bed 60 of Meishan were combined to yield the mean
346 abundance of each composition in each sample throughout the study succession (Table 3).
347

348 *3.1. Bed 23*

349

350 Bed 23 of the upper Changhsing Formation comprises dark gray thin-to
351 medium-bedded bioclastic limestone interbedded with thin-bedded muddy limestone and
352 siliceous mudstone layers. Small-scale wavy cross bedding is commonly present in the
353 bioclastic limestone, while horizontal stratification occurs in the muddy limestone and
354 siliceous mudstone (Fig. 4G, H). Grain bedding structures are also occasionally present in
355 the bioclastic limestone unit. The bioclastic limestone usually has a packstone to
356 grainstone texture. The former texture is very common, while a grainstone texture is also
357 occasionally present (Fig. 5C). This unit is usually strongly bioturbated in comparison
358 with the weakly bioturbated thin siliceous layers that are usually horizontally stratified
359 (Fig. 3). The autochthonous and allochthonous fossil assemblage is highly diverse and
360 dominated by foraminifers, crinoids, and brachiopods with minor constituents of
361 ostracods, echinoids, bryozoans, sponge spicules, calcareous sponges, gastropods,
362 radiolarians, and macroalgae (Fig. 6). The matrix comprises micrite (about 20-23%, Fig.
363 6). Cavities, pyrites and other undetermined particles are also commonly present (Table
364 3). The alternating occurrence of horizontal stratification and small-scale cross bedding

365 and/or grain-grading bedding structures indicates that Bed 23 was deposited on a
366 carbonate ramp between fair-weather wavebase and storm wavebase (Fig. 3; Zhang et al.,
367 2005).
368
369 *3.2. Bed 24*
370
371 Bed 24, the topmost unit of the Changhsing Formation, consists mainly of thin-
372 to medium-bedded bioclastic packstone rich in large ammonoids and other macrofossils
373 (Fig. 4E). This bed has attracted intense attentions in terms of fossil record and
374 sedimentary characterization because of its stratigraphic position just beneath the biotic
375 extinction horizon (base of Bed 25; Jin et al., 2000). Bed 24, 71-90 cm in thickness, is
376 usually labelled as Bed 24a-e (Yin et al., 1996) and consists of 14 layers, with the thinnest
377 being 2 cm thick (Cao and Zheng, 2007). The conodonts from Bed 24 belong to the
378 *Clarkina yini* Zone (Mei et al., 1998), which is distinct from the underlying *C.*
379 *changxingensis* Zone (Beds 22-23).
380 Bed 24a-c has similar petrographic features to Bed 23 (Figs. 5D, 6). The dark
381 organic-rich muddy limestone or siliceous mudstone, usually about 2 cm in thickness, has

382 well-developed horizontal stratifications and possesses packstone to micritic textures
383 with tiny, highly fragmented fossil skeletons of brachiopods and ostracods. These
384 horizontally stratified layers are usually weakly bioturbated. In contrast, the bioclastic
385 limestone unit, usually > 5cm thick, possesses small-scale wavy cross bedding and
386 bioclastic packstone to grainstone texture. These layers are also highly bioturbated
387 (Zheng et al., 2013). All skeletal components of Bed 23 also persist into Bed 24 (Fig. 6).
388 Accordingly, Bed 24a-c was likely deposited in the same environment as Bed 23.
389 Although Bed 24d has similar petrographic texture to Bed 24a-c (Fig. 6), the
390 presence of abundant fecal pellets and peloids characterizes the grain assemblage of Bed
391 24d. Fossil fragment contents in rocks from both Bed 24d and Bed 24a-c are also
392 comparable with one another (Fig. 6). In addition, burrows are commonly present near
393 the boundary between bioclastic limestone unit and organic-rich muddy limestone or
394 siliceous mudstone layer. Bed 24d yields abundant trace fossils (see Section 5).
395 Pronounced cross-bedding and vertical burrows characterize the upper part of Bed 24d
396 (Fig. 4J). The top of Bed 24d is, however, weakly bioturbated and characterized by
397 smooth cone-shaped surfaces, which was termed a hard-ground structure representing
398 interrupted or highly condensed deposits (Cao and Zheng, 2009). Cao and Zheng (2009)

399 regarded this irregular contact as a sequence boundary indicating a changeover interface
400 from lowermost level to rapid rise. The same contact, however, has been interpreted as an
401 erosional surface, serving as a sequence base of a 3rd-order depositional sequence
402 following a major fall in sea level (Zhang et al., 1997; Yin et al., 2014). This
403 interpretation is reinforced by the presence of a diverse shallow-water facies trace fossil
404 assemblage including vertical burrows of *Balanogossites* (Fig. 4J; see also Section 5).
405 Cao and Zheng (2007) have also noted that abundant burrows of *Planolites* and *Skolithos*
406 and mud-crack structures are present near the boundary between Beds 24d and 24e.
407 Accordingly, Bed 24d, overall, is inferred to have been deposited in the upper part of the
408 subtidal zone of a carbonate ramp (Fig. 3; Zhang et al., 1997).
409 The topmost 10 cm thick limestone of Bed 24 is labelled Bed 24e, which
410 consists of eight natural layers (Cao and Zheng, 2009) and these were sampled at six
411 horizons here (Bed 24e-1 to Bed 24e-6). Trace fossils occur near the irregular contact
412 between Beds 24d and 24e-1 (see Section 5). Bed 24e, except for the topmost 3 cm (24e-5,
413 24e-6), is a dark gray bioclastic packstone containing abundant fossil fragments of
414 foraminifers, brachiopods, and crinoids. Other fossil groups such as bryozoans,
415 gastropods, macroalgae, ostracods, calcareous sponges, and sponge spicules are also seen

416 in thin sections, which have no major difference from the underlying Bed 24d (Fig. 6).
417 The uneven top surface is always capped by several muddy laminae. Cylindrical, vertical
418 burrows, ranging from 0.1 to 0.5 cm in diameter and from 3.0 to 1.0 cm in length occur in
419 the upper bedding surface. Bed 24e saw a slight increase in lime mud in the matrix and
420 pyrite within the bed (see below). Bed 24e therefore was probably deposited in the
421 fair-weather wave action zone (Fig. 3) and was interpreted as a lowstand platform margin
422 wedge of a 3rd sequence (Zhang et al., 1997; Yin et al., 2014).
423 The topmost 2-3-cm-interval, labelled as Bed 24e-5 and 24e-6, is characterized
424 by relatively low contents of P and Ca and high Ni content (Kaiho et al., 2001, 2006b).
425 Bed 24e-5, about 1.0-1.1 cm in thickness, comprises bioclastic packstone and contains
426 abundant fossil fragments of foraminifers, crinoids, brachiopods, and ostracods.
427 Fragments of calcareous sponges, sponge spicules, gastropods, bryozoans and
428 macroalgae are also occasionally present, and these are comparable in major fossil
429 components with Beds 24e-1 to 24e-4 (Fig. 6). Moreover, abundant, reasonably large
430 horizontal burrows (*Planolites*) are densely packed on the surface of Bed 24e-6 (also see
431 Section 5).
432 The contact between Beds 24e-5 and 24e-6 is a laminated wavy lime layer (Fig.

7D). Bed 24e-6 is a 10- to 19-mm-thick bioclastic packstone and dominated by silica bars, which were interpreted as sponge spicules (Kaiho et al., 2006). The elongate bars are actually longitudinal outlines and the circular grains are cross sections of spicules (Fig. 7A-C). This identification is reinforced by the abundant isolated silicified sponge spicule specimens extracted from Bed 24e-6 (Fig. 7E). Contrasting to the predominance of sponge spicules, fragmentary contents of foraminifers, crinoids, echinoids and brachiopods decline dramatically. The skeletal grain assemblage experienced a dramatic reduction in both abundance and diversity across the contact between Beds 24e-5 and 24e-6 (Fig. 7E), to which the PTME was calibrated (Kaiho et al., 2006a).

3.3. Bed 25

This bed is the so-called "Boundary clay bed" or "White clay bed" (Zhao et al., 1981; Sheng et al., 1984; Yang et al., 1987). Its thickness ranges from 2 cm to 6 cm depending on the weathering intensity, the higher the intensity the thicker the bed. The bed grades upward into Bed 26 as a consequence of a gradual increase in organic and calcareous content and decrease in volcanic ash layers. The total thickness of these two

beds is around 10 cm.

The basal part of Bed 25 comprises a 0.1- to 0.2-mm-thick layer of greyish black mudstone rich in Fe grains, termed Bed 25-1, which usually becomes a reddish ferruginous layer capping the dark Bed 24e-6 and is conspicuous at outcrops in all Meishan quarries owing to weathering. Previously, this Fe-rich layer was termed the "pyrite lamina" layer (Wignall and Hallam, 1993; Shen et al., 2007) or Pyrite layer (Cao and Zheng, 2009), based on the abundant pyrite-like grains visible at outcrops. Elemental analysis shows that these Fe grains are either Fe-Ni grains (Kaiho et al., 2001, 2006b) or goethites (Liang et al., 2002). Pyrite framboids are also commonly present in this layer (Shen et al., 2007). In addition, Zheng et al. (2013) detected abundant irregular volcanic glasses from this layer.

The reddish ferruginous surface of Bed 25-1, together with the absence of both the *N. iranica* and *N. hauschkei* conodont zones, was considered as evidence indicating an exposure surface and representing a hiatus (Korte et al., 2004). However, the presence of marine fossils such as foraminifers and brachiopods (Rui et al., 1988; Yin et al., 2001) in Bed 25 and abundant sponge spicules and other fossil fragments in Bed 24e-6 (Fig. 6) indicates the absence of a paleo-exposure surface or an aerial hiatus. The absence of these

467 two conodont zones may relate to biofacies controls and cannot bracket a hiatus, as
468 discussed in Section 2.1.

469 The overlying thin layer (Bed 25-2), 0.3-1 mm thick, is dark yellowish orange,
470 and encompasses mainly gypsum and Fe (Table 4). The remaining part of Bed 25 (Layer
471 25-3, 2-4 cm thick; Kaiho et al., 2006b) is a light gray illite–montmorillonite–kaolinite
472 claystone (white clay) (Table 4). Gypsum and pyrite are very common in thin section. No
473 fossil fragments are seen in thin section (Fig. 5A). Marine fossils of conodonts,
474 foraminifers, ostracods and tiny brachiopods have been found from this bed, but are
475 always sparse (Rui et al., 1988; Jiang et al., 2007). Benthic carbonate skeletal fossils
476 diminished dramatically in this bed. Calcareous shells are often pyritized and attached
477 with crystals and framboidal pyrites on the surface (Rui et al., 1988). Conodonts from
478 Bed 25 are included in the *C. meishanensis* Zone (Fig. 2). Microspherules and β-type
479 quartz crystals are much more abundant in this bed than in other ash clay beds, and could
480 be products of acid volcanic eruptions (He et al., 1987). However, comparable
481 microsphaerules are also abundant in the background soils in Meishan and other PTB
482 sections in South China, suggesting that they may be the modern industrial products
483 rather than geological objects (Zhang et al., 2014). Both Hf-isotope and elemental

analysis of magmatic zircons suggests these ash clays near the PTB in South China may have been sourced from volcanism taking place along the convergent continent margins during the formation of the Pangea supercontinent (Gao et al., 2013).

3.4. Bed 26

Bed 26, the so-called "black clay bed" (Yang et al., 1987), comprises black shale, 4-6 cm in thickness. Nine pronounced yellow clay layers are interbedded in the black shale. Horizontal laminae and pyrite are common. The clay layer is composed mainly of montmorillonite–illite, which is similar to that of Bed 25 (Table 4). Fossil fragments are very rare in most parts of this bed (Fig. 5B) except for the top 2-cm-interval where fossil fragments are fairly abundant in calcareous nodules (Fig. 8), including foraminifers, ostracods, echinoids, bryozoans, and brachiopods (Table 3; Figs. 6, 8). Microspherules or/and α-quartz (in the form of β quartz pseudomorphs; He, 1981) are rich in the lower part, but they may be the products of modern industry (Zhang et al., 2014). Various burrowing systems are common in the upper part of Bed 26, from which Cao and Zheng (2009, fig. 5b) identified *Chondrites*, *Planolites* and *Zoophycos*. The identification of the

501 last ichnogenus, however, is problematic based on insufficient information illustrated by
502 these authors. The upper part of the bed, Bed 26b, therefore is highly bioturbated (Fig. 3;
503 Cao and Zheng, 2009).

504 Skeletal fossils are rare but considerably diverse, including ammonoids,
505 brachiopods, bivalves, ostracods, and conodonts. Co-occurrence of the Triassic-type
506 faunas (i.e., *Otoceras*, *Claraia* and many conodont species) and Permian-type elements
507 (i.e., ammonoids *Pseudogastroceras* and *Xinodiscus*, and many brachiopods and
508 foraminifera) is particularly interesting. Brachiopods are small in size and thin-shelled,
509 and include species of *Orbicoiella*, *Prelissoryhnchia*, *Cathaysia*, *Paryphella*,
510 *Tethyochonetes*, and *Spinomarginifera* (Chen et al., 2006b; Chen and McNamara, 2006).
511 The presence of the relatively diverse fossil assemblage in the upper part of Bed 26
512 indicates the earliest re-colonization of epifauna on the barren soft substratum
513 immediately after volcanic eruption. Most of these shelly fossils are complete and well
514 preserved regardless of the delicacy of the skeleton. The change from Bed 26 to Bed 27 is
515 gradual and no boundary surface can be recognized. Crystal and framboidal pyrite are
516 concentrated in a discontinuous dark lamina with rich organics (Shen et al., 2007). The
517 slow sedimentation rate, and quiet and anoxic environment (Shen et al., 2007) suggest

518 that Bed 26 probably represents a semi-closed, low-energy subtidal zone (Fig. 3). The
519 succession of Beds 24e, 25 and 26, overall, shows that continuing fall of sea level through
520 Bed 24e turned to a rise in the upper part of Bed 26, with the lowest point of sea level
521 corresponding probably to the base of Bed 25 (Yin et al., 2014).
522
523 *3.5. Bed 27*
524
525 Bed 27 comprises biotic packstone to wackestone with occasionally micrite
526 texture and contains fairly abundant fossil skeletons and pyrite crystals throughout the
527 bed (see Section 6). Relatively complete shells of ostracodes, foraminifers and
528 thin-shelled brachiopods are reasonably abundant. This bed contains three major irregular
529 contact surfaces, termed hardground surfaces (Cao and Shang, 1998) and firmground
530 surfaces (Cao and Zheng, 2009), at various levels (Fig. 9). Of these, the first irregular
531 surface is rather pronounced, about 5 cm above the base of Bed 27 and near the boundary
532 between Beds 27a and 27b. The second occurs near the contact between Bed 27c and 27d,
533 while the third is not prominent and occurs within Bed 27d (Fig. 9). These 'firmground'
534 surfaces divide Bed 27 into three depositional cycles, with each beginning with dark

muddy limestone and grading upwards into pale bioclastic limestone. Rich organic and muddy laminae parallel to the bedding plane decrease upward from the base within each cycle. The upper unit of each cycle was disturbed by repeated burrowings, which form part of the firmground (see Section 5). Microscopic examination reveals that the dark, early-lithified rock contains a minor percent of clay, rich organic shreds and bioclasts (Fig. 9; Table 4).

Microfossils in Bed 27 are much more abundant and diverse than previously thought (Fig. 6). Of these, foraminifera are most abundant among all clades. Echinoids are also remarkably abundant, although they cannot be identified beyond a certain taxonomic level (Figs. 10-12). Bed 27a contains fossil skeletons of foraminifers, ostracods, echinoids, and brachiopods (Fig. 10), which is similar in component composition to Bed 26 (Fig. 6). Bed 27b comprises marls and clays in the lower part, in which fossil fragments are very rare (Fig. 9). The remainder of Bed 27b yields a fossil fragment abundance (FFA) composed mainly of foraminifers and brachiopods (Fig. 6). Both Beds 27c and 27d contain much more abundant and diverse FFA than Bed 27b (Figs. 10-12), both of which are dominated by foraminifers, ostracods and brachiopods with minor constituents of echinoids (Fig. 6).

552 It should be noted that Bed 27 is usually subdivided into four layers (Yin et al.,
553 2001). Cao and Zheng (2009), however, divided this bed into six layers (units) including a
554 stromatolite layer (Bed 27-5) and mudstone (Bed 27-6) in the upper part of Bed 27. Later,
555 Zheng et al. (2013) denied the existence of the stromatolite layer and divided Bed 27 into
556 five layers; no stromatolitic structures are seen in our thin sections either. Except for the
557 topmost 0.5 cm thick layer of carbonaceous mudstone, another four layers are similar to
558 those recognized by Yin et al. (2001). In addition, Cao and Zheng (2009) and Zheng et al.
559 (2013) interpreted the irregular surface separating Beds 27a and 27b (Fig. 9) as
560 firmground surface as a result of a rapid transgression. Here, we agree with the
561 firmground interpretation of these irregular surfaces within Bed 27 (Cao and Zheng, 2009;
562 Zheng et al., 2013) because of the presence of abundant burrows typical of the
563 *Glossifungites* ichnofacies (Seilacher, 1967) and distinct lithological interfaces, typically
564 dark muddy micrite overlain by light gray, coarser-grained bioclastic
565 packstone-wackestone, within Bed 27 (Fig. 9; see also Section 5). Firmgrounds of the
566 *Glossifungites* ichnofacies, also termed omission surfaces (Knaust, 1998), have been
567 extensively used in sequence stratigraphy to identify and characterize discontinuity
568 surfaces (Pemberton and Frey, 1985; MacEachern et al., 1992, 2007; Buatois and

569 Mángano, 2011). Within Bed 27, the unlined burrows penetrating into muddy limestone
570 are passively filled with coarser grains from the overlying stratum. This means that the
571 burrows remained open after the trace maker had left, thereby permitting bioclast grains
572 from subsequent depositional events to fill the open, stable burrows. Although the
573 majority of documented *Glossifungites* ichnofacies are from shallow-marine settings
574 (Knaust, 1998; Buatois and Mángano, 2011), this ichnofacies is also present in relatively
575 deep marine contexts, such as incision of submarine canyons during relative sea-level
576 falls (e.g. Dasgupta and Buatois, 2012) or autogenic erosional episodes by turbidity
577 currents and bottom currents (Savrda et al., 2001; Gérard and Bromley, 2008; Hubbard
578 and Shultz, 2008). As such, the *Glossifungites* ichnofacies from Bed 27 may represent an
579 omission surface, but cannot indicate a precise depositional environment for Bed 27.
580 Integration of lithofacies, paleoecologic and ichnofacies indicates that Bed 27 may have
581 been deposited on a carbonate ramp near the storm wave action zone (Fig. 3), as
582 suggested by Zhang et al. (1997; 2005).
583
584 *3.6. Bed 28*
585

586 Bed 28 comprises yellow claystone having similar composition to Bed 25 (Table
587 4), dominated by montmorillonite mixed with illite. Apart from conodonts (Jiang et al.,
588 2007), no other fossils have been recovered from this bed.
589
590 *3.7. Beds 29-59*
591
592 Bed 29 encompasses wackestone with rare foraminifer tests (Fig. 13). Pyrite is
593 commonly seen in thin section and pyrite content increases up-section. A minor omission
594 surface, equivalent to the erosional surface of Zhang et al. (2007) is developed in the
595 middle part of Bed 29 (Zhang et al., 2007). Fossil fragments are very rare and their
596 contents decrease upwards within the bed (Fig. 6; Table 3). Bed 30 is a marlstone, which
597 has a micritic texture and lacks any fossil fragments (Table 3). Both beds contain
598 laminated stratification and lack any cross bedding, indicating a low-energy environment.
599 Beds 29-30 therefore may have been deposited in the upper part of the offshore setting
600 that is below fair-weather wavebase (Chen et al., 2007).
601 Beds 31-51 are typified by alternating black shale, greenish gray mudstone, and
602 gray marlstone in the lower part, and interbeds of gray calcareous mudstone and pale

603 muddy limestone in its upper part. They are subdivided into 39 cm-scale cycles (Chen et
604 al., 2007; Fig. 3). In general, the lower unit of the cycle is characterized by black shale or
605 greenish mudstone rich in bivalve and ammonoid fossils (Fig. 4F, I), while the upper unit
606 is dominated by calcareous mudstone and marlstone. The mudstone-dominated cycles
607 are transitional to the marl-dominated cycles up-section, indicating a long-term
608 up-shallowing cycle (Chen et al., 2002, 2007; Tian et al., 2014). In addition to the
609 lithologic variation, Beds 31-34 are characterized by the calcareous mudstone and shale
610 where laminated stratifications are commonly preserved (Fig. 4C), while the upper part
611 of the formation (Beds 35-51) is typified by an increasing number of laminated marl beds
612 (Fig. 3). Fossil fragments occur occasionally in Beds 45, 50 and 51, characterized by
613 foraminifer and ostracod skeletons (Table 3; Fig. 6). Horizontal burrows of *Planolites* are
614 present in Beds 36-51, which also yield a few shell beds of bivalves (i.e., *Claraia*
615 *griesbachi*) and ammonoids (*Ophiceras* spp.) (Chen et al., 2007). This unit was
616 interpreted as the result of sedimentation relatively deep offshore (Fig. 3; Zhang et al.,
617 2005; Chen et al., 2007).

618 Beds 52-53 comprise alternations of shale and marlstone, yielding reasonably
619 abundant burrows of *Chondrites* and *Planolites*. Increasing fossil fragment content is

620 seen in both Beds 52 and 53, in which foraminifer, ostracod and echinoid shell fragments
621 are remarkable (Fig. 13), although they are definitely minority components in thin
622 section (Fig. 6; Table 3). Moreover, horizontal stratification is commonly present in both
623 shale and marlstone. These two beds were interpreted as the result of sedimentation in the
624 relatively deep offshore below storm wavebase (Chen et al., 2007).

625 Towards the top of the Yinkeng Formation, the succession (Beds 54-59) is
626 dominated by marl-dominated cycles. A thin- to medium-bedded marl is hummocky
627 cross-stratified (HCS; Fig. 4A, B, D) and often displays multidirectional tool marks on
628 its base, and horizons of loading and soft sediment deformation are very common (Chen
629 et al., 2002). Fossil fragments are reasonably abundant in Beds 54-59 (Fig. 13), although
630 they are still in the minority in thin section (Fig. 6; Table 3). Foraminifers, ostracod and
631 echinoids characterize their FFA (Fig. 6; Table 3). Trace fossils are also commonly
632 present in these beds, including *Planolites* isp. 2, *Treptichnus* sp., and *Thalassinoides* isp.
633 3. Moreover, the sedimentary structure HCS was interpreted as having been generated by
634 offshore storm currents. Beds 54-59 therefore may have been deposited offshore, near
635 storm wavebase (Chen et al., 2007).
636

4. Biotic changeover through the P-Tr transition

4.1. Biodiversity variations over the P-Tr transition

Comprehensive paleontological studies of the Meishan section were undertaken in the 1980s (Zhao et al., 1981; Sheng et al., 1984; Yang et al., 1987; Shi and Chen, 1987). The fossil record employed by Jin et al. (2000) to document the PTME pattern, which shows an abrupt extinction calibrated to the base of Bed 25, was sourced mainly from these studies. Since then, more diverse faunas and floras have been documented from Meishan, including foraminifers (Song et al., 2007, 2009), radiolarians (He et al., 2005), brachiopods (Chen et al., 2002, 2005a, 2006b; Li and Shen, 2008; Chen and Liao, 2009), conodonts (Nicoll et al., 2002; Tong and Yang, 2004; Luo et al., 2006, 2008; Jiang et al., 2007, 2008; Zhang et al., 2007, 2009; Yuan et al., 2014), ostracods (Crasquin et al., 2010; Forel and Crasquin, 2011), palynolomorphs (Zhang et al., 2007), and arcritarchs (Li et al., 2004). Additional macrofossils were collected throughout the upper Changhsing Formation to the Yinkeng Formation. Several shelly fossil communities from Beds 24, 26, 27, 32, 40, and 53-55 were quantitatively analysed (Chen et al., 2010a).

Shen et al. (2011b) and Wang et al. (2014) demonstrated a steep decline zone of species richness corresponding to the interval between Beds 25 and 28 in Meishan by a means of quantitative analysis on fossil records from more than ten PTB sections (including Meishan) from South China. In contrast, Song et al. (2013a) calculated species richness of each layer marked in microstratigraphic analysis (Beds 24-29) based on the updated fossil record mentioned above. Species richness of single layers experienced a stepwise but minor decline within Bed 24. Two distinct declines in species richness were well demonstrated and calibrated to Beds 25 and 28. The same pattern is also indicated in seven PTB sections in South China (Song et al., 2013a). Above Bed 28, species richness remains very low in the remaining part of the Yinkeng Formation.

Here, additional fossil specimens, primarily brachiopods, ammonoids and bivalves, have been collected from Beds 24e, 26, 27 to document biotic turnover across the PTB. Moreover, microfossils were observed in the petrologic thin sections used for microfacies analysis (see Section 3). Of these, foraminifers are the most abundant skeletal fragments among all clades. Most of these foraminifer tests, however, were illustrated by Song et al. (2007, 2009), so the newly obtained fossil record does not affect the biotic extinction pattern revealed by Song et al. (2013a).

671

672 *4.2. Fossil fragment content variations through the P-Tr transition*

673

674 The abundance and diversity of skeletal grains within the late Changhsingian
675 samples (Beds 22-24) is remarkably high. Skeletal grains from all sampled levels except
676 for the top 1-2 cm (Bed 24e-6) of Bed 24e comprise 68-74% of the total rock volume in
677 the uppermost Changhsing Formation (Fig. 14). Fossil fragment assemblages are
678 strikingly similar to one another in all sampled layers within the interval between Bed 22
679 and 24e-5, and each of these is dominated by foraminifers, crinoids and brachiopods.
680 Other major constituents include ostracods, bryozoans, sponge spicules, and macroalgae
681 (Fig. 14). Skeletal grains of gastropods, calcareous sponges and radiolarians are relatively
682 rare and absent in some horizons (Fig. 14).

683 It is noteworthy that FFAs do not appear to differ at all across the contact
684 between Beds 24d and 24e, although an omission surface, also a 3rd sequence boundary
685 (Zhang et al., 1997), separates these two layers (Zhang et al., 1997). In contrast, FFAs
686 experienced a dramatic reduction in diversity across a lime laminae layer between Beds
687 24e-5 and 24e-6 (Figs. 6, 14). Above this lamina layer (Fig. 7D), skeletal grains of Bed

688 24e-6 comprise about 60% of all rock in thin section in comparison with nearly 70% in
689 Beds 22-24e-5 (Fig. 14). The overwhelming majority of the FFA in Bed 24e-6 is sponge
690 spicules (35%) with minor constituents of foraminifers (8%), brachiopods (7%), crinoids
691 (6%), and echinoids (4%) (Table 3; Fig. 6). Furthermore, fusulinids disappeared forever
692 at this lamina (Kaiho et al., 2006b). The FFA experiences a loss of five major orders (i.e.,
693 ostracods, bryozoans, calcareous sponges, gastropods, and macroalgae) across the
694 boundary between Beds 24e-5 and 24e-6 (Figs. 6, 14). More importantly, this horizon
695 coincides with a pronounced negative carbon isotope excursion and a sulfur isotopic
696 excursion anomaly (Kaiho et al., 2006a, b), and thus marks the actual biotic extinction
697 horizon (Kaiho et al., 2006b).

698 Fossil fragment contents form a high plateau in both abundance and diversity,
699 comprising nearly 70% of total rock and including almost all skeletal clades recognized
700 from the Changshing Formation. They underwent a dramatic depletion in both abundance
701 and diversity in Beds 25-26a, which are nearly barren of skeletal grains (Fig. 14). This
702 severe depletion therefore is calibrated to the base of Bed 25, coinciding with the PTME
703 (Jin et al., 2000; Shen et al., 2011b) or the first phase of the PTME (Song et al., 2013a).
704 After the PTME, skeletal grains started to rebound in Bed 26b, the top 2-cm interval of

705 the bed and 8-10 cm above the base of Bed 25. Fossil fragments in Bed 26b, however,
706 comprise only 32% of all rock in comparison with nearly 70% before the PTME (Figs. 6,
707 14). The FFA in Bed 26b comprises mainly foraminifers, ostracods, brachiopods,
708 bryozoans, and echinoids (Fig. 7). Both foraminifers and echinoids are the most abundant
709 among all clades (Fig. 6). Of particular interest is the presence of both echinoids and
710 bryozoans, with bryozoans represented by fenestellid fragments. These two clades have
711 generally been believed to have gone extinct at the PTME (Sepkoski, 1981, 2002), but
712 instead they occur in the aftermath of the PTME at Meishan. Their body fossils were also
713 found in association with the *H. parvus* Zone in the neighbouring Huangzhishan section
714 of western Zhejiang Province (Chen et al., 2009).
715 Fossil fragment abundance remains almost same as in Bed 26b, comprising
716 nearly 31-38% through the entire Bed 27, except for Bed 27b, in which skeletal grains are
717 only 10% of all rock. Thus, fossil fragments rebounded and reached nearly half their
718 pre-extinction level with a major depletion occurring in mid-Bed 27 (Fig. 14). If
719 considering the FFA of the entire Bed 27, which contains elements of brachiopods,
720 bryozoans, foraminifers, and ostracods (Table 3), then recovery of FFA diversity in Bed
721 27 is marked by the re-appearance of 45.5% of all pre-extinction orders.

FFA experienced a major loss in Bed 29, down to less than 10% (Fig. 14). Fossil fragments are absent in Beds 28-44. After rebounding in Bed 45, the skeletal grain assemblage underwent a stepwise abundance recovery in Beds 50-51 and remained at a relatively stable level, occupying nearly 16% of all rock in Beds 52-60. FFA diversity, however, remains at a rather low level, with the re-appearance of only three orders: foraminifera, ostracods and echinoids (Fig. 14).

4.3. Community structural changes of shelly faunas

The P-Tr shelly communities are characterized by a mixture of large-sized ammonoids and small brachiopods in the uppermost Changhsing Formation and by numerous shell beds in the Yinkeng Formation (Fig. 15). Chen et al. (2010a) recognized six macrofossil communities from the uppermost Permian to lowest Triassic in Meishan, including the *Rotodiscoceras* sp.*–Paracrithyris pigmaea* (*R–P*) Community (Bed 24), *Tethyochonetes liaoi* (*T*) Community (Bed 26), *Paryphella triquetra–Tethyochonetes liaoi* (*P–T*) Community (Bed 27), *Claraia griesbachi–Ophiceras* sp. (*C–O*) Community (Bed 32), *Claraia wangi* (*C*) Community (Beds 40), and

739 *Meishanorhynchia–Lytophiceras* (*M–L*) Community (Beds 53-55).

740 Several diversity indices (Shannon and Simpson indices and Dominance) are
741 usually employed to measure community structures. It should be noted that the Shannon
742 measures are the only standard diversity indices that generate meaningful independent
743 alpha and beta components when the community weights are unequal or sampling is
744 uneven (Jost, 2007). Dominance index (D) measures 'evenness' of the community from 0
745 to 1, 0 being the most even distribution amongst taxa. Simpson index = 1–Dominance
746 index, and values range from 0 (one taxon dominates the community completely) to 1 (all
747 taxa are equally present) (Hammer et al., 2001). Note that these diversity indices are
748 useful in estimating diversity but are not themselves measures of diversity. Their
749 numerical equivalent indicates changes of true diversity (Jost, 2007; Kosnik and Wagner,
750 2006). Conversion of both Shannon and Dominance indices to true diversities developed
751 by Jost (2006, 2007) is performed to indicate true diversity changes over the P-Tr
752 transition. In addition, the bias-corrected Simpson evenness index (Olszewski, 2004) is
753 also applied to estimate the evenness within and among communities examined here.
754 Detailed community structural indices are listed on Table 5.

755 The late Changhsingian *R–P* community has Shannon index (H) of 2.029, which

is slightly smaller than the same index of 2.796 for the Changhsingian brachiopod *Cathaysia–Martinia* (*C–M*) community reported from the Shaiwa Group of southern Guizhou Province, southwest China (Chen et al., 2006a), but is slightly larger than the same index of 1.879 for the Wuchiapingian brachiopod *Edriosteges poyangensis–Spinomarginifera lopingensis* (*E–S*) Community reported from the basal Lungtan Formation of the Daijiagou section, Chongqing city, southwest China (Chen et al., 2005b). Dominance of the *R–P* community, D = 0.1519, also lies between the same indices of the above Changhsingian and Wuchiapingian brachiopod communities, with D = 0.07375 and 0.178, respectively (Chen et al., 2010b, table 4). It is also true for evenness of community (E) that the *R–P* community has E of 0.8453, which lies between 0.9262 and 0.822, the values of E for the *C–M* and *E–S* communities, respectively (Chen et al., 2010b). Accordingly, the *R–P* community is typical of Late Permian shelly communities.

In contrast, H values of all post-extinction communities, 1.47, 1.565, 0.7559, 0, and 1.288 for the *T*, *P–T*, *C–O*, *C*, and *M–L* communities, respectively (Table 5) are much smaller than the same values of the Changhsingian and Wuchiapingian communities, H = 2.796 and 1.879, respectively. These post-extinction communities therefore are much less diverse than the pre-extinction communities of the Late Permian, indicating the severe

773 impact of the PTME on marine communities.

774 Changes in both standard diversity Shannon index [Exp (H)] and dominance
775 index (D') between neighboring pairs of communities show that major losses in diversity
776 coincide with the turnovers of the *R–P/T* and *P–T/ C–O* communities, losing 43.6% and
777 55.5% respectively. Similarly, standard diversity dominance (D') increases by 34% and
778 54%, respectively (Table 6). Thus, community structural collapse indicated by a decrease
779 in diversity, coupled with increase in dominance, coincides with two extinctions
780 bracketed at the bases of Beds 25 and 28 at Meishan (Song et al., 2013a). In addition, Exp
781 (H) value increases by 262.6% from the *C* to *M–L* communities, and also increases by
782 70%, coupled with a decrease of 15.2% in D' values, from the *C–O* to *M–L* communities,
783 suggesting an improvement in shelly community structures in Beds 53-55 at Meishan.

784 Structural improvement of the *M-L* community is also reinforced by comparison
785 between the *M–L* community and the Anisian *Madonia* sp.*–Rhaetina angustaeformis*
786 (*M–R*) Community, which marks the recovery of benthic communities in the Anisian
787 (Chen et al., 2010b). The Anisian community has H and D values of 2.051 and 0.1501
788 respectively (Chen et al., 2010b, table 4), but the same values for the *M-L* community are
789 H = 1.288 and D = 0.4379, respectively. Consequently, the *M–L* community embraces

much more improved diversity indices than other Griesbachian communities in Meishan, but instead has a much lower diversity and higher dominance index than both pre-extinction and recovery communities.

5. Trace fossils and bioturbation

At Meishan, Bottjer et al. (1988) made the first attempt to ecologically test the PTME based on trace-fossil assemblages. These authors, however, could not collect sufficient trace fossils because of restricted exposure at that time, but they noted that ichnotaxa from the PTB beds are dominated by *Planolites* and *Chondrites*, which indicate generally a poorly oxygenated environment (Bottjer et al., 1988). Later, Cao and Shang (1998) reported a few ichnotaxa such as *Thalassinoides*, *Planolites* and *Skolithos* from the PTB beds of Meishan, but *Skolithos* was later rejected by these authors (Cao and Zheng, 2009; Zheng et al., 2013). Zhang and Tong (2010) also examined trace fossils recorded in drilling cores through the P-Tr transition in Meishan. Although these authors clarified that trace fossil evidence suggests two ecologic crises, coinciding with Beds 24e-27 and Beds 34-39, respectively (Zhang and Tong, 2010), the documented

807 ichnofossils are too few to support such a conclusion (see Section 7). As a result, several
808 lines of evidence show that trace fossils are reasonably abundant in the PTB beds in
809 Meishan. They however remain poorly understood owing to inadequate trace fossil
810 specimens.

811 Here, we document our observations at all PTB sites newly exposed during the
812 construction of the geological park in the GSSP Meishan in the 2000s, which uncovered
813 extensive fresh exposures along all the quarries (Fig. 1E). Abundant trace fossils were
814 collected from Beds 8-9 and 23-24 of the Changhsing Formation and Beds 26-27 and
815 35-57 of the Yinkeng Formation. The ichnofabric indices (ii, *sensu* Droser and Bottjer,
816 1986) and bedding plane bioturbation index (BPBI, Miller and Smail, 1997) throughout
817 the upper Changhsing Formation and entire Yinkeng Formation are also examined.

818

819 *5.1. P-Tr ichnotaxa and their stratigraphic distributions in Meishan*

820

821 *5.1.1. Stratigraphic distribution of ichnoassemblages*

822

823 A total of 17 ichnospecies in 13 ichnogenera and a problematic ichnotaxon have

824 been found in the P-Tr transition at Meishan (Figs. 16-18). Major characteristics,
825 stratigraphic distributions and interpretation of each ichnotaxon are tabulated here (Table
826 7). Trace fossils are distributed mainly in Beds 8-9 and Beds 23-24 of the Changhsing
827 Formation, and in Beds 27, 35-53, 55-57 of the Yinkeng Formation. Of these, the lower
828 Changhsing Formation (Beds 8-9) ichnoassemblage is dominated by relatively large
829 burrows of *Thalassinoides* isp. 1 (Fig. 16A, D) and resting traces of *Lockeia* isp. (Fig.
830 16F). *Paleophycus* isp. (Fig. 16B) is also commonly present in Beds 8-9.
831 The trace-fossil assemblage from Beds 23-24e is characterized by tree-like
832 traces of *Dendrorhaphe* isp. (Fig. 17F) and abundant burrows of problematic status. The
833 latter is represent by simple, straight, unbranched burrows (Fig. 17B-C), each originating
834 at a small, close end and extending distally to form a horn-shaped burrow with an open
835 distal end (Fig. 17B-C). Burrow diameters vary from 20-27 mm. Some burrows penetrate
836 the bedding at acute angles, and others are horizontally distributed on bedding planes.
837 The burrow has a distinct circular wall, about 2-5 mm thick. These burrows are preserved
838 in dark organic muddy limestone and filled with light-colored, coarse-grained sediments.
839 These morphologies suggest that this problematic form differs from all known ichnotaxa.
840 Another feature of the Bed 24 ichnoassemblage is the presence of abundant

841 ichnofossils near the contact between Beds 24d and 24e, including several distinct
842 burrowing ichnotaxa: *Balanoglossites triadicus*, *Taenidium* isp., *Thalassinoides* isp. 1,
843 and *Planolites* isp. 1. Of these, *Balanoglossites* is represented by vertical tubes (Fig. 16C)
844 that penetrate to a depth of 5-10 cm perpendicular to bedding. This ichnogenus occurs
845 usually at omission surfaces that served as sequence boundaries (i.e., Knaust, 1998).
846 These traces are preserved in limestone of the upper part of Bed 24d (Fig. 3). *Taenidium*
847 burrows (Fig. 16E, 17E) are also very common in Bed 24d-e, and they are usually
848 cylindrical, straight, unbranched, and backfilled. This ichnoassemblage as a whole
849 represents the *Balanoglossites* ichnofacies associated with the omission surface, as
850 described by Knaust (1998, 2004). In addition, horizontal burrows of *Planolites* isp. are
851 densely packed on top of Bed 24e (Fig. 17A, E), which is just beneath the base of Bed 25,
852 in which the PTME horizon is placed (Jin et al., 2000).
853 Abundant burrows were also found in association with an omission surface
854 within Bed 27. These burrows and the possible firmground surface have long remained
855 disputed, although several recent studies have addressed an ichnoassemblage of this bed
856 (Cao and Shang, 1998; Cao and Zheng, 2009; Zheng et al., 2013). Burrow systems
857 preserved in Bed 27 therefore are re-studied here (see below).

858 Beds 28-34 are barren of trace fossils. The remaining part of the lower Yinkeng
859 Formation (Beds 35-51) yields rare trace fossils, which are dominated by simple,
860 horizontal burrows of *Planolites* isp. 2 (Fig. 18A-B). Increasing numbers of ichnotaxa
861 occur in the upper Yinkeng Formation and are characterized by the presence of the
862 tree-like burrow system of *Chondrites* isp. (Bed 52; Fig. 18C) and relatively complicated
863 burrows of *Thalassinoides* isp. 3 (Fig. 18D-E) and *Treptichnus* isp. (Fig. 18G-H).
864
865 *5.1.2. Ichnofabric changes within Bed 27*
866
867 Within Bed 27, intensive burrowing on an omission surface, characteristic of the
868 *Glossifungites* ichnofacies, caused a pronounced relief on the firmground surface up to 3
869 cm high near the boundary between Beds 27a and 27b (Figs. 19-20). The firmground of
870 *Glossifungites* ichnofacies is partly covered by a faintly laminar black muddy limestone
871 that seems resistant to weathering. Highly irregular relief at the surface of the firmground
872 indicates that the solid rock was affected deep subsolution (Savrda, 1992). Trace fossils
873 increase upward to the contact between Beds 27c and 27d, which is overlain by finely
874 laminated muddy limestone (Bed 27d) again.

To reconstruct complete burrowing systems within Bed 27, one complete sample of the bed (from base to top) was cut and separated into three blocks (Fig. 19). The transverse view from three polished slabs shows the colonizing zonation (CZ) from base to top of the bed by various ichnocoenoses within a 16-cm-thick unit (Fig. 20).

CZ I: This is a historical zone, a unit that is beyond the reach of even the deepest burrows (Fig. 20). CZ I includes the first 2-3 cm of the lower part of Bed 27, which comprises gray, calcareous mudstone to muddy limestone and is almost barren of trace fossils. Minor bioturbation is also limited. Body fossils are scarce, except some small, thin-bedded brachiopods and foraminifers. Pyrite framboids and crystals are relatively rich and occur in both sediments and fossil shells (see Section 6).

CZ II: This is a transitional zone (Fig. 20), which is extremely heterogeneous from the activity of deeper burrows (Savrda, 1992). Sediments in this zone were semi-lithified to form a firmground substratum. Firmground sediments are dark-colored, and are disrupted by passively filled burrows of an ichnoassemblage characteristic of the *Glossifungites* ichnofacies. Representative ichnogenera include *Arenicolites*, *Gastrochaenolites*, *Psilonichnus*, and *Thalassinoides*. Of these, *Arenicolites* comprises vertical burrows that penetrate into the dark gray sediments. *Gastrochaenolites* comprises

892 tear-shaped borings, now filled with light gray, coarse-grained sediments in a
893 dark-colored firmground lime muddy substrate. This ichnogenus is commonly present in
894 the *Trypanites* ichnofacies as well (Wilson and Palmer, 1998; Benner and Ekdale, 2004).
895 The vertical cylindrical burrows of *Psilonichnus* are inclined, with bedding in the distal
896 end (Buatois and Mángano, 2011). *Thalassinoides* is typified by its Y-shaped ramification.
897 All these burrows have unlined walls and are filled with light gray-colored,
898 coarse-grained sediments of the overlying layer, indicating that these burrows were
899 passively filled.
900 CZ III: This is a very thin, highly condensed omission surface (Fig. 20), which is
901 characterized by some coarse-grained, reworked sediments that were generated by
902 frequent activity of wave currents. This omission surface is distinguished from the
903 underlying firmground ichnocoenosis of *Glossifungites* ichnofacies and overlying
904 softground ichnocoenosis of *Cruziana* ichnofacies (see below).
905 CZ IV: This is a mixed unit (Fig. 20), which is saturated with water and totally
906 homogenized by bioturbation. This unit, about 5 cm thick, yields ichnocoenoses
907 represented by minute burrows of *Diplocraterion* isp. and tear-shaped borings, which
908 resemble the vertical features of *Chondrites* and small *Planolites*. Owing to the soft

909 nature of substrate and intensive bioturbation, burrow boundaries and morphologies have
910 become blurred, making it difficult to identify them confidently to ichnogenus level. This
911 ichnoassemblage, together with the soft substrate, is characteristic of the softground
912 ichnocoenosis of *Cruziana* ichnofacies (Seilacher, 1977).
913 CZ V: This thin unit is devoid of bioturbation and comprises finely laminated
914 muddy layers (Fig. 20), which yield small pyrite framboids (see Section 6), indicating the
915 establishment of a quiet, low energy and probably reduced environment.
916
917 *5.2. Extent of bioturbation*
918
919 Ichnofabric indices (Droser and Bottjer, 1986) of the Upper Changhsing
920 Formation (Beds 22–24) are usually rather low (ii1-2) with several peaks reaching 3 (ii3)
921 except for the horizons near the boundary between Beds 24d and 24e (Fig. 3) that records
922 an ichnofabric index of 4 (ii4), but bioturbated strata are about 80% of the entire
923 measured units of the Changhsing Formation. Ichnofabric indices decrease to 2 (ii 2)
924 again at the upper part of Bed 24e, then increase to 3 (ii3) at the top of the bed. No
925 ichnofabrics are observed in Beds 25-26a. The ii value surges to 3 (ii3) in Beds 26b-27,

926 with 40% strata bioturbated. Beds 28-34 are void of ichnofabrics again. The ii value of
927 Beds 35-57 remains rather low (ii1) except for several peaks reaching 2 (ii2) in Beds 42,
928 46, 52-53, and 56-57 (Fig. 3). Only 15% of the examined units are bioturbated.
929 Accordingly, ichnofabric indices of the upper Changhsing Formation vary from 2 to 4
930 (ii2–4). Averagely 80% strata of the upper Changhsing Formation are significantly
931 bioturbated. Ichnofabric indices from Bed 27 remain relatively high (ii4), although only
932 40% strata are bioturbated. The remaining part of the lower Yinkeng Formation records a
933 rather low ii value (ii1) and no strata are significantly bioturbated. Ichnofabric indices in
934 the middle and upper parts of the Yinkeng Formation vary from 1 to 2 (ii1-2). On average,
935 15% of strata are significantly bioturbated.
936 In the upper Changhsing Formation, the two bedding planes in Bed 23
937 containing *Dendrorhaphe* isp. (Fig. 17F) and the problematic trace (Fig. 17D), show
938 coverage of 90% and thus indicate a BPBI of 5 (Fig. 3). The same BPBI value (ii 5) is also
939 estimated from two horizons of Beds 24d, containing *Taenidium* burrows. Bedding planes
940 from other horizons in the upper Changhsing Formation generally have bioturbation
941 coverage varying from 10% to 60%, indicating BPBI of 1-5. For the top bedding plane of
942 Bed 24e, just below the mass extinction horizon, containing *Planolites* (Fig. 17A, E) the

943 coverage was up to 90%, indicating a BPBI of 5. Beds 25-26a have the lowest BPBI, with
944 almost no bioturbation recorded. Several bedding planes from Beds 26b-27 show changes
945 in coverage from 20% to 40%, indicating a BPBI of 2-4. Bedding plane coverage in Beds
946 28-34 is generally rather low because bioturbation is broadly absent. Beds 35-51, overall,
947 have bioturbation coverage <10%, but some bedding planes containing *Planolites* show
948 coverage up to 20%, indicating a BPBI of 2. Another bedding plane containing
949 *Chondrites* has coverage up to 90%, indicating a BPBI of 5. In the upper Yinkeng
950 Formation, one bedding plane containing *Thalassinoides* shows coverage up to 20%,
951 indicating a BPBI of 2.
952
953 *5.3. Changeover of trace-fossil diversity over the P-Tr transition*
954
955 Ichnodiversity, represented by ichnogeneric richness, decreased remarkably
956 over the P-Tr transition. Eight ichnogenera are commonly encountered in the uppermost
957 Changhsing Formation: *Balanoglossites*, *Dendrorhaphe*, *Lockeia*, *Paleophycus*,
958 *Planolites*, Problematica, *Taenidium*, and *Thalassinoides* (Fig. 21A). Only *Planolites* is
959 present at the top of Bed 24e, dropping to 87.5% in the upper part of Bed 24e. All

960 ichnotaxa disappear at the top of Bed 24e, coinciding with the PTME. As a consequence,
961 Beds 25-26a are barren of ichnotaxa. The ichnofauna rebounded in Bed 26b and
962 diversified in Bed 27, including seven ichnogenera: *Arenicolites*, *Diplocraterion*,
963 *Gastrochaenolites*, *Psilonichnus*, *Thalassinoides*, *Chondrites*, and *Planolites*. Of
964 particular interest is the presence of four vertically burrowing ichnogenera (*Arenicolites*,
965 *Diplocraterion*, *Gastrochaenolites*, *Psilonichnus*) and one relatively complicated
966 burrowing ichnogenus (*Thalassinoides*), implying that ichnodiversity almost reached the
967 pre-extinction level in Bed 27 (Fig. 21A). All ichnotaxa disappeared soon after (in Bed
968 28). As a consequence, Beds 28-34, ranging through conodont zones *I. isarcica* and *I.*
969 *planata* Zones, lack any ichnotaxa and remained poorly bioturbed (Fig. 3).The
970 post-extinction rebound of ichnotaxa is marked by the presence of *Planolites* in Bed 35.
971 Since then, ichnodiversity remained at a rather low level and did not increase until the
972 middle-late Griesbachian, which saw the rise of *Chondrites* in Bed 52. Although
973 *Chondrites* disappeared in the middle-late Griesbachian, the trace-fossil assemblage
974 slightly diversified and included *Planolites*, *Treptichnus* and *Thalassinoides*.
975 As a result, P-Tr ichnotaxa underwent two pronounced reductions in diversity
976 coinciding with the two episodes of PTME calibrated to the bases of Beds 25 and 28.

977 Ichnofaunas fell to their lowest diversity in the early Griesbachian, and experienced a
978 slow increase in diversity throughout the middle-late Griesbachian (Fig. 21A). However,
979 post-extinction trace-fossil diversity never returned to the pre-extinction level.
980
981 *5.4. Burrow size variations through the P-Tr transition*
982
983 Nine bedding planes were examined to determine the size distribution of burrow
984 diameters of *Arenicolites*, *Dendrorhaphe*, *Diplocraterion*, *Paleophycus*, *Planolites*,
985 Problematica, *Taenidium*, *Thalassinoides*, and *Treptichnus* (Fig. 22). Burrow size change
986 over the P-Tr transition is apparent, especially in *Planolites*, as well as other traces such
987 as *Balanoglossites*, *Chondrites*, *Dendrorhaphe*, *Taenidium*, *Thalassinoides*, *Treptichnus*,
988 and Problematica (Fig. 22). *Planolites* is distributed in ten horizons throughout the
989 uppermost Changhsingian to middle-upper Griesbachian, and thus is a good proxy for
990 size variation of trace fossils over the P-Tr transition. Mean diameters of the Changhsing
991 Formation *Planolites* burrows are 7 mm, 8.5 mm, and 5.5 mm, respectively from three
992 horizons, with maximum burrow diameter up to 9.2 mm (Fig. 22A). Burrow sizes
993 decrease remarkably across the boundary between Beds 24 and 25, the PTME horizon

994 (Fig. 1B), with mean burrow diameters of 1.7 mm and the greatest burrow diameter only
995 2.2 mm in Bed 27 (Fig. 22A). Burrow sizes of *Planolites* remain very small throughout
996 the early-middle Griesbachian and become larger by the late Griesbachian (Beds 54-57).
997 These late Griesbachian traces are still much smaller than their counterparts recorded in
998 the pre-extinction strata (Fig. 22A). Comparable size change over the P-Tr transition is
999 also demonstrated by both the greatest size and mean size of *Thalassinoides* from the
1000 same interval (Fig. 22B).

1001 Several other ichnotaxa in the uppermost Permian have mean and maximum
1002 diameters, such as *Balanoglossites* (4.6 mm, 6.4 mm), *Dendrorhape* (12 mm, 17 mm),
1003 problematica (22 mm, 28 mm), and *Taenidium* (7.8-8.8 mm, 9.2 mm), that are obviously
1004 larger than that of those ichnotaxa confined to the lowest Triassic, i.e., *Chondrites* (2.8
1005 mm, 5.6 mm) and *Treptichnus* (6.3 mm, 6.3 mm) (Fig. 22C-D). When the measurements
1006 of all 273 burrows measured from the P-Tr strata of Meishan are combined, both mean
1007 and maximum diameters exhibit remarkable reduction across the boundary between Beds
1008 24 and 25 and remain very low values until Bed 27. The same values further decline from
1009 Bed 27 to Beds 28-34, and then undergo a stepwise increase through Beds 35-57 (Fig.
1010 21B)

Trace-fossil size variations over the P-Tr transition are consistent with figures from northern Italy (Twitchett, 1999; Twitchett and Barras, 2004) and South China (Chen et al., 2011). It should be noted that the Early Triassic *Planolites* traces are much smaller than their Changhsingian counterparts at Meishan (Fig. 22A), unlike the same traces elsewhere (Pruss and Bottjer, 2004). *Planolites* is supposed to be the least susceptible to mass extinction because this simple trace can be produced by a variety of organisms (Pruss and Bottjer, 2004). Accordingly, the Changhsingian *Planolites* and their Early Triassic counterparts may have been made by different organisms.

5.5. Trace fossil form and complexity

The Changhsing Formation trace fossils are morphologically diversified, and include simple, horizontal burrows (*Planolites*), vertical or oblique burrows (*Balanoglossites* and Problematica), resting traces (*Lockeia*), and complex forms (*Dendrorhape*, *Taenidium*, and *Thalassinoides*). They, however, disappear across the PTME horizon (base of Bed 25). Both *Planolites* and *Thalassinoides* rebound in Bed 27, but decrease markedly in size in comparison with their Changhsingian counterparts.

1028 *Thalassinoides* is also less complex than the same trace recorded in the Changhsingian.
1029 Complex forms, and resting and vertical traces of the Changhsingian (*Balanoglossites*,
1030 *Lockeia*, *Taenidium*, *Dendrorhape*, and Problematica) vanish in Bed 27. Instead, the
1031 relatively complex burrow systems of the *Glossifungites* ichnofacies, i.e., *Arenicolites*,
1032 *Gastrochaenolites*, *Psilonichnus*, and *Thalassinoides*, characterize the ichnoassemblage
1033 in the lower part of Bed 27. Vertical burrows of *Diplocraterion*, together with *Chondrites*
1034 and *Planolites* also occur in the upper part of Bed 27. Accordingly, ichnotaxa recovered
1035 from the pre-extinction level are similar to those in Bed 27 in terms of complexity,
1036 although these burrows are much smaller than their counterparts elsewhere.
1037 Early Griesbachian traces are dominated by small, simple, horizontal burrows of
1038 *Planolites*, as reported elsewhere (Twitchett and Barras, 2004; Pruss and Bottjer, 2004;
1039 Fraiser and Bottjer, 2009; Chen et al., 2011, 2012). In the middle-late Griesbachian trace
1040 fossils become slightly more complex and are marked by the presence of *Chondrites*,
1041 *Thalassinoides* and *Treptichnus*, although these burrows are still very small. Nevertheless,
1042 these middle-late Griesbachian burrows are branched and form slightly complex
1043 networks, and thus are more complex than the *Planolites*-dominated ichnoassemblage in
1044 the early Griesbachian.

1045 As a result, trace-fossil complexity, reflecting behavioral complexity of the
1046 trace-makers, decreased dramatically during the PTME. Then, the trace-fossil
1047 assemblage shows an increase in complexity, varying from simple, horizontal traces (i.e.,
1048 *Planolites*) in the early Griesbachian to relatively complex traces (*Chondrites*,
1049 *Thalassinoides* and *Treptichnus*) in the middle-upper Griesbachian. In particular, the
1050 reappearance of *Thalassinoides* and *Treptichnus* probably implies increasing behavioral
1051 complexity that typically indicates the beginning of biotic recovery elsewhere (Twitchett
1052 and Barras, 2004).
1053
1054 *5.6. Infaunal tiering*
1055
1056 Levels of tiering above and below the sediment were greatly reduced after the
1057 PTME (Ausich and Bottjer, 1982, 2002). At Meishan, the change in infaunal tiering over
1058 the P-Tr transition is reflected by the penetration depth of burrows (Fig. 21C), which was
1059 measured in the field. Vertical burrows of the Changhsing Formation may extend a
1060 maximum depth of 10 cm into the sediment, indicating a rather deep tiering level (ii5). In
1061 contrast, burrows of *Planolites* and *Thalassinoides* recorded in Bed 27 may penetrate to <

2 cm into the sediment. In particular, *Thalassinoides* commonly shows the second tiering level (ii2) (Bottjer and Droser, 1994). Early Griesbachian *Planolites* has burrows extending to a maximum depth of only 0.5 cm (Fig. 21C) indicating the lowest tiering level (ii1) (Bottjer and Droser, 1994). Thus, tiering fell to its minimum level in the early Griesbachian. An increase in tiering level during the middle Griesbachian is marked by the presence of *Chondrites*, an anoxic burrow system penetrating to a depth up to 1-2 cm and indicating the second tiering level (ii2) (Bottjer and Droser, 1994). The same tiering level is also reflected in upper Griesbachian *Thalassinoides* and *Treptichnus* burrows, which may extend to a maximum depth of 1-2 cm (Fig. 21C). Accordingly, the tiering level decreases significantly across the PTME horizon in Meishan, and then increases throughout the Griesbachian (Fig. 21C).

6. Size variations of pyrite framboids and redox conditions over the P-Tr transition

Pyrite is commonly present in the latest Changhsingian to Griesbachian rocks at Meishan (Wignall and Hallam, 1993), which is also confirmed by our observations of thin sections through the P-Tr transition at Meishan. Several pyrite-enriched beds have

1079 been treated as indications of anoxic conditions at Meishan (Wignall and Hallam, 1993).
1080 In particular, pyrite framboids, which are spherical aggregates of pyrite microcrystals, are
1081 rather abundant in these pyrite-enriched beds near the PTB at Meishan (Jiang et al., 2006;
1082 Shen et al., 2007). Pyrite framboids in ancient and modern sediments are interpreted as
1083 the result of redox conditions (e.g., Bond and Wignall, 2010), and these authors show that
1084 small framboids, usually 3-5 μm in diameter, indicate euxinic conditions (H_2S-bearing,
1085 O_2-free bottom waters). Accordingly, pyrite framboids have been considered as one of
1086 the most important pieces of evidence indicating redox conditions over the P-Tr transition
1087 worldwide (Wignall et al., 1998, 2005; Jiang et al., 2006; Shen et al., 2007; Gorjan et al.,
1088 2007; Bond and Wignall, 2010; Algeo et al., 2011b).
1089 At Meishan, Jiang et al. (2006) reported that pyrite framboids are commonly
1090 present in all beds through the PTB (Beds 24-29), based on etched residues from bulk
1091 samples. Shen et al. (2007) also observed framboids *in situ* on polished blocks and etched
1092 residues. Both studies detected that framboids are abundant in Bed 25. Contrasting to
1093 Jiang et al.'s (2006) observation, Shen et al. (2007) found no pyrite framboids in Bed 27.
1094 However, unequal sampling in various beds near the PTB, for instance, 40 g each from
1095 Beds 25 and 26, but only 5 g each from Beds 24, 27, 28 and 29 may have biased their

1096 observation (Shen et al., 2007). Bed 27 comprises various lithologies from its base to top,
1097 which may have been deposited in different environments (Figs. 19-20). Thus, pyrite
1098 framboids may be absent in these bioturbated layers (i.e., CZs II, III-IV in Bed 24; Fig.
1099 20), but instead may occur in finely laminated layers without bioburbation (i.e., CZs I and
1100 V; Fig. 20).

1101 We have also observed pyrite framboids in continuous thin sections throughout
1102 Beds 24-30. We used a FEI Quanta 400 Scanning Electron Microscope (SEM) equipped
1103 with a GENESERS 2000 energy dispersive spectrometer (EDS) at the State Key
1104 Laboratory of Biogeology and Environmental Geology, China University of Geosciences,
1105 Wuhan, China. SEM images and EDS spectra were produced by the Zeiss VPSEM
1106 coupled with an energy dispersive X-ray spectrometer. We confirmed Jiang et al.'s (2006)
1107 observation that both pyrite framboids and crystals occur in Bed 27 on brachiopod shells
1108 and in foraminiferal tests and sediments (Fig. 23). In addition, we measured framboid
1109 sizes in samples from Beds 29-60 using the SEM. Pyrite framboids are abundant in
1110 samples from 17 horizons over the P-Tr transition (Fig. 24). The majority of framboid
1111 diameters in most measured beds are smaller than, or around 5 μm, except for Beds 28
1112 and 44, in which most framboids have diameters of 7-8μm. Moreover, framboid

1113 diameters are concentrated in a narrow size range (< 10μm) in Beds 27, 28, 43, and 58. In
1114 contrast, they have a greater size range in Beds 24b, 24e, 25-26, 29-30, 39, 42, 49, 51-52
1115 and 56, with maximum diameter up to 20μm in Bed 51.
1116 Bond and Wignall (2010, table 1) proposed several characters, including
1117 framboid diameter and pyrite morphology, to determine redox conditions during
1118 deposition. In general, when framboids are small (mean diameters: 3-5 μm), abundant,
1119 with a narrow size range, and form the dominant pyrite fraction, they could have been
1120 deposited in euxinic condition (with a persistently sulfidic lower water column). If
1121 framboids are small (mean diameters: 4-6 μm), abundant, with a few, larger forms, and
1122 dominate the pyrite fraction, then they could have been deposited in anoxic condition
1123 (without oxygen in bottom waters for long periods). When framboids have mean
1124 diameters of 6-10 μm and are moderately common, with a few, larger framboids together
1125 with some crystalline pyrite, they could have been deposited in lower dysoxic condition
1126 (with weakly oxygenated bottom waters). In upper dysoxic condition (with partial
1127 oxygen restriction in bottom waters) framboids are commonly to rarely present, with a
1128 broad range of sizes, only a small proportion of framboids < 5μm, and the majority of
1129 pyrite as crystals. In oxic condition (without oxygen restriction), no framboids are present,

1130 and pyrite crystals occur rarely.

1131 If these five criteria given by Bond and Wignall (2010) are followed, we can
1132 determine redox conditions over the P-Tr transition in Meishan. Bed 24 contains
1133 abundant framboids, usually around 5 μm in diameter with some larger framboids, and
1134 their size range is relatively broad, pointing to anoxic conditions. Framboids in Beds
1135 25-26 are usually 3-5 μm in diameter, a narrow size range, and no pyrite crystals are
1136 present, suggesting euxinic conditions (Fig. 25). Framboids from Bed 27 have a relatively
1137 large diameter and a broad size range (Fig. 24), and are also associated with some large
1138 pyrite crystals, pointing to a lower to upper dysoxic condition (Fig. 25). Pyrite framboids
1139 are moderately common in Bed 28 and have mean diameters of 8-9 μm, but no larger
1140 framboids and crystalline pyrite occur. Thus, Bed 28 is inferred to be deposited in a
1141 transitional zone between anoxic and lower dysoxic conditions based on the criteria
1142 determining redox conditions proposed by Bond and Wignall (2010). Redox conditions
1143 became euxinic soon after in Bed 29, in which framboids are very small (3-5 μm) and
1144 have a narrow size range, without pyrite crystals. It should be noted that no pyrite
1145 framboids were found in Beds 30-35, although a pronounced negative excursion of
1146 carbon isotopes (Xie et al., 2007) and environmental stress indicated by biomarker

1147 signals (Yin et al., 2012) occur in these beds. Framboids from Beds 39 and 42 indicate
1148 euxinic-anoxic transitional conditions in terms of diameter, size range and association
1149 with pyrite crystals. Framboids from Bed 43 are 4-6 μm in diameter, but have some larger
1150 forms and are also associated with some pronounced pyrite crystals, and thus indicate a
1151 lower to upper dysoxic condition. Then, redox conditions indicated by pyrite framboids
1152 changed to anoxic to euxinic transitional conditions. Surprisingly, framboids from Bed
1153 58 suggest euxinic condition, which coincides with the last negative excursion of carbon
1154 isotopes in the middle-late Griesbachian detected by Burgess et al. (2014).
1155
1156 **7. Assessing ecologically PTME and its aftermath**
1157
1158 *7.1. Testing ecologically extinction patterns*
1159
1160 The updated fossil record from Meishan shows two pronounced declines of
1161 species richness at the bases of Beds 25 and 28 (Song et al., 2013a; Fig. 26). Similarly,
1162 fossil fragment contents recorded in thin sections also show two distinct drops in both
1163 abundance and diversity corresponding to the top of Bed 24e and base of Bed 28 (Figs. 6,

14). Further, ichnodiversity also declined within Beds 24 and 27. In Bed 24, trace fossils are rather abundant and comprise four distinct ichnogenera: *Balanoglossites*, *Planolites*, *Taenidium* and *Thalassinoides* in horizons near the boundary between Beds 24d and 24e, but only *Planolites* persisted into Bed 24e-6, in which relatively large burrows are densely packed, indicating a considerably high bioturbation level. All ichnotaxa disappeared in Beds 25-26a. Similarly, ichnotaxa decline from five ichnogenera (*Arenicolites*, *Gastrochaenolites*, *Planolites*, *Psilonichnus*, and *Thalassinoides*) in CZ II (Bed 27b) to three ichnogenera (*Diplocraterion*, *Chondrites* and *Planolites*) in CZ IV (Bed 27c), and then further declined and disappeared at the top of Bed 27d. Other proxies of trace fossils and bioturbation also show two pronounced declines corresponding to the bases of Beds 25 and 28. Clearly, the PTME ecologic crisis comprised two phases, coinciding with metazoan extinctions calibrated to the bases of Beds 25 and 28 (Song et al., 2013a).

In addition, both fossil fragment contents and ichnodiversity show that a pronounced decline in diversity and abundance started at the stratal interval 10 to 19 mm below the top of Bed 24e. The boundary between Beds 24e-5 and 24e-6 is the most distinct eliminated horizon of skeletal fragment of major fossil groups, coinciding with

1181 end-Permian sulfur anomaly (Kaiho et al., 2006a) and the start of the negative
1182 end-Permian carbon isotopic excursion (Kaiho et al., 2009), and thus may indicate the
1183 PTME. Abundant sponge spicules above this event horizon indicate that they lasted in
1184 seawater for a while, although complete sponge fossils disappeared at the PTME event. It
1185 is therefore unlikely that the disappearance of calcareous fossils at the top of bed 24e-6
1186 was a result of an increase in the input of terrestrial material associated with the facies
1187 shift, as indicated by the lithologic shift from the limestone of Bed 24 to the claystone of
1188 Bed 25 and black shale of Bed 26. Instead, the extinction of calcareous biota and the
1189 associated environmental perturbation was most likely caused the lithologic change from
1190 limestone to mudstone. As a result, the sharp decline in biotic abundance and diversity
1191 10-19 mm below the top of Bed 24e may signal the first episode of the PTME previously
1192 inferred from statistical paleontological data (Song et al., 2013a).
1193
1194 *7.2. Ecologic collapse lagging behind biodiversity crisis during the PTME*
1195
1196 At Meishan, the Permian biota experienced a dramatic drop in diversity at the
1197 base of Bed 25, with 172 species (94%) being wiped out in Beds 25-26 and no

1198 pronounced reduction of species richness in Bed 28 (Jin et al., 2000). The updated fossil
1199 record obtained from Meishan shows that species richness was reduced by at least 79%
1200 across the boundary between Beds 24e and 25, compared to 65% loss in species richness
1201 across the boundary between Beds 27d and 28 (Song et al., 2013a). This means that
1202 marine animals suffered a more severe depletion in species richness in the first phase of
1203 the PTME than in the second phase of the same event (Fig. 26). The biodiversity decline
1204 pattern from Meishan is confirmed by the same pattern at a further seven PTB sections in
1205 South China (Song et al., 2013a). It should also be noted that generic richness declined by
1206 a similar magnitude, 85% and 82%, in the first and second phases of the PTME,
1207 respectively in Meishan, but both generic and species richness underwent a stepwise
1208 decline from the uppermost Changhsingian to lowest Griesbachian (Fig. 26).
1209 Consequently, biotic diversity suffered a larger loss in the first episode than in the second
1210 episode of the PTME in terms of the number of lost taxa. This pattern is reinforced by
1211 fossil fragment content variations across the PTME horizons. Fossil components usually
1212 occupy nearly 70% in all rock in strata below Bed 25, but only about 30% in Bed 27, and
1213 FFA lost nearly 60% in thin section (Fig. 14). Over the same period, 11 Permian orders
1214 declined to five orders in Bed 27, losing 54.5% in ordinal richness.

1215 Both the standard diversity Shannon index [Exp (H)] and dominance index (D')
1216 assess whether the shelly community possesses a healthy structure. Exp (H) values
1217 declined by 43.6% from the *R–P* to *T* communities, and 55.5% from the *P–T* to *C–O*
1218 communities, coinciding with the first and second phases of the PTME, respectively. This
1219 means that the shelly communities suffered a greater loss in community diversity in the
1220 second phase of the PTME than in the first phase. Similarly, standard diversity
1221 dominance (D') increases by 34% and 54% during the two pronounced drops in diversity,
1222 respectively (Table 6). This means that the shelly communities became more uneven after
1223 the second phase of the PTME than after the first phase. Thus, shelly communities
1224 underwent relatively more serious ecologic crisis in the second phase than in the first
1225 phase of the PTME. This observation is also reinforced by ichnofaunal variations and
1226 ichnofabric changes over the P-Tr transition in Meishan.
1227 The presence of seven ichnogenera in Bed 27 suggests that ichnogeneric
1228 richness nearly recovered to the pre-extinction level, although there was a taxonomic loss
1229 in Beds 25-26a. In contrast, a more dramatic ichnofaunal loss occurred in the second
1230 phase of the PTME, corresponding to Bed 28. As a consequence, Beds 28-34 are barren
1231 of ichnotaxa. Thus, ichnofaunas suffered a more severe decline in the second phase of the

1232 PTME. This pattern is also strengthened by burrow size variations and tiering level
1233 changes, both of which remained relatively high in the Changhsingian, and experienced a
1234 stepwise decline through Beds 23-27, then fell to their lowest values in the early
1235 Griesbachian (Beds 28-34). Ichnofabric variation also shows that Bed 27 still remains
1236 highly bioturbated and yields rather complex burrow systems of the *Glossifungites*
1237 ichnofacies and *Cruziana* ichnofacies, which are commonly present in the pre-extinction
1238 period, thus showing the largest turnover at the base of Bed 28 rather than at the base of
1239 Bed 25. In contrast, ichnotaxa became very rare after the second phase of the PTME,
1240 although 2-3 ichnotaxa rebounded in the middle-late Griesbachian. Consequently, the
1241 greatest losses of ichnotaxa correspond to the top of Bed 27, simultaneous with the
1242 second phase of metazoan extinction in Meishan (Song et al., 2013a). This ichnodiversity
1243 drop coincides with a remarkable decrease in tiering level (Fig. 21) and burrowing
1244 intensity (Fig. 3). Ichnofabric indices recorded in the upper Changhsing Formation are
1245 rather high (ii4-5) (Fig. 3). Complex traces of both the *Glossifungites* and *Cruziana*
1246 ichnofacies recorded in Bed 27 (Figs. 19-20) also indicate a fairly high ichnofabric index
1247 (ii3-4). Consequently, there was not a sharp decrease, but a gradual decrease, in
1248 burrowing intensity (ii4-5 down to ii3-4) over the first phase of the PTME. This is in

1249 sharp contrast to the pronounced drop in biodiversity of metazoans in this phase of the
1250 PTME (Fig. 26), suggesting a gradual worsening in environmental conditions.

1251 In contrast, almost all of the complex traces of the *Glossifungites* and *Cruziana*
1252 ichnofacies disappeared in the second phase of the PTME. The early Griesbachian
1253 *Planolites* is confined to discrete horizons (ii1-2) separated by metres of unbioturbated
1254 sediment, and indicates a rather low ichnofabric index (ii1) (Fig. 3). A low ichnofabric
1255 index indicates an absence or rarity of burrowing infauna, which in turn implies a stressed
1256 environment immediately after the PTME (Chen et al., 2011). Accordingly, the great loss
1257 of burrowing infauna and associated environmental stress occur at the horizon between
1258 Beds 27 and 28. These facts imply that ecologic collapse of marine ecosystems
1259 post-dated the metazoan biodiversity crisis at Meishan.

1260 Contrasting to the two-stage extinction pattern (Song et al., 2013a), Shen et al.
1261 (2011b) and Wang et al. (2014) argued that the severest biodiversity declines fell in a
1262 short period equivalent to Beds 25-28 of Meishan, and there was one prolonged
1263 extinction rather than two discrete episodes. Indeed, Beds 25-28 represent a very short
1264 duration of about 60 ky (Burgess et al., 2014). However, all lines of evidence, including
1265 fossil fragment contents, and ichnofabric and community structural changes, show that

1266 the P-Tr ecologic crisis clearly comprises two pronounced steps, at the bases of Beds 25
1267 and 28 (Figs. 14, 21, 26). Nevertheless, whether the mass extinction occurred as one
1268 prolonged event or two pulses, all studies agree that Beds 25-28 of Meishan and their
1269 equivalents represent a critical period when the greatest biotic turnover of life on Earth
1270 took place in Meishan. During this critical turnover period, the ecologic crisis clearly
1271 lagged behind the diversity decline. As a result, the Meishan fossil record shows that the
1272 mass extinction started with a dramatic depletion of biodiversity and ended with a severe
1273 ecologic crisis.
1274
1275 *7.3. Dramatic increase in seawater surface temperature and its consequence*
1276
1277 Recent oxygen isotopic studies of conodont bioapatites reveal that sea surface
1278 temperature rose ~9 °C from Bed 24e to Bed 27a in Meishan (Joachimski et al., 2012;
1279 Sun et al., 2012; Fig. 26). However, the precise relationship between temperature
1280 increase and biotic extinction remains unclear owing to the lack of oxygen isotopic values
1281 from Bed 25, the base of which coincides with the PTME (Shen et al., 2011b) or the first
1282 phase of the PTME (Song et al., 2013a). The same is also true for the relationship

between the temperature rise and the dramatic negative carbonate carbon isotopic excursion (Fig. 26). The solution is to undertake more detailed study of conodont oxygen isotopes of the PTB beds from less condensed sections than Meishan to evaluate whether temperature change leads or lags the extinction (Burgess et al., 2014). Hinojosa et al. (2012) found a negative shift in $\delta^{44/40}$Ca of conodont bioapatite in the Great Bank of Guizhou, South China during the same interval as temperature increase in Meishan. This $\delta^{44/40}$Ca excursion is also coupled with a major shift in $\delta^{13}C_{carb}$ composition from an average of approximately +3.5‰ in the latest Permian to approximately −1‰ in the earliest Triassic (Payne et al., 2004). The anomaly of $\delta^{44/40}$Ca therefore was interpreted as a consequence, in part, of acidification of the ocean. Thus, oceanic acidification in platform areas of the Great Bank of Guizhou may have resulted from elevated seawater temperature (Burgess et al., 2014). However, this ocean acidification seems not to have spread to the Meishan area because rather abundant and diverse complex traces of both *Glossifungites* and *Cruziana* ichnofacies occur in Bed 27 (Figs. 19-20), although calcareous skeletons decreased significantly in Beds 25-28 (Fig. 14).

Previously, the irregular surface occurring in the middle of Bed 27 at Meishan was interpreted as a submarine dissolution surface, explained by a regional ocean

1300 acidification in South China (Payne et al., 2007, but see Wignall et al., 2009). This
1301 pronounced irregular surface, however, was re-interpreted as a distinct firmground
1302 surface, on which abundant complex traces of *Glossifungites* ichnofacies occur (see
1303 Section 3.5). Firmgrounds of *Glossifungites* ichnofacies are usually characteristic of
1304 initial transgression, and such horizons are usually employed to define sequence
1305 boundaries (Buatois and Mángano, 2011). Thus, no sign of acidification is recorded in
1306 Bed 27 in Meishan.

1307 Another potential consequence of elevated temperature is intensified chemical
1308 weathering (Sheldon, 2006) and consequent increased physical erosion of soils on land
1309 (Sephton et al., 2005; Xie et al., 2007), or a combination of these processes. These
1310 processes are also indicated by the increased chemical index of alteration (CIA) profile
1311 immediately after the first phase of the PTME (Bed 25; Fig. 26). It should be noted that
1312 the CIA value was calculated as $Al_2O_3/(Al_2O_3+K_2O+Na_2O)$ (Zhao et al., 2013a), a
1313 modification of the original CIA equation (Nesbitt and Young, 1982). Increased chemical
1314 weathering during the PTME and its aftermath is also mirrored by the Eu/Eu* profile of
1315 conodont bioapatites (Zhao et al., 2013a). The latter rare-earth elemental (REE) proxy is a
1316 useful tracer of sediment provenance because fractionation between Eu^{+2} and Eu^{+3} does

not occur under Earth-surface conditions (Elderfield and Greaves, 1982). Eu^{+2} tends to become segregated into feldspar during magmatic differentiation, resulting in Eu/Eu* values >1.0 in the crystal fraction and <1.0 in the residual fluid (Zhao et al., 2013a). Eu/Eu* ratios >1.0 are characteristic of magmas from lower crustal or mantle sources where substantial feldspar crystallization has taken place (Condie, 2001). Although the REE "fingerprint" of the ash-rich clastics is reflected by both CIA and Eu/Eu* profiles that match one another throughout P-Tr transition in Meishan (Fig. 26) and these ash beds near the PTB likely sourced from regional convergent continent marginal volcanisms (Gao et al., 2013, 2014), the shift toward Eu/Eu* values of 1.0–1.5 in Bed 24e, immediately preceding the PTME, may be evidence of a transient influx of volcanic material with a lower crustal or mantle source. Zhao et al. (2013a) argued that these mantle-sourced ash fingerprints indicated by Eu/Eu* values could be the product of the Siberian trap eruption (Reichow et al., 2009). Thus, this volcanic eruption could have caused the severe biocrisis and rapid increase in sea-surface temperature occurring ~20-80 kyr later following the estimate of maximum and minimum sedimentation rates given by Burgess et al. (2014).

Burgess et al. (2014) also estimated the rate of temperature rise in Beds 25-28 as

1334 an ~1 °C increase per 6,000 y, which is comparable with the rate and magnitude of the
1335 increase at the Paleocene–Eocene Thermal Maximum (Zeebe et al., 2009) and
1336 Pleistocene/Holocene postglacial warming (~2 °C/5 ka) (Lea et al., 2000). However, this
1337 estimate of the rate of temperature rise needs to be cautious because no temperature data
1338 is available from Bed 25 and the temperature rise spans Beds 24e-27 (Sun et al., 2012).
1339 To sum up, although the killing mechanism of the ~9 °C increase of seawater surface
1340 temperature on organisms remains unclear, this rapid temperature increase coincides with
1341 biotic turnover and ecologic collapse during the PTME at Meishan. Nevertheless, the
1342 elevated temperature seems to have had little effect on ichnofaunas and ichnofabrics, as
1343 indicated by abundant ichnofaunas living in the firmground of the *Glossifungites*
1344 ichnofacies (Bed 27), but instead resulted in dramatic losses of fossil skeletons in
1345 sediments (Fig. 14).
1346 In addition, Sun et al. (2012) reported the acme of high seawater temperatures
1347 occurred in the late Griesbachian, corresponding to the upper *I. isarcica* Zone and lower
1348 *C. planata* Zone (Sun et al., 2012, fig. 2), which range from Beds 48-54. These two zones
1349 are amended herein (Fig. 2) and are equivalent to the upper part of *C. planata* Zone in the
1350 revised conodont zation (Fig. 2). This acme of high temperature postdates the second

1351 negative shift excursion of carbon isotops of Xie et al. (2007) and includes the second
1352 negative shifting excursion of carbon isotopes of Burgess et al. (2014). Surprisingly, this
1353 interval saw an increase in biodiversity (Chen et al., 2002, 2007), ichnological
1354 amoraliation and bioturbation (Fig. 3). Accordingly, the acme of high temperature has
1355 little effect on faunas.
1356
1357 *7.4. Anoxic events and biotic response*
1358
1359 *7.4.1. Anoxic events* At Meishan, Wignall and Hallam (1993) recognized an anoxic
1360 event associated with the PTME, but considered that the greatest acme of anoxia, coupled
1361 with a maximum flooding event, occurs in the lower Yinkeng Formation. Wignall and
1362 Twitchett (2002) believed that the oxygen-deficient waters spread into exceedingly
1363 shallow settings near the PTB in the Tethys regions (i.e., South China). More recently,
1364 multiple geochemical signals indicate the existence of anoxic to euxinic conditions
1365 before, during and after the PTME at Meishan.
1366 An exceptional increase in sea surface temperature is also believed to be
1367 synchronous with the flooding of shelf areas with anoxic and euxinic waters during the

1368 P-Tr transition (Sun et al., 2012). Both extremely high values of total organic content
1369 (TOC) (Yin et al., 2012) and reduced sizes of pyrite framboids (Fig. 26) indicate euxinic
1370 to anoxic condition in Beds 25-26, coinciding with the PTME. However, pyrite
1371 framboids from Bed 27 are generally larger than 5 μm in diameter with abundant crystals
1372 and thus indicate the upper part of dysoxic conditions (Fig. 25). Moreover, high
1373 bioturbation levels are also observed in upper part of Bed 26 and multiple layers of Bed
1374 27. Thus, a euxinic to anoxic condition was probably limited only to Beds 25-26a, which
1375 is less than 20 ka based on duration estimate of conodont zones from these beds (Table 2),
1376 a much shorter period than previously thought. The anoxic condition of the water column
1377 is also reflected by the abrupt increase of Ce/Ce* values of conodont bioapatite from
1378 ~0.7–0.8 in Beds 23-24 to 0.9–1.1 in Beds 25-27b (Zhao et al., 2013a; Fig. 26). Values of
1379 0.7–1.0 are sustained through Beds 27c to 30, above which Ce/Ce* decreases to 0.5–0.7.
1380 It should be noted that Ce/Ce* ratios derived from Bed 27a-d are not totally in accordance
1381 with size analysis of pyrite framboids, which shows that Bed 27a-d may represent redox
1382 conditions ranging from anoxia to upper level of dysoxia (Fig. 25). Although Ce/Ce*
1383 values from Meishan may have been biased by the fingerprint of clay input, Ce/Ce*
1384 values of 0.9–1.1 indicate an anoxic depositional system (Zhao et al., 2013a; Shen et al.,

1385 2012). This inference is consistent with the results of earlier studies documenting anoxia
1386 around the PTME in South China PTB sections (Grice et al., 2005; Algeo et al., 2007;
1387 Shen et al., 2007; Cao et al., 2009; Bond and Wignall, 2010; Luo et al., 2010) and
1388 globally (Algeo et al., 2010, 2011b; Brennecka et al., 2011).

1389 Euxinic condition may have occurred prior to the PTME in Meishan, i.e., Beds
1390 22-24, demonstrated by the anomaly of sulfur isotopes (Shen et al., 2011a) and various
1391 biomarker signals in Beds 22-24 (Grice et al., 2005; Cao et al., 2009; Luo et al., 2010,
1392 2011). Algeo et al. (2011a) also interpreted the anoxic and euxinic conditions as a result
1393 of an expansion of the oxygen minimum zone (OMZ) in the water column over the P-Tr
1394 transition. These authors considered that the OMZ may have expanded prior to the PTME
1395 in Meishan.

1396 A post-extinction reduced condition is also indicated by a pronounced negative
1397 excursion of carbon isotopes in Beds 34-36 (Xie et al., 2007; Luo et al., 2010; Fig. 26),
1398 coupled with an increase in TOC and terrestrial input indicated by various biomarker
1399 signals (Yin et al., 2012), and elevated contents of CO_2 (Fraiser and Bottjer, 2007). The
1400 CIA profile slightly increases in Beds 34-36, indicating elevated chemical weathering on
1401 land, which is consistent with the increased TOC and terrestrial input (Yin et al., 2012). In

addition, conodont bioapatite from Beds 33–39 generally yields lower Ce/Ce* ratios (0.4–0.7) that may indicate an oxic to suboxic depositional environment. Conodont bioapatite Ce, however, was probably derived mainly from detrital clay minerals and taken up during diagenesis, as indicated by other REE proxies (Zhao et al., 2013). If so, the observed Ce/Ce* ratios only reflect the REE composition of the source clays (Zhao et al., 2013a).

Alternatively, size variations of pyrite framboids indicate that Beds 27-29 record a dramatic redox change from upper dysoxic to euxinic conditions (Fig. 25). A euxinic to anoxic condition prevailed throughout Bed 29 to Bed 42 (Fig. 25). The combination of mean size of framboids and presence of both larger framboids and crystal pyrites indicates Bed 43 may be deposited in a lower to upper dysoxic condition. If a redox interpretation is warranted, then this pattern suggests that the anoxic episode following the PTME in Meishan lasted a relatively long duration, probably ~50 kyr. Moreover, mean sizes and morphologies of framboids from Beds 44-58 also generally reflect an anoxic to euxinic condition, which, however, is not supported by various ichnological proxies.

1419 *7.4.2. Biotic response*

1420

1421 The pre-extinction anoxic to euxinic conditions are generally supported by the
1422 presence of abundant small pyrite framboids, 3-5 μm in diameter, in Beds 23-24 (Figs.
1423 23-24). However, biodiversity of metazoans remains very stable, with 64-78 species in
1424 34-44 genera in each layer through Beds 24a to 24e (Fig. 26). Bed 24 contains 82 species
1425 in 47 genera, and there are similar numbers in Bed 23 (Jin et al., 2000). Thus, no major
1426 losses in species and generic richness are recognizable in Beds 23-24. Fossil fragment
1427 contents are almost the same in each layer through Beds 22-24, except for the top 1-2 cm
1428 of Bed 24e, in which there is a pronounced loss in fossil components across the boundary
1429 between Beds 24e-5 and 24e-6 (Figs. 6, 14). Fossil fragment contents fell by >16% in thin
1430 section from Beds 24e-5 to 24e-6. The FFA of Bed 24e-5 comprises 10 major fossil
1431 groups that are commonly present in all Permian limestones, but five clades, ostracods,
1432 bryozoans, calcareous sponges, gastropods, and macroalgae, disappeared, losing 50%,
1433 across this boundary (Figs. 6, 14). The FFA of Bed 24e-6 is dominated by sponge spicules
1434 (35%) and thus has a high dominance and low diversity and evenness, in contrast to the
1435 low dominance, high diversity/evenness FFA in Bed 24e-5 (Fig. 6). Furthermore, the last

1436 occurrence of Permian fusulinids was also bracketed to the base of Bed 24e-6 (Kaiho et
1437 al., 2006b).

1438 Ichnodiversity also declined significantly across the boundary between Beds
1439 24e-5 and 24e-6 (Fig. 21A). These relatively complex or vertical burrows such as
1440 *Balanoglossites* and *Thalassinoides*, which usually occur in oxygenated settings,
1441 disappeared at the base of Bed 24e-6. Instead, only simple, horizontal burrows of
1442 *Planolites* occur in Bed 24e-6. Ichnofabrics, however, do not exhibit a major change
1443 across the same boundary (Fig. 3), with abundant *Planolites* burrows being densely
1444 packed on the surface of Bed 24e-6. However, most geochemical studies do not have such
1445 a high sampling intensity, and thus neglected this boundary.

1446 Both metazoan biodiversity and fossil fragment contents experienced dramatic
1447 declines in Beds 25-26a. Other ecologic measures, such as community structures,
1448 ichnodiversity, burrow size, tiering level, and ichonfabric variation, also indicate an
1449 ecologic crisis in Beds 25-26a, coinciding with the anoxia indicated by both pyrite
1450 framboid sizes and various geochemical signals (Fig. 26). However, the metazoan fauna
1451 from Bed 27 is rather abundant and diverse, including 66 species in 34 genera (Song et al.,
1452 2013a). Both community structural indices and fossil fragment contents indicate that

1453 metazoans had recovered well in Bed 27. The presence of abundant complex burrows in
1454 Bed 27 indicates the infaunal proliferation in the firmground of *Glossifungites*
1455 ichnofacies (Fig. 20). The occasional occurrence of pyrite framboids in Bed 27 may
1456 indicate a very short period of anoxic condition, but Bed 27, as a whole, represents a
1457 dysoxic to oxic condition in which benthos and infaunas proliferated.

1458 By contrast, all data, including the low ichnodiversity (only *Planolites*), small
1459 burrow size, low trace complexity, low ichnofabric from Beds 29-51 indices and low
1460 tiering level as well as low-diversity metazoans (Chen et al., 2007, 2010a), support the
1461 view that anoxic conditions may have prevailed throughout the early Griesbachian in
1462 Meishan (Wignall and Hallam, 1993; Xie et al., 2007; Yin et al., 2012). Of these, Beds
1463 29-34 are barren of trace fossils and bioturbation. This is supported by trace fossil size,
1464 which is also regarded as a proxy for paleoenvironmental conditions (Twitchett, 1999;
1465 Pruss and Bottjer, 2004). In general, small-sized traces are usually found in poorly
1466 oxygenated sediments (Savrda and Bottjer, 1987) or brackish environments (Pemberton
1467 et al., 1982; Buatois et al., 2005) or habitats with low nutrient supply (Jumars and
1468 Wheatcroft, 1989). Thus small traces are characteristic of stressed environments
1469 (Twitchett, 1999; Pruss and Bottjer, 2004). The dramatic size reduction of trace fossils

1470 after the PTME indicates environmental stresses associated with the PTME, and the small
1471 sizes of Early Triassic traces suggest prolonged environmental stress following the event
1472 (Bottjer et al., 2008).
1473
1474 *7.5. Testing extinction mechanisms*
1475 Multiple scenarios have been proposed to interpret the killing mechanisms of the
1476 PTME, including widespread anoxia, hypercapnia, massive volcanic eruption, global
1477 warming, ocean acidification, and increased sediment flux (Erwin, 2006; Knoll et al.,
1478 2007; Clapham and Payne, 2011; Algeo and Twitchett, 2010; Algeo et al., 2011a;
1479 Joachimski et al., 2012; Sun et al., 2012; Burgess et al., 2014; Song et al., 2014). However,
1480 the true causes of this biocrisis still remain unclear due to the incomplete record of
1481 evidence supporting any of these alternatives.
1482 Recently, Song et al. (2013a) suggested that different extinction mechanisms
1483 may have driven each of these two pulses given their differences in biodiversity and
1484 ecologic losses. These authors considered that anoxia may be related to the first-pulse
1485 losses of biota, but played a crucial role in the second-pulse biocrisis (Song et al., 2013a).
1486 Elevated sea-surface temperature not only resulted in the spread of anoxia but also killed

1487 directly shallow-water taxa, while the anoxia killed the deep-water organisms (Song et al.,
1488 2014). However, extinction and survival selectivity of various fossil groups is more
1489 complicated than previously thought (i.e., Song et al., 2013a, 2014). This is because
1490 various elements of the same clade may have different lifestyles. For instance, the P-Tr
1491 brachiopods have six types of lifestyles based on attachment modes on the substratum:
1492 burrowing, body cementation, pedicle attaching on substratum, body spines anchoring on
1493 substratum, pedicle attaching on objects, and clasping spines on other shells/or objects
1494 (Chen et al., 2006a, 2011b). These brachiopods having the last two types of attachment
1495 modes behaviour like nektons. Moreover, some shallow-water elements were also able to
1496 survive in deep niches during the latest Permian (Chen et al., 2006a). It is also true for the
1497 P-Tr bivalves that embrace several lifestyles (Huang et al., 2014). Accordingly, our high
1498 resolution comprehensive analyses of biodiversity, community structural, fossil fragment,
1499 ichnological, and redox condition changes associated with these two discrete events
1500 allow an evaluation of the proposed kill mechanisms for these two ecologic crises.
1501 Most of the Permian brachiopods became extinct in the first extinction. The
1502 survivors are dominated by chonetids or chonetid-like productids or small, thin-shelled
1503 spiriferids/rhynchonellids that usually have attachment modes of clasping spines on other

1504 shells/or objects or pedicle-attaching on other shells or objects (Chen et al., 2005a,
1505 2011b). These survivors attached their bodies on some float objects (i.e., other shells and
1506 algae) suspending above the seafloor (Chen et al., 2005a, 2011b), and thus provided
1507 brachiopods higher adaptability surviving the deleterious environments, i.e., increased
1508 acidity of precipitation (Wignall, 2007), large-scale marine acidification (Clapham and
1509 Payne, 2011) and widespread anoxia (Wignall and Twitchett, 2002; Payne and Clapham,
1510 2012) during the first biocrisis. Inarticulated brachiopods i.e., lingulids also survived this
1511 event, although having a burrowing lifestyle. This is because linguilds are able to survive
1512 in poorly oxygenated waters due to having respiratory pigment acting the function to
1513 transport oxygen or to store oxygen within the body tissues under anoxic conditions or
1514 during cessation of respiration (Williams et al., 1997).
1515 Similarly, Huang et al. (2014) argued that the anoxia or acidification may have
1516 impacted seriously on bivalve's extinction and survival selectivity during the first
1517 extinction based on ecologic analysis of the P-Tr bivalves. As a result, both brachiopod's
1518 and bivalve's evidence indicates that anoxia impacted clearly by in the first-pulse
1519 biocrisis (Chen et al., 2011b; Huang et al., 2014). The acidification associated with this
1520 extinction cannot be excluded (Clapham and Payne, 2011; Hinojosa et al., 2012). The

1521 anoxia or acidification, however, lasted a very short duration, ~30 ka, as discussed above.

1522 Furthermore, a rapid increase of about ~9°C of sea-surface temperature (within a

1523 period of ~30 ka) across Beds 24e-27a (Sun et al., 2012) must have facilitated respiratory

1524 frequency and accelerated oxygen consumption of most brachiopods and become lethal

1525 to brachiopods, and thus causes morality, regardless their shallower or deeper habitats

1526 (Chen et al., 2014b in this volume). The rapidly elevated seawater temperature also

1527 coincides with the first dramatic losses of body fossil biodiversity and fossil fragments as

1528 well as moderate losses of ichnodiversity and community diversity, and a moderate

1529 decrease in bioturbation, tiering levels of infaunas and burrow sizes.

1530 However, marine ecosystems seem not to have collapsed completely during the

1531 first-pulse crisis (Chen and Benton, 2012), some organisms survived the short

1532 environmental and climatic devastation. Thus, both biodiversity and ichnodiversity, and

1533 all of ichnological and community structural measures rebounded rapidly in Bed 27a-d

1534 (Fig. 26).

1535 Like the first extinction, the second-pulse biocrisis is also associated with a clay

1536 bed (Bed 28), in which pyrite framboids indicate a lower dysoxic to anoxic condition (Fig.

1537 25). However, the redox condition became euxinic soon after and is indicated by

framboids obtained from the base of Bed 29. Thus, a dramatic change from upper dysoxic to oxic condition in Bed 27 to euxinic condition in basal Bed 29 indicates an anoxia/euxinia coincided with the 2nd biocrisis, which is followed by a long period of euxinic to anoxic conditions, which was probably driven by a relatively long (>62 ka) acme of high temperature (up to 35-37^{o}C) in earliest Griesbachian. Accordingly, both epifaunal and infaunal ecosystems collapsed after suffering such a long period of lethally hot seawater temperature and widespread anoxia in earliest Triassic oceans (Fig. 26). This is reinforced by the replacement of free-lying brachiopod-dominated communities in Bed 27 with nekton-dominated communities in Beds 31-37 (Chen et al., 2010a) and Beds 28-34 barren of bioturbation and ichnofossils (Figs. 3, 26). As stated above, these surviving brachiopods yielded from Beds 26-27 should have enhanced resistant ability to anoxic or acidified water mass near seafloor because they survived from the first-pulse crisis. The morality of the free-lying brachiopods in the second-pulse crisis is probably due to the loss of other shells or float algae, on which the brachiopods attach using either pedicle or clasping spines.

Accordingly, the killing mechanisms for these two extinction events near the PTB seem not to be fundamentally different from one another, although no sign of acidification has

been reported in the second phase of the PTME. However, a short anoxia or acidification probably caused by a rapid increase in seawater temperature may have played an important role in the first-pulse biocrisis, while the long-lasting and widespread anoxia induced by a long period of high temperature condition may have killed most organisms in the second-pulse crisis.

7.6. Post-extinction amelioration of marine ecosystems in late Griesbachian

Post-extinction benthic communities did not appear to return to normal until the early Middle Triassic (Chen and Benton, 2012). The deleterious environment that prevailed in early Triassic oceans may be largely responsible for this long-delayed recovery (Bottjer et al., 2008). In particular, Early Triassic carbon isotopic records show several negative excursions that indicate sharp global warming (Payne et al., 2004), and these coincide with diversity drops. Furthermore, intrinsic relationships between organisms and ecosystem structures may also have slowed down biotic recovery following the PTME (Chen and Benton, 2012). Recent studies show that the biotic recovery process may be mirrored by stepwise establishment of trophic structures of marine ecosystems throughout Olenekian-Anisian interval (Chen and Benton, 2012).

1572 However, biotic recovery may occur earlier in oxygenated environments (Twitchett et al.,
1573 2004; Beatty et al., 2008; Zonneveld et al., 2010). As a result, Early Triassic marine
1574 environments were not always deleterious globally. Chen et al. (2007) also detected that
1575 marine environments had greatly ameliorated during the late Griesbachian in Meishan.
1576 The sea-floor recuperation, including shallowing water depth, increasing oxygenation
1577 and oceanic productivity, coincides with an increase in benthic biodiversity, signalling
1578 that ecologic and environmental restoration might have initiated in the late Griesbachian
1579 (Chen et al., 2002, 2007).

1580 The example of elevated recovery of the benthic community in late
1581 Griesbachian at Meishan is also strengthened by community structural changes and
1582 ichnofabric variation through the PTB to late Griesbachian. The Exp (H) value increases
1583 by 262.6% from the *C* to *M–L* communities, and also increases 70%, coupled with a
1584 decrease of 15.2% in D' values, from the *C–O* to *M–L* communities, suggesting an
1585 improvement in shelly community structures in the upper Yinkeng Formation at Meishan
1586 (Chen et al., 2002, 2007).

1587 Trace fossils and ichnofabrics documented here also show that the late
1588 Griesbachian trace-fossil assemblage is marked by significant increases in ichnodiversity,

1589 burrow size, trace complexity, tiering level, and bioturbation level, in comparison with
1590 early Griesbachian ichnoassemblages, although they did not achieve Changhsingian
1591 levels (Fig. 21). Thus, the Meishan trace fossils, together with increasing diversity in the
1592 shelly community, sedimentary structures (HCS), up-shallowing sedimentary cycle and
1593 geochemical proxies (Chen et al., 2007), suggest that biotic recovery recorded in the
1594 upper Yinkeng Formation may be categorized as recovery stage 2 (*sensu* Twitchett, 2006),
1595 and also mark the return of parts of the meso-consumer functioning group within the
1596 ecosystem trophic structure, which usually occurs in the Spathian around the world (Chen
1597 and Benton, 2012).
1598
1599 **8. Conclusions**
1600
1601 Updated conodont biostratigraphy allows the establishment of eight conodont
1602 zones from the latest Changhsingian to early Griesbachian at Meishan, the *C. yini, C.*
1603 *meishanensis*, *H. changxingensis*, *C. taylorae*, *H. parvus*, *I. staeschei*, *I. isarcica*, and *C.*
1604 *planate* zones. Microstratigraphic analysis shows that a major turnover in fossil fragment
1605 contents and ichnodiversity occurs across the boundary between Beds 24e-5 and 24e-6,

1606 suggesting the actual mass extinction horizon in thin section. Bed 27 contains a
1607 firmground of *Glossifungites* ichnofacies rather than the previously proposed submarine
1608 dissolution surface or hardground surface. Fossil fragment contents show a dramatic
1609 decline in both fossil component percentage and assemblage diversity in Beds 25-26a,
1610 coinciding with metazoan mass extinction. Fossil fragment content, ichnodiversity and
1611 all ichnofabric proxies (including burrow size, tiering level, and bioturbation level)
1612 throughout the uppermost Changhsing to Yinkeng formations indicate that the P-Tr
1613 ecologic crisis comprises two discrete stages, coinciding with the first and second phases
1614 of the PTME, in support of a proposed two-stage extinction pattern of metazoans over the
1615 P-Tr transition. The PTME was of short duration, lasting about 60 kyr. A biodiversity
1616 crisis indicates the start of the extinction interval, but its end is marked by the ecologic
1617 collapse of ecosystems. Thus, the ecologic crisis lagged behind the biodiversity decline
1618 during the PTME. Pyrite framboid size variations suggest that the depositional redox
1619 condition was anoxic to euxinic in the latest Changhsingian, became euxinic in Beds
1620 25-26a, turned to be dyoxic in Bed 27, then varied from euxinic to anoxic through most of
1621 the Griesbachian. Although metazoan biodiversity and fossil fragment contents show
1622 dramatic declines, coinciding with a ~9 °C increase in seawater surface temperature, from

1623 Bed 24e to Bed 27 in Meishan, all ecologic proxies show much smaller effects from the
1624 elevated seawater temperature. Bed 27 contains abundant infauna and shows no signs of
1625 ocean acidification. Pre-extinction anoxic-euxinic conditions had little effect on both
1626 metazoans and infauna. The anoxic event associated with the PTME may have lasted for
1627 much less time than previously thought, and is limited to Beds 25-26a at Meishan. Fossil
1628 fragment contents, ichnofaunas, ichnofabrics and pyrite framboid size all show that
1629 anoxic conditions did not exist in Bed 27. Early Griesbachian anoxia is possible, and may
1630 have caused the rarity of ichnofaunas and metazoans in the lower Yinkeng Formation.
1631 The ichnofauna is characterized by small, simple horizontal burrows of *Planolites*, while
1632 metazoan faunas are characterized by low diversity, high abundance,
1633 opportunist-dominated communities. The killing mechanisms for these two extinction
1634 events near the PTB similar to one another. A rapid increase of ~9 ^{o}C in seawater
1635 temperature and its inducing short anoxia or acidification may have played an important
1636 role in the first-pulse biocrisis, while the long-time and widespread anoxia probably
1637 caused by long-time high temperature condition may have resulted in morality of most
1638 organisms in the second-pulse crisis. Initial recovery of marine ecosystems coupled with
1639 environmental amelioration occurred in the late Griesbachian, marking the return of parts

of the meso-consumer functioning group.

Acknowledgements

We thank J. Tong for help in the field and H.J. Song for discussion on foraminiferal taxonomy of collections from the PTB beds in Meishan. This work was supported by the 973 Program and China 111 Program. It is a contribution to IGCPs 572 and 630.

References

Algeo, T.J., Twitchett, R.J., 2010. Anomalous Early Triassic sediment fluxes due to elevated weathering rates and their biological consequences. Geology 38, 1023–1026.

Algeo, T.J., Chen, Z.Q., Fraiser, M.L., Twitchett, R.J., 2011a. Terrestrial-marine teleconnections in the collapse and rebuilding of Early Triassic marine ecosystems. Palaeogeography, Palaeoclimatology, Palaeoecology 308, 1–11.

Algeo, T.J., Hannigan, R., Rowe, H., Brookfield, M., Baud, A., Krystyn, L., Ellwood, B.B., 2007. Sequencing events across the Permian–Triassic boundary, Guryul

1657 Ravine (Kashmir, India). Palaeogeography, Palaeoclimatology, Palaeoecology 252,
1658 328–346.
1659 Algeo, T.J., Henderson, C.M., Ellwood, B., Rowe, H., Elswich, E., Bates, S., Lyons, T.,
1660 Hower, J.C., Smith, C., Maynard, B., Hays, L.E., Summons, R.E., Fulton, J.,
1661 Freeman, K.H., 2012. Evidence for a diachronous late Permian marine crisis from
1662 the Canadian Arctic region. Geological Society of America Bulletin 124,
1663 1424–1448.
1664 Algeo, T.J., Hinnov, L., Moser, J., Maynard, J.B., Elswick, E., Kuwahara, K., Sano, H.,
1665 2010. Changes in productivity and redox conditions in the Panthalassic Ocean during
1666 the latest Permian. Geology 38, 187–190.
1667 Algeo, T.J., Kuwahara, K., Sano, H., Bates, S., Lyons, T., Elswick, E., Hinnov, L.,
1668 Ellwood, B., Moser, J., Maynard, J.B., 2011b. Spatial variation in sediment fluxes,
1669 redox conditions, and productivity in the Permian–Triassic Panthalassic Ocean.
1670 Palaeogeography, Palaeoclimatology, Palaeoecology 308, 65–83.
1671 Ausich, W.I., Bottjer, D.J., 2002. Sessile invertebrates. In: Briggs, D.E.G., Crowther, P.R.
1672 (eds.), Palaeobiology II. Blackwell Science, Oxford, pp. 384-386.
1673 Baldwin, C.T., McCave, I.N., 1999. Bioturbation in an active deep-sea area: Implications

for models of trace fossil tiering. Palaios 14, 375-388.

Beatty, T.W., Zonneveld, J.-P., Henderson, C.M., 2008. Anomalously diverse Early Triassic ichnofossil assemblages in northwest Pangea: a case for a shallow-marine habitable zone. Geology 36, 771–774.

Benner, J.S., Ekdale, A.A., 2004. Macroborings (*Gastrochaenolites*) in Lower Ordovician Hardgrounds of Utah: Sedimentologic, Paleoecologic, and Evolutionary Implications. Palaios 19, 543–550.

Benton, M.J., Twitchett, R.J., 2003. How to kill (almost) all life: the end-Permian extinction event. Trends in Ecology and Evolution 18, 358–365.

Bond, D.P.G., Wignall, P.B., 2010. Pyrite framboid study of marine Permian–Triassic boundary sections: a complex anoxic event and its relationship to contemporaneous mass extinction. Geological Society of America Bulletin 122, 1265–1279.

Bottjer, D.J., Droser, M.L., Jablonski, D., 1988. Fine-scale resolution of mass extinction events: Trace fossil evidence from the Permian-Triassic boundary in South China. Geological Society of America, Abstracts with Programs 20, p. A106.

Bottjer, D.J., Clapham, M.E., Frasier, M.L., Powers, C.M., 2008. Understanding mechanisms for the end-Permian mass extinction and the protracted Early Triassic

aftermath and recovery. GSA Today 18, 4–10.

Bowring, S.A., Erwin, D.H., Jin, Y.G., Martin, M.W., David, E.K., Wang, W., 1998. U/Pb zircon geochronology and tempo of the end-Permian mass extinction. Science 280, 1039–1045.

Brennecka, G.A., Herrmann, A.D., Algeo, T.J., Anbar, A.D., 2011. Rapid expansion of oceanic anoxia immediately before the end-Permian mass extinction. Proceedings of the National Academy of Sciences, U.S.A. 108, 17631–17634.

Bromley, R.G., 1996. Trace Fossils: Biology, Taphonomy and Applications (2nd edition). Chapman & Hall, London, 361 pp.

Bromley, R.G., Ekdale, A.A., 1984. *Chondrites*: a trace fossil indicator of anoxia in sediments. Science 224, 872-874.

Buatois, L.A., Mángano, M.G., 2011. Ichnology: Organism-Substrate Interactions in Space and Time. Cambridge University Press, New York. 1–358.

Buatois, L.A., Gingras, M.K., MacEachern, J., Mangano, M.G., Zonneveld, J.P., Pemberton, S.G., Netto, R.G., Martin, A., 2005. Colonization of brackish-water systems through time: Evidence from the trace-fossil record. Palaios 20, 321-347.

Burgess, S.D., Bowring, S., Shen, Z.Q., 2014. High-precision timeline for Earth's most

severe extinction. Proceedings of National Academy of Sciences, U.S.A. 111, 3316–3321.

Cao, C.Q., Shang, Q.H., 1998. Microstratigraphy of Permo-Triassic transitional sequence of the Meishan section, Zhejiang, China. Palaeoworld 9, 147-152.

Cao, C.Q., Zheng, Q.F., 2007. High-resolution lithostratigraphy of the Changhsingian stage in Meishan section, Zhejiang. Journal of Stratigraphy 31, 14-22.

Cao C Q, Zheng Q F. 2009. Geological event sequences of the Permian-Triassic transition recorded in the microfacies in Meishan section. Science China Series D-Earth Sciences 52, 1529–1536

Cao, C.Q., Wang, W., Jin, Y., 2002. Carbon isotope excursions across the Permian-Triassic boundary in the Meishan section, Zhejiang Province, China. Chinese Science Bulletin 47, 1125-1129.

Cao, C., Love, G.D., Hays, L.E., Wang, W., Shen, S., Summons, R.E., 2009. Biogeochemical evidence for euxinic oceans and ecological disturbance presaging the end-Permian mass extinction event. Earth and Planetary Science Letters 281, 188–201.

Chen, J., Chen, Z.Q., Tong, J.N., 2010b. Palaeoecology and taphonomy of two

brachiopod shell beds from the Anisian (Middle Triassic) of Guizhou, Southwest China: recovery of benthic communities from the end-Permian mass extinction. Global and Planetary Change 73, 149-160.

Chen, J., Chen, Z.Q., Tong, J., 2011b. Environmental determinants and ecologic selectivity of benthic faunas from nearshore to bathyal zones in the end-Permian mass extinction: brachiopod evidence from South China. Palaeogeography, Palaeoclimatology, Palaeoecology 308, 84-97.

Chen, J.H., 2004. Macroevolution of bivalves after the end-Permian mass extinction in South China. In: Rong, J.Y., Fong, Z.J. (eds), Biotic mass extinction and recovery—evidence from Palaeozoic and Triassic of South China. China University of Science & Technology Press, Hefei. pp. 647–700.

Chen, Z.Q., Benton, M.J., 2012. The timing and pattern of biotic recovery following the end-Permian mass extinction. Nature Geoscience 5, 375–383.

Chen, Z.Q., Liao, Z.T., 2009. Brachiopod faunas across the Wuchiapingian-Changhsingian (Late Permian) boundary at the stratotype section and subsurface of Changxing area, South China. Neues Jahrbuch für Geologie und Paläontologie 254, 315–335.

1742 Chen, Z.Q., McNamara, K.J., 2006. End-Permian extinction and subsequent recovery of
1743 the Ophiuroidea (Echinodermata). Palaeogeography, Palaeoclimatology,
1744 Palaeoecology 236, 321–344.
1745 Chen, Z.Q., Algeo, T.J., Bottjer, D.J., 2014a. Global review of the Permian–Triassic mass
1746 extinction and subsequent recovery: Part I. Earth-Science Reviews 137, 1-5.
1747 Chen, Z.Q., Campi, M., Shi, G.R., Kaiho, K., 2005b. Post-extinction brachiopod faunas
1748 from the Late Permian Wuchiapingian coal series of South China. Acta
1749 Palaeontologica Polonica 50, 343-363.
1750 Chen, Z.Q., Fraiser, M.L., Bolton, C., 2012. Early Triassic trace fossils from Gondwana
1751 Interior Sea: Implication for ecosystem recovery following the end-Permian mass
1752 extinction in south high-latitude region. Gondwana Research 22, 238-255.
1753 Chen, Z.Q., Kaiho, K., George, A.D., 2005a. Survival strategies of brachiopod faunas
1754 from the end-Permian mass extinction. Palaeogeography, Palaeoclimatology,
1755 Palaeoecology 224, 232–269.
1756 Chen, Z.Q., Kaiho, K., George, A.D., Tong, J., 2006b. Survival brachiopod faunas of the
1757 end-Permian mass extinction from northern Italy and south China. Geological
1758 Magazine 143, 301-327.

1759 Chen, Z.Q., Shi, G.R., Kaiho, K., 2002. A new genus of rhynchonellid brachiopod from
1760 the Lower Triassic of South China and implications for timing the recovery of
1761 Brachiopoda after the end-Permian mass extinction. Palaeontology 45, 149-164.
1762 Chen, Z.Q., Shi, G.R., Yang, F.Q., Gao, Y.Q., Tong, J.N., Peng, Y.Q., 2006a. An
1763 ecologically mixed brachiopod fauna from Changhsingian deep-water basin of South
1764 China: consequence of end-Permian global warming. Lethaia 39, 79–90.
1765 Chen, Z.Q., Tong, J.N., Fraiser, M.L., 2011a. Trace fossil evidence for restoration of
1766 marine ecosystems following the end-Permian mass extinction in the Lower Yangtze
1767 region, South China. Palaeogeography, Palaeoclimatology, Palaeoecology 299,
1768 449–474.
1769 Chen, Z.Q., Tong, J.N., Liao, Z.T., Chen, J., 2010a. Structural changes of marine
1770 communities over the Permian–Triassic transition: ecologically assessing the
1771 end-Permian mass extinction and its aftermath. Global and Planetary Change 73,
1772 123–140.
1773 Chen, Z.Q., Tong, J., Zhang, K., Yang, H., Liao, Z., Song, H., Chen, J., 2009.
1774 Environmental and biotic turnover across Permian–Triassic boundary from shallow
1775 carbonate platform in western Zhejiang, South China. Australian Journal of Earth

1776 Sciences 56, 775–797.

1777 Chen, Z.Q., Tong, J., Kaiho, K., Kawahata, H., 2007. Onset of biotic and environmental

1778 recovery from the end-Permian mass extinction within 1-2 million years: A case

1779 study of the Lower Triassic of the Meishan section, South China. Palaeogeography,

1780 Palaeoclimatology, Palaeoecology 252, 176-187.

1781 Chen, Z.Q., Wang, J.L., Yang, H., Tu, C.Y., Polov, Y., He, W.H., 2014b. Permian-Triassic

1782 evolutionary dynamics of the Brachiopoda: paleobiogeography,

1783 extinction-survival-recovery, latitudinal diversity gradients, body size variations,

1784 and longevity changes. Earth-Science Reviews (under review, in this volume).

1785 Claoue-Long, J.C., Zhang, Z.C., Ma, G.G. and Du, S.H., 1991. The age of the

1786 Permian-Triassic boundary. Earth and Planetary Science Letters 105, 182–190.

1787 Clapham, M., Payne, J., 2011. Acidification, anoxia, and extinction: a multiple logistic

1788 regression analysis of extinction selectivity during the Middle and Late Permian.

1789 Geology 39, 1059–1062.

1790 Condie, K.C., 2001. Mantle Plumes and Their Record in Earth History. Cambridge

1791 University Press, Cambridge. 306 pp.

1792 Crasquin, S., Forel, M.B., Feng, Q.L., Yuan, A.H., Baudin, F., Collin, P.Y., 2010.

1793 Ostracods (Crustacea) through the Permian-Triassic boundary in South China: the
1794 Meishan stratotype (Zhejiang Province). Journal of Systematic Palaeontology 8,
1795 331-370.
1796 Dasgupta, S., Buatois, L.A., 2012. Unusual occurrence and stratigraphic significance of
1797 the *Glossifungites* ichnofacies in a submarine paleo-canyon — Example from a
1798 Pliocene shelf-edge delta, Southeast Trinidad. Sedimentary Geology 269-270,
1799 69-77.
1800 Droser, M.L., Bottjer, D.J., 1986. A semiquantitative field classification of ichnofabric.
1801 Journal of Sedimentary Petrology 56, 558-559.
1802 Ekdale, A.A., Bromley, R.G., 2001. A day and a night in the life of a cleft-foot clam:
1803 *Protovirgularia-Lockeia-Lophoctenium*. Lethaia 34, 119-124.
1804 Ekdale, A.A., Bromley, R.G., 2003. Paleoethologic interpretation of complex
1805 *Thalassinoides* in shallow-marine limestone, Lower Ordovician, southern Sweden.
1806 Palaeogeography, Palaeoclimatology, Palaeoecology 192, 221-227.
1807 Elderfield, H., Greaves,M.J., 1982. The rare earth elements in seawater. Nature 296,
1808 214–219.
1809 Erwin, D.H., 2001. Lessons from the past: biotic recoveries from mass extinctions.

1810 Proceedings of the National Academy of Sciences, U.S.A. 98, 5399–5403.

1811 Erwin, D.H., 2006. How Life on Earth Nearly Ended 250 Million Years Ago. Princeton

1812 University Press, Princeton, 306 pp.

1813 Farabegoli, E., Perri, M.C., 2012. Millennial physical events and the end-Permian mass

1814 mortality in the western Palaeotethys: timing and primary causes. In: Talent, J.A.

1815 (ed.), Earth and Life, International Year of Planet Earth, Springer, London, pp.

1816 719-758.

1817 Flugel, E., 1982. Microfacies Analysis of Limestone, Springer, New York, 663 pp.

1818 Forel, M.-B., Crasquin, S., 2011. Lower Triassic ostracods (Crustacea) from the Meishan

1819 section, Permian-Triassic boundary GSSP (Zhejiang Province, South China). Journal

1820 of Systematic Palaeontology 9, 455-466.

1821 Fraiser, M.L., Bottjer, D.J., 2007. Elevated atmospheric CO_2 and the delayed biotic

1822 recovery from the end-Permian mass extinction. Palaeogeography,

1823 Palaeoclimatology, Palaeoecology 252, 164–175.

1824 Fraiser, M.L., Bottjer, D.J., 2009. Opportunistic behavior of invertebrate marine

1825 tracemakers during the Early Triassic aftermath of the end-Permian mass extinction.

1826 Australian Journal of Earth Sciences 56, 841–857.

1827 Gao, Q.L., Zhang, N., Xia, W.C., Feng, Q.L., Chen, Z.Q., Zheng, J.P., Griffin, W.L.,
1828 O'Reilly, S.Y., Pearson, N.J., Wang, G.Q., Wu, S., Zhong, W.L., Sun, X.F., 2013.
1829 Origin of volcanic ash beds across the Permian-Triassic boundary, Daxiakou, South
1830 China: Petrology and U-Pb age, trace elements and Hf-isotope composition of zircon.
1831 Chemical Geology 360-361, 41-53.
1832 Gao, Q.L., Chen, Z.Q., Zhang, N., Xia, W.C., Wang, G.Q., Jiang, T.F., Xia, X.F., 2014.
1833 Ages, trace elements and Hf-isotopic compositions of zircon from claystones around
1834 the Permian-Triassic boundary in the Zunyi section, South China: implications for
1835 nature and tectonic setting of the volcanism. Journal of Earth Sciences 26 (in press).
1836 Gorjan, P., Kaiho, K., Kakegawa, T., Niitsuma, S., Chen, Z.Q., Kajiwara, Y., Nicora, A.,
1837 2007. Paleoredox, biotic and sulfur-isotopic changes associated with the
1838 end-Permian mass extinction in the western Tethys. Chemical Geology 244,
1839 483-492.
1840 Gouramis, C., Webb, J.A., Warren, A.A., 2003. Fluviodeltaic sedimentology and
1841 ichnology of part of the Silurian Grampians Group, western Victoria. Australian
1842 Journal of Earth Sciences 50, 811–825.
1843 Grice, K., Cao, C., Love, G.D., Bottcher, M.E., Twitchett, R.J., Grosjean, E., Summons,

1844 R.E., Turgeon, S.C., Dunning, W., Jin, Y., 2005. Photic zone euxinia during the
1845 Permian-Triassic superanoxic event. Science 307, 706-709
1846 Hammer, O., Harper, D.A.T., Ryan, P.D., 2001. PAST: palaeontological statistics
1847 software package for education and data analysis. Palaeontologia Electronica 4, 1–9.
1848 Häntzschel, W., 1975. Trace fossils and problematica. In: Teichert, C. (ed.), Treatise of
1849 Invertebrate Paleontology (2nd Edition), Part W, Miscellanea, Supp 1. University of
1850 Kansas and Geological Society of America, Lawrence, Kansas, 269 pp.
1851 He, J.W., 1981. Clay minerals in the Changhsingian stratotype section and the basal part
1852 of Yinkeng Formation, with reference to the Permo-Triassic boundary (in Chinese).
1853 Journal of Stratigraphy 5, 197–206
1854 He, J.W., Rui, L., Chai, Z.F., 1987. The latest Permian and earliest Triassic volcanic
1855 activities in the Meishan area of Changxing, Zhejiang. Journal of Stratigraphy 11,
1856 194–199.
1857 He, W., Feng, Q., Gu, S., Jin, Y., 2005. Changxingian (Upper Permian) Radiolarian fauna
1858 from Meishan D section, Changxing, Zhejiang, China, and its possible
1859 paleoecological significance. Journal of Paleontology 79, 209–218.
1860 Hinojosa, J.L., Brown, S.T., Chen, J., DePaolo, D.J., Paytan, A., Shen, S.Z., Payne, J.L.,

2012. Evidence for end-Permian ocean acidification from calcium isotopes in biogenic apatite. Geology 40, 743-746.

Huang, C.J., Tong, J.N., Hinnov, L., Chen, Z.Q., 2011. Did the great dying of life take 700 ky? Evidence from global astronomical correlation of the Permian-Triassic boundary interval. Geology 39, 779-782.

Huang, Y.F., Tong, J.N., Fraiser, M.L., Chen, Z.Q., 2014. Extinction patterns among bivalves in South China during the Permian-Triassic crisis. Palaeogeography, Palaeoclimatology, Palaeoecology 399, 78-88.

Hubbard, S.M., Shultz, M.R., 2008. Deep burrows in submarine fan-channel deposits of the Cerro Toro Formation (Cretaceous), Chilean Patagonia: implications for firmground development and colonization in the deep sea. Palaios 23, 223–232.

Jacobsen, N., Twitchett, R.J., Krystyn, L., 2011. Palaeoecological methods for assessing marine ecosystem recovery following the Late Permian mass extinction event. Palaeogeography, Palaeoclimatology, Palaeoecology 308, 200–212.

Jiang, H.S., Lai, X., Luo, G., Aldridge, R., Zhang, K., Wignall, P.B., 2007. Restudy of conodont zonation and evolution across the P/T boundary at Meishan section, Changxing, Zhejiang, China. Global and Planetary Change 55, 39-55.

1878 Jiang, H.S., Aldridge, R.J., Lai, X.L., Sun, Y.D., Luo, G.M., 2008. Observations on the
1879 surface microreticulation of platform elements of *Neogondolella* (Conodonta) from
1880 the Upper Permian, Meishan, China. Lethaia 41, 263-274.
1881 Jiang, H.S., Lai, X.L., Sun, Y.D., Wignall, P.B., Liu, J., Yan, C., 2014. Permian-Triassic
1882 conodonts from Dajiang (Guizhou, South China) and their implication for the age of
1883 microbialite deposition in the aftermath of the end-Permian mass extinction. Journal
1884 of Earth Science 25, 413-430.
1885 Jiang, H.S., Lai, X.L., Yan, C.B., Aldridge, R.J., Wignall, P., Sun, Y.D., 2011. Revised
1886 conodont zonation and conodont evolution across the Permian-Triassic boundary at
1887 the Shangsi section, Guangyuan, Sichuan, SouthChina. Global and Planetary Change,
1888 77, 103-115,
1889 Jiang,Y., Tang,Y.,Dai, S., Zou,X.,Qian,H., Zhou,G., 2006. Pyrites and sulfur isotopic
1890 composition near the Permian–Triassic boundary in Meishan. Zhejiang. Acta
1891 Geologica Sinica 80, 1202–1207.
1892 Jin, Y., Wang, Y., Wang, W., Shang, Q., Cao, C., Erwin, D.H., 2000. Pattern of marine
1893 mass extinction near the Permian-Triassic boundary in South China. Science 289,
1894 432-436.

1895 Joachimski, M.M., Lai, X., Shen, S., Jiang, H., Luo, G., Chen, B., Chen, J., Sun, Y., 2012.
1896 Climate warming in the latest Permian and the Permian–Triassic mass extinction.
1897 Geology 40, 195–198.
1898 Jost, L., 2006. Entropy and diversity. Oikos 113, 363–375.
1899 Jost, L., 2007. Partitioning diversity into independent alpha and beta components.
1900 Ecology 88, 2427–2439.
1901 Jumars, P.A., Wheatcroft, R.A., 1989. Responses of benthos to changing food quality and
1902 quantity with a focus of deposit feeding and bioturbation. In: Berger, W.H., Smetacek,
1903 V.S., Wefer, G., (eds.), Productivity in the Ocean: Past and Present. Wiley, Chichester,
1904 pp. 235-253.
1905 Kaiho, K., Chen, Z.Q., Miura, Y., Kawahata, H., Kajiwara, Y., Sato, H., 2006b. Close-up
1906 of the end-Permian mass extinction horizon recorded in the Meishan section, South
1907 China: Sedimentary, elemental, and biotic characterization with a negative shift of
1908 sulfate sulfur isotope ratio. Palaeogeography, Palaeoclimatology, Palaeoecology 239,
1909 396-405.
1910 Kaiho, K., Kajiwara, Y., Chen, Z.Q., Gorjan, P., 2006a. A sulfur isotope event at the end
1911 of the Permian. Chemical Geology 235, 33-47

1912 Kaiho, K., Chen, Z.Q., Sawada, K., 2009. Possible causes for a negative shift of stable
1913 carbon isotope ratio before, during, and after the end-Permian mass extinction in
1914 Meishan, South China. Australian Journal of Earth Sciences 56, 799-808.
1915 Kaiho, K., Kajiwara, Y., Nakano, T., Miura, Y., Chen, Z.Q., Shi, G.R., 2001. End-Permian
1916 catastrophe by a bolide impact: evidence of a gigantic release of sulfur from the
1917 mantle. Geology 29, 815-818.
1918 Keighley, D.G., Pickeril, P.K., 1994. The ichnogenus *Beaconites* and its distinction from
1919 *Ancorichnus* and *Taenidium*. Palaeontology 37, 305-337.
1920 Knaust, D., 1998. Trace fossils and ichnofabrics on the Lower Muschelkalk carbonate
1921 ramp (Triassic) of Germany: tool for high-resolution sequence stratigraphy.
1922 Geologische Rundschau 87, 21-31.
1923 Knaust, D., 2004. Cambro–Ordovician trace fossils from the SW Norwegian Caledonides.
1924 Geological Journal 39, 1–24.
1925 Knoll, A.H., Bambach, R.K., Oayne, J.L., Pruss, S., Fischer, W.W., 2007.
1926 Paleophysiology and end-Permian mass extinction. Earth and Planetary Science
1927 Letters 256, 295–313.
1928 Korte, C., Kozur, H., Joachimski, M.M., Strauss, H., Veizer, J., Schwark, L., 2004a.

1929 Carbon, sulfur, oxygen and strontium isotope records, organic geochemistry and
1930 biostratigraphy across the Permian/Triassic boundary in Abadeh, Iran. International
1931 Journal of Earth Sciences 93, 565–581
1932 Kosnik, M.A., Wagner, P.J., 2006. Effects of taxon abundance distributions on expected
1933 numbers of sampled taxa. Evolutionary Ecology Research 8, 195–211.
1934 Kozur, H., 2007. Biostratigraphy and event stratigraphy in Iran around the
1935 Permian–Triassic Boundary (PTB): Implications for the causes of the PTB biotic
1936 crisis. Global and Planetary Change 55, 155–176.
1937 Lea, D.W., Pak, D.K., Spero, H.J., 2000. Climate impact of late quaternary equatorial
1938 pacific sea surface temperature variations. Science 289, 1719–1724.
1939 Li, J., Cao, C.Q., Servais, T., Zhu, Y.H., 2004. Later Permian acritarchs from Meishan
1940 (SE China) in the context of Permian palaeobiogeography and palaeoecology. Neues
1941 Jahrbuch für Geologie und Paläontologie, Monatshefte 7, 427-448.
1942 Li, W.Z., Shen, S.Z., 2008. Lopingian (Late Permian) brachiopods around the
1943 Wuchiapingian-Changhsingian boundary at the Meishan sections C and D,
1944 Changxing, South China. Geobios 41, 307–320.
1945 Liang H., 2002, End-Permian catastrophic event of marine acidification by hydrated

sulfuric acid: Mineralogical evidence from Meishan section of South China: Chinese Science Bulletin 47, 1393-1397.

Liao, Z.T., 1984. New genera and species of Late Permian and earliest Triassic brachiopods from Jiangsu, Zhejiang and Anhui Provinces. Acta Palaeontologica Sinica 23, 276–285.

Luo, G.M., Lai,X.L., Jiang, H.S., Zhang, K.X., 2006. Size variation of the end Permian conodont *Neogondolella* at Meishan section, Changxing, Zhejiang and its significance. Science in China, Series D 49, 337–347.

Luo, G.M., Lai, X.L., Shi, G.R., Jiang, H.S., Yin, H.F., Xie, S.C., Tong, J.N., Zhang, K.X., He, W.H., Wignall, P.B., 2008. Size variation of conodont elements of the *Hindeodus-Isarciciella* clade during the Permian-Triassic transition in South China and its implication for mass extinction. Palaeogeography, Palaeoclimatology, Palaeoecology 264, 176-187.

Luo, G.M., Huang, J.H., Xie, S.C., Wignall, P.B., Tang, X.Y., Huang, X.Y., Yin, H.F., 2010. Relationships between carbon isotope evolution and variation of microbes during the Permian-Triassic transition at Meishan section, South China. International Journal of Earth Sciences 99, 775-784.

Luo, G.M., Wang, Y.B., Yang, H., Algeo, T.J., Kump, L., Huang, J.H., Xie, S.C., 2011. Stepwise and large-magnitude negative shift in delta C-13 (carb) preceded the main marine mass extinction of the Permian-Triassic crisis interval. Palaeogeography, Palaeoclimatology, Palaeoecology 299, 70-82.

MacEachern, J.A., Raychaudhuri, I., Pemberton, S.G., 1992. Stratigraphic applications of the *Glossifungites* ichnofacies: delineating discontinuities in the rock record. In: Pemberton, S.G. (ed.), Applications of Ichnology to Petroleum Exploration: A Core Workshop: SEPM Core Workshop No. 17, pp. 169–198 Tulsa, USA.

MacEachern, J.A., Bann, K.L., Pemberton, S.G., Gingras,M.K., 2007. The ichnofacies paradigm: high-resolution paleoenvironmental interpretation of the rock record. In: MacEachern, J.A., Bann, K.L., Gingras, M.K., Pemberton, S.G. (eds), Applied Ichnology: SEPM Short Course Notes No. 52, pp. 27–64. Tulsa, USA.

Mei, S.L., Zhang, K.X., Wardlaw, B.R., 1998. A refined succession of Changhsingian and Griesbachian neogondolellid conodonts from the Meishan section, candidate of the Global Stratotype Section and Point of the Permian-Triassic boundary. Palaeogeography, Palaeoclimatology, Palaeoecology 143, 213-226.

Miller, M.F., Smail, S.E., 1997. A semiquantitative method for evaluating bioturbation

on bedding planes. Palaios 12, 391–396.

Mundil, R., Metcalfe, I., Ludwig, K.R., Renne, P.R., Oberli, F., Nicoll, R.S., 2001. Timing of the Permian–Triassic biotic crisis: implications from new zircon U/Pb age data (and their limitations). Earth and Planetary Science Letters 187, 131–145.

Mundil, R., Ludwig, K.R.,Metcalfe, I., Renne, P.R., 2004. Age and timing of the Permian mass extinctions: U/Pb dating of closed-system zircons. Science 305, 1760–1763.

Myrow, P.M., 1995. *Thalassinoides* and the enigma of early Paleozoic open-framework burrow systems. Palaios 10, 58-74.

Nicoll, R.S., Metcafle, I., Wang, C.Y., 2002. New species of the conodont genus Hindeodus and conodont biostratigraphy of the Permian–Triassic boundary interval. Journal of Asian Earth Sciences 20, 609–631.

Olszewski, T.D., 2004. A unified mathematical framework for the measurement of richness and evenness within and among multiple communities. Oikos 104, 377–378.

Orchard, M.J., Krystyn, L., 1998.Conodonts of the lowermost Triassic of Spiti, and new zonation based on *Neogondolella* successions. Rivista Italiana di Paleontogia e Stratigrafia 104, 341–368.

Orchard, M.J., Nassichuk, W.W., Rui, L., 1994. Conodonts from the Lower Griesbachian *Otoceras latilobatum* bed of Selong, Tibet and the position of the Permian–Triassic boundary. Canadian Society of Petroleum Geologists, Proceedings of Pangea Conference, Memoir 17, 823–843.

Payne, J.L., Clapham, M.E., 2012. End-Permian mass extinction in the oceans: An ancient analog for the twenty-first century? Annual Reviews of Earth and Planetary Sciences 40, 89–111.

Payne, J.L., Lehrmann, D.J., Wei, J.Y., Orchard, M.J., Schrag, D.P., Knoll, A.H., 2004. Large perturbations of the carbon cycle during recovery from the end-Permian extinction. Science 205, 505-509.

Payne, J.L., Lehrmann, D.J., Wei, J., Knoll, A.H., 2006. The pattern and timing of biotic recovery from the end-Permian extinction on the Great Bank of Guizhou, Guizhou Province, China. Palaios 21, 63–85.

Payne, J.L., Lehrmann, D.J., Follett, D., Seibel, M., Kump, L.R., Riccardi, A., Altiner, D., Sano, H., Wei, J., 2007. Erosional truncation of uppermost Permian shallow-marine carbonates and implications for Permian–Triassic boundary events. Geological Society of America, Bulletin 119, 771–784.

2014 Pemberton, S.G., Frey, R.W., 1985. The *Glossifungites* ichnofacies: modern examples
2015 from the Georgia coast, USA. In: Curran, H.A., (ed.), Biogenic Structures: Their Use
2016 in Interpreting Depositional Environments: SEPM Special Publication, 35, pp.
2017 237–259, Tulsa, USA.
2018 Pemberton, S.G., Flach, P.D., Mossop, G.D., 1982. Trace fossils from the Athabasca Oil
2019 Sands, Alberta, Canada. Science 217, 825-827.
2020 Pemberton, S.G., MacEachern, J.A., Saunders, T., 2004. Stratigraphic applications of
2021 substratespecific ichnofacies: delineating discontinuities in the fossil record. In:
2022 McIlroy, D. (ed.), The Application of Ichnology to Palaeoenvironmental and
2023 Stratigraphic Analysis: Geological Society of London, Special Publication, 228,
2024 29–62.
2025 Perri, M.C., Farabegoli, E., 2003. Conodonts across the Permian–Triassic boundary in
2026 the Southern Alps. Courier Forschungsinstitute Senckenberg 245, 281–313.
2027 Pruss, S.B., Bottjer, D.J., 2004. Early Triassic fossils of the western United States and
2028 their implications for prolonged environmental stress from the end-Permian mass
2029 extinction. Palaios 19, 551-564.
2030 Reichow, M.K., Pringle, M.S., Al'Mukhamedov, A.I., Allen, M.B., Andreichev, V.L.,

Buslov, M.M., Davies, C.E., Fedoseev, G.S., Fitton, J.G., Inger, S., Medvedev, A.Y., Mitchell, C., Puchkov, V.N., Safanova, I.Y., Scott, R.A., Saunders, A.D., 2009. The timing and extent of the eruption of the Siberian Traps large igneous province: implications for the end-Permian environmental crisis. Earth and Planetary Sciences Letters 277, 9–20.

Renne, P.R., Black, M.T., Zheng, Z.C., Richards, M.A., Basu, A.R., 1995. Synchrony and causal relations between Permian–Triassic boundary crisis and Siberian flood volcanism. Science 269, 1413–1416.

Renne, P.R., Mundil, R., Balco, G., Min, K., Ludwig, K.R., 2010. Joint determination of 40K decay constants and 40Ar*/40K for the Fish Canyon sanidine standard, and improved accuracy for 40Ar/39Ar geochronology. Geochimica et Cosmochimica Acta 74, 5349–5367.

Riccardi, A., Arthur,M.A., Kump, L.R., 2006. Sulfur isotopic evidence for chemocline upward excursions during the end-Permian mass extinction. Geochimica et Cosmochimica Acta 70, 5740–5752.

Rindsberg, A.K., Kopaska-Merkel, D.C., 2005. *Treptichnus* and *Arenicolites* from the Steven C. Minkin Paleozoic footprint Site (Langsettian, Alabama, USA). In: Buta,

R.J., Rindsberg, A.K., Kopaska-Merkel, D.C., (eds.), Pennsylvanian Footprints in the Black Warrior Basin of Alabama: Monograph, 1. Alabama Paleontological Society, pp. 121–141.

Rui, L., He, J., Chen, C., Wang, Y., 1988. Discovery of fossil animals from the basal clay of Permian–Triassic boundary in the Meishan area of Changxing, Zhejiang and its significance. Journal of Stratigraphy 12, 48–52.

Savrda, C.E., 1992. Trace fossils and benthic oxygenation. In: Maples, C.G., West, R.R. (eds), Trace Fossils, Short Courses in Paleontology 5. University of Tennessee Press, Knoxvill pp. 172–196.

Savrda, C.E., Bottjer, D.J., 1987. The exaerobic zone, a new oxygen-deficient marine biofacies. Nature 327, 54-56.

Savrda, C.E., Browning, J.V., Krawinkel, H., Hesselbo, S.P., 2001. Firmground ichnofabrics in deep-water sequence stratigraphy, Tertiary clinoform-toe deposits, New Jersey slope. Palaios 16, 294–305.

Seilacher, A. 1967. Bathymetry of trace fossils. Marine Geology 5, 413-428.

Seilacher, A. 1977. Pattern analysis of *Paleodictyon* and related trace fossils. In: Crimes, T.P., Harper, J.C. (eds.), Trace Fossils 2. Geological Journal Special Issue No. 9,

289-334.

Seilacher, A., 2007. Trace Fossil Analysis. Springer, Berlin. 226 pp.

Sephton, M.A., Looy, C.V., Brinkhuis, H., Wignall, P.B., de Leeuw, J.W., Visscher, H., 2005. Catastrophic soil erosion during the end-Permian biotic crisis. Geology 33, 941–944.

Sepkoski Jr., J.J., 1982. A Compendium of Fossil Marine Families: Milwaukee Public Museum Contributions in Biology and Geology, 51, p. 125.

Sepkoski Jr., J.J., 2002. A Compendium of Fossil Marine Animal Genera: Bulletin of American Paleontology 363, 1-563.

Sheldon, N.D., 2006. Abrupt chemical weathering increase across the Permian–Triassic boundary. Palaeogeography, Palaeoclimatology, Palaeoecology 231, 315–321.

Shen, J., Algeo, T.J., Zhou, L., Feng, Q., Yu, J., Ellwood, B., 2012. Volcanic perturbations of the marine environment in South China preceding the latest Permian mass extinction and their biotic effects. Geobiology 10, 82-103.

Shen, S.Z., James L. Crowley, J.L., Wang, Y., Bowring, S.A., Erwin, D.H., Sadler, P.M., Cao, C.Q., Rothman, D.H., Henderson, C.M., Ramezani, J., Zhang, H., Shen, Y.A., Wang, X.D., Wang, W., Mu, L., Li, W.Z., Tang, Y.G., Liu, X.L., Liu, L.J., Zeng, Y.,

2082 Jiang, Y.F., Jin, Y.G., 2011b. Calibrating the end-Permian mass extinction. Science
2083 9, 1367-1372,
2084 Shen, W.J., Lin, Y.T., Xu, L., Li, J. F., Wu, Y.S., Sun, Y.G., 2007. Pyrite framboids in the
2085 Permian-Triassic boundary section at Meishan, China: Evidence for dysoxic
2086 deposition. Palaeogeography, Palaeoclimatology, Palaeoecology 253, 323-331.
2087 Shen, Y.A., Farquhar, J., Zhang, H., Masterson, A., Zhang, T., Wing, B.A., 2011a.
2088 Multiple S-isotopic evidence for episodic shoaling of anoxic water during Late
2089 Permian mass extinction. Nature Communications 2, 210e.
2090 Sheng, J., Chen, C., Wang, Y., Rui, L., Liao, Z., Bando, Y., Ishii, K., Nakazawa, K.,
2091 Nakamura, K., 1984. Permian–Triassic boundary in Middle and Eastern Tethys.
2092 Journal of Faculty of Science, Hokkaido University 21, 133–181.
2093 Sheng, J.Z., Chen, C.Z., Wang, Y.G., Rui, L., Liao, Z.T., He, J.W., Jiang, N.Y., Wang,
2094 C.Y., 1987. New evidence on the Permian and Triassic boundary of Jiangsu,
2095 Zhejiang and Anhui. In: Nanjing Institute of Geology and Palaeontology, Academia
2096 Sinica (ed.), Stratigraphy and Palaeontology of Systemic Boundaries in China.
2097 Permian–Triassic Boundary (1). Nanjing University Press, Nanjing, pp. 1–21
2098 Shi, C., Chen, D., 1987. The Changhsingian ostracodes from Meishan, Changxing,

Zhejiang. In: Nanjing Institute of Geology and Palaeontology, Academia Sinica (Ed.), Stratigraphy and Palaeontology of systemic boundaries in China. Permian-Triassic boundary (1). Nanjing University Press, Nanjing, pp. 23-80.

Song, H., Tong, J., Chen, Z.Q., 2009. Two episodes of foraminiferal extinction near the Permian–Triassic boundary at the Meishan section, South China. Australian Journal of Earth Sciences 56, 765–773.

Song, H., Tong, J., Zhang, K., Wang, Q., Chen, Z.Q., 2007. Foraminiferal survivors from the Permian–Triassic mass extinction in the Meishan section, South China. Palaeoworld 16, 105–119.

Song, H.J., Wignall, P.B., Tong, J.N., Yin, H.F., 2013a. Two pulses of extinction during the Permian-Triassic crisis. Nature Geoscience 6, 52-56.

Song, H.J., Wignall, P.B., Chu, D.L., Tong, J.N., Sun, Y.D., Song, H.Y., He, W.H., Tian, L., 2014. Anoxia/High temperature double whammy during the Permian-Triassic marine crisis and its aftermath. Scientific Reports 4, 4132.

Song, H.Y., Tong, J.N., Algeo, T.J., Horacek, M., Qiu, H.O., Song, H.J., Tian, L., Chen, Z.Q., 2013b. Large vertical $\delta^{13}C$ gradients in Early Triassic seas of the South China craton: Implications for oceanographic changes related to Siberian Traps volcanism.

2116 Global and Planetary Change 105, 7–20.

2117 Sun, Y.D., Joachimski, M.M., Wignall, P.B., Yan, C.B., Chen, Y.L., Jiang, H.S., Wang,

2118 L., Lai, X.L., 2012. Lethally hot temperatures during the Early Triassic greenhouse.

2119 Science 338, 366–370.

2120 Tian, S.F., Chen, Z.Q., Huang, C.J., 2014. Orbital forcing and sea-level changes in the

2121 earliest Triassic of the Meishan section, South China. Journal of Earth Science 25,

2122 64-73.

2123 Tong, J.N., Yang, Y., 1998. Advance in the study of the Lower Triassic conodonts at

2124 Meishan section, Changxing, Zhejiang Province. Chinese Science Bulletin 43,

2125 1350–1353.

2126 Twitchett, R.J., 1999. Palaeoenvironments and faunal recovery after the end-Permian

2127 mass extinction. Palaeogeography, Palaeoclimatology, Palaeoecology 154, 27-37.

2128 Twitchett, R.J., 2006. The palaeoclimatology, palaeoecology and palaeoenvironmental

2129 analysis of mass extinction events. Palaeogeography, Palaeoclimatology,

2130 Palaeoecology 232, 190-213.

2131 Twitchett, R.J., Barras, C.G., 2004. Trace fossils in the aftermath of mass extinction

2132 events. In: McIlroy, D. (Ed.), Application of Ichnology to Palaeoenvironmental and

Stratigraphic Analysis. Geological Society of London, Special Publication 228, pp. 395-415.

Twitchett, R.J., Krystyn, L., Baud, A., Wheeley, J.R., Richoz, S., 2004. Rapid marine recovery after the end-Permian mass-extinction event in the absence of marine anoxia. Geology 32, 805-808.

Wang, C., Visscher, H., 2007. Abundance anomalies of aromatic biomarkers in the Permian–Triassic boundary section at Meishan, China—evidence of end-Permian terrestrial ecosystem collapse. Palaeogeography, Palaeoclimatology, Palaeoecology 252, 291–303.

Wang, Y., Sadler, P.M., Shen, S.Z., Erwin, D.H., Zhang, Y.C., Wang, X.D., Wang, W., Crowley, J.L., Henderson, C.M., 2014. Quantifying the process and abruptness of the end-Permian mass extinction. Paleobiology 40, 113-129.

Wignall, P.B., 2007. The end-Permian mass extinction—how bad did it get? Geobiology 5, 303–309.

Wignall, P.B., Hallam, A., 1993. Griesbachian (earliest Triassic) palaeoenvironmental changes in the Salt Range, Pakistan and southeast China and their bearing on the Permo–Triassic mass extinction. Palaeogeography, Palaeoclimatology,

2150 Palaeoecology 102, 215-37.

2151 Wignall, P.B., Twitchett, R.J., 2002. Extent, duration and nature of the Permian-Triassic

2152 superanoxic event. Geological Society of America, Special Paper 356, 395-413.

2153 Wignall, P.B., Morante, R., Newton, R., 1998. The Permo–Triassic transition in

2154 Spitsbergen; δ^{3}Corg chemostratigraphy, Fe and S geochemistry, facies, fauna and

2155 trace fossils. Geological Magazine 135, 47-62.

2156 Wignall, P.B., Newton, R., Brookfield, M.E., 2005. Pyrite framboid evidence for

2157 oxygen-poor deposition during the Permian–Triassic crisis in Kashmir.

2158 Palaeogeography, Palaeoclimatology, Palaeoecology 216, 183–188.

2159 Wignall, P.B., Kershaw, S., Collin, P.Y., Crasquin-Soleau, S., 2009. Comment: erosional

2160 truncation of uppermost Permian shallow-marine carbonates and implications for

2161 Permian–Triassic boundary events. Geological Society of America, Bulletin 121,

2162 954–956.

2163 Williams, A., James, M.A., Emig, C.C., Mackay, S., Rhodes, M.C., Cohen, B.L.,

2164 Gawthrop, A.B., Peck, L.S., Curry, G.B., Ansell, A.D., Cusack, M., Walton, D.,

2165 Brunton, C.H.C., MacKinnon, D.I., Richardson, J.R., 1997. Treatise on Invertebrate

2166 Paleontology Part H, Brachiopoda, Revised, Volume 1: Introduction. The Geological

Society of America and The University of Kansas, Boulder, Colorado and Lawrence, Kansas, 539 pp.

Wilson, M.A., Palmer, T.J., 1998. The earliest *Gastrochaenolites* (Early Pennsylvanian, Arkansas, USA): an upper Paleozoic bivalve boring? Journal of Paleontology, 72, 769–772.

Wu, H.C., Zhang, S.H., Hinnov, L.A., Jiang, G.Q., Feng, Q.L., Li, H.Y., Yang, T.S., 2013. Time-calibrated Milankovitch cycles for the Late Permian. Nature Communications 4, 2452.

Xie, S.C., Pancost, R.D., Yin, H.F., Wang, H.M., Evershed, R.P., 2005. Two episodes of microbial change coupled with Permo/Triassic faunal mass extinction. Nature 343, 494-497.

Xie, S., Pancost, R.D., Huang, J., Wignall, P.B., Yu, J., Tang, X., Chen, L., Huang, X., Lai, X., 2007. Changes in the global carbon cycle occurred as two episodes during the Permian–Triassic crisis. Geology 35, 1083–1086.

Xu, D.Y., Yan, Z., 1993. Carbon-isotope iridium event markers near the Permian-Triassic boundary in the Meishan section, Zhejiang Province, China. Palaeogeography, Palaeoclimatology, Palaeoecology 104, 171-176.

2184 Yang, W., Jiang, N., 1981. Sedimentary features and microfacies of the Changhsing
2185 Formation and Permian-Triassic boundary. Bulletins of the Nanjing Institute of
2186 Geology and Palaeontology, Academia Sinica 2, 113-133.
2187 Yang, Z., Yin, H., Wu, S., Yang, F., Ding, M., Xu, G., 1987. Permian-Triassic boundary
2188 stratigraphy and fauna of South China. Ministry of Geology and Mineral Resources,
2189 People's Republic of China, Geological Memoirs Series 2, Number 6. Geological
2190 Publishing House, Beijing, 379 pp.
2191 Yang, Z., Wu, S., Yin, H., Xu, G., Zhang, K., Bi, X., 1993. Permo-Triassic events of South
2192 China. Geological Publishing House, Beijing, 153 pp.
2193 Yin, H., Ding, M., Zhang, K., Tong, J., Yang, F., Lai, X., 1995. Dongwuan-Indosinian
2194 (Late Permian-Middle Triassic) Ecostratigraphy of the Yangtze Region and its
2195 Margins. Science Press, Beijing, 338 pp.
2196 Yin, H., Zhang, K., Tong, J., Yang, Z., Wu, S., 2001. The Global Stratotype Section and
2197 Point (GSSP) of the Permian-Triassic Boundary. Episodes 24(2), 102-114.
2198 Yin, H., Sweet, W.C., Glenister, B.F., Kotlyar, G., Kozur, H., Newell, N.D., Sheng, J.,
2199 Yang, Z. and Zakharov, Y.D., 1996, Recommendation of the Meishan section as
2200 Global Stratotype Section and Point for basal boundary of Triassic System:

2201 Newsletter on Stratigraphy 34, 81–108.

2202 Yin, H.F., Feng, Q.L., Lai, X.L., Baud, A., Tong, J.N., 2007. The protracted

2203 Permo-Triassic crisis and multi-episode extinction around the Permian-Triassic

2204 boundary. Global and Planetary Change 55, 1-20.

2205 Yin, H.F., Huang, S.J., Zhang, K.X., Hansen, H.J., Yang, F.Q., Ding, M.H., Bie, X.M.,

2206 1992, The effects of volcanism on the Permo-Triassic mass extinction in South

2207 China, *in* Sweet, W.C., Yang, Z.Y, Dickins, J.M., Yin, H.F. (eds), Permo-Triassic

2208 Events in the Eastern Tethys. Cambridge, UK, Cambridge University Press, p.

2209 169-174.

2210 Yin, H.F., Xie, S., Luo, G., Algeo, T.J., Zhang, K., 2012. Two episodes of environmental

2211 change at the Permian-Triassic boundary of the GSSP section Meishan.

2212 Earth-Science Reviews 115, 163-172.

2213 Yin, H.F., Jiang, H.S., Xia, W.C., Feng, Q.L., Zhang, N., Shen, J., 2014. The end-Permian

2214 regression in South China and its implication on mass extinction. Earth-Science

2215 Reviews 137, 19-33.

2216 Yuan, D.X., Shen, S.Z., Henderson, C.M., Chen, J., Zhang, H., Feng, H.Z., 2014. Revised

2217 conodont-based integrated high-resolution timescale for the Changhsingian Stage

and end-Permian extinction interval at the Meishan sections, South China. Lithos 204, 220-245.

Zeebe, R.E., Zachos, J.C., Dickens, G.R., 2009. Carbon dioxide forcing alone insufficient to explain Palaeocene–Eocene thermal maximum warming. Nature Geoscience 2, 576–580.

Zhang, H., Shen, S.Z., Cao, C.Q., Zheng, Q.F., 2014. Origins of microspherules from the Permian-Triassic boundary event layers in South China. Lithos 204, 246-257.

Zhang, K.X., Lai, X.L., Tong, J.N., Jiang, H.S., 2009. Progresses on study of conodont sequence for the GSSP section at Meishan, Changxing, Zhejiang Province, South China. Acta Palaeontologica Sinica 48, 485-495.

Zhang, K.X., Tong, J.N., Shi, G.R., Lai, L.X., Peng, Y.Q., Yu, J.X., He, W., Jin, Y.L., 2007. Early Triassic conodont-palynological biostratigraphy of the Meishan D section in Changxing, Zhejiang Province, South China. Palaeogeography, Palaeoclimatology, Palaeoecology 252, 4–23

Zhang, K.X., Tong, J.N., Yin, H.F., Wu, S.B., 1997. Sequence stratigraphy of the Permian-Triassic boundary section of Changxing, Zhejiang, Southern China. Acta Geologica Sinica 71, 90-103.

2235 Zhang, K.X., Tong, J.N., Hou, G.J., Wu, S.B., Zhu, Y.H., Lin, Q.X., 2005. Regional
2236 Geological report, the People's Republic of China (Meishanzhen Map H50E006023,
2237 Changxingian Map, H50E006024, Scale:1:50000). University of Geosciences Press,
2238 264 pp., Wuhan, China.
2239 Zhao, J., Sheng, J., Yao, Z., Liang, X., Chen, C., Rui, L., Liao, Z., 1981. The
2240 Changhsingian and Permian-Triassic boundary of South China, Bulletin of the
2241 Nanjing Institute of Geology and Palaeontology, Academia Sinica 2, 1-95.
2242 Zhao, X.M., Tong, J.N., 2010. Two episodic changes of trace fossils through the
2243 Permian-Triassic transition in the Meishan section cores, Zhejiang Province, Science
2244 China, Earth Science 40, 1241-1249.
2245 Zheng, Q.F., Cao, C.Q., Zhang, M.Y., 2013. Sedimentary features of the Permian-Triassic
2246 boundary sequence of the Meishan section in Changxing County, Zhejiang Province.
2247 Science China, Earth Sciences 56, 956-969.
2248 Zhao, L., Chen, Y., Chen, Z.Q., Cao, L., 2013b. Uppermost Permian to Lower Triassic
2249 conodont zonation from Three Gorges area, South China. Palaios 28, 523-540.
2250 Zhao, L., Chen, Z.Q., Algeo, T.J., Chen, J., Chen, Y., Tong, J., Gao, S., Zhou, L., Hu, Z.,
2251 Liu, Y., 2013a. Rare-earth element patterns in conodont albid crowns: Evidence for

massive inputs of volcanic ash during the latest Permian biocrisis? Global and Planetary Change 105, 135-151.

Zonneveld, J.-P., Gingras, M.K., Beatty, T.W., 2010. Diverse ichnofossil assemblage following the P–T mass extinction, Lower Triassic, Alberta and British Columbia, Canada: evidence for shallow marine refugia on the northwestern coast of Pangaea. Palaios 25, 368–392.

Figure captions

Fig. 1. The GSSP for the Permian-Triassic boundary at Meishan, Changxing county, northwestern Zhejiang Province, east China. A, location of the Meishan section. B, close-up of the white volcanic ash bed (Bed 25) in Meishan. C, geopark of the GSSP Meishan showing GSSP position at the Meishan section D. D, the P-Tr boundary beds showing biostratigraphic boundary through the mid-Bed 27 and the mass extinction horizon at the base of Bed 25. E, outcrop of the P-Tr boundary beds and Yinkeng Formation along strike on the Meishan hill from the geopark section.

2269 **Fig. 2**. Biostratigraphy of the P-Tr transition at the Meishan section with the updated

2270 conodont zones and correlations with ammonoid, bivalve, brachiopod and microfloral

2271 assemblages from Meishan as well as conodont zones from North Italy, Iran and

2272 Germany, and India. Note that the updated conodont zonation is revised from those

2273 documented by Jiang et al. (2007) and Zhang et al. (2009) and our new observations.

2274 White arrows indicate that conodont zones extend to horizons below Bed 22 of Meishan

2275 and its equivalents.

2276 **Fig. 3**. P-Tr succession exposed in the GSSP Meishan showing lithology, facies types,

2277 depositional environments, stratigraphic distributions of trace fossils, and bioturbation

2278 levels. Ichnofabric indices (ii: Droser and Bottjer, 1986) are assessed as 1 to 6, indicating

2279 bioturbation from lowest to highest levels. Bedding plane bioturbation index (bpbi) is

2280 evaluated based on bedding plane coverage of burrows (Miller and Smail, 1997). Facies

2281 symbols: om = offshore mudstone facies, bs = basinal black shale facies, ow = offshore

2282 wackestone facies, os = offshore siltstone facies; ew = epeiric sea wackestone facies,

2283 HCS = hummocky cross stratification, hb = horizontal bedding. Depositional

2284 environment (DE): ns = nearshore, fw = fair-weather wave base, sw = subtidal zone to

2285 fair-weather wave base, swb = storm wavebase.

Fig. 4. Lithology and fossils from the exposure of the P-Tr transition in Meishan. A-B, D, field photograph, polished surface and microphotograph showing hummocky cross-stratified (HCS) muddy limestone (Bed 54), upper Yinkeng Formation; pen is 15 cm long; scale bars are 2 cm. C, pale mudstone and calcareous mudstone (Bed 41) showing horizontal stratification, lower Yinkeng Formation; pen is 15 cm long. E, F, I, ammonoid fossils across the P-Tr boundary with large ammonoid shell (E) in Bed 24e of the Changhsing Formation contrasting to small shells (F, I) recorded in the middle and upper Yinkeng Formation; coins are 1.5 cm in diameter; scale bar is 1 cm. G, dark thin-bedded limestone interbedded with bioclastic limestone bands, Bed 24e; pen is 10 cm long. H, irregular contact between Beds 24d and 24e; cross-bedding is pronounced in the uppermost Bed 24d; scale bar is 1 cm. J, vertical burrow of *Balanoglossites* in the upper part of Bed 24d; scale bar is 1.5 cm.

Fig.5. Microfacies and fossil fragment assemblages from Beds 23-26, upper Changhsing Formation. A, microphotograph of claystone, Bed 25. B, microphotograph showing horizontal laminae (black arrow) of black shale, Bed 26. C, bioclastic packstone of Bed 23a showing brachiopod (b), crinoid (c), and ostracod (o) fragments. D, bioclastic packstone of Bed 24c showing abundant foraminifer (f), brachiopod (b), crinoid (c),

2303 ostracod (o) and other fragments.

2304 **Fig. 6.** Pie diagrams showing percentage of major components in all rocks sampled from

2305 Beds 22-60 in Meishan. Detailed fossil fragment contents (%) of each sample are

2306 tabulated in Table 3. Component symbols: 1 = foraminifers, 2 = ostracods, 3 = crinoids, 4

2307 = echinoids, 5 = brachiopods, 6 = bryozoans, 7 = sponge spicules, 8 = calcareous sponges,

2308 9 = gastropods, 10 = radiolarians, 11 = macroalgae, 12 = micrites, 13 = cavities, 14 =

2309 other particles (fecal pellets, peloids, pyrites and undetermined particles).

2310 **Fig.7**. Microfacies across the boundary between Beds 24e-5 and 24e-6. A, transverse

2311 view of one sponge spicule. B-C, cross-section view of sponge spicules. D,

2312 microphotograph showing the laminated horizon separating bioclastic layer (Bed 24e-5)

2313 from the overlying sponge spicule-rich layer (Bed 24e-6). E, SEM image of one isolated

2314 specimen of a sponge spicule. B-C, scale bars are both 50μm; E, Scale bar is 40 μm.

2315 **Fig. 8**. Microfacies and fossil fragment assemblages from Bed 26b, 8-10 cm above the

2316 base of Bed 25. A, microphotograph showing foraminifer (f), bryozoan (bry), echinoid

2317 (e), and brachiopod (bra) fragments. B, microphotograph showing ostracod (o), echinoid

2318 (e), and brachiopod (bra) fragments. C, microphotograph showing brachiopod (bra) and

2319 echinoid (e) fragments. D, microphotograph showing bryozoan (bry) and brachiopod (bra)

2320 fragments. E, microphotograph showing foraminifer (f) and echinoid (e) fragments. F,

2321 microphotograph showing brachiopod (bra) and foraminifer (f) fragments. G,

2322 microphotograph showing foraminifer (f) and echinoid (e) fragments. H,

2323 microphotograph showing bryozoan (bry) and foraminifer (f) fragments. I,

2324 microphotograph showing foraminifer (f) and echinoid (e) fragments. J,

2325 microphotograph showing foraminifer (f) fragments. K, microphotograph showing

2326 bryozoan (bry) and echinoid (e) fragments. L, microphotograph showing foraminifer (f)

2327 and echinoid (e) fragments. All scale bars are all 100 μm.

2328 **Fig. 9**. Polished surface of Bed 27 and its microfacies features. A, polished surface

2329 showing the entire bed is subdivided into four parts (labelled a, b, c, d) by two sets of

2330 pronounced irregular surfaces, in which burrows (red arrows) are commonly present. B,

2331 microphotograph of the basal part of Bed 27a, 11-13 cm above the base of Bed 25,

2332 showing foraminifer (f) and brachiopod (bra) fragments. C, microphotograph of the

2333 upper part of Bed 27a, 13-15 cm above the base of Bed 25, showing foraminifers (f) and

2334 other fossil fragments. D, microphotograph of the lower part of Bed 27b, 15-17 cm above

2335 the base of Bed 25, showing claystone-dominated texture. E, microphotograph of the

2336 upper part of Bed 27b, 18-20 cm above the base of Bed 25, showing echinoid (e) and

2337 other fossil fragments. F, microphotograph of the upper part of Bed 27c, 21-23 cm above

2338 the base of Bed 25, showing abundant foraminifer (f), echinoid (e) and brachiopod (bra)

2339 fragments. G, microphotograph of Bed 27d, 23-28 cm above the base of Bed 25, showing

2340 abundant ostracod (o), foraminifer (f), echinoid (e), and other fragments. H,

2341 microphotograph of the upper part of Bed 26b, 8-10 cm above the base of Bed 25,

2342 showing abundant foraminifer (f) and other fossil fragments.

2343 **Fig. 10**. Bioclastic packstone to wackestone showing various fossil fragments from Bed

2344 27a, 13-15 cm above the base of Bed 25. A, foraminifer (f). B, brachiopod (bra) and other

2345 fragments. C, foraminifer (f), echinoid (e) and other undetermined fragments. D,

2346 foraminifer (f). E, foraminifer (f). F, foraminifer (f), brachiopod (b) and other

2347 undetermined fragments. G, I-K, foraminifer tests. H, echinoid (e) fragment. Scale bars

2348 are all 50 μm.

2349 **Fig. 11**. Bioclastic packstone and various fossil fragments from Bed 27c, 21-23 cm above

2350 the base of Bed 25. A, foraminifer (f) and brachiopod (bra) fragments. B, foraminifer

2351 *Frodina permica* test. C, echinoid (e) and brachiopod (b) fragments; D, bryozoan (bry) ,

2352 foraminifer (f) and other undetermined fragments. E, foraminifer (f) *Nodosinelloides*

2353 *netschajewi* test and echinoid (e) fragments. F, foraminifer test of *Hemigordius* sp. G,

brachiopod (bra) fragment. H, bryozoan (bry) fragment. I, foraminifer (f) *Hemigordius* sp. test. J, foraminiferal (f) fragment. K, echinoid (e) and foraminifer (f) fragments. L-M, echinoid fragments. Scale bars are all 50 μm.

Fig. 12. Bioclastic packstone to wackestone showing various fossil fragments from Bed 27d, 23-28 cm above the base of Bed 25. A, foraminifer test of *Nodosinelloides* sp. B, brachiopod (b), foraminifer (f), and echinoid (e) fragments. C-D, foraminifer tests of *Nodosinelloides* sp. and *Nodosaria* sp., respectively. E, brachiopod (bra), foraminifer (f), and other fragments. F, echinoid fragment. G, sponge spicule. H, foraminiferal fragment of *Tuberitina maljavkini*. I, echinoid fragment. J, brachiopod (bra) and sponge spicule (ss); K, foraminifer test of *Nodosinelloides* sp. L, foraminifer Nodosinelloides aequiampla and brachiopod (bra) fragments. M, foraminifer (f) fragment. N, ostracod (o), foraminifer (f), and echinoid (e) fragments. O, brachiopod (bra) and echinoid (e) fragments; P, brachiopod (bra) and echinod (e) fragments. B, scale bar is 100 μm; F-G, scale bars are 20μm; other scale bars are all 50 μm.

Fig. 13. Microfacies and fossil fragment assemblage from strata of Bed 29 and above. A, bioclastic wackestone with ostracod (o) and brachiopod (bra) fragments, Bed 29. B, bioclastic wackestone with brachiopod (bra) and ostracod (o) fragments, Bed 29. C,

2371 echinoid fragment, Bed 53. D, ostracods test, Bed 52. F, ostracod test, Bed 53. I, K, M,

2372 ostracods tests, Bed 54. N, ostracods test, Bed 55. P-R, ostracod tests, Beds 56, 57 and 58,

2373 respectively. E, foraminifer fragment, Bed 29. J, L, foraminifer fragments, Beds 52 and

2374 53, respectively. G, foraminifer *Nodosaria* sp., Bed 56. H, foraminifer *Nodosaria*

2375 *rostrata* Trifonova, Bed 56. O, micrite containing pyrite particles (black) and tiny tubes

2376 (t), Bed 44. Scale bars are all 50 μm.

2377 **Fig. 14**. Fossil fragment distributions over the P-Tr transition (Beds 22-60) in Meishan.

2378 Vertical axis represents percentage of various fossil fragments in all rock.

2379 **Fig. 15**. Shell beds from the Yinkeng Formation in Meishan. A, *Claraia* concentrations

2380 (white arrows) from Bed 40; scale bar is 1 cm; B, shell concretions of *Claraia griesbachi*

2381 (c) and *Ophiceras* sp. (o) of the *O-P* community from Bed 32; coin is 1.5 cm in diameter;

2382 C, shell concretions of *Claraia griesbachi* from Bed 35; coin is 1.5 cm in diameter; D,

2383 shell concretions of *Claraia wangi* of the *C* community from Bed 40; coin is 1.5 cm in

2384 diameter; E, shell concretions of *Claraia griesbachi* from Bed 36; coin is 1.5 cm in

2385 diameter; F, shell concretions of *Meishanorhynchia* (m), *Lytophiceras* (ly) and

2386 ophiceratid (o) of the *M-L* community from Bed 55; Scale bar is 4 mm.

2387 **Fig. 16**. Trace fossils from the Changhsing Formation of the Meishan section. A, D,

Thalassinoides sp. 1 on base of Bed 8; coin is 1.5 cm; B, *Paleophycus* isp. from Bed 9; scale bar is 1 cm; C, *Balanoglossites triadicus* from Bed 24d; coin is 1.5 cm in diameter; E, *Taenidium* isp. from upper surface of Bed 24d; coin is 1.5 cm in diameter; F, *Lockeia* isp. on the upper surface of Bed 9; coin is 1.5 cm in diameter.

Fig. 17. Trace fossils from the Changhsing Formation (Beds23-24) continued. A, E, horizontal burrows of *Planolites* isp. 1 from upper surface of Bed 24e-6; USB is 2 cm long; B-C, problematica from upper surface of Bed 23; Coins are 1.5 cm in diameter; D, *Taenidium* isp. from upper surface of Bed 24e; Coin is 1.5 cm in diameter; F, *Dendrorhaphe* isp. from upper surface of Bed 23; Coin is 1.5 cm in diameter.

Fig. 18. Trace fossils from the Yinkeng Formation. A-B, F, *Planolites* from upper surfaces of Bed 36, 41, and 56, respectively; coins are 1.5 cm, 2 cm and 1.5 cm in diameter, respectively; C, *Chondrites* isp. on upper surface of Bed 52; Coin is 1.5 cm in diameter; D-E, *Thalassionoides* isp. 3 from upper surfaces of Bed 53 and 56, respectively; coins are 1.5 in diameter; G-H, sketch reconstruction and trace of *Treptichnus* isp. on upper surface of Bed 57; coin is 1.5 cm in diameter.

Fig. 19. Polished slabs and sketches showing the successions of trace-fossil assemblages in Bed 27. A–C, vertical cross section of Bed 27 showing the ichnofabric change from a

2405 firmground ichnocoenoses of *Glossifungites* ichnofacies in the lower to a softground

2406 ichnocoenose in the upper. Note these three sample blocks (A-C) were cut from one

2407 complete sample of Bed 27. D–F, portraits of blocks A–C, respectively. Ar. = *Arenicolites*

2408 isp., Ch. = *Chondrites* isp. 1, Ga. = *Gastrochaenolites* isp., Pa. = *Planolites* isp. 2, Ps. =

2409 *Psilonichnus*; isp., Th. = *Thalassinoides* isp. 2.

2410 **Fig. 20**. Polished surface and its portrait of Bed 27 showing burrow systems in

2411 firmground of the *Glossifungites* ichnofacies and vertical colonization by ichnofaunas on

2412 different substrates. A, polished slab across the entire Bed 27 (from base to top). B, sketch

2413 reconstruction showing ichnofabrics manifested in Fig. 25A. C, cartoon reconstruction

2414 showing the generalized colonization zonation of ichnofaunas. For abbreviations of

2415 ichnotaxon names see caption of Fig. 19.

2416 **Fig. 21**. Trace fossil evolution at Meishan. A, ichnodiversity change throughout the

2417 uppermost Changhsingian to Griesbachian in Meishan. B, burrow size variations (in

2418 mean diameter and maximum diameter) over the P-Tr transition. C, tiering level change

2419 through the P-Tr transition.

2420 **Fig. 22**. Burrow sizes of selected ichnogenera through the P-Tr transition. A, burrow size

2421 variation of *Planolites* through the P-Tr transition. B, burrow size variation of

2422 *Thalassinoides* through the P-Tr transition. C, burrow sizes of both *Dendrorhaphe* and

2423 problematic trace from the upper Changhsing Formation. D, burrow sizes of

2424 *Balanoglossites*, *Taenidium*, *Chondrites*, and *Treptichnus* from the P-Tr transition in

2425 Meishan.

2426 **Fig. 23**. Pyrite framboids and crystals preserved on fossil skeletons and in sediments of

2427 Bed 27. A-C, pyrite crystals (white arrows) on brachiopod shells of *Paryphella*. D-E,

2428 pyrite crystals (white arrows) preserved in sediments and foraminiferal test; scale bars are

2429 40 μm; F-G, pyrite crystals (white arrows) preserved in foraminiferal tests; scale bars are

2430 all 40 μm. H, L, SEM images showing pyrite framboids preserved on brachiopod shells

2431 of Bed 27; I-K, pyrite framboids preserved in sediments of Bed 27; M-N, EDS results

2432 showing mineral composition of framboids of Fig. 23L and Fig. 23J, respectively.

2433 **Fig. 24**. Sizes of pyrite framboids from 17 horizons through the P-Tr transition in

2434 Meishan. MD = mean diameter, SD = standard derivation, N = Number of framboid

2435 grains.

2436 **Fig. 25**. Redox conditions indicated by pyrite framboid sizes through the P-Tr transition

2437 at Meishan. Two SEM images show morphologies of pyrite framboids from Bed 24 (left)

2438 and Bed 39 (right). PTB = Permo-Triassic boundary; PTME = Permo-Triassic mass

extinction.

Fig. 26. Composite figure showing exceptionally increased seawater surface temperature, carbon isotopic excursion, Chemical index of alternation (CIA) and Eu/Eu* profiles, through the P-Tr transition at Meishan. Total organic content (TOC) and Ce/Ce* profiles, framboid size variation, specific and generic richness variations, and community structural changes indicated by true diversity index (Exp (H)) and dominance (D) through the P-Tr transition in Meishan. Note: seawater temperature data after Joachimski et al. (2012) and Sun et al. (2012); CIA value is calculated using published data by Zhang et al. (2005); Carbon isotopic excursion after Burgess et al. (2014); Eu/Eu* and Ce/Ce* values after Zhao et al. (2013a). TOC profile after Yin et al. (2012). Framboid size data from this study. Detailed bioturbation data see Fig. 3; II = Ichnofabric indices; BPBI = Bedding plane bioturbation index. Datum source of burrow diameters sees Fig. 24. More details of fossil fragment contents see Fig. 14. Species and genus richness data after Song et al. (2013a). Community structure data from Chen et al. (2010a).

Table captions

2456 Table 1. Radiometric ages obtained from the P-Tr succession at the GSSP Meishan (in

2457 Ma).

2458 Table 2. Key conodont zones with their durations across the PTB in Meishan.

2459 Table 3. Percentage of major components in all rocks sampled from Beds 22-60 in

2460 Meishan.

2461 Table 4. X-ray diffraction (XRD) data of the PTB beds at Meishan (sourced from Liang,

2462 2002).

2463 Table 5. Structural indices of the latest Permian to earliest Triassic shelly communities

2464 from Meishan (Chen et al., 2010a).

2465 Table 6. Major indices showing community structural changes over the P-Tr transition in

2466 Meishan

2467 Table 7. Characteristics of major trace fossils from the uppermost Permian to lowest

2468 Triassic in Meishan

2469

Complete biotic and sedimentary records of the Permian-Triassic transition from Meishan section, South China: ecologically assessing mass extinction and its aftermath

Zhong-Qiang Chen[a,*], Hao Yang[a], Mao Luo[b], Michael J. Benton[c], Kunio Kaiho[d], Laishi Zhao[e], Yuangeng Huang[a], Kexing Zhang[a], Yuheng Fang[a], Haishui Jiang[a], Huan Qiu[e], Yang Li[e], Chengyi Tu[a], Lei Shi[a], Lei Zhang[e], Xueqian Feng[a], Long Chen[a]

[a] *State Key Laboratory of Biogeology and Environmental Geology, China University of Geosciences (Wuhan), Wuhan 430074, China*

[b] *School of Earth and Environment, The University of Western Australia, Crawley, WA 3009, Australia*

[c] *School of Earth Sciences, University of Bristol, Bristol, BS8 1RJ, UK;*

[d] *Institute of Geology and Paleontology, Tohoku University, Sendai 980-8578, Japan;*

[e] *State Key Laboratory of Geological Processes and Mineral Resources, China University of Geosciences (Wuhan), Wuhan 430074, China*

Formatted: Right: -0.01 cm

Formatted: Superscript

Formatted: Superscript

* Corresponding author (Z.Q. Chen). *E-mail address:* zhong.qiang.chen@cug.edu.cn

ABSTRACT

The Meishan section, South China is the Global Stratotype Section and Point (GSSP) for the Permian-Triassic boundary (PTB), and also is well known for the best record demonstrating the Permian-Triassic mass extinction (PTME) all over the world. This section has also been studied using multidisciplinary approaches to reveal the possible causes for the greatest Phanerozoic biocrisis of life on Earth; many important scenarios interpreting the great dying have been proposed on the basis of data from Meishan. Nevertheless, ~~hot~~ debates on biotic extinction patterns and possible killers still continue. This paper reviews all fossil and sedimentary records from the Permo-Triassic (P-Tr) transition, based on previously published data and our newly obtained data from Meishan, and assesses ecologically the PTME and its aftermath to determine the biotic response to climatic and environmental extremes associated with the biocrisis. Eight updated conodont zones: *C. yini*, *C. meishanensis*, *H. ~~Changhsingensis~~changxingensis*, *C. taylorae*, *H. parvus*, *I. staeschei*, *I. isarcica*, and *C. planate* Zones are proposed for the

PTB beds at Meishan. Major turnover in fossil fragment contents and ichnodiversity occurs across the boundary between Bed 24e-5 and Bed 24e-6, suggesting an extinction horizon in thin section. The irregular surface in the middle of Bed 27 is re-interpreted as a firmground of *Glossifungites* ichnofacies rather than the previously proposed submarine ~~solution~~dissolution surface or hardground surface. Both fossil fragment contents and ichnodiversity underwent dramatic declines in Beds 25–26a, coinciding with metazoan mass extinction. Fossil fragment content, ichnodiversity and all ichnofabric proxies (including burrow size, tiering level, bioturbation level) indicate that the P-Tr ecologic crisis comprises two discrete stages, coinciding with the first and second phases of the PTME in Meishan. Ecologic crisis lagged behind biodiversity decline during the PTME. Pyrite framboid size variations suggest that depositional redox condition was anoxic to euxinic in the latest Changhsingian, became euxinic in Beds 25–26a, turned dysoxic in Bed 27, then varied from euxinic to anoxic through most of the Griesbachian. The ~~10~~ 9 °C increase in seawater surface temperature from Bed 24e to Bed 27 at Meishan seems to result in dramatic declines in biodiversity and fossil fragment contents in Beds 25–26a, but had little effect on all ecologic proxies. Both metazoans and infauna seem not to be affected by the pre-extinction anoxic-euxinic condition. The anoxic event associated with

52 the PTME may have occurred in a much shorter period than previously thought and is
53 only recorded in Beds 25–26a at Meishan. Fossil fragment contents, ichnofaunas,
54 ichnofabrics and pyrite framboid size all show that no signs of oceanic acidification and
55 anoxia existed in Bed 27. The early Griesbachian anoxia may have resulted in rarity of
56 ichnofauna and metazoans in the lower Yinkeng Formation, in which the ichnofauna is
57 characterized by small, simple horizontal burrows of *Planolites*, and metazoan faunas are
58 characterized by low diversity, high abundance, opportunist-dominated communities.
59 The rapid increase of ~9 °C in sea-surface temperature and a short anoxia or acidification
60 coincided with the first-pulse biocrisis, while a prolonged and widespread anoxia
61 probably due to a long period of high seawater temperate condition may be crucial in
62 morality of most organisms in the second-pulse PTME. Marine ecosystems started to
63 recover, coupled with environmental amelioration, in the late Griesbachian.
64

65 *Keywords:* mass extinction, Permian-Triassic, fossil fragment, trace fossils, redox
66 condition, Meishan section
67
68

Contents

Formatted: Indent: Left 2.36 ch, First line: 2 ch

Formatted: Font: Not Italic

1. Introduction

As the greatest biocrisis of life on Earth (Sepkoski, 1981), the Permian-Triassic mass extinction (PTME) changed Earth's ecosystems fundamentally (Benton and Twitchett, 2003; Erwin, 2006). After they had recovered, the marine ecosystems after the PTME gave rise to the forerunners of modern-day ecosystems, both the Triassic and modern ecosystems being comparable to each other in composition of functioning groups and trophic structure (Chen and Benton, 2012). However, the causes of this enigmatic biocrisis have long been disputed despite intense study, and the same is true of the profoundly delayed recovery following the PTME (Erwin, 2001). Thus, studies of these issues have enjoyed a surge in scientific interest in the past 30 years that shows no sign of abating (Chen et al., 2014a).

Although this era-boundary crisis has been widely recognized in Permian–Triassic boundary (PTB) sections around the world, many important hypotheses have been proposed based on paleontological and experimental data sampled from the Meishan section of Changhsing County, Zhejiang Province, east China (Fig. 1A; Renne et al., 1995; Bowring et al., 1998; Jin et al., 2000; Yin et al., 2001, 2012; Kaiho et

al., 2001, 2006a, b; Mundil et al., 2001, 2004; Grice et al., 2005; Xie et al., 2005, 2007; Riccardi et al., 2007; Wang and Visscher, 2007; Cao et al., 2009; Chen et al., 2009, 2010a; Song et al., 2009, 2013a, b; Shen et al., 2011b; Huang et al., 2011; Wu et al., 2013; Wang et al., 2014; Burgess et al., 2014; Fig. 1A). This section is the Global Stratotype Section and Point (GSSP) for the PTB (Yin et al., 2001; Fig. 1C) and also well known for the best record of both biotic and geochemical signals demonstrating the PTME all over the world. Here, the exposures of the PTB beds are spectacular, extending about 2 km laterally along the Meishan hill (Fig. 1E). The PTME has been well demonstrated by Jin et al. (2000), whose study based on paleontological data from Meishan reveals that this extinction event was abrupt and dramatic, with most Permian organisms being wiped out within a very short interval, which was precisely calibrated to the base of Bed 25, a white clay bed, in Meishan (Fig. 1B, D), while the PTB is placed at the middle of Bed 27, about 16-20 cm above the base of Bed 25 in the same section (Yin et al., 2001; Fig. 1C). As such, the biocrisis clearly pre-dated the PTB (Fig. 1D). The P-Tr ecologic crisis is also marked by a pronounced negative carbon isotopic excursion (Xu and Yan, 1993; Jin et al., 2000; Kaiho et al., 2001; Cao et al., 2002; Xie et al., 2005, 2007; Fig. 2) and is also associated with an end-Permian sulfur event (Kaiho et al., 2006; Riccardi et al., 2006).

144 After Jin et al.'s (2000) influential study, which was largely based on fossil data
145 obtained in 1980s (i.e., Zhao et al., 1981; Sheng et al., 1984; Liao, 1984; Sheng et al.,
146 1987; Shi and Wang, 1987), abundant brachiopod and foraminifer faunas have been
147 detected from Beds 25–27, immediately above the PTME horizon in Meishan (Chen et al.,
148 2005a, 2006b; Song et al., 2007, 2009). Quantitative analysis of the updated foraminifer
149 data from Meishan revealed a two-stage extinction pattern near the P-Tr boundary (Song
150 et al., 2009), which agrees well with two distinct peaks of cyanobacteria, detected by
151 biomarker analysis from the same section, suggesting two extinction events
152 corresponding to Beds 25 and 28 (Xie et al., 2005). The two-stage extinction pattern is
153 also strengthened by extremely abundant benthic fossils obtained from a shallow
154 platform facies of the PTB section at Huangzhishan, about 40 km from Meishan (Chen et
155 al., 2009). However, Shen et al. (2011b) clarified an abrupt biotic decline in a short
156 interval equivalent to Beds 25-28 of Meishan based on quantitative analysis of fossil
157 records from Meishan and other PTB sections in South China. In contrast, Song et al.
158 (2013a) demonstrated nicely a two-stage extinction pattern for the P-Tr crisis based on
159 quantitative analysis of paleontological data derived from Meishan and a further six PTB
160 sections in South China. Thus, debate on whether the PTME was either a single crisis or

episodic extinctions still continues (Shen et al., 2011b; Song et al., 2013a; Wang et al., 2014). Regardless of whether the extinction was single or a two-phase pattern, an increasing number of faunas have been found in Beds 25-28 of Meishan and its counterparts across all of South China, although this interval may just last 60 kyr (Burgess et al., 2014).

In addition, a further extinction event resulting in depletion of Permian reefs in South China was calibrated to the base of Bed 24e at Meishan (Yang et al., 1993). Yin et al. (2007) re-documented biotic and geochemical signal changes across this horizon, which is reinforced by several lines of evidence, including reduction in conodont sizes (Luo et al., 2006), possible extinction of radiolarians in deep habitats and a negative shift in organic carbon isotope values (Cao et al., 2009). To sum up, biotic variations based on sound paleontology over the P-Tr transition have been far less studied in comparison with the intense geochemical studies of this catastrophe in most PTB sections. Current, updated fossil records from extensive PTB sections are crucial to reveal the true biotic responses to these environmental crises.

As briefly summarized above, there have been great advances in research on the PTME at Meishan in recent years. Multiple scenarios interpreting the causes of the P-Tr

biocrisis have been proposed based on experimental data sampled from this section. Nevertheless, any reasonable models interpreting the P-Tr crisis need to be tested by analysis of precise biotic extinction patterns and physiological reactions of victims and survivors (Knoll et al., 2007). As a result, we herein document the updated, complete fossil and sedimentary records, including microfacies, microfossils, body and trace fossils, and pyrite framboids, throughout the P-Tr transition and attempt to test biotic responses to various environmental and climatic catastrophes from the GSSP Meishan.

2. Biochronostratigraphy: an update

2.1. Biostratigraphy and correlations

After Yin et al.'s (2001) placement of the PTB at the base of Bed 27c, marked by the first appearance datum (FAD) of the conodont *Hindeodus parvus*, Jiang et al. (2007) established gondolellid and hindeodid conodont zones across the PTB in Meishan. The former include the *Clarkina yini*, *C. meishanensis* and *C. taylorae* Zones, while the latter comprise the *Hindeodus latidentatus*, *H. praeparvus*, *H. ~~Changhsingensis~~changxingensis*,

H. parvus, *Isarcicella staeschei*, and *I. isarcica* Zones (Jiang et al., 2007, fig. 2). Later, Zhang et al. (2009) integrated them as one conodont zonation series: *C. yini* Zone (Bed 24), *C. meishanensis* Zone (Bed 25), *H. ~~Changhsingensis~~ changxingensis* Zone (Beds 26-27b), *H. parvus* Zone (Bed 27c), *I. staechei* Zone (Beds 27d-28), *I. isarcica* Zone (Beds 29-51), and *C. tulongensis*-*C. planata* Zone (Beds 52-72, top of the Yinkeng Formation).

Given that *C. taylorae* is confined to Bed 27a-28 in Meishan (Jiang et al., 2007; Zhang et al., 2009) and has also been widely reported from PTB beds around the world (Orchard et al., 1994; Orchard and Krystn, 1998; Nicoll et al., 2002; Algeo et al., 2012; Zhao et al., 2013b), the *C. taylorae* Zone is regarded as a discrete zone beneath the *H. parvus* Zone and retained for Bed 27a-b (Fig. 2). In addition, we have also re-examined stratigraphic distributions of some key conodont species based on previously published data and newly extracted specimens from Meishan. An updated conodont zonation is proposed for the P-Tr succession of the GSSP Meishan (Fig. 2). The new conodont zones, with their stratigraphic ranges in brackets, include *C. ~~Changhsingensis~~ changxingensis* Zone (Beds 22-23), *C. yini* Zone (Bed 24), *C. meishanensis* Zone (Bed 25), *H. ~~Changhsingensis~~ changxingensis* Zone (Bed 26), *C. taylorae* Zone (Bed 27a-b), *H.*

Formatted: English (U.K.)

Formatted: German (Germany)

parvus Zone (Bed 27c-d), *I. staeschei* Zone (Beds 28-29a), *I. isarcica* Zone (Bed 29b), *C. planata* Zone (Beds 30-54), and *Neoclarkina discreta* Zone (Bed 35 and above) (Fig. 2).

It is noteworthy that Yuan et al. (2014) confined the *C. changxingensis* Zone to mid-Bed 10 to mid-Bed 22, *C. yini* Zone to mid-Bed 22 to Bed 24d, and *C. meishanensis* Zone to Bed 24e to Bed 25. The fist occurrence of the nominal species of these conodont zones seems to be lower than they occurred in our samples. In particular, *C. meishanensis* occurs in the so-called 'white boundary clay' bed and above strata in most PTB sections in South China (Zhang et al., 2007; Jiang et al., 2007, 2011, Zhao et al., 2013b) and is rarely present in the Permian bioclastic limestone. The *C. meishanensis* Zone is also associated with a pronounced negative shifting excursion of carbon isotopes in most of the PTB sections in South China. Accordingly, the bases of these Changhsingian conodont zones remain tentative and need to be confirmed when additional conodont samples are processed in future.

Other important findings from the PTB beds include restriction of *Isarcicella peculiaris* to Bed 28 and the first occurrences of *Hindeodus eurypyge* and *Isarcicella lobata* at the bases of Bed 27a and Bed 28, respectively (Jiang et al. 2007; fig. 2). These species also have the potential to serve as key elements marking the PTB beds (Jiang et al.,

2007, 2011, 2014). Of these, *I. lobata*, confined to Beds 28-29 in Meishan, was proposed as a distinct zone between the *H. parvus* and *I. staeschei* Zones in the southern Alps (Perri and Farabegoli, 2003, 2012; Fig. 2). This species therefore occurred slightly earlier in the southern Alps than in the GSSP Meishan. In the new conodont zonation, the *I. isarcica* Zone is retained for Bed 29b, and thus has a much narrower stratigraphic range than before. The *C. planata* Zone is newly proposed for Beds 30-54 and the *Neoclarkina discreta* Zone for Bed 55 and higher strata in Meishan (Fig. 2) based on re-examination of their stratigraphic distributions (Zhang et al., 2007, 2009).

The updated conodont zonation enables the PTB beds of Meishan to be correlated precisely with their counterparts recorded elsewhere in the Tethys region, such as North Italy, Iran, Germanic basin, and Spiti of Himalaya region (Fig. 2). The *H. parvus*, *I. staeschei* and *I. isarcica* Zones have also been recognized in both Spiti and North Italy (Fig. 2). Both *H. parvus* and *I. isarcica* Zones occur in the Abdadeh region, Iran (Korte et al., 2004). Korte et al. (2004) also argued that there might be a hiatus between Beds 24e and 25 because both the *C. iranica* and *C. hauschkei* Zones, between the *C. yini-C. zhangi* and *C. meishanensis-H. praeparvus* Zones, are absent in Meishan. *C. hauschkei* does occur in Meishan, but shares the same stratigraphic range with both ~~N~~*C. yini* and ~~N~~*C.*

246 *zhangi* in Bed 24 (Jiang et al., 2007, 2011). More importantly, no sedimentary gap has
247 been found in this interval in the GSSP Meishan (see below). The last occurrence of both
248 *C. yini* and *C. zhangi* has been calibrated to the top of Bed 24e (Yin et al., 2001; Zhang et
249 al., 2007; Jiang et al., 2007). The depositional succession between the *C. meishanensis*
250 and *C. yini* Zones shows no sign of a hiatus. Thus, both ~~*N*~~*C. hauschkei* and ~~*N*~~*C. iranica*
251 either can be recognized from the upper part of the *N. yini* Zone in the future, or do not
252 occur due to different biofacies controls (Korte et al., 2004).
253 Recognition and correlations of PTB beds in conodont-barren sections have long
254 remained problematic. Chen et al. (2009) established the bivalves *Claraia huzhouensis-C.*
255 cf. *bioni* and *Eumorphotis venetiana-Towapteria scythica-Pteria ussurica variablilis*
256 Assemblages from the PTB beds of both the Meishan and adjacent Huangzhishan
257 sections. The former is coeval with the *C. meishanensis* and *H. ~~Changhsingensis~~*
258 *changxingensis* Zones of the GSSP Meishan (Chen et al., 2009). The small, weakly
259 costated *Claraia*-like species "*Peribositra*" *baoqingensis* from Bed 26 of Meishan (Zhao
260 et al., 1981) has been re-assigned to *Claraia* (Chen, 2004). These primitive *Claraia*
261 species from Meishan are diagnostic of the *C. huzhouensis-C.* cf. *bioni* Assemblage and
262 locate the PTME in the shallow-water, conodont-barren PTB sections in South China

263 (Chen et al., 2009). The latter bivalve assemblage is contemporaneous with the *H. parvus*
264 Zone in the Huangzhishan section, pointing to an age of earliest Triassic (Chen et al.,
265 2009). Both *Claraia wangi* and *C. griesbachi* are also ~~very~~ abundant in Beds 29b-54 in
266 Meishan, and thus form the *C. wangi-C. griesbachi* Assemblage (Chen et al., 2010a),
267 which is coeval with the *I. isarcica* and *C. planata* Zones (Fig. 2). The ammonoids
268 *Rotodiscoceras*, *Hypophiceras*, *Ophiceras*, and *Lytophiceras* characterize the
269 assemblages from Beds 22-24, Beds 25-26, Beds 27-50, and Beds 51-55, respectively in
270 Meishan (Fig. 2; Zhao et al., 1984; Sheng et al., 1984; Yin et al., 2001; Chen et al., 2010a).
271 Brachiopods are also reasonably abundant in Beds 25-26, Bed 27 and Beds 51-55 of
272 Meishan (Chen et al., 2002, 2006b, 2007). They are assignable to the *Tethyochonetes*
273 *liaoi* Assemblage (Beds 25-26), *Paryphella triquetra* Assemblage (Bed 27), and
274 *Meishanorhynchia meishanensis* Assemblage (Beds 51-55) (Chen et al., 2010a). Song et
275 al. (2007, 2009) also reported diverse foraminifers from the Changhsing and lowest
276 Yinkeng Formations in Meishan, but did not establish biozones. A palynological
277 *Lundbladispora-Taeniaesporites- Equisetosporites* Assemblage was established from
278 Beds 33-53 of the Yinkeng Formation (Zhang et al., 2007), which, therefore, correlates
279 collectively with the conodont *C. planata* Zone (Fig. 2).

280

281 *2.2. Geochronology*

282

283 In Meishan, volcanic ash beds are well exposed and conspicuous in the
284 uppermost Permian to Lower Triassic successions. In particular, Beds 25 and 28 near the
285 PTB have been dated by multiple research groups using various techniques (Table 1). The
286 most updated radiometric ages for Beds 25 and 28 are 251.941 ± 0.037 Ma and 251.880 ±
287 0.031 Ma, respectively (Burgess et al., 2014), which constrain the duration between those
288 two phases of the PTME (Song et al., 2013a) or the duration of the PTME (Shen et al.,
289 2011b; Wang et al., 2014) as 60 ka (Burgess et al., 2014). Burgess et al. (2014) have also
290 given updated estimates for sediment accumulation rates through the P-Tr transition,
291 which show that sedimentation rates of the Changhsing Formation decline towards the
292 end of the Permian, reach the lowest value during the time of extinction (Beds 25-28), and
293 then increase gently in the early Griesbachian (Beds 28-37) and steeply in the
294 early-middle Griesbachian (Beds 37-48) in Meishan (Burgess et al., 2014). In addition,
295 these authors estimated that the abrupt decline in $\delta^{13}C_{carb}$ in Bed 24e took place at
296 251.950 ± 0.042 Mya, while the FAD of *H. parvus* at the GSSP Meishan is at 251.902 ±

297 0.024 Mya (Burgess et al., 2014).

298

299 *2.3. Duration of key conodont zones across the P-Tr boundary*

300

301 At Meishan, intense high-precision dating of volcanic ash beds (Table 1) and
302 high resolution conodont zones (Fig. 2) allow reasonable estimates of the duration of
303 each conodont zone. The widespread *H. parvus* Zone is estimated to have lasted 16 ka
304 (Table 2), while the *C. meishanensis* Zone, the PTME marker, lasted 8 ka, which is much
305 shorter than previously thought. The last conodont zone prior to the PTME, the *C. yini*
306 Zone, may have lasted 28 ka (Table 2).

307

308 **3. Microstratigraphy, fossil fragment contents and paleoenvironmental analysis of**
309 **the P-Tr transition**

310

311 At Meishan, the P-Tr succession comprises the Changhsing and Yinkeng
312 Formations below and above. The former unit is a 41-m-thick carbonate succession
313 consisting of medium- to thin-bedded limestone, while the Yinkeng Formation is about

15 m thick and dominated by mudstone and muddy limestone in the lower part and characterized by thin-bedded limestone in the upper part (Fig. 3). These two formations have been frequently described (Zhao et al., 1981; Sheng et al., 1984, 1987; Yang et al., 1987; Yin et al., 1996, 2001; Zhang et al., 2005). Cao and Zheng (2007) re-described the Changhsing Formation (Beds 1-24) and recognized 247 natural, single layers, each 2 to 37 cm in thickness. Chen et al. (2007) gave an updated description for the Yinkeng Formation (Beds 25-59), in which 183 natural layers are recognizable. In addition, Cao and Shang (1998) conducted the first cm-scale stratigraphy, also termed microstratigraphy, of the P-Tr boundary beds in Meishan. Since then, ~~Microstratigraphy~~ microstratigraphy of the ~~PTB beds (~~Beds 24-29~~)~~ of the Meishan section has ~~also~~ been intensely studied (~~Cao and Shang, 1998;~~ Cao and Zheng, 2009; Zhao and Tong, 2010; Zheng et al., 2013).

The top two beds of the Changhsing Formation, Beds 23-24, record important sedimentary and paleontological information just prior to the PTME, while most parts of the Yinkeng Formation record the severe biotic extinction and its consequences. Thus, microstratigraphy of the uppermost Changhsing Formation to Yinkeng Formation succession (Beds 23-59) is summarized here in view of the previously published data and

our new observations in petrologic thin sections. These thin sections were sampled almost continuously in Beds 24e to 29 and in a 20-cm-interval in Beds 22 to 24d of the Changhsing Formation. The~~ir~~ sampling interval is 0.5 m throughout Bed 30 to Bed 59 of the Yinkeng Formation in the GSSP Meishan.

~~In addition, p~~Point counting is a relatively quick method that quantifies the occurrence of skeletal fragments of major fossil groups in different horizons under the microscope (Flugel, 1984; Payne et al., 2006). However, care must be taken when using the point-counting method because large shell fragments of some clades may bias counting results (Jacobsen et al., 2011). As an alternative, Jacobsen et al. (2011) proposed the equal area approach to quantify the occurrence of skeletal fragments in thin section. In order to eliminate biases of counting areas, it is suggested that at least eight equal area fields of view ought to be counted per thin section sample (Jacobsen et al., 2011). Similar to the equal area approach, fragment percentage data of various clades from each thin section are estimated based on the observation of 300 to 350 views under a magnification of × 50 in one sample, collected for microfacies analysis of the PTB beds. Then, percentages of various skeletal components, micrite, cavities and undertermined particles (i.e., pyrites and other minerals) from samples throughout Bed 22 to Bed 60 of Meishan

were combined to yield the mean abundance of each composition in each sample throughout the study succession (Table 3).

3.1. Bed 23

Bed 23 of the upper Changhsing Formation comprises dark gray thin-to medium-bedded bioclastic limestone interbedded with thin-bedded muddy limestone and siliceous mudstone layers. Small-scale wavy cross bedding is commonly present in the bioclastic limestone, while horizontal stratification occurs in the muddy limestone and siliceous mudstone (Fig. 4G, H). Grain ~~grading~~ bedding structures are also occasionally present in the bioclastic limestone unit. The bioclastic limestone usually has a packstone to grainstone texture. The former texture is very common, while a grainstone texture is also occasionally present (Fig. 5C). This unit is usually strongly bioturbated in comparison with the weakly bioturbated thin siliceous layers that are usually horizontally stratified (Fig. 3). The autochthonous and allochthonous fossil assemblage is highly diverse and dominated by foraminifers, crinoids, and brachiopods with minor constituents of ostracods, echinoids, bryozoans, sponge spicules, calcareous sponges,

gastropods, radiolarians, and macroalgae (Fig. 6). The matrix comprises micrite (about 20-23%, Fig. 6). Cavities, pyrites and other undetermined particles are also commonly present (Table 3). The alternating occurrence of horizontal stratification and small-scale cross bedding and/or grain-grading bedding structures indicates that Bed 23 was deposited on a carbonate ramp between fair-weather wavebase and storm wavebase (Fig. 3; Zhang et al., 2005).

3.2. Bed 24

Bed 24, the topmost unit of the Changhsing Formation, consists mainly of thin- to medium-bedded bioclastic packstone rich in large ammonoids and other macrofossils (Fig. 4E). This bed has attracted intense attentions in terms of fossil record and sedimentary characterization because of its stratigraphic position just beneath the biotic extinction horizon (base of Bed 25; Jin et al., 2000). Bed 24, 71-90 cm in thickness, is usually labelled as Bed 24a-e (Yin et al., 1996) and consists of 14 layers, with the thinnest being 2 cm thick (Cao and Zheng, 2007). The conodonts from Bed 24 belong to the *Clarkina yini* Zone (Mei et al., 1998), which is distinct from the underlying *C~~larkina~~.*

Formatted: Font: Not Italic

382 ~~*Changhsingensis*~~ *changxingensis* Zone (Beds 22-23).

383 Bed 24a-c has similar petrographic features to Bed 23 (Figs. 5D, 6). The dark
384 organic-rich muddy limestone or siliceous mudstone, usually ~~less than 1~~ about 2 cm in
385 thickness, has well-developed horizontal stratifications and possesses packstone to
386 micritic textures with tiny, highly fragmented fossil skeletons of brachiopods and
387 ostracods. These horizontally stratified layers are usually weakly bioturbated. In contrast,
388 the bioclastic limestone unit, usually > 5cm thick, possesses small-scale wavy cross
389 bedding and bioclastic packstone to grainstone texture. These layers are also highly
390 bioturbated (Zheng et al., 2013). All skeletal components of Bed 23 also persist into Bed
391 24 (Fig. 6). Accordingly, Bed 24a-c was likely deposited in the same environment as Bed
392 23.

393 Although Bed 24d has similar petrographic texture to Bed 24a-c (Fig. 6), the
394 presence of abundant fecal pellets and peloids characterizes the grain assemblage of Bed
395 24d. Fossil fragment contents in rocks from both Bed 24d and Bed 24a-c are also
396 comparable with one another (Fig. 6). In addition, burrows are commonly present near
397 the boundary between bioclastic limestone unit and organic-rich muddy limestone or
398 siliceous mudstone layer. Bed 24d yields abundant trace fossils (see Section 5).

399 Pronounced cross-bedding and vertical burrows characterize the upper part of Bed 24d
400 (Fig. 4J). The top of Bed 24d is, however, weakly bioturbated and characterized by
401 smooth cone-shaped surfaces, which was termed a hard-ground structure representing
402 interrupted or highly condensed deposits (Cao and Zheng, 2009). Cao and Zheng (2009)
403 regarded this irregular contact as a sequence boundary indicating a changeover interface
404 from lowermost level to rapid rise. The same contact, however, has been interpreted as an
405 erosional surface, serving as a sequence base of a 3rd-order depositional sequence
406 following a major fall in sea level (Zhang et al., 1997; Yin et al., 2014). This
407 interpretation is reinforced by the presence of a diverse shallow-water facies trace fossil
408 assemblage including vertical burrows of *Balanogossites* (Fig. 4J; see also Section 5).
409 Cao and Zheng (2007) have also noted that abundant burrows of *Planolites* and *Skolithos*
410 and mud-crack structures are present near the boundary between Beds 24d and 24e.
411 Accordingly, Bed 24d, overall, is inferred to have been deposited in the upper part of the
412 subtidal zone of a carbonate ramp (Fig. 3; Zhang et al., 1997).
413 The topmost 10 cm thick limestone of Bed 24 is labelled Bed 24e, which
414 consists of eight natural layers (Cao and Zheng, 2009) and these were sampled at six
415 horizons here (Bed 24e-1 to Bed 24e-6). Trace fossils occur near the irregular contact

between Beds 24d and 24e-1 (see Section 5). Bed 24e, except for the topmost 3 cm (24e-5, 24e-6), is a dark gray bioclastic packstone containing abundant fossil fragments of foraminifers, brachiopods, and crinoids. Other fossil groups such as bryozoans, gastropods, macroalgae, ostracods, calcareous sponges, and sponge spicules are also seen in thin sections, which have no major difference from the underlying Bed 24d (Fig. 6). The uneven top surface is always capped by several muddy laminae. Cylindrical, ~~straight,~~ vertical burrows, ranging from 0.1 to 0.5 cm in diameter and from 3.0 to 1.0 cm in length occur in the ~~lateral margin of the~~ upper ~~natural~~ bedding ~~f~~surface. Bed 24e saw a slight increase in lime mud in the matrix and pyrite within the bed (see below). Bed 24e therefore was probably deposited in the fair-weather wave action zone (Fig. 3) and was interpreted as a lowstand platform margin wedge of a 3rd sequence (Zhang et al., 1997; Yin et al., 2014).

The topmost 2-3-cm-interval, labelled as Bed 24e-5 and 24e-6, is characterized by relatively low contents of P and Ca and high Ni content (Kaiho et al., 2001, 2006b). Bed 24e-5, about 1.0-1.1 cm in thickness, comprises bioclastic packstone and contains ~~very~~ abundant fossil fragments of foraminifers, crinoids, brachiopods, and ostracods. Fragments of calcareous sponges, sponge spicules, gastropods, bryozoans and

macroalgae are also occasionally present, and these are comparable in major fossil components with Beds 24e-1 to 24e-4 (Fig. 6). Moreover, abundant, reasonably large horizontal burrows (*Planolites*) are densely packed on the surface of Bed 24e-6 (also see Section 5).

The contact between Beds 24e-5 and 24e-6 is a laminated wavy lime layer (Fig. 7D). Bed 24e-6 is a 10- to 19-mm-thick bioclastic packstone and dominated by silica bars, which were interpreted as sponge spicules (Kaiho et al., 2006). The elongate bars are actually longitudinal outlines and the circular grains are cross sections of spicules (Fig. 7A-C). This identification is reinforced by the abundant isolated silicified sponge spicule specimens extracted from Bed 24e-6 (Fig. 7E). Contrasting to the predominance of sponge spicules, fragmentary contents of foraminifers, crinoids, echinoids and brachiopods decline dramatically. The skeletal grain assemblage experienced a dramatic reduction in both abundance and diversity across the contact between Beds 24e-5 and 24e-6 (Fig. 7E), to which the PTME was calibrated (Kaiho et al., 2006a).

3.3. Bed 25

This bed is the so-called “Boundary clay bed” or “White clay bed” (Zhao et al., 1981; Sheng et al., 1984; Yang et al., 1987). Its thickness ranges from 2 cm to 6 cm depending on the weathering intensity, the higher the intensity the thicker the bed. The bed grades upward into Bed 26 as a consequence of a gradual increase in organic and calcareous content and decrease in volcanic ash layers. The total thickness of these two beds is around 10 cm.

The basal part of Bed 25 comprises a 0.1- to 0.2-mm-thick layer of ~~grayish~~ greyish black mudstone rich in Fe grains, termed Bed 25-1, which usually becomes a reddish ferruginous layer capping the dark Bed 24e-6 and is conspicuous at outcrops in all Meishan quarries owing to weathering. Previously, this Fe-rich layer was termed the “pyrite lamina” layer (Wignall and Hallam, 1993; Shen et al., 2007) or Pyrite layer (Cao and Zheng, 2009), based on the abundant pyrite-like grains visible at outcrops. Elemental analysis shows that these Fe grains are either Fe-Ni grains (Kaiho et al., 2001, 2006b) or goethites (Liang et al., 2002). Pyrite framboids are also commonly present in this layer (Shen et al., 2007). In addition, Zheng et al. (2013) detected abundant irregular volcanic glasses from this layer.

The reddish ferruginous surface of Bed 25-1, together with the absence of both

467 the *N. iranica* and *N. hauschkei* conodont zones, was considered as evidence indicating an
468 exposure surface and representing a hiatus (Korte et al., 2004). However, the presence of
469 marine fossils such as foraminifers and brachiopods (Rui et al., 1988; Yin et al., 2001) in
470 Bed 25 and abundant sponge spicules and other fossil fragments in Bed 24e-6 (Fig. 6)
471 indicates the absence of a paleo-exposure surface or an aerial hiatus. The absence of these
472 two conodont zones may relate to biofacies controls and cannot bracket a hiatus, as
473 discussed in Section 2.1.
474 The overlying thin layer (Bed 25-2), 0.3-1 mm thick, is dark yellowish orange,
475 and encompasses mainly gypsum and Fe (Table 4). The remaining part of Bed 25 (Layer
476 25-3, 2-4 cm thick; Kaiho et al., 2006b) is a light gray illite–montmorillonite–kaolinite
477 claystone (white clay) (Table 4). Gypsum and pyrite are very common in thin section. No
478 fossil fragments are seen in thin section (Fig. 5A). Marine fossils of conodonts,
479 foraminifers, ostracods and tiny brachiopods have been found from this bed, but are
480 always sparse (Rui et al., 1988; Jiang et al., 2007). Benthic carbonate skeletal fossils
481 diminished dramatically in this bed. Calcareous shells are often pyritized and attached
482 with crystals and framboidal pyrites on the surface (Rui et al., 1988). Conodonts from
483 Bed 25 are included in the *C. meishanensis* Zone (Fig. 2). Microspherules and β-type

quartz crystals are much more abundant in this bed than in other ash clay beds, and could be products of acid volcanic eruptions (He et al., 1987). However, comparable microsphaerules are also ~~very~~ abundant in the background soils in Meishan and other PTB sections in South China, suggesting that they may be the modern industrial products rather than geological objects (Zhang et al., 2014). Both Hf-isotope and elemental analysis of magmatic zircons suggests these ash clays near the PTB in South China may have been sourced from volcanism taking place along the convergent continent margins during the formation of the Pangea supercontinent (Gao et al., 2013).

3.4. Bed 26

Bed 26, the so-called "black clay bed" (Yang et al., 1987), comprises black shale, 4-6 cm in thickness. Nine pronounced yellow clay layers are interbedded in the black shale. Horizontal laminae and pyrite are common. The clay layer is composed mainly of montmorillonite–illite, which is similar to that of Bed 25 (Table 4). Fossil fragments are very rare in most parts of this bed (Fig. 5B) except for the top 2-cm-interval where fossil fragments are fairly abundant in calcareous nodules (Fig. 8), including foraminifers,

ostracods, echinoids, bryozoans, and brachiopods (Table 3; Figs. 6, 8). Microspherules or/and α-quartz (in the form of β quartz pseudomorphs; He, 1981) are rich in the lower part, but they may be the products of modern industry (Zhang et al., 2014). Various burrowing systems are common in the upper part of Bed 26, from which Cao and Zheng (2009, fig. 5b) identified *Chondrites*, *Planolites* and *Zoophycos*. The identification of the last ichnogenus, however, is problematic based on insufficient information illustrated by these authors. The upper part of the bed, Bed 26b, therefore is highly bioturbated (Fig. 3; Cao and Zheng, 2009).

Skeletal fossils are rare but considerably diverse, including ammonoids, brachiopods, bivalves, ostracods, and conodonts. Co-occurrence of the Triassic-type faunas (i.e., *Otoceras*, *Claraia* and many conodont species) and Permian-type elements (i.e., ammonoids *Pseudogastroceras* and *Xinodiscus*, and many brachiopods and foraminifera) is particularly interesting. Brachiopods are small in size and thin-shelled, and include species of *Orbicoiella*, *Prelissoryhnchia*, *Cathaysia*, *Paryphella*, *Tethyochonetes*, and *Spinomarginifera* (Chen et al., 2006b; Chen and McNamara, 2006). The presence of the relatively diverse fossil assemblage in the upper part of Bed 26 indicates the earliest re-colonization of epifauna on the barren soft substratum

immediately after volcanic eruption. Most of these shelly fossils are complete and well preserved regardless of the delicacy of the skeleton. The change from Bed 26 to Bed 27 is gradual and no boundary surface can be recognized. Crystal and framboidal pyrite are concentrated in a discontinuous dark lamina with rich organics (Shen et al., 2007). The slow sedimentation rate, and quiet and anoxic environment (Shen et al., 2007) suggest that Bed 26 probably represents a semi-closed, low-energy subtidal zone (Fig. 3). The succession of Beds 24e, 25 and 26, overall, shows that continuing fall of sea level through Bed 24e turned to a rise in the upper part of Bed 26, with the lowest point of sea level corresponding probably to the base of Bed 25 (Yin et al., 2014).

3.5. Bed 27

Bed 27 comprises biotic packstone to wackestone with occasionally micrite texture and contains fairly abundant fossil skeletons and pyrite crystals throughout the bed (see Section 6). Relatively complete shells of ostracodes, foraminifers and thin-shelled brachiopods are reasonably abundant. This bed contains three major irregular contact surfaces, termed hardground surfaces (Cao and Shang, 1998) and firmground

surfaces (Cao and Zheng, 2009), at various levels (Fig. 9). Of these, the first irregular surface is rather pronounced, about 5 cm above the base of Bed 27 and near the boundary between Beds 27a and 27b. The second occurs near the contact between Bed 27c and 27d, while the third is not prominent and occurs within Bed 27d (Fig. 9). These 'firmground' surfaces divide Bed 27 into three depositional cycles, with each beginning with dark muddy limestone and grading upwards into pale bioclastic limestone. Rich organic and muddy laminae parallel to the bedding plane decrease upward from the base within each cycle. The upper unit of each cycle was disturbed by repeated burrowings, which form part of the firmground (see Section 5). Microscopic examination reveals that the dark, early-lithified rock contains a minor percent of clay, rich organic shreds and bioclasts (Fig. 9; Table 4).

Microfossils in Bed 27 are much more abundant and diverse than previously thought (Fig. 6). Of these, foraminifera are most abundant among all clades. Echinoids are also remarkably abundant, although they cannot be identified beyond a certain taxonomic level (Figs. 10-12). Bed 27a contains fossil skeletons of foraminifers, ostracods, echinoids, and brachiopods (Fig. 10), which is similar in component composition to Bed 26 (Fig. 6). Bed 27b comprises marls and clays in the lower part, in

552 which fossil fragments are very rare (Fig. 9). The remainder of Bed 27b yields a fossil
553 fragment abundance (FFA) composed mainly of foraminifers and brachiopods (Fig. 6).
554 Both Beds 27c and 27d contain much more abundant and diverse FFA than Bed 27b (Figs.
555 10-12), both of which are dominated by foraminifers, ostracods and brachiopods with
556 minor constituents of echinoids (Fig. 6).
557 It should be noted that Bed 27 is usually subdivided into four layers (Yin et al.,
558 2001). Cao and Zheng (2009), however, divided this bed into six layers (units) including a
559 stromatolite layer (Bed 27-5) and mudstone (Bed 27-6) in the upper part of Bed 27. Later,
560 Zheng et al. (2013) denied the existence of the stromatolite layer and divided Bed 27 into
561 five layers; no stromatolitic structures are seen in our thin sections either. Except for the
562 topmost 0.5 cm thick layer of carbonaceous mudstone, another four layers are similar to
563 those recognized by Yin et al. (2001). In addition, Cao and Zheng (2009) and Zheng et al.
564 (2013) interpreted the irregular surface separating Beds 27a and 27b (Fig. 9) as
565 firmground surface as a result of a rapid transgression. Here, we agree with the
566 firmground interpretation of these irregular surfaces within Bed 27 (Cao and Zheng, 2009;
567 Zheng et al., 2013) because of the presence of abundant burrows typical of the
568 *Glossifungites* ichnofacies (Seilacher, 1967) and distinct lithological interfaces, typically

569 dark muddy micrite overlain by light gray, coarser-grained bioclastic

570 packstone-wackestone, within Bed 27 (Fig. 9; see also Section 5). Firmgrounds of the

571 *Glossifungites* ichnofacies, also termed omission surfaces (Knaust, 1998), have been

572 extensively used in sequence stratigraphy to identify and characterize discontinuity

573 surfaces (Pemberton and Frey, 1985; MacEachern et al., 1992, 2007; Buatois and

574 Mángano, 2011). Within Bed 27, the unlined burrows penetrating into muddy limestone

575 are passively filled with coarser grains from the overlying stratum. This means that the

576 burrows remained open after the trace maker had left, thereby permitting bioclast grains

577 from subsequent depositional events to fill the open, stable burrows. Although the

578 majority of documented *Glossifungites* ichnofacies are from shallow-marine settings

579 (Knaust, 1998; Buatois and Mángano, 2011), this ichnofacies is also present in relatively

580 deep marine contexts, such as incision of submarine canyons during relative sea-level

581 falls (e.g. Dasgupta and Buatois, 2012) or autogenic erosional episodes by turbidity

582 currents and bottom currents (Savrda et al., 2001; Gérard and Bromley, 2008; Hubbard

583 and Shultz, 2008). As such, the *Glossifungites* ichnofacies from Bed 27 may represent an

584 omission surface, but cannot indicate a precise depositional environment for Bed 27.

585 Integration of lithofacies, paleoecologic and ichnofacies indicates that Bed 27 may have

586 been deposited on a carbonate ramp near the storm wave action zone (Fig. 3), as
587 suggested by Zhang et al. (1997; 2005).
588
589 *3.6. Bed 28*
590
591 Bed 28 comprises yellow claystone having similar composition to Bed 25 (Table
592 4), dominated by montmorillonite mixed with illite. Apart from conodonts (Jiang et al.,
593 2007), no other fossils have been recovered from this bed.
594
595 *3.7. Beds 29-59*
596
597 Bed 29 encompasses wackestone with rare foraminifer tests (Fig. 13). Pyrite is
598 commonly seen in thin section and pyrite content increases up-section. A minor omission
599 surface, equivalent to the erosional surface of Zhang et al. (2007) is developed in the
600 middle part of Bed 29 (Zhang et al., 2007). Fossil fragments are very rare and their
601 contents decrease upwards within the bed (Fig. 6; Table 3). Bed 30 is a marlstone, which
602 has a ~~wackestone to~~ micritic texture and lacks any fossil fragments (Table 3). Both beds

603 contain laminated stratification and lack any cross bedding, indicating a low-energy
604 environment. Beds 29-30 therefore may have been deposited in the upper part of the
605 offshore setting that is below fair-weather wavebase (Chen et al., 2007).

606 Beds 31-51 are typified by alternating black shale, greenish gray mudstone, and
607 gray marlstone in the lower part, and interbeds of gray calcareous mudstone and pale
608 muddy limestone in its upper part. They are subdivided into 39 cm-scale cycles (Chen et
609 al., 2007; Fig. 3). In general, the lower unit of the cycle is characterized by black shale or
610 greenish mudstone rich in bivalve and ammonoid fossils (Fig. 4F, I), while the upper unit
611 is dominated by calcareous mudstone and marlstone. The mudstone-dominated cycles
612 are transitional to the marl-dominated cycles up-section, indicating a long-term
613 up-shallowing cycle (Chen et al., 2002, 2007; Tian et al., 2014). In addition to the
614 lithologic variation, Beds 31-34 are characterized by the calcareous mudstone and shale
615 where laminated stratifications are commonly preserved (Fig. 4C), while the upper part
616 of the formation (Beds 35-51) is typified by an increasing number of laminated marl beds
617 (Fig. 3). Fossil fragments occur occasionally in Beds 45, 50 and 51, characterized by
618 foraminifer and ostracod skeletons (Table 3; Fig. 6). Horizontal burrows of *Planolites* are
619 present in Beds 36-51, which also yield a few shell beds of bivalves (i.e., *Claraia*

620 *griesbachi*) and ammonoids (*Ophiceras* spp.) (Chen et al., 2007). This unit was
621 interpreted as the result of sedimentation relatively deep offshore (Fig. 3; Zhang et al.,
622 2005; Chen et al., 2007).

623 Beds 52-53 comprise alternations of shale and marlstone, yielding reasonably
624 abundant burrows of *Chondrites* and *Planolites*. Increasing fossil fragment content is
625 seen in both Beds 52 and 53, in which foraminifer, ostracod and echinoid shell fragments
626 are remarkable (Fig. 13), although they are definitely minority components in thin
627 section (Fig. 6; Table 3). Moreover, horizontal stratification is commonly present in both
628 shale and marlstone. These two beds were interpreted as the result of sedimentation in the
629 relatively deep offshore below storm wavebase (Chen et al., 2007).

630 Towards the top of the Yinkeng Formation, the succession (Beds 54-59) is
631 dominated by marl-dominated cycles. A thin- to medium-bedded marl is hummocky
632 cross-stratified (HCS; Fig. 4A, B, D) and often displays multidirectional tool marks on
633 its base, and horizons of loading and soft sediment deformation are very common (Chen
634 et al., 2002). Fossil fragments are reasonably abundant in Beds 54-59 (Fig. 13), although
635 they are still in the minority in thin section (Fig. 6; Table 3). Foraminifers, ostracod and
636 echinoids characterize their FFA (Fig. 6; Table 3). Trace fossils are also commonly

present in these beds, including *Planolites* isp. 2, *Treptichnus* sp., and *Thalassinoides* isp. 3. ~~Of these~~Moreover, the sedimentary structure HCS was interpreted as having been generated by offshore storm currents. Beds 54-59 therefore may have been deposited offshore, near storm wavebase (Chen et al., 2007).

Formatted: Font: Italic
Formatted: Font: Italic
Formatted: Font: Italic

4. Biotic changeover through the P-Tr transition

4.1. Biodiversity variations over the P-Tr transition

Comprehensive paleontological studies of the Meishan section were undertaken in the 1980s (Zhao et al., 1981; Sheng et al., 1984; Yang et al., 1987; Shi and Chen, 1987). The fossil record employed by Jin et al. (2000) to document the PTME pattern, which shows an abrupt extinction calibrated to the base of Bed 25, was sourced mainly from these studies. Since then, more diverse faunas and floras have been documented from Meishan, including foraminifers (Song et al., 2007, 2009), radiolarians (He et al., 2005), brachiopods (Chen et al., 2002, 2005a, 2006b; Li and Shen, 2008; Chen and Liao, 2009), conodonts (Nicoll et al., 2002; Tong and Yang, 2004; Luo et al., 2006, 2008; Jiang et al.,

2007, 2008; Zhang et al., 2007, 2009; Yuan et al., 2014), ostracods (Crasquin et al., 2010; Forel and Crasquin, 2011), palynolomorphs (Zhang et al., 2007), and arcritarchs (Li et al., 2004). Additional macrofossils were collected throughout the upper Changhsing Formation to the Yinkeng Formation. Several shelly fossil communities from Beds 24, 26, 27, 32, 40, and 53-55 were quantitatively analysed (Chen et al., 2010a).

Shen et al. (2011b) and Wang et al. (2014) demonstrated a steep decline zone of species richness corresponding to the interval between Beds 25 and 28 in Meishan by a means of quantitative analysis on fossil records from more than ten PTB sections (including Meishan) from South China. In contrast, Song et al. (2013a) calculated species richness of each layer marked in microstratigraphic analysis (Beds 24-29) based on the updated fossil record mentioned above. Species richness of single layers experienced a stepwise but minor decline within Bed 24. Two distinct declines in species richness were well demonstrated and calibrated to Beds 25 and 28. The same pattern is also indicated in seven PTB sections in South China (Song et al., 2013a). Above Bed 28, species richness remains very low in the remaining part of the Yinkeng Formation.

Here, additional fossil specimens, primarily brachiopods, ammonoids and bivalves, have been collected from Beds 24e, 26, 27 to document biotic turnover across

671 the PTB. Moreover, microfossils were observed in the petrologic thin sections used for
672 microfacies analysis (see Section 3). Of these, foraminifers are the most abundant skeletal
673 fragments among all clades. Most of these foraminifer tests, however, were illustrated by
674 Song et al. (2007, 2009), so the newly obtained fossil record does not affect the biotic
675 extinction pattern revealed by Song et al. (2013a).
676
677 *4.2. Fossil fragment content variations through the P-Tr transition*
678
679 The abundance and diversity of skeletal grains within the late Changhsingian
680 samples (Beds 22-24) is remarkably high. Skeletal grains from all sampled levels except
681 for the top 1-2 cm (Bed 24e-6) of Bed 24e comprise 68-74% of the total rock volume in
682 the uppermost Changhsing Formation (Fig. 14). Fossil fragment assemblages are
683 strikingly similar to one another in all sampled layers within the interval between Bed 22
684 and 24e-5, and each of these is dominated by foraminifers, crinoids and brachiopods.
685 Other major constituents include ostracods, bryozoans, sponge spicules, and macroalgae
686 (Fig. 14). Skeletal grains of gastropods, calcareous sponges and radiolarians are relatively
687 rare and absent in some horizons (Fig. 14).

688 It is noteworthy that FFAs do not appear to differ at all across the contact
689 between Beds 24d and 24e, although an omission surface, also a 3rd sequence boundary
690 (Zhang et al., 1997), separates these two layers (Zhang et al., 1997). In contrast, FFAs
691 experienced a dramatic reduction in diversity across a lime laminae layer between Beds
692 24e-5 and 24e-6 (Figs. 6, 14). Above this lamina layer (Fig. 7D), skeletal grains of Bed
693 24e-6 comprise about 60% of all rock in thin section in comparison with nearly 70% in
694 Beds 22-24e-5 (Fig. 14). The overwhelming majority of the FFA in Bed 24e-6 is sponge
695 spicules (35%) with minor constituents of foraminifers (8%), brachiopods (7%), crinoids
696 (6%), and echinoids (4%) (Table 3; Fig. 6). Furthermore, fusulinids disappeared forever
697 at this lamina (Kaiho et al., 2006b). The FFA experiences a loss of five major orders (i.e.,
698 ostracods, bryozoans, calcareous sponges, gastropods, and macroalgae) across the
699 boundary between Beds 24e-5 and 24e-6 (Figs. 6, 14). More importantly, this horizon
700 coincides with a pronounced negative carbon isotope excursion and a sulfur isotopic
701 excursion anomaly (Kaiho et al., 2006a, b), and thus marks the actual biotic extinction
702 horizon (Kaiho et al., 2006b).
703 Fossil fragment contents form a high plateau in both abundance and diversity,
704 comprising nearly 70% of total rock and including almost all skeletal clades recognized

705 from the Changshing Formation. They underwent a dramatic depletion in both abundance
706 and diversity in Beds 25-26a, which are nearly barren of skeletal grains (Fig. 14). This
707 severe depletion therefore is calibrated to the base of Bed 25, coinciding with the PTME
708 (Jin et al., 2000; Shen et al., 2011b) or the ~~main phase~~first phase of the PTME (Song et al.,
709 2013a). After the PTME, skeletal grains started to rebound in Bed 26b, the top 2-cm
710 interval of the bed and 8-10 cm above the base of Bed 25. Fossil fragments in Bed 26b,
711 however, comprise only 32% of all rock in comparison with nearly 70% before the PTME
712 (Figs. 6, 14). The FFA in Bed 26b comprises mainly foraminifers, ostracods, brachiopods,
713 bryozoans, and echinoids (Fig. 7). Both foraminifers and echinoids are the most abundant
714 among all clades (Fig. 6). Of particular interest is the presence of both echinoids and
715 bryozoans, with bryozoans represented by fenestellid fragments. These two clades have
716 generally been believed to have gone extinct at the PTME (Sepkoski, 1981, 2002), but
717 instead they occur in the aftermath of the PTME at Meishan. Their body fossils were also
718 found in association with the *H. parvus* Zone in the neighbouring Huangzhishan section
719 of western Zhejiang Province (Chen et al., 2009).

720 Fossil fragment abundance remains almost same as in Bed 26b, comprising
721 nearly 31-38% through the entire Bed 27, except for Bed 27b, in which skeletal grains are

722 only 10% of all rock. Thus, fossil fragments rebounded and reached nearly half their
723 pre-extinction level with a major depletion occurring in mid-Bed 27 (Fig. 14). If
724 considering the FFA of the entire Bed 27, which contains elements of brachiopods,
725 bryozoans, foraminifers, and ostracods (Table 3), then ~~Recovery~~ recovery of FFA
726 diversity in Bed 27 is marked by the re-appearance of 45.5% of all pre-extinction orders
727 ~~(Table 3)~~.

728 FFA experienced a major loss in Bed 29, down to less than 10% (Fig. 14). Fossil
729 fragments are absent in Beds 28-44. After rebounding in Bed 45, the skeletal grain
730 assemblage underwent a stepwise abundance recovery in Beds 50-51 and remained at a
731 relatively stable level, occupying nearly 16% of all rock in Beds 52-60. FFA diversity,
732 however, remains at a rather low level, with the re-appearance of only three orders:
733 foraminifera, ostracods and echinoids (Fig. 14).

734

735 *4.3. Community structural changes of shelly faunas*

736

737 The P-Tr shelly communities are characterized by a mixture of large-sized
738 ammonoids and small brachiopods in the uppermost Changhsing Formation and by

739 numerous shell beds in the Yinkeng Formation (Fig. 15). Chen et al. (2010a) recognized
740 six macrofossil communities from the uppermost Permian to lowest Triassic in Meishan,
741 including the *Rotodiscoceras* sp.–*Paracrithyris pigmaea* (*R–P*) Community (Bed 24),
742 *Tethyochonetes liaoi* (*T*) Community (Bed 26), *Paryphella triquetra–Tethyochonetes*
743 *liaoi* (*P–T*) Community (Bed 27), *Claraia griesbachi–Ophiceras* sp. (*C–O*) Community
744 (Bed 32), *Claraia wangi* (*C*) Community (Beds 40), and
745 *Meishanorhynchia–Lytophiceras* (*M–L*) Community (Beds 53-55).
746 Several diversity indices (Shannon and Simpson indices and Dominance) are
747 usually employed to measure community structures. It should be noted that the Shannon
748 measures are the only standard diversity indices that generate meaningful independent
749 alpha and beta components when the community weights are unequal or sampling is
750 uneven (Jost, 2007). Dominance index (D) measures 'evenness' of the community from 0
751 to 1, 0 being the most even distribution amongst taxa. Simpson index = 1–Dominance
752 index, and values range from 0 (one taxon dominates the community completely) to 1 (all
753 taxa are equally present) (Hammer et al., 2001). Note that these diversity indices are
754 useful in estimating diversity but are not themselves measures of diversity. Their
755 numerical equivalent indicates changes of true diversity (Jost, 2007; Kosnik and Wagner,

2006). Conversion of both Shannon and Dominance indices to true diversities developed by Jost (2006, 2007) is performed to indicate true diversity changes over the P-Tr transition. In addition, the bias-corrected Simpson evenness index (Olszewski, 2004) is also applied to estimate the evenness within and among communities examined here. Detailed community structural indices are listed on Table 5.

The late Changhsingian *R–P* community has Shannon index (H) of 2.029, which is slightly smaller than the same index of 2.796 for the Changhsingian brachiopod *Cathaysia–Martinia* (*C–M*) community reported from the Shaiwa Group of southern Guizhou Province, southwest China (Chen et al., 2006a), but is slightly larger than the same index of 1.879 for the Wuchiapingian brachiopod *Edriosteges poyangensis–Spinomarginifera lopingensis* (*E–S*) Community reported from the basal Lungtan Formation of the Daijiagou section, Chongqing city, southwest China (Chen et al., 2005b). Dominance of the *R–P* community, D = 0.1519, also lies between the same indices of the above Changhsingian and Wuchiapingian brachiopod communities, with D = 0.07375 and 0.178, respectively (Chen et al., 2010b, table 4). It is also true for evenness of community (E) that the *R–P* community has E of 0.8453, which lies between 0.9262 and 0.822, the values of E for the *C–M* and *E–S* communities, respectively (Chen et al.,

773 2010b). Accordingly, the *R–P* community is typical of Late Permian shelly communities.

774 In contrast, H values of all post-extinction communities, 1.47, 1.565, 0.7559, 0,

775 and 1.288 for the *T*, *P–T*, *C–O*, *C*, and *M–L* communities, respectively (Table 5) are much

776 smaller than the same values of the Changhsingian and Wuchiapingian communities, H =

777 2.796 and 1.879, respectively. These post-extinction communities therefore are much less

778 diverse than the pre-extinction communities of the Late Permian, indicating the severe

779 impact of the PTME on marine communities.

780 Changes in both standard diversity Shannon index [Exp (H)] and dominance

781 index (D') between neighboring pairs of communities show that major losses in diversity

782 coincide with the turnovers of the *R–P/T* and *P–T/ C–O* communities, losing 43.6% and

783 55.5% respectively. Similarly, standard diversity dominance (D') increases by 34% and

784 54%, respectively (Table 6). Thus, community structural collapse indicated by a decrease

785 in diversity, coupled with increase in dominance, coincides with two extinctions

786 bracketed at the bases of Beds 25 and 28 at Meishan (Song et al., 2013a). In addition, Exp

787 (H) value increases by 262.6% from the *C* to *M–L* communities, and also increases by

788 70%, coupled with a decrease of 15.2% in D' values, from the *C–O* to *M–L* communities,

789 suggesting an improvement in shelly community structures in Beds 53-55 at Meishan.

790 Structural improvement of the *M-L* community is also reinforced by comparison
791 between the *M–L* community and the Anisian *Madonia* sp.*–Rhaetina angustaeformis*
792 (*M–R*) Community, which marks the recovery of benthic communities in the Anisian
793 (Chen et al., 2010b). The Anisian community has H and D values of 2.051 and 0.1501
794 respectively (Chen et al., 2010b, table 4), but the same values for the *M-L* community are
795 H = 1.288 and D = 0.4379, respectively. Consequently, the *M–L* community embraces
796 much more improved diversity indices than other Griesbachian communities in Meishan,
797 but instead has a much lower diversity and higher dominance index than both
798 pre-extinction and recovery communities.
799
800 **5. Trace fossils and bioturbation**
801
802 At Meishan, Bottjer et al. (1988) made the first attempt to ecologically test the
803 PTME based on trace-fossil assemblages. These authors, however, could not collect
804 sufficient trace fossils because of restricted exposure at that time, but they noted that
805 ichnotaxa from the PTB beds are dominated by *Planolites* and *Chondrites*, which indicate
806 generally a poorly oxygenated environment (Bottjer et al., 1988). Later, Cao and Shang

807 (1998) reported a few ichnotaxa such as *Thalassinoides*, *Planolites* and *Skolithos* from
808 the PTB beds of Meishan, but *Skolithos* was later rejected by these authors (Cao and
809 Zheng, 2009; Zheng et al., 2013). Zhang and Tong (2010) also examined trace fossils
810 recorded in drilling cores through the P-Tr transition in Meishan. Although these authors
811 clarified that trace fossil evidence suggests two ecologic crises, coinciding with Beds
812 24e-27 and Beds 34-39, respectively (Zhang and Tong, 2010), the documented
813 ichnofossils are too few to support such a conclusion (see Section 7). As a result, several
814 lines of evidence show that trace fossils are reasonably abundant in the PTB beds in
815 Meishan. They however remain poorly understood owing to inadequate trace fossil
816 specimens.
817 Here, we document our observations at all PTB sites newly exposed during the
818 construction of the geological park in the GSSP Meishan in the 2000s, which uncovered
819 extensive fresh exposures along all the quarries (Fig. 1E). Abundant trace fossils were
820 collected from Beds 8-9 and 23-24 of the Changhsing Formation and Beds 26-27 and
821 35-57 of the Yinkeng Formation. The ichnofabric indices (ii, *sensu* Droser and Bottjer,
822 1986) and bedding plane bioturbation index (BPBI, Miller and Smail, 1997) throughout
823 the upper Changhsing Formation and entire Yinkeng Formation are also examined.

824

825 *5.1. P-Tr ichnotaxa and their stratigraphic distributions in Meishan*

826

827 *5.1.1. Stratigraphic distribution of ichnoassemblages*

828

829 A total of 17 ichnospecies in 13 ichnogenera and a problematic ichnotaxon have
830 been found in the P-Tr transition at Meishan (Figs. 16-18). Major characteristics,
831 stratigraphic distributions and interpretation of each ichnotaxon are tabulated here (Table
832 7). Trace fossils are distributed mainly in Beds 8-9 and Beds 23-24 of the Changhsing
833 Formation, and in Beds 27, 35-53, 55-57 of the Yinkeng Formation. Of these, the lower
834 Changhsing Formation (Beds 8-9) ichnoassemblage is dominated by relatively large
835 burrows of *Thalassinoides* isp. 1 (Fig. 16A, D) and resting traces of *Lockeia* isp. (Fig.
836 16F). *Paleophycus* isp. (Fig. 16B) is also commonly present in Beds 8-9.

837 The trace-fossil assemblage from Beds 23-24e is characterized by tree-like
838 traces of *Dendrorhaphe* isp. (Fig. 17F) and abundant burrows of problematic status. The
839 latter is represent by simple, straight, unbranched burrows (Fig. 17B-C), each originating
840 at a small, close end and extending distally to form a horn-shaped burrow with an open

841 distal end (Fig. 17B-C). Burrow diameters vary from 20-27 mm. Some burrows penetrate
842 the bedding at acute angles, and others are horizontally distributed on bedding planes.
843 The burrow has a distinct circular wall, about 2-5 mm thick. These burrows are preserved
844 in dark organic muddy limestone and filled with light-colored, coarse-grained sediments.
845 These morphologies suggest that this problematic form differs from all known ichnotaxa.
846 Another feature of the Bed 24 ichnoassemblage is the presence of abundant
847 ichnofossils near the contact between Beds 24d and 24e, including several distinct
848 burrowing ichnotaxa: *Balanoglossites triadicus*, *Taenidium* isp., *Thalassinoides* isp. 1,
849 and *Planolites* isp. 1. Of these, *Balanoglossites* is represented by vertical tubes (Fig. 16C)
850 that penetrate to a depth of 5-10 cm perpendicular to bedding. This ichnogenus occurs
851 usually at omission surfaces that served as sequence boundaries (i.e., Knaust, 1998).
852 These traces are preserved in limestone of the upper part of Bed 24d (Fig. 3). *Taenidium*
853 burrows (Fig. 16E, 17E) are also very common in Bed 24d-e, and they are usually
854 cylindrical, straight, unbranched, and backfilled. This ichnoassemblage as a whole
855 represents the *Balanoglossites* ichnofacies associated with the omission surface, as
856 described by Knaust (1998, 2004). In addition, horizontal burrows of *Planolites* isp. are
857 densely packed on top of Bed 24e (Fig. 17A, E), which is just beneath the base of Bed 25,

858 in which the PTME horizon is placed (Jin et al., 2000).

859 Abundant burrows were also found in association with an omission surface
860 within Bed 27. These burrows and the possible firmground surface have long remained
861 disputed, although several recent studies have addressed an ichnoassemblage of this bed
862 (Cao and Shang, 1998; Cao and Zheng, 2009; Zheng et al., 2013). Burrow systems
863 preserved in Bed 27 therefore are re-studied here (see below).

864 Beds 28-34 are barren of trace fossils. The remaining part of the lower Yinkeng
865 Formation (Beds 35-51) yields rare trace fossils, which are dominated by simple,
866 horizontal burrows of *Planolites* isp. 2 (Fig. 18A-B). Increasing numbers of ichnotaxa
867 occur in the upper Yinkeng Formation and are characterized by the presence of the
868 tree-like burrow system of *Chondrites* isp. (Bed 52; Fig. 18C) and relatively complicated
869 burrows of *Thalassinoides* isp. 3 (Fig. 18D-E) and *Treptichnus* isp. (Fig. 18G-H).

870

871 *5.1.2. Ichnofabric changes within Bed 27*

872

873 Within Bed 27, intensive burrowing on an omission surface, characteristic of the
874 *Glossifungites* ichnofacies, caused a pronounced relief on the firmground surface up to 3

875 cm high near the boundary between Beds 27a and 27b (Figs. 19-20). The firmground of
876 *Glossifungites* ichnofacies is partly covered by a faintly laminar black muddy limestone
877 that seems resistant to weathering. Highly irregular relief at the surface of the firmground
878 indicates that the solid rock was affected deep subsolution (Savrda, 1992). Trace fossils
879 increase upward to the contact between Beds 27c and 27d, which is overlain by finely
880 laminated muddy limestone (Bed 27d) again.

881 To reconstruct complete burrowing systems within Bed 27, one complete sample
882 of the bed (from base to top) was cut and separated into three blocks (Fig. 19). The
883 transverse view from three polished slabs shows the colonizing zonation (CZ) from base
884 to top of the bed by various ichnocoenoses within a 16-cm-thick unit (Fig. 20).

885 CZ I: This is a historical zone, a unit that is beyond the reach of even the deepest
886 burrows (Fig. 20). CZ I includes the first 2-3 cm of the lower part of Bed 27, which
887 comprises gray, calcareous mudstone to muddy limestone and is almost barren of trace
888 fossils. Minor bioturbation is also limited. Body fossils are scarce, except some small,
889 thin-bedded brachiopods and foraminifers. Pyrite framboids and crystals are relatively
890 rich and occur in both sediments and fossil shells (see Section 6).

891 CZ II: This is a transitional zone (Fig. 20), which is extremely heterogeneous

892 from the activity of deeper burrows (Savrda, 1992). Sediments in this zone were
893 semi-lithified to form a firmground substratum. Firmground sediments are dark-colored,
894 and are disrupted by passively filled burrows of an ichnoassemblage characteristic of the
895 *Glossifungites* ichnofacies. Representative ichnogenera include *Arenicolites*,
896 *Gastrochaenolites*, *Psilonichnus*, and *Thalassinoides*. Of these, *Arenicolites* comprises
897 vertical burrows that penetrate into the dark gray sediments. *Gastrochaenolites* comprises
898 tear-shaped borings, now filled with light gray, coarse-grained sediments in a
899 dark-colored firmground lime muddy substrate. This ichnogenus is commonly present in
900 the *Trypanites* ichnofacies as well (Wilson and Palmer, 1998; Benner and Ekdale, 2004).
901 The vertical cylindrical burrows of *Psilonichnus* are inclined, with bedding in the distal
902 end (Buatois and Mángano, 2011). *Thalassinoides* is typified by its Y-shaped ramification.
903 All these burrows have unlined walls and are filled with light gray-colored,
904 coarse-grained sediments of the overlying layer, indicating that these burrows were
905 passively filled.
906 CZ III: This is a very thin, highly condensed omission surface (Fig. 20), which is
907 characterized by some coarse-grained, reworked sediments that were generated by
908 frequent activity of wave currents. This omission surface is distinguished from the

underlying firmground ichnocoenosis of *Glossifungites* ichnofacies and overlying softground ichnocoenosis of *Cruziana* ichnofacies (see below).

CZ IV: This is a mixed unit (Fig. 20), which is saturated with water and totally homogenized by bioturbation. This unit, about 5 cm thick, yields ichnocoenoses represented by minute burrows of *Diplocraterion* isp. and tear-shaped borings, which resemble the vertical features of *Chondrites* and small *Planolites*. Owing to the soft nature of substrate and intensive bioturbation, burrow boundaries and morphologies have become blurred, making it difficult to identify them confidently to ichnogenus level. This ichnoassemblage, together with the soft substrate, is characteristic of the softground ichnocoenosis of *Cruziana* ichnofacies (Seilacher, 1977).

CZ V: This thin unit is devoid of bioturbation and comprises finely laminated muddy layers (Fig. 20), which yield small pyrite framboids (see Section 6), indicating the establishment of a quiet, low energy and probably reduced environment.

5.2. Extent of bioturbation

Ichnofabric indices (Droser and Bottjer, 1986) of the Upper Changhsing

926 Formation (Beds 22–24) are usually rather low (ii1-2) with several peaks reaching 3 (ii3)
927 except for the horizons near the boundary between Beds 24d and 24e (Fig. 3) that records
928 an ichnofabric index of 4 (ii4), but bioturbated strata are about 80% of the entire
929 measured units of the Changhsing Formation. Ichnofabric indices decrease to 2 (ii 2)
930 again at the upper part of Bed 24e, then increase to 3 (ii3) at the top of the bed. No
931 ichnofabrics are observed in Beds 25-26a. The ii value surges to 3 (ii3) in Beds 26b-27,
932 with 40% strata bioturbated. Beds 28-34 are void of ichnofabrics again. The ii value of
933 Beds 35-57 remains rather low (ii1) except for several peaks reaching 2 (ii2) in Beds 42,
934 46, 52-53, and 56-57 (Fig. 3). Only 15% of the examined units are bioturbated.
935 Accordingly, ichnofabric indices of the upper Changhsing Formation vary from 2 to 4
936 (ii2–4). Averagely 80% strata of the upper Changhsing Formation are significantly
937 bioturbated. Ichnofabric indices from Bed 27 remain relatively high (ii4), although only
938 40% strata are bioturbated. The remaining part of the lower Yinkeng Formation records a
939 rather low ii value (ii1) and no strata are significantly bioturbated. Ichnofabric indices in
940 the middle and upper parts of the Yinkeng Formation vary from 1 to 2 (ii1-2). On average,
941 15% of strata are significantly bioturbated.
942 In the upper Changhsing Formation, the two bedding planes in Bed 23

943 containing *Dendrorhaphe* isp. (Fig. 17F) and the problematic trace (Fig. 17D), show
944 coverage of 90% and thus indicate a BPBI of 5 (Fig. 3). The same BPBI value (ii 5) is also
945 estimated from two horizons of Beds 24d, containing *Taenidium* burrows. Bedding planes
946 from other horizons in the upper Changhsing Formation generally have bioturbation
947 coverage varying from 10% to 60%, indicating BPBI of 1-5. For the top bedding plane of
948 Bed 24e, just below the mass extinction horizon, containing *Planolites* (Fig. 17A, E) the
949 coverage was up to 90%, indicating a BPBI of 5. Beds 25-26a have the lowest BPBI, with
950 almost no bioturbation recorded. Several bedding planes from Beds 26b-27 show changes
951 in coverage from 20% to 40%, indicating a BPBI of 2-4. Bedding plane coverage in Beds
952 28-34 is generally rather low because bioturbation is broadly absent. Beds 35-51, overall,
953 have bioturbation coverage <10%, but some bedding planes containing *Planolites* show
954 coverage up to 20%, indicating a BPBI of 2. Another bedding plane containing
955 *Chondrites* has coverage up to 90%, indicating a BPBI of 5. In the upper Yinkeng
956 Formation, one bedding plane containing *Thalassinoides* shows coverage up to 20%,
957 indicating a BPBI of 2.
958
959 *5.3. Changeover of trace-fossil diversity over the P-Tr transition*

960

961 Ichnodiversity, represented by ichnogeneric richness, decreased remarkably

962 over the P-Tr transition. Eight ichnogenera are commonly encountered in the uppermost

963 Changhsing Formation: *Balanoglossites*, *Dendrorhaphe*, *Lockeia*, *Paleophycus*,

964 *Planolites*, Problematica, *Taenidium*, and *Thalassinoides* (Fig. 21A). Only *Planolites* is

965 present at the top of Bed 24e, dropping to 87.5% in the upper part of Bed 24e. All

966 ichnotaxa disappear at the top of Bed 24e, coinciding with the PTME. As a consequence,

967 Beds 25-26a are barren of ichnotaxa. The ichnofauna rebounded in Bed 26b and

968 diversified in Bed 27, including seven ichnogenera: *Arenicolites*, *Diplocraterion*,

969 *Gastrochaenolites*, *Psilonichnus*, *Thalassinoides*, *Chondrites*, and *Planolites*. Of

970 particular interest is the presence of four vertically burrowing ichnogenera (*Arenicolites*,

971 *Diplocraterion*, *Gastrochaenolites*, *Psilonichnus*) and one relatively complicated

972 burrowing ichnogenus (*Thalassinoides*), implying that ichnodiversity almost reached the

973 pre-extinction level in Bed 27 (Fig. 21A). All ichnotaxa disappeared soon after (in Bed

974 28). As a consequence, Beds 28-34, ranging through conodont zones *I. isarcica* and *I.*

975 *planata* Zones, lack any ichnotaxa and remained poorly bioturbed (Fig. 3).The

976 post-extinction rebound of ichnotaxa is marked by the presence of *Planolites* in Bed 35.

977 Since then, ichnodiversity remained at a rather low level and did not increase until the
978 middle-late Griesbachian, which saw the rise of *Chondrites* in Bed 52. Although
979 *Chondrites* disappeared in the middle-late Griesbachian, the trace-fossil assemblage
980 slightly diversified and included *Planolites*, *Treptichnus* and *Thalassinoides*.
981 As a result, P-Tr ichnotaxa underwent two pronounced reductions in diversity
982 coinciding with the two episodes of PTME calibrated to the bases of Beds 25 and 28.
983 Ichnofaunas fell to their lowest diversity in the early Griesbachian, and experienced a
984 slow increase in diversity throughout the middle-late Griesbachian (Fig. 21A). However,
985 post-extinction trace-fossil diversity never returned to the pre-extinction level.
986
987 *5.4. Burrow size variations through the P-Tr transition*
988
989 Nine bedding planes were examined to determine the size distribution of burrow
990 diameters of *Arenicolites*, *Dendrorhaphe*, *Diplocraterion*, *Paleophycus*, *Planolites*,
991 Problematica, *Taenidium*, *Thalassinoides*, and *Treptichnus* (Fig. 22). Burrow size change
992 over the P-Tr transition is apparent, especially in *Planolites*, as well as other traces such
993 as *Balanoglossites*, *Chondrites*, *Dendrorhaphe*, *Taenidium*, *Thalassinoides*, *Treptichnus*,

994 and Problematica (Fig. 22). *Planolites* is distributed in ten horizons throughout the
995 uppermost Changhsingian to middle-upper Griesbachian, and thus is a good proxy for
996 size variation of trace fossils over the P-Tr transition. Mean diameters of the Changhsing
997 Formation *Planolites* burrows are 7 mm, 8.5 mm, and 5.5 mm, respectively from three
998 horizons, with maximum burrow diameter up to 9.2 mm (Fig. 22A). Burrow sizes
999 decrease remarkably across the boundary between Beds 24 and 25, the PTME horizon
1000 (Fig. 1B), with mean burrow diameters of 1.7 mm and the greatest burrow diameter only
1001 2.2 mm in Bed 27 (Fig. 22A). Burrow sizes of *Planolites* remain very small throughout
1002 the early-middle Griesbachian and become larger by the late Griesbachian (Beds 54-57).
1003 These late Griesbachian traces are still much smaller than their counterparts recorded in
1004 the pre-extinction strata (Fig. 22A). Comparable size change over the P-Tr transition is
1005 also demonstrated by both the greatest size and mean size of *Thalassinoides* from the
1006 same interval (Fig. 22B).

1007 Several other ichnotaxa in the uppermost Permian have mean and maximum
1008 diameters, such as *Balanoglossites* (4.6 mm, 6.4 mm), *Dendrorhape* (12 mm, 17 mm),
1009 problematica (22 mm, 28 mm), and *Taenidium* (7.8-8.8 mm, 9.2 mm), that are obviously
1010 larger than that of those ichnotaxa confined to the lowest Triassic, i.e., *Chondrites* (2.8

1011 mm, 5.6 mm) and *Treptichnus* (6.3 mm, 6.3 mm) (Fig. 22C-D). When the measurements
1012 of all 273 burrows measured from the P-Tr strata of Meishan are combined, both mean
1013 and maximum diameters exhibit remarkable reduction across the boundary between Beds
1014 24 and 25 and remain very low values until Bed 27. The same values further decline from
1015 Bed 27 to Beds 28-34, and then undergo a stepwise increase through Beds 35-57 (Fig.
1016 21B)

1017 Trace-fossil size variations over the P-Tr transition are consistent with figures
1018 from northern Italy (Twitchett, 1999; Twitchett and Barras, 2004) and South China (Chen
1019 et al., 2011). It should be noted that the Early Triassic *Planolites* traces are much smaller
1020 than their Changhsingian counterparts at Meishan (Fig. 22A), unlike the same traces
1021 elsewhere (Pruss and Bottjer, 2004). *Planolites* is supposed to be the least susceptible to
1022 mass extinction because this simple trace can be produced by a variety of organisms
1023 (Pruss and Bottjer, 2004). Accordingly, the Changhsingian *Planolites* and their Early
1024 Triassic counterparts may have been made by different organisms.

1025

1026 *5.5. Trace fossil form and complexity*

1027

The Changhsing Formation trace fossils are morphologically diversified, and include simple, horizontal burrows (*Planolites*), vertical or oblique burrows (*Balanoglossites* and Problematica), resting traces (*Lockeia*), and complex forms (*Dendrorhape*, *Taenidium*, and *Thalassinoides*). They, however, disappear across the PTME horizon (base of Bed 25). Both *Planolites* and *Thalassinoides* rebound in Bed 27, but decrease markedly in size in comparison with their Changhsingian counterparts. *Thalassinoides* is also less complex than the same trace recorded in the Changhsingian. Complex forms, and resting and vertical traces of the Changhsingian (*Balanoglossites*, *Lockeia*, *Taenidium*, *Dendrorhape*, and Problematica) vanish in Bed 27. Instead, the relatively complex burrow systems of the *Glossifungites* ichnofacies, i.e., *Arenicolites*, *Gastrochaenolites*, *Psilonichnus*, and *Thalassinoides*, characterize the ichnoassemblage in the lower part of Bed 27. Vertical burrows of *Diplocraterion*, together with *Chondrites* and *Planolites* also occur in the upper part of Bed 27. Accordingly, ichnotaxa recovered from the pre-extinction level are similar to those in Bed 27 in terms of complexity, although these burrows are much smaller than their counterparts elsewhere.

Early Griesbachian traces are dominated by small, simple, horizontal burrows of *Planolites*, as reported elsewhere (Twitchett and Barras, 2004; Pruss and Bottjer, 2004;

1045 Fraiser and Bottjer, 2009; Chen et al., 2011, 2012). In the middle-late Griesbachian trace
1046 fossils become slightly more complex and are marked by the presence of *Chondrites*,
1047 *Thalassinoides* and *Treptichnus*, although these burrows are still very small. Nevertheless,
1048 these middle-late Griesbachian burrows are branched and form slightly complex
1049 networks, and thus are more complex than the *Planolites*-dominated ichnoassemblage in
1050 the early Griesbachian.

1051 As a result, trace-fossil complexity, reflecting behavioral complexity of the
1052 trace-makers, decreased dramatically during the PTME. Then, the trace-fossil
1053 assemblage shows an increase in complexity, varying from simple, horizontal traces (i.e.,
1054 *Planolites*) in the early Griesbachian to relatively complex traces (*Chondrites*,
1055 *Thalassinoides* and *Treptichnus*) in the middle-upper Griesbachian. In particular, the
1056 reappearance of *Thalassinoides* and *Treptichnus* probably implies increasing behavioral
1057 complexity that typically indicates the beginning of biotic recovery elsewhere (Twitchett
1058 and Barras, 2004).

1059

1060 *5.6. Infaunal tiering*

1061

Levels of tiering above and below the sediment were greatly reduced after the PTME (Ausich and Bottjer, 1982, 2002). At Meishan, the change in infaunal tiering over the P-Tr transition is reflected by the penetration depth of burrows (Fig. 21C), which was measured in the field. Vertical burrows of the Changhsing Formation may extend a maximum depth of 10 cm into the sediment, indicating a rather deep tiering level (ii5). In contrast, burrows of *Planolites* and *Thalassinoides* recorded in Bed 27 may penetrate to < 2 cm into the sediment. In particular, *Thalassinoides* commonly shows the second tiering level (ii2) (Bottjer and Droser, 1994). Early Griesbachian *Planolites* has burrows extending to a maximum depth of only 0.5 cm (Fig. 21C) indicating the lowest tiering level (ii1) (Bottjer and Droser, 1994). Thus, tiering fell to its minimum level in the early Griesbachian. An increase in tiering level during the middle Griesbachian is marked by the presence of *Chondrites*, an anoxic burrow system penetrating to a depth up to 1-2 cm and indicating the second tiering level (ii2) (Bottjer and Droser, 1994). The same tiering level is also reflected in upper Griesbachian *Thalassinoides* and *Treptichnus* burrows, which may extend to a maximum depth of 1-2 cm (Fig. 21C). Accordingly, the tiering level decreases significantly across the PTME horizon in Meishan, and then increases throughout the Griesbachian (Fig. 21C).

6. Size variations of pyrite framboids and redox conditions over the P-Tr transition

Pyrite is ~~rather~~ commonly present in the latest Changhsingian to Griesbachian rocks at Meishan (Wignall and Hallam, 1993), which is also confirmed by our observations of thin sections through the P-Tr transition at Meishan. Several pyrite-enriched beds have been treated as indications of anoxic conditions at Meishan (Wignall and Hallam, 1993). In particular, pyrite framboids, which are spherical aggregates of pyrite microcrystals, are rather abundant in these pyrite-enriched beds near the PTB at Meishan (Jiang et al., 2006; Shen et al., 2007). Pyrite framboids in ancient and modern sediments are interpreted as the result of redox conditions (e.g., Bond and Wignall, 2010), and these authors show that small framboids, usually 3-5 μm in diameter, indicate euxinic conditions (H_2S-bearing, O_2-free bottom waters). Accordingly, pyrite framboids have been considered as one of the most important pieces of evidence indicating redox conditions over the P-Tr transition worldwide (Wignall et al., 1998, 2005; Jiang et al., 2006; Shen et al., 2007; Gorjan et al., 2007; Bond and Wignall, 2010; Algeo et al., 2011b).

At Meishan, Jiang et al. (2006) reported that pyrite framboids are ~~very~~ commonly present in all beds through the PTB (Beds 24-29), based on etched residues from bulk samples. Shen et al. (2007) also observed framboids *in situ* on polished blocks and etched residues. Both studies detected that framboids are ~~very~~ abundant in Bed 25. Contrasting to Jiang et al.'s (2006) observation, Shen et al. (2007) found no pyrite framboids in Bed 27. However, unequal sampling in various beds near the PTB, for instance, 40 g each from Beds 25 and 26, but only 5 g each from Beds 24, 27, 28 and 29 may have biased their observation (Shen et al., 2007). Bed 27 comprises various lithologies from its base to top, which may have been deposited in different environments (Figs. 19-20). Thus, pyrite framboids may be ~~rare~~ absent in these bioturbated layers (i.e., CZs II, III-IV in Bed 24; Fig. 20), but instead may occur in finely laminated layers without bioburbation (i.e., CZs I and ~~I~~V; Fig. 20).

We have also observed pyrite framboids in continuous thin sections throughout Beds 24-30. We used a FEI Quanta 400 Scanning Electron Microscope (SEM) equipped with a GENESERS 2000 energy dispersive spectrometer (EDS) at the State Key Laboratory of Biogeology and Environmental Geology, China University of Geosciences, Wuhan, China. SEM images and EDS spectra were produced by the Zeiss VPSEM

coupled with an energy dispersive X-ray spectrometer. We confirmed Jiang et al.'s (2006) observation that both pyrite framboids and crystals occur in Bed 27 on brachiopod shells and in foraminiferal tests and sediments (Fig. 23). In addition, we measured framboid sizes in samples from Beds 29-60 using the SEM. Pyrite framboids are ~~very~~ abundant in samples from 17 horizons over the P-Tr transition (Fig. 24). The majority of framboid diameters in most measured beds are smaller than, or around 5 μm, except for Beds 28 and 44, in which most framboids have diameters of 7-8μm. Moreover, framboid diameters are concentrated in a narrow size range (< 10μm) in Beds 27, 28, 43, and 58. In contrast, they have a greater size range in Beds 24b, 24e, 25-26, 29-30, 39, 42, 49, 51-52 and 56, with maximum diameter up to 20μm in Bed 51.

Bond and Wignall (2010, table 1) proposed several characters, including framboid diameter and pyrite morphology, to determine redox conditions during deposition. In general, when framboids are small (mean diameters: 3-5 μm), abundant, with a narrow size range, and form the dominant pyrite fraction, they could have been deposited in euxinic condition (with a persistently sulfidic lower water column). If framboids are small (mean diameters: 4-6 μm), abundant, with a few, larger forms, and dominate the pyrite fraction, then they could have been deposited in anoxic condition

(without oxygen in bottom waters for long periods). When framboids have mean diameters of 6-10 μm and are moderately common, with a few, larger framboids together with some crystalline pyrite, they could have been deposited in lower dysoxic condition (with weakly oxygenated bottom waters). In upper dysoxic condition (with partial oxygen restriction in bottom waters) framboids are commonly to rarely present, with a broad range of sizes, only a small proportion of framboids < 5μm, and the majority of pyrite as crystals. In oxic condition (without oxygen restriction), no framboids are present, and pyrite crystals occur rarely.

If these five criteria given by Bond and Wignall (2010) are followed, we can determine redox conditions over the P-Tr transition in Meishan. Bed 24 contains abundant framboids, usually around 5 μm in diameter with some larger framboids, and their size range is relatively broad, pointing to anoxic conditions. Framboids in Beds 25-26 are usually 3-5 μm in diameter, a narrow size range, and no pyrite crystals are present, suggesting euxinic conditions (Fig. 25). Framboids from Bed 27 have a relatively large diameter and a broad size range (Fig. 24), and are also associated with some large pyrite crystals, pointing to a lower to upper dysoxic condition (Fig. 25). Pyrite framboids are moderately common in Bed 28 and have mean diameters of 8-9 μm, but no larger

framboids and crystalline pyrite occur. Thus, Bed 28 is inferred to be deposited in a transitional zone between anoxic and lower dysoxic conditions based on the criteria determining redox conditions proposed by Bond and Wignall (2010). Redox conditions became euxinic soon after in Bed 29, in which framboids are very small (3-5 μm) and have a narrow size range, without pyrite crystals. It should be noted that no pyrite framboids were found in Beds 30-35, although a pronounced negative excursion of carbon isotopes (Xie et al., 2007) and environmental stress indicated by biomarker signals (Yin et al., 2012) occur in these beds. Framboids from Beds 39 and 42 indicate euxinic-anoxic transitional conditions in terms of diameter, size range and association with pyrite crystals. Framboids from Bed 43 are ~~64~~ ~~10~~ 6 μm in diameter, but have some larger forms and are also associated with some pronounced pyrite crystals, and thus indicate a lower to upper dysoxic condition. Then, redox conditions indicated by pyrite framboids changed to anoxic to euxinic transitional conditions. Surprisingly, framboids from Bed 58 suggest euxinic condition, which coincides with the last negative excursion of carbon isotopes in the middle-late Griesbachian detected by Burgess et al. (2014).

7. Assessing ecologically PTME and its aftermath

1164

1165 *7.1. Testing ecologically extinction patterns*

1166

1167 The updated fossil record from Meishan shows two pronounced declines of

1168 species richness at the bases of Beds 25 and 28 (Song et al., 2013a; Fig. 26). Similarly,

1169 fossil fragment contents recorded in thin sections also show two distinct drops in both

1170 abundance and diversity corresponding to the top of Bed 24e and base of Bed 28 (Figs. 6,

1171 14). Further, ichnodiversity also declined within Beds 24 and 27. In Bed 24, trace fossils

1172 are rather abundant and comprise four distinct ichnogenera: *Balanoglossites*, *Planolites*,

1173 *Taenidium* and *Thalassinoides* in horizons near the boundary between Beds 24d and 24e,

1174 but only *Planolites* persisted into Bed 24e-6, in which relatively large burrows are

1175 densely packed, indicating a considerably high bioturbation level. All ichnotaxa

1176 disappeared in Beds 25-26a. Similarly, ichnotaxa decline from five ichnogenera

1177 (*Arenicolites*, *Gastrochaenolites*, *Planolites*, *Psilonichnus*, and *Thalassinoides*) in CZ II

1178 (Bed 27b) to three ichnogenera (*Diplocraterion*, *Chondrites* and *Planolites*) in CZ IV

1179 (Bed 27c), and then further declined and disappeared at the top of Bed 27d. Other proxies

1180 of trace fossils and bioturbation also show two pronounced declines corresponding to the

1181 bases of Beds 25 and 28. Clearly, the PTME ecologic crisis comprised two phases,
1182 coinciding with metazoan extinctions calibrated to the bases of Beds 25 and 28 (Song et
1183 al., 2013a).

1184 In addition, both fossil fragment contents and ichnodiversity show that a
1185 pronounced decline in diversity and abundance started at the stratal interval 10 to 19 mm
1186 below the top of Bed 24e. The boundary between Beds 24e-5 and 24e-6 is the most
1187 distinct eliminated horizon of skeletal fragment of major fossil groups, coinciding with
1188 end-Permian sulfur anomaly (Kaiho et al., 2006a) and the start of the negative
1189 end-Permian carbon isotopic excursion (Kaiho et al., 2009), and thus may indicate the
1190 PTME. Abundant sponge spicules above this event horizon indicate that they lasted in
1191 seawater for a while, although complete sponge fossils disappeared at the PTME event. It
1192 is therefore unlikely that the disappearance of calcareous fossils at the top of bed 24e-6
1193 was a result of an increase in the input of terrestrial material associated with the facies
1194 shift, as indicated by the lithologic shift from the limestone of Bed 24 to the claystone of
1195 Bed 25 and black shale of Bed 26. Instead, the extinction of calcareous biota and the
1196 associated environmental perturbation was most likely caused the lithologic change from
1197 limestone to mudstone. As a result, the sharp decline in biotic abundance and diversity

10-19 mm below the top of Bed 24e may signal the first episode of the PTME previously inferred from statistical paleontological data (Song et al., 2013a).

7.2. Ecologic collapse lagging behind biodiversity crisis during the PTME

At Meishan, the Permian biota experienced a dramatic drop in diversity at the base of Bed 25, with 172 species (94%) being wiped out in Beds 25-26 and no pronounced reduction of species richness in Bed 28 (Jin et al., 2000). The updated fossil record obtained from Meishan shows that species richness was reduced by at least 79% across the boundary between Beds 24e and 25, compared to 65% loss in species richness across the boundary between Beds 27d and 28 (Song et al., 2013a). This means that marine animals suffered a more severe depletion in species richness in the first phase of the PTME than in the second phase of the same event (Fig. 26). The biodiversity decline pattern from Meishan is confirmed by the same pattern at a further seven PTB sections in South China (Song et al., 2013a). It should also be noted that generic richness declined by a similar magnitude, 85% and 82%, in the first and second phases of the PTME, respectively in Meishan, but both generic and species richness underwent a stepwise

1215 decline from the uppermost Changhsingian to lowest Griesbachian (Fig. 26).
1216 Consequently, biotic diversity suffered a larger loss in the first episode than in the second
1217 episode of the PTME in terms of the number of lost taxa. This pattern is reinforced by
1218 fossil fragment content variations across the PTME horizons. Fossil components usually
1219 occupy nearly 70% in all rock in strata below Bed 25, but only about 30% in Bed 27, and
1220 FFA lost nearly 60% in thin section (Fig. 14). Over the same period, 11 Permian orders
1221 declined to five orders in Bed 27, losing 54.5% in ordinal richness.
1222 Both the standard diversity Shannon index [Exp (H)] and dominance index (D')
1223 assess whether the shelly community possesses a healthy structure. Exp (H) values
1224 declined by 43.6% from the *R–P* to *T* communities, and 55.5% from the *P–T* to *C–O*
1225 communities, coinciding with the first and second phases of the PTME, respectively. This
1226 means that the shelly communities suffered a greater loss in community diversity in the
1227 second phase of the PTME than in the first phase. Similarly, standard diversity
1228 dominance (D') increases by 34% and 54% during the two pronounced drops in diversity,
1229 respectively (Table 6). This means that the shelly communities became more uneven after
1230 the second phase of the PTME than after the first phase. Thus, shelly communities
1231 underwent relatively more serious ecologic crisis in the second phase than in the first

1232 phase of the PTME. This observation is also reinforced by ichnofaunal variations and
1233 ichnofabric changes over the P-Tr transition in Meishan.
1234 The presence of seven ichnogenera in Bed 27 suggests that ichnogeneric
1235 richness nearly recovered to the pre-extinction level, although there was a taxonomic loss
1236 in Beds 25-26a. In contrast, a more dramatic ichnofaunal loss occurred in the second
1237 phase of the PTME, corresponding to Bed 28. As a consequence, Beds 28-34 are barren
1238 of ichnotaxa. Thus, ichnofaunas suffered a more severe decline in the second phase of the
1239 PTME. This pattern is also strengthened by burrow size variations and tiering level
1240 changes, both of which remained relatively high in the Changhsingian, and experienced a
1241 stepwise decline through Beds 23-27, then fell to their lowest values in the early
1242 Griesbachian (Beds 28-34). Ichnofabric variation also shows that Bed 27 still remains
1243 highly bioturbated and yields rather complex burrow systems of the *Glossifungites*
1244 ichnofacies and *Cruziana* ichnofacies, which are commonly present in the pre-extinction
1245 period, thus showing the largest turnover at the base of Bed 28 rather than at the base of
1246 Bed 25. In contrast, ichnotaxa became very rare after the second phase of the PTME,
1247 although 2-3 ichnotaxa rebounded in the middle-late Griesbachian. Consequently, the
1248 greatest losses of ichnotaxa correspond to the top of Bed 27, simultaneous with the

second phase of metazoan extinction in Meishan (Song et al., 2013a). This ichnodiversity drop coincides with a remarkable decrease in tiering level (Fig. 21) and burrowing intensity (Fig. 3). Ichnofabric indices recorded in the upper Changhsing Formation are rather high (ii4-5) (Fig. 3). Complex traces of both the *Glossifungites* and *Cruziana* ichnofacies recorded in Bed 27 (Figs. 19-20) also indicate a fairly high ichnofabric index (ii3-4). Consequently, there was not a sharp decrease, but a gradual decrease, in burrowing intensity (ii4-5 down to ii3-4) over the first phase of the PTME. This is in sharp contrast to the pronounced drop in biodiversity of metazoans in this phase of the PTME (Fig. 26), suggesting a gradual worsening in environmental conditions.

In contrast, almost all of the complex traces of the *Glossifungites* and *Cruziana* ichnofacies disappeared in the second phase of the PTME. The early Griesbachian *Planolites* is confined to discrete horizons (ii1-2) separated by metres of unbioturbated sediment, and indicates a rather low ichnofabric index (ii1) (Fig. 3). A low ichnofabric index indicates an absence or rarity of burrowing infauna, which in turn implies a stressed environment immediately after the PTME (Chen et al., 2011). Accordingly, the great loss of burrowing infauna and associated environmental stress occur at the horizon between Beds 27 and 28. These facts imply that ecologic collapse of marine ecosystems

post-dated the metazoan biodiversity crisis at Meishan.

Contrasting to the two-stage extinction pattern (Song et al., 2013a), Shen et al. (2011b) and Wang et al. (2014) argued that the severest biodiversity declines fell in a short period equivalent to Beds 25-28 of Meishan, and there was one prolonged extinction rather than two discrete episodes. Indeed, Beds 25-28 represent a very short duration of about 60 ky (Burgess et al., 2014). However, all lines of evidence, including fossil fragment contents, and ichnofabric and community structural changes, show that the P-Tr ecologic crisis clearly comprises two pronounced steps, at the bases of Beds 25 and 28 (Figs. 14, 21, 26). Nevertheless, whether the mass extinction occurred as one prolonged event or two pulses, all studies agree that Beds 25-28 of Meishan and their equivalents represent a critical period when the greatest biotic turnover of life on Earth took place in Meishan. During this critical turnover period, the ecologic crisis clearly lagged behind the diversity decline. As a result, the Meishan fossil record shows that the mass extinction started with a dramatic depletion of biodiversity and ended with a severe ecologic crisis.

7.3. Dramatic increase in seawater surface temperature and its consequence

Recent oxygen isotopic studies of conodont bioapatites reveal that sea surface temperature rose ~9~~10~~ °C from Bed 24e to Bed 27a in Meishan (Joachimski et al., 2012; Sun et al., 2012; Fig. 26). However, the precise relationship between temperature increase and biotic extinction remains unclear owing to the lack of oxygen isotopic values from Bed 25, the base of which coincides with the PTME (Shen et al., 2011b) or the first phase of the PTME (Song et al., 2013a). The same is also true for the relationship between the temperature rise and the dramatic negative carbonate carbon isotopic excursion (Fig. 26). The solution is to undertake more detailed study of conodont oxygen isotopes of the PTB beds from less condensed sections than Meishan to evaluate whether temperature change leads or lags the extinction (Burgess et al., 2014).

Hinojosa et al. (2012) found a negative shift in $\delta^{44/40}$Ca of conodont bioapatite in the Great Bank of Guizhou, South China during the same interval as temperature increase in Meishan. This $\delta^{44/40}$Ca excursion is also coupled with a major shift in $\delta^{13}C_{carb}$ composition from an average of approximately +3.5‰ in the latest Permian to approximately –1‰ in the earliest Triassic (Payne et al., 2004). The anomaly of $\delta^{44/40}$Ca therefore was interpreted as a consequence, in part, of acidification of the ocean. Thus,

oceanic acidification in platform areas of the Great Bank of Guizhou may have resulted from elevated seawater temperature (Burgess et al., 2014). However, this ocean acidification seems not to have spread to the Meishan area because rather abundant and diverse complex traces of both *Glossifungites* and *Cruziana* ichnofacies occur in Bed 27 (Figs. 19-20), although calcareous skeletons decreased significantly in Beds 25-28 (Fig. 14).

Previously, the irregular surface occurring in the middle of Bed 27 at Meishan was interpreted as a submarine ~~solution~~dissolution surface, explained by a regional ocean acidification in South China (Payne et al., 2007, but see Wignall et al., 2009). This pronounced irregular surface, however, was re-interpreted as a distinct firmground surface, on which abundant complex traces of *Glossifungites* ichnofacies occur (see Section 3.5). Firmgrounds of *Glossifungites* ichnofacies are usually characteristic of initial transgression, and such horizons are usually employed to define sequence boundaries (Buatois and Mángano, 2011). Thus, no sign of acidification is recorded in Bed 27 ~~at~~ in Meishan.

Another potential consequence of elevated temperature is intensified chemical weathering (Sheldon, 2006) and consequent increased physical erosion of soils on land

(Sephton et al., 2005; Xie et al., 2007), or a combination of these processes. These processes are also indicated by the increased chemical index of alteration (CIA) profile immediately after the first phase of the PTME (Bed 25; Fig. 26). It should be noted that the CIA value was calculated as $Al_2O_3/(Al_2O_3+K_2O+Na_2O)$ (Zhao et al., 2013a), a modification of the original CIA equation (Nesbitt and Young, 1982). Increased chemical weathering during the PTME and its aftermath is also mirrored by the Eu/Eu* profile of conodont bioapatites (Zhao et al., 2013a). The latter rare-earth elemental (REE) proxy is a useful tracer of sediment provenance because fractionation between Eu^{+2} and Eu^{+3} does not occur under Earth-surface conditions (Elderfield and Greaves, 1982). Eu^{+2} tends to become segregated into feldspar during magmatic differentiation, resulting in Eu/Eu* values >1.0 in the crystal fraction and <1.0 in the residual fluid (Zhao et al., 2013a). Eu/Eu* ratios >1.0 are characteristic of magmas from lower crustal or mantle sources where substantial feldspar crystallization has taken place (Condie, 2001). Although the REE "fingerprint" of the ash-rich clastics is reflected by both CIA and Eu/Eu* profiles that match one another throughout P-Tr transition in Meishan (Fig. 26) and these ash beds near the PTB likely sourced from regional convergent continent marginal volcanisms (Gao et al., 2013, 2014), the shift toward Eu/Eu* values of 1.0–1.5 in Bed 24e,

Formatted

immediately preceding the PTME, may be evidence of a transient influx of volcanic material with a lower crustal or mantle source. Zhao et al. (2013a) argued that these mantle-sourced ash fingerprints indicated by Eu/Eu* values could be the product of the Siberian trap eruption (Reichow et al., 2009). Thus, this volcanic eruption could have caused the severe biocrisis and rapid increase in sea-surface temperature occurring ~20~~ kyr and~~ 80 kyr later~~, respectively~~ following the estimate of maximum and minimum sedimentation rates given by Burgess et al. (2014).

~~In addition,~~ Burgess et al. (2014) also estimated the rate of temperature rise in Beds 25-28 as an ~1 °C increase per 6,000 y, which is comparable with the rate and magnitude of the increase at the Paleocene–Eocene Thermal Maximum (Zeebe et al., 2009) and Pleistocene/Holocene postglacial warming (~2 °C/5 ka) (Lea et al., 2000). However, this estimati~~on~~ of the rate of temperature rise needs to be cautious because no temperature data is available from Bed 25 and the temperature rise spans Beds 24e-27 (Sun et al., 2012). To sum up~~Accordingly~~, although the killing mechanism of the ~~10~~ 9 °C increase of seawater surface temperature on organisms remains unclear, this rapid temperature increase coincides with biotic turnover and ecologic collapse during the PTME at Meishan. Nevertheless, the elevated temperature seems to have had little effect

on ichnofaunas and ichnofabrics, as indicated by abundant ichnofaunas living in the firmground of the *Glossifungites* ichnofacies (Bed 27), but instead resulted in dramatic losses of fossil skeletons in sediments (Fig. 14).

In addition, Sun et al. (2012) reported the acme of high seawater temperatures occurred in the late Griesbachian, corresponding to the upper *I. isarcica* Zone and lower *C. planata* Zone (Sun et al., 2012, fig. 2), which range from Beds 48-54. These two zones are amended herein (Fig. 2) and are equivalent to the upper part of *C. planata* Zone in the revised conodont zation (Fig. 2). This acme of high temperature postdates the second negative shift excursion of carbon isotops of Xie et al. (2007) and includes the second negative shifting excursion of carbon isotopes of Burgess et al. (2014). Surprisingly, this interval saw an increase in biodiversity (Chen et al., 2002, 2007), ichnological amoraliation and bioturbation (Fig. 3). Accordingly, the acme of high temperature has little effect on faunas.

Formatted: Font: Italic
Formatted: Font: Italic
Formatted: Font: Italic
Formatted: Font: Italic
Formatted: Font: Italic
Formatted: Font: Italic

7.4. Anoxic events and biotic response ~~and biotic response~~

~~7.4.1. Anoxic events~~7.4.1. Anoxic events

1368 At Meishan, Wignall and Hallam (1993) recognized an anoxic event associated
1369 with the PTME, but considered that the greatest acme of anoxia, coupled with a
1370 maximum flooding event, occurs in the lower Yinkeng Formation. Wignall and Twitchett
1371 (2002) believed that the oxygen-deficient waters spread into exceedingly shallow settings
1372 near the PTB in the Tethys regions (i.e., South China). More recently, multiple
1373 geochemical signals indicate the existence of anoxic to euxinic conditions before, during
1374 and after the PTME at Meishan.
1375 An exceptional increase in sea surface temperature is also believed to be
1376 synchronous with the flooding of shelf areas with anoxic and euxinic waters during the
1377 P-Tr transition (Sun et al., 2012). Both extremely high values of total organic content
1378 (TOC) (Yin et al., 2012) and reduced sizes of pyrite framboids (Fig. 26) indicate euxinic
1379 to anoxic condition in Beds 25-26, coinciding with the PTME. However, pyrite
1380 framboids from Bed 27 are generally larger than 5 μm in diameter with abundant crystals
1381 and thus indicate the upper part of dysoxic conditions (Fig. 25). Moreover, high
1382 bioturbation levels are also observed in upper part of Bed 26 and multiple layers of Bed
1383 27. Thus, a euxinic to anoxic condition~~s~~ was probably limited only to Beds 25-26a, which
1384 is less than 20 ka based on duration estimate of conodont zones from these beds (Table 2),

a much shorter period than previously thought. The anoxic condition of the water column is also reflected by the abrupt increase of Ce/Ce* values of conodont bioapatite from ~0.7–0.8 in Beds 23-24 to 0.9–1.1 in Beds 25-27b (Zhao et al., 2013a; Fig. 26). Values of 0.7–1.0 are sustained through Beds 27c to 30, above which Ce/Ce* decreases to 0.5–0.7. It should be noted that Ce/Ce* ratios derived from Bed 27a-d are not totally in accordance with size analysis of pyrite framboids, which shows that Bed 27a-d may represent redox conditions ranging from anoxia to upper level of dysoxia (Fig. 25). Although Ce/Ce* values from Meishan may have been biased by the fingerprint of clay input, Ce/Ce* values of 0.9–1.1 indicate an anoxic depositional system (Zhao et al., 2013a; Shen et al., 2012). This inference is consistent with the results of earlier studies documenting anoxia around the PTME in South China PTB sections (Grice et al., 2005; Algeo et al., 2007; Shen et al., 2007; Cao et al., 2009; Bond and Wignall, 2010; Luo et al., 2010) and globally (Algeo et al., 2010, 2011b; Brennecka et al., 2011).

Formatted: Not Highlight

Euxinic condition may have occurred prior to the PTME in Meishan, i.e., Beds 22-24, demonstrated by the anomaly of sulfur isotopes (Shen et al., 2011a) and various biomarker signals in Beds 22-24 (Grice et al., 2005; Cao et al., 2009; Luo et al., 2010, 2011). Algeo et al. (2011a) also interpreted the anoxic and euxinic conditions as a result

of an expansion of the oxygen minimum ~~oxygen~~ zone (OM~~O~~Z) in the water column over the P-Tr transition. These authors considered that the OMZ may have expanded prior to the PTME in Meishan.

A post-extinction reduced condition is also indicated by a pronounced negative excursion of carbon isotopes in Beds 34-36 (Xie et al., 2007; Luo et al., 2010; Fig. 26), coupled with an increase in TOC and terrestrial input indicated by various biomarker signals (Yin et al., 2012), and elevated contents of CO_2 (Fraiser and Bottjer, 2007). The CIA profile slightly increases in Beds 34-36, indicating elevated chemical weathering on land, which is consistent with the increased TOC and terrestrial input (Yin et al., 2012).

~~However~~In addition ~~,~~ conodont bioapatite from Beds 33–39 generally yields lower Ce/Ce* ratios (0.4–0.7) that may indicate an oxic to suboxic depositional environment. Conodont bioapatite Ce, however, was probably derived mainly from detrital clay minerals and taken up during diagenesis, as indicated by other REE proxies (Zhao et al., 2013). If so, the observed Ce/Ce* ratios only reflect the REE composition of the source clays (Zhao et al., 2013a).

Alternatively, size variations of pyrite framboids indicate that Beds 27-29 record a dramatic redox change from upper dysoxic to euxinic conditions (Fig. 25). A euxinic to

Formatted: Don't adjust space between Latin and Asian text, Don't adjust space between Asian text and numbers

Formatted

Formatted

Formatted: Font: (Default) Times New Roman, 12 pt

Formatted: Font: (Default) Times New Roman, 12 pt

Formatted: Font: (Default) Times New Roman, 12 pt

Formatted: Font: (Default) Times New Roman, 12 pt

Formatted

Formatted

Formatted: Indent: First line: 1.5 cm, Don't adjust space between Latin and Asian text, Don't adjust space between Asian text and numbers

anoxic condition prevailed throughout Bed 29 to Bed 42 (Fig. 25). The combination of mean size of framboids and presence of both larger framboids and crystal pyrites indicates Bed 43 may be deposited in a lower to upper dysoxic condition. If a redox interpretation is warranted, then this pattern suggests that the anoxic episode following the PTME ~~at~~ in Meishan ~~had~~ lasted a relatively ~~short~~ long duration, probably ~~no more than~~ ~50 kyr. Moreover, mean sizes and morphologies of framboids from Beds 44-58 also generally reflect an anoxic to euxinic condition, which, however, is not supported by various ichnological proxies.

7.~~4.2~~4.2. Biotic response

The pre-extinction anoxic to euxinic conditions are generally supported by the presence of abundant small pyrite framboids, 3-5 μm in diameter, in Beds 23-24 (Figs. 23-24). However, biodiversity of metazoans remains very stable, with 64-78 species in 34-44 genera in each layer through Beds 24a to 24e (Fig. 26). Bed 24 contains 82 species in 47 genera, and there are similar numbers in Bed 23 (Jin et al., 2000). Thus, no major losses in species and generic richness are recognizable in Beds 23-24. Fossil fragment

contents are almost the same in each layer through Beds 22-24, except for the top 1-2 cm of Bed 24e, in which there is a pronounced loss in fossil components across the boundary between Beds 24e-5 and 24e-6 (Figs. 6, 14). Fossil fragment contents fell by >16% in thin section from Beds 24e-5 to 24e-6. The FFA of Bed 24e-5 comprises 10 major fossil groups ~~orders~~ that are commonly present in all Permian limestones, but five ~~orders~~clades, ostracods, bryozoans, calcareous sponges, gastropods, and macroalgae, disappeared, losing 50%, across this boundary (Figs. 6, 14). The FFA of Bed 24e-6 is dominated by sponge spicules (35%) and thus has a high dominance and low diversity and evenness, in contrast to the low dominance, high diversity/evenness FFA in Bed 24e-5 (Fig. 6). Furthermore, the last occurrence of Permian fusulinids was also bracketed to the base of Bed 24e-6 (Kaiho et al., 2006b).

Ichnodiversity also declined significantly across the boundary between Beds 24e-5 and 24e-6 (Fig. 21A). These relatively complex or vertical burrows such as *Balanoglossites* and *Thalassinoides*, which usually occur in oxygenated settings, disappeared at the base of Bed 24e-6. Instead, only simple, horizontal burrows of *Planolites* occur in Bed 24e-6. Ichnofabrics, however, do not exhibit a major change across the same boundary (Fig. 3), with abundant *Planolites* burrows being densely

packed on the surface of Bed 24e-6. However, most geochemical studies do not have such a high sampling intensity, and thus neglected this boundary.

Both metazoan biodiversity and fossil fragment contents experienced dramatic declines in Beds 25-26a. Other ecologic measures, such as community structures, ichnodiversity, burrow size, tiering level, and ichonfabric variation, also indicate an ecologic crisis in Beds 25-26a, coinciding with the anoxia indicated by both pyrite framboid sizes and various geochemical signals (Fig. 26). However, the metazoan fauna from Bed 27 is rather abundant and diverse, including 66 species in 34 genera (Song et al., 2013a). Both community structural indices and fossil fragment contents indicate that metazoans had recovered well in Bed 27. The presence of abundant complex burrows in Bed 27 indicates ~~that~~ the infaunal ~~was little affected by the anoxic event and proliferated~~ proliferation in the firmground of *Glossifungites* ichnofacies (Fig. 20). The occasional occurrence of pyrite framboids in Bed 27 may indicate a very short period of anoxic condition, but Bed 27, as a whole, represents a dysoxic to oxic condition in which benthos and infaunas proliferated.

By contrast, all data, including the low ichnodiversity (only *Planolites*), small burrow size, low trace complexity, low ichnofabric from Beds 29-51 indices and low

Formatted: Indent: First line: 0 cm

tiering level as well as low-diversity metazoans (Chen et al., 2007, 2010a), support the view that anoxic conditions may have prevailed throughout the early Griesbachian in Meishan (Wignall and Hallam, 1993; Xie et al., 2007; Yin et al., 2012). Of these, Beds 29-34 are barren of trace fossils and bioturbation. This is supported by trace fossil size, which is also regarded as a proxy for paleoenvironmental conditions (Twitchett, 1999; Pruss and Bottjer, 2004). In general, small-sized traces are usually found in poorly oxygenated sediments (Savrda and Bottjer, 1987) or brackish environments (Pemberton et al., 1982; Buatois et al., 2005) or habitats with low nutrient supply (Jumars and Wheatcroft, 1989). Thus small traces are characteristic of stressed environments (Twitchett, 1999; Pruss and Bottjer, 2004). The dramatic size reduction of trace fossils after the PTME indicates environmental stresses associated with the PTME, and the small sizes of Early Triassic traces suggest prolonged environmental stress following the event (Bottjer et al., 2008).

7.5. Testing extinction mechanisms

Multiple scenarios have been proposed to interpret the killing mechanisms of the PTME, including widespread anoxia, hypercapnia, massive volcanic eruption, global

Formatted: Indent: First line: 0.42 cm
Formatted: Font: Italic
Formatted: Font: Italic
Formatted: Indent: First line: 0 cm
Formatted: Indent: First line: 1.5 cm, Line spacing: Double
Formatted: Font: (Default) Times New Roman, 12 pt
Formatted: Font: (Default) Times New Roman, 12 pt
Formatted: Font: (Default) Times New Roman, 12 pt
Formatted: Font: (Default) Times New Roman, 12 pt
Formatted: Font: (Default) Times New Roman, 12 pt
Formatted: Font: (Default) Times New Roman, 12 pt
Formatted: Font: (Default) Times New Roman, 12 pt

warming, ocean acidification, and increased sediment flux (Erwin, 2006; Knoll et al., 2007; Clapham and Payne, 2011; Algeo and Twitchett, 2010; Algeo et al., 2011a; Joachimski et al., 2012; Sun et al., 2012; Burgess et al., 2014; Song et al., 2014). However, the true causes of this biocrisis still remain unclear due to the incomplete record of evidence supporting any of these alternatives.

Recently, Song et al. (2013a) suggested that different extinction mechanisms may have driven each of these two pulses given their differences in biodiversity and ecologic losses. These authors considered that anoxia may be related to the first-pulse losses of biota, but played a crucial role in the second-pulse biocrisis (Song et al., 2013a). Elevated sea-surface temperature not only resulted in the spread of anoxia but also killed directly shallow-water taxa, while the anoxia killed the deep-water organisms (Song et al., 2014). However, extinction and survival selectivity of various fossil groups is more complicated than previously thought (i.e., Song et al., 2013a, 2014). This is because various elements of the same clade may have different lifestyles. For instance, the P-Tr brachiopods have six types of lifestyles based on attachment modes on the substratum: burrowing, body cementation, pedicle attaching on substratum, body spines anchoring on substratum, pedicle attaching on objects, and clasping spines on other shells/or objects

Formatted: Font: (Default) Times New Roman, 12 pt
Formatted: Font: (Default) Times New Roman, 12 pt
Formatted: Font: (Default) Times New Roman, 12 pt
Formatted: Font: (Default) Times New Roman, 12 pt
Formatted
Formatted: Font: Times New Roman
Formatted
Formatted: Font: Times New Roman
Formatted: Font: Times New Roman
Formatted: Font: Times New Roman
Formatted
Formatted
Formatted
Formatted
Formatted
Formatted: Font: Times New Roman

(Chen et al., 2006a, 2011b). These brachiopods having the last two types of attachment modes behaviour like nektons. Moreover, some shallow-water elements were also able to survive in deep niches during the latest Permian (Chen et al., 2006a). It is also true for the P-Tr bivalves that embrace several lifestyles (Huang et al., 2014). Accordingly, our high resolution comprehensive analyses of biodiversity, community structural, fossil fragment, ichnological, and redox condition changes associated with these two discrete events allow an evaluation of the proposed kill mechanisms for these two ecologic crises.

Most of the Permian brachiopods became extinct in the first extinction. The survivors are dominated by chonetids or chonetid-like productids or small, thin-shelled spiriferids/rhynchonellids that usually have attachment modes of clasping spines on other shells/or objects or pedicle-attaching on other shells or objects (Chen et al., 2005a, 2011b). These survivors attached their bodies on some float objects (i.e., other shells and algae) suspending above the seafloor (Chen et al., 2005a, 2011b), and thus provided brachiopods higher adaptability surviving the deleterious environments, i.e., increased acidity of precipitation (Wignall, 2007), large-scale marine acidification (Clapham and Payne, 2011) and widespread anoxia (Wignall and Twitchett, 2002; Payne and Clapham, 2012) during the first biocrisis. Inarticulated brachiopods i.e., lingulids also survived this

Formatted: Font: Times New Roman
Formatted: Font: Times New Roman
Formatted: Font: Times New Roman
Formatted: Font: Times New Roman
Formatted: Font: Times New Roman
Formatted: Font: Times New Roman
Formatted
Formatted
Formatted
Formatted
Formatted
Formatted
Formatted
Formatted: Font: (Default) Times New Roman, 12 pt
Formatted
Formatted: Font: (Default) Times New Roman, 12 pt
Formatted: Font: (Default) Times New Roman, 12 pt
Formatted: Font: (Default) Times New Roman, 12 pt
Formatted: Font: (Default) Times New Roman, 12 pt
Formatted: Font: (Default) Times New Roman, 12 pt
Formatted

event, although having a burrowing lifestyle. This is because linguilds are able to survive in poorly oxygenated waters due to having respiratory pigment acting the function to transport oxygen or to store oxygen within the body tissues under anoxic conditions or during cessation of respiration (Williams et al., 1997).

Similarly, Huang et al. (2014) argued that the anoxia or acidification may have impacted seriously on bivalve's extinction and survival selectivity during the first extinction based on ecologic analysis of the P-Tr bivalves. As a result, both brachiopod's and bivalve's evidence indicates that anoxia impacted clearly by in the first-pulse biocrisis (Chen et al., 2011b; Huang et al., 2014). The acidification associated with this extinction cannot be excluded (Clapham and Payne, 2011; Hinojosa et al., 2012). The anoxia or acidification, however, lasted a very short duration, ~30 ka, as discussed above.

Furthermore, a rapid increase of about ~9°C of sea-surface temperature (within a period of ~30 ka) across Beds 24e-27a (Sun et al., 2012) must have facilitated respiratory frequency and accelerated oxygen consumption of most brachiopods and become lethal to brachiopods, and thus causes morality, regardless their shallower or deeper habitats (Chen et al., 2014b in this volume). The rapidly elevated seawater temperature also coincides with the first dramatic losses of body fossil biodiversity and fossil fragments as

Formatted: Indent: First line: 1.5 cm, Line spacing: Double

well as moderate losses of ichnodiversity and community diversity, and a moderate decrease in bioturbation, tiering levels of infaunas and burrow sizes.

However, marine ecosystems seem not to have collapsed completely during the first-pulse crisis (Chen and Benton, 2012), some organisms survived the short environmental and climatic devastation. Thus, both biodiversity and ichnodiversity, and all of ichnological and community structural measures rebounded rapidly in Bed 27a-d (Fig. 26).

Like the first extinction, the second-pulse biocrisis is also associated with a clay bed (Bed 28), in which pyrite framboids indicate a lower dysoxic to anoxic condition (Fig. 25). However, the redox condition became euxinic soon after and is indicated by framboids obtained from the base of Bed 29. Thus, a dramatic change from upper dysoxic to oxic condition in Bed 27 to euxinic condition in basal Bed 29 indicates an anoxia/euxinia coincided with the 2nd biocrisis, which is followed by a long period of euxinic to anoxic conditions, which was probably driven by a relatively long (>62 ka) acme of high temperature (up to 35-37^{o}C) in earliest Griesbachian. Accordingly, both epifaunal and infaunal ecosystems collapsed after suffering such a long period of lethally hot seawater temperature and widespread anoxia in earliest Triassic oceans (Fig. 26).

Formatted: Indent: First line: 1 cm, Line spacing: Double

Formatted: Superscript

This is reinforced by the replacement of free-lying brachiopod-dominated communities in Bed 27 with nekton-dominated communities in Beds 31-37 (Chen et al., 2010a) and Beds 28-34 barren of bioturbation and ichnofossils (Figs. 3, 26). As stated above, these surviving brachiopods yielded from Beds 26-27 should have enhanced resistant ability to anoxic or acidified water mass near seafloor because they survived from the first-pulse crisis. The morality of the free-lying brachiopods in the second-pulse crisis is probably due to the loss of other shells or float algae, on which the brachiopods attach using either pedicle or clasping spines.

Accordingly, the killing mechanisms for these two extinction events near the PTB seem not to be fundamentally different from one another, although no sign of acidification has been reported in the second phase of the PTME. However, a short anoxia or acidification probably caused by a rapid increase in seawater temperature may have played an important role in the first-pulse biocrisis, while the long-lasting and widespread anoxia induced by a long period of high temperature condition may have killed most organisms in the second-pulse crisis.

Formatted: Normal, Indent: First line: 1.5 cm, Line spacing: Double, Don't adjust space between Latin and Asian text, Don't adjust space between Asian text and numbers

7.~~5~~6. Post-extinction amelioration of marine ecosystems in late Griesbachian

1572

1573 Post-extinction benthic communities did not appear to return to normal until the
1574 early Middle Triassic (Chen and Benton, 2012). The deleterious environment that
1575 prevailed in early Triassic oceans may be largely responsible for this long-delayed
1576 recovery (Bottjer et al., 2008). In particular, Early Triassic carbon isotopic records show
1577 several negative excursions that indicate sharp global warming (Payne et al., 2004), and
1578 these coincide with diversity drops. Furthermore, intrinsic relationships between
1579 organisms and ecosystem structures may also have slowed down biotic recovery
1580 following the PTME (Chen and Benton, 2012). Recent studies show that the biotic
1581 recovery process may be mirrored by stepwise establishment of trophic structures of
1582 marine ecosystems throughout Olenekian-Anisian interval (Chen and Benton, 2012).
1583 However, biotic recovery may occur earlier in oxygenated environments (Twitchett et al.,
1584 2004; Beatty et al., 2008; Zonneveld et al., 2010). As a result, Early Triassic marine
1585 environments were not always deleterious globally. Chen et al. (2007) also detected that
1586 marine environments had greatly ameliorated during the late Griesbachian in Meishan.
1587 The sea-floor recuperation, including shallowing water depth, increasing oxygenation
1588 and oceanic productivity, coincides with an increase in benthic biodiversity, signalling

1589 that ecologic and environmental restoration might have initiated in the late Griesbachian
1590 (Chen et al., 2002, 2007).

1591 The example of elevated recovery of the benthic community in late
1592 Griesbachian at Meishan is also strengthened by community structural changes and
1593 ichnofabric variation through the PTB to late Griesbachian. The Exp (H) value increases
1594 by 262.6% from the *C* to *M–L* communities, and also increases 70%, coupled with a
1595 decrease of 15.2% in D' values, from the *C–O* to *M–L* communities, suggesting an
1596 improvement in shelly community structures in the upper Yinkeng Formation at Meishan
1597 (Chen et al., 2002, 2007).

1598 Trace fossils and ichnofabrics documented here also show that the late
1599 Griesbachian trace-fossil assemblage is marked by significant increases in ichnodiversity,
1600 burrow size, trace complexity, tiering level, and bioturbation level, in comparison with
1601 early Griesbachian ichnoassemblages, although they did not achieve Changhsingian
1602 levels (Fig. 21). Thus, the Meishan trace fossils, together with increasing diversity in the
1603 shelly community, sedimentary structures (HCS), up-shallowing sedimentary cycle and
1604 geochemical proxies (Chen et al., 2007), suggest that biotic recovery recorded in the
1605 upper Yinkeng Formation may be categorized as recovery stage 2 (*sensu* Twitchett, 2006),

and also mark the return of parts of the meso-consumer functioning group within the ecosystem trophic structure, which usually occurs in the Spathian around the world (Chen and Benton, 2012).

8. Conclusions

Updated conodont biostratigraphy allows the establishment of eight conodont zones from the latest Changhsingian to early Griesbachian at Meishan, the *C. yini, C. meishanensis*, *H. ~~changhsingensis~~changxingensis*, *C. taylorae*, *H. parvus*, *I. staeschei*, *I. isarcica*, and *C. planate* zones. Microstratigraphic analysis shows that a major turnover in fossil fragment contents and ichnodiversity occurs across the boundary between Beds 24e-5 and 24e-6, suggesting the actual mass extinction horizon in thin section. Bed 27 contains a firmground of *Glossifungites* ichnofacies rather than the previously proposed submarine ~~solution~~dissolution surface or hardground surface. Fossil fragment contents show a dramatic decline in both fossil component percentage and assemblage diversity in Beds 25-26a, coinciding with metazoan mass extinction. Fossil fragment content, ichnodiversity and all ichnofabric proxies (including burrow size, tiering level, and

1623 bioturbation level) throughout the uppermost Changhsing to Yinkeng formations indicate
1624 that the P-Tr ecologic crisis comprises two discrete stages, coinciding with the first and
1625 second phases of the PTME, in support of a proposed two-stage extinction pattern of
1626 metazoans over the P-Tr transition. The PTME was of short duration, lasting about 60 kyr.
1627 A biodiversity crisis indicates the start of the extinction interval, but its end is marked by
1628 the ecologic collapse of ecosystems. Thus, the ecologic crisis lagged behind the
1629 biodiversity decline during the PTME. Pyrite framboid size variations suggest that the
1630 depositional redox condition was anoxic to euxinic in the latest Changhsingian, became
1631 euxinic in Beds 25-26a, turned to be dyoxic in Bed 27, then varied from euxinic to anoxic
1632 through most of the Griesbachian. Although metazoan biodiversity and fossil fragment
1633 contents show dramatic declines, coinciding with a ~~10~~ 9 °C increase in seawater surface
1634 temperature, from Bed 24e to Bed 27 in Meishan, all ecologic proxies show much smaller
1635 effects from the elevated seawater temperature. Bed 27 contains abundant infauna and
1636 shows no signs of ocean acidification. Pre-extinction anoxic-euxinic conditions had little
1637 effect on both metazoans and infauna. The anoxic event associated with the PTME may
1638 have lasted for much less time than previously thought, and is limited to Beds 25-26a at
1639 Meishan. Fossil fragment contents, ichnofaunas, ichnofabrics and pyrite framboid size all

show that anoxic conditions did not exist in Bed 27. Early Griesbachian anoxia is possible, and may have caused the rarity of ichnofaunas and metazoans in the lower Yinkeng Formation. The ichnofauna is characterized by small, simple horizontal burrows of *Planolites*, while metazoan faunas are characterized by low diversity, high abundance, opportunist-dominated communities. The killing mechanisms for these two extinction events near the PTB similar to one another. A rapid increase of ~9 °C in seawater temperature and its inducing short anoxia or acidification may have played an important role in the first-pulse biocrisis, while the long-time and widespread anoxia probably caused by long-time high temperature condition may have resulted in morality of most organisms in the second-pulse crisis. Initial recovery of marine ecosystems coupled with environmental amelioration occurred in the late Griesbachian, marking the return of parts of the meso-consumer functioning group.

Formatted: Superscript

Acknowledgements

We thank J. Tong for help in the field and H.J. Song for discussion on foraminiferal taxonomy of collections from the PTB beds in Meishan. This work was supported by the

973 Program and China 111 Program. It is a contribution to IGCPs 572 and 630.

References

Algeo, T.J., Twitchett, R.J., 2010. Anomalous Early Triassic sediment fluxes due to elevated weathering rates and their biological consequences. Geology 38, 1023–1026.

Algeo, T.J., Chen, Z.Q., Fraiser, M.L., Twitchett, R.J., 2011a. Terrestrial-marine teleconnections in the collapse and rebuilding of Early Triassic marine ecosystems. Palaeogeography, Palaeoclimatology, Palaeoecology 308, 1–11.

Algeo, T.J., Hannigan, R., Rowe, H., Brookfield, M., Baud, A., Krystyn, L., Ellwood, B.B., 2007. Sequencing events across the Permian–Triassic boundary, Guryul Ravine (Kashmir, India). Palaeogeography, Palaeoclimatology, Palaeoecology 252, 328–346.

Algeo, T.J., Henderson, C.M., Ellwood, B., Rowe, H., Elswich, E., Bates, S., Lyons, T., Hower, J.C., Smith, C., Maynard, B., Hays, L.E., Summons, R.E., Fulton, J., Freeman, K.H., 2012. Evidence for a diachronous late Permian marine crisis from

Formatted: Indent: Left: 0 cm, Hanging: 1.77 ch, First line: -1.77 ch

Formatted: Font: (Default) Times New Roman, 12 pt

Formatted: Indent: Left: 0 cm, Hanging: 1.77 ch

Formatted

Formatted: Font: (Default) Times New Roman, 12 pt

Formatted: Font: (Default) Times New Roman, 12 pt

Formatted: Font: (Default) Times New Roman, 12 pt

Formatted

the Canadian Arctic region. Geological Society of America Bulletin 124, 1424–1448.

Algeo, T.J., Hinnov, L., Moser, J., Maynard, J.B., Elswick, E., Kuwahara, K., Sano, H., 2010. Changes in productivity and redox conditions in the Panthalassic Ocean during the latest Permian. Geology 38, 187–190.

Algeo, T.J., Kuwahara, K., Sano, H., Bates, S., Lyons, T., Elswick, E., Hinnov, L., Ellwood, B., Moser, J., Maynard, J.B., 2011b. Spatial variation in sediment fluxes, redox conditions, and productivity in the Permian–Triassic Panthalassic Ocean. Palaeogeography, Palaeoclimatology, Palaeoecology 308, 65–83.

Ausich, W.I., Bottjer, D.J., 2002. Sessile invertebrates. In: Briggs, D.E.G., Crowther, P.R. (eds.), Palaeobiology II. Blackwell Science, Oxford, pp. 384-386.

Baldwin, C.T., McCave, I.N., 1999. Bioturbation in an active deep-sea area: Implications for models of trace fossil tiering. Palaios 14, 375-388.

Beatty, T.W., Zonneveld, J.-P., Henderson, C.M., 2008. Anomalously diverse Early Triassic ichnofossil assemblages in northwest Pangea: a case for a shallow-marine habitable zone. Geology 36, 771–774.

Benner, J.S., Ekdale, A.A., 2004. Macroborings (*Gastrochaenolites*) in Lower

Ordovician Hardgrounds of Utah: Sedimentologic, Paleoecologic, and Evolutionary Implications. Palaios 19, 543–550.

Benton, M.J., Twitchett, R.J., 2003. How to kill (almost) all life: the end-Permian extinction event. Trends in Ecology and Evolution 18, 358–365.

Bond, D.P.G., Wignall, P.B., 2010. Pyrite framboid study of marine Permian–Triassic boundary sections: a complex anoxic event and its relationship to contemporaneous mass extinction. Geological Society of America Bulletin 122, 1265–1279.

Bottjer, D.J., Droser, M.L., Jablonski, D., 1988. Fine-scale resolution of mass extinction events: Trace fossil evidence from the Permian-Triassic boundary in South China. Geological Society of America, Abstracts with Programs 20, p. A106.

Bottjer, D.J., Clapham, M.E., Frasier, M.L., Powers, C.M., 2008. Understanding mechanisms for the end-Permian mass extinction and the protracted Early Triassic aftermath and recovery. GSA Today 18, 4–10.

Bowring, S.A., Erwin, D.H., Jin, Y.G., Martin, M.W., David, E.K., Wang, W., 1998. U/Pb zircon geochronology and tempo of the end-Permian mass extinction. Science 280, 1039–1045.

Brennecka, G.A., Herrmann, A.D., Algeo, T.J., Anbar, A.D., 2011. Rapid expansion of

oceanic anoxia immediately before the end-Permian mass extinction. Proceedings of the National Academy of Sciences, U.S.A. 108, 17631–17634.

Bromley, R.G., 1996. Trace Fossils: Biology, Taphonomy and Applications (2nd edition). Chapman & Hall, London, 361 pp.

Bromley, R.G., Ekdale, A.A., 1984. *Chondrites*: a trace fossil indicator of anoxia in sediments. Science 224, 872-874.

Buatois, L.A., Mángano, M.G., 2011. Ichnology: Organism-Substrate Interactions in Space and Time. Cambridge University Press, New York. 1–358.

Buatois, L.A., Gingras, M.K., MacEachern, J., Mangano, M.G., Zonneveld, J.P., Pemberton, S.G., Netto, R.G., Martin, A., 2005. Colonization of brackish-water systems through time: Evidence from the trace-fossil record. Palaios 20, 321-347.

Burgess, S.D., Bowring, S., Shen, Z.Q., 2014. High-precision timeline for Earth's most severe extinction. Proceedings of National Academy of Sciences, U.S.A. 111, 3316–3321.

Cao, C.Q., Shang, Q.H., 1998. Microstratigraphy of Permo-Triassic transitional sequence of the Meishan section, Zhejiang, China. Palaeoworld 9, 147-152.

Cao, C.Q., Zheng, Q.F., 2007. High-resolution lithostratigraphy of the Changhsingian

stage in Meishan section, Zhejiang. Journal of Stratigraphy 31, 14-22.

Cao C Q, Zheng Q F. 2009. Geological event sequences of the Permian-Triassic transition recorded in the microfacies in Meishan section. Science China Series D-Earth Sciences 52, 1529–1536

Cao, C.Q., Wang, W., Jin, Y., 2002. Carbon isotope excursions across the Permian-Triassic boundary in the Meishan section, Zhejiang Province, China. Chinese Science Bulletin 47, 1125-1129.

Cao, C., Love, G.D., Hays, L.E., Wang, W., Shen, S., Summons, R.E., 2009. Biogeochemical evidence for euxinic oceans and ecological disturbance presaging the end-Permian mass extinction event. Earth and Planetary Science Letters 281, 188–201.

Chen, J., Chen, Z.Q., Tong, J.N., 2010b. Palaeoecology and taphonomy of two brachiopod shell beds from the Anisian (Middle Triassic) of Guizhou, Southwest China: recovery of benthic communities from the end-Permian mass extinction. Global and Planetary Change 73, 149-160.

Chen, J., Chen, Z.Q., Tong, J., 2011b. Environmental determinants and ecologic selectivity of benthic faunas from nearshore to bathyal zones in the end-Permian

Formatted: Font: Times New Roman, 12 pt

Formatted: Left, Indent: Left: 0 cm, Hanging: 1.77 ch

Formatted: Font: Times New Roman, 12 pt

mass extinction: brachiopod evidence from South China. Palaeogeography, Palaeoclimatology, Palaeoecology 308, 84-97.

Chen, J.H., 2004. Macroevolution of bivalves after the end-Permian mass extinction in South China. In: Rong, J.Y., Fong, Z.J. (eds), Biotic mass extinction and recovery—evidence from Palaeozoic and Triassic of South China. China University of Science & Technology Press, Hefei. pp. 647–700.

Chen, Z.Q., Benton, M.J., 2012. The timing and pattern of biotic recovery following the end-Permian mass extinction. Nature Geoscience 5, 375–383.

Chen, Z.Q., Liao, Z.T., 2009. Brachiopod faunas across the Wuchiapingian-Changhsingian (Late Permian) boundary at the stratotype section and subsurface of Changxing area, South China. Neues Jahrbuch für Geologie und Paläontologie 254, 315–335.

Chen, Z.Q., McNamara, K.J., 2006. End-Permian extinction and subsequent recovery of the Ophiuroidea (Echinodermata). Palaeogeography, Palaeoclimatology, Palaeoecology 236, 321–344.

Chen, Z.Q., Algeo, T.J., Bottjer, D.J., 2014a. Global review of the Permian–Triassic mass extinction and subsequent recovery: Part I. Earth-Science Reviews 137, 1-5. ~~(in~~

press), http://dx.doi.org/10.1016/j.earscirev.2014.05.007

Chen, Z.Q., Campi, M., Shi, G.R., Kaiho, K., 2005b. Post-extinction brachiopod faunas from the Late Permian Wuchiapingian coal series of South China. Acta Palaeontologica Polonica 50, 343-363.

Chen, Z.Q., Fraiser, M.L., Bolton, C., 2012. Early Triassic trace fossils from Gondwana Interior Sea: Implication for ecosystem recovery following the end-Permian mass extinction in south high-latitude region. Gondwana Research 22, 238-255.

Chen, Z.Q., Kaiho, K., George, A.D., 2005a. Survival strategies of brachiopod faunas from the end-Permian mass extinction. Palaeogeography, Palaeoclimatology, Palaeoecology 224, 232–269.

Chen, Z.Q., Kaiho, K., George, A.D., Tong, J., 2006b. Survival brachiopod faunas of the end-Permian mass extinction from northern Italy and south China. Geological Magazine 143, 301-327.

Chen, Z.Q., Shi, G.R., Kaiho, K., 2002. A new genus of rhynchonellid brachiopod from the Lower Triassic of South China and implications for timing the recovery of Brachiopoda after the end-Permian mass extinction. Palaeontology 45, 149-164.

Chen, Z.Q., Shi, G.R., Yang, F.Q., Gao, Y.Q., Tong, J.N., Peng, Y.Q., 2006a. An

ecologically mixed brachiopod fauna from Changhsingian deep-water basin of South China: consequence of end-Permian global warming. Lethaia 39, 79–90.

Chen, Z.Q., Tong, J.N., Fraiser, M.L., 2011a. Trace fossil evidence for restoration of marine ecosystems following the end-Permian mass extinction in the Lower Yangtze region, South China. Palaeogeography, Palaeoclimatology, Palaeoecology 299, 449–474.

Chen, Z.Q., Tong, J.N., Liao, Z.T., Chen, J., 2010a. Structural changes of marine communities over the Permian–Triassic transition: ecologically assessing the end-Permian mass extinction and its aftermath. Global and Planetary Change 73, 123–140.

Chen, Z.Q., Tong, J., Zhang, K., Yang, H., Liao, Z., Song, H., Chen, J., 2009. Environmental and biotic turnover across Permian–Triassic boundary from shallow carbonate platform in western Zhejiang, South China. Australian Journal of Earth Sciences 56, 775–797.

Chen, Z.Q., Tong, J., Kaiho, K., Kawahata, H., 2007. Onset of biotic and environmental recovery from the end-Permian mass extinction within 1-2 million years: A case study of the Lower Triassic of the Meishan section, South China. Palaeogeography,

Palaeoclimatology, Palaeoecology 252, 176-187.

Chen, Z.Q., Wang, J.L., Yang, H., Tu, C.Y., Polov, Y., He, W.H., 2014b. Permian-Triassic evolutionary dynamics of the Brachiopoda: paleobiogeography, extinction-survival-recovery, latitudinal diversity gradients, body size variations, and longevity changes. Earth-Science Reviews (under review, in this volume).

Claoue-Long, J.C., Zhang, Z.C., Ma, G.G. and Du, S.H., 1991. The age of the Permian-Triassic boundary. Earth and Planetary Science Letters 105, 182–190.

Clapham, M., Payne, J., 2011. Acidification, anoxia, and extinction: a multiple logistic regression analysis of extinction selectivity during the Middle and Late Permian. Geology 39, 1059–1062.

Condie, K.C., 2001. Mantle Plumes and Their Record in Earth History. Cambridge University Press, Cambridge. 306 pp.

Crasquin, S., Forel, M.B., Feng, Q.L., Yuan, A.H., Baudin, F., Collin, P.Y., 2010. Ostracods (Crustacea) through the Permian-Triassic boundary in South China: the Meishan stratotype (Zhejiang Province). Journal of Systematic Palaeontology 8, 331-370.

Dasgupta, S., Buatois, L.A., 2012. Unusual occurrence and stratigraphic significance of

the *Glossifungites* ichnofacies in a submarine paleo-canyon — Example from a Pliocene shelf-edge delta, Southeast Trinidad. Sedimentary Geology 269-270, 69-77.

Droser, M.L., Bottjer, D.J., 1986. A semiquantitative field classification of ichnofabric. Journal of Sedimentary Petrology 56, 558-559.

Ekdale, A.A., Bromley, R.G., 2001. A day and a night in the life of a cleft-foot clam: *Protovirgularia-Lockeia-Lophoctenium*. Lethaia 34, 119-124.

Ekdale, A.A., Bromley, R.G., 2003. Paleoethologic interpretation of complex *Thalassinoides* in shallow-marine limestone, Lower Ordovician, southern Sweden. Palaeogeography, Palaeoclimatology, Palaeoecology 192, 221-227.

Elderfield, H., Greaves,M.J., 1982. The rare earth elements in seawater. Nature 296, 214–219.

Erwin, D.H., 2001. Lessons from the past: biotic recoveries from mass extinctions. Proceedings of the National Academy of Sciences, U.S.A. 98, 5399–5403.

Erwin, D.H., 2006. How Life on Earth Nearly Ended 250 Million Years Ago. Princeton University Press, Princeton, 306 pp.

Farabegoli, E., Perri, M.C., 2012. Millennial physical events and the end-Permian mass

1827 mortality in the western Palaeotethys: timing and primary causes. In: Talent, J.A.
1828 (ed.), Earth and Life, International Year of Planet Earth, Springer, London, pp.
1829 719-758.
1830 Flugel, E., 1982. Microfacies Analysis of Limestone, Springer, New York, 663 pp.
1831 Forel, M.-B., Crasquin, S., 2011. Lower Triassic ostracods (Crustacea) from the Meishan
1832 section, Permian-Triassic boundary GSSP (Zhejiang Province, South China). Journal
1833 of Systematic Palaeontology 9, 455-466.
1834 Fraiser, M.L., Bottjer, D.J., 2007. Elevated atmospheric CO_2 and the delayed biotic
1835 recovery from the end-Permian mass extinction. Palaeogeography,
1836 Palaeoclimatology, Palaeoecology 252, 164–175.
1837 Fraiser, M.L., Bottjer, D.J., 2009. Opportunistic behavior of invertebrate marine
1838 tracemakers during the Early Triassic aftermath of the end-Permian mass extinction.
1839 Australian Journal of Earth Sciences 56, 841–857.
1840 Gao, Q.L., Zhang, N., Xia, W.C., Feng, Q.L., Chen, Z.Q., Zheng, J.P., Griffin, W.L.,
1841 O'Reilly, S.Y., Pearson, N.J., Wang, G.Q., Wu, S., Zhong, W.L., Sun, X.F., 2013.
1842 Origin of volcanic ash beds across the Permian-Triassic boundary, Daxiakou, South
1843 China: Petrology and U-Pb age, trace elements and Hf-isotope composition of zircon.

Chemical Geology 360-361, 41-53.

Gao, Q.L., Chen, Z.Q., Zhang, N., Xia, W.C., Wang, G.Q., Jiang, T.F., Xia, X.F., 2014. Ages, trace elements and Hf-isotopic compositions of zircon from claystones around the Permian-Triassic boundary in the Zunyi section, South China: implications for nature and tectonic setting of the volcanism. Journal of Earth Sciences 26 (in press).

Gorjan, P., Kaiho, K., Kakegawa, T., Niitsuma, S., Chen, Z.Q., Kajiwara, Y., Nicora, A., 2007. Paleoredox, biotic and sulfur-isotopic changes associated with the end-Permian mass extinction in the western Tethys. Chemical Geology 244, 483-492.

Gouramis, C., Webb, J.A., Warren, A.A., 2003. Fluviodeltaic sedimentology and ichnology of part of the Silurian Grampians Group, western Victoria. Australian Journal of Earth Sciences 50, 811–825.

Grice, K., Cao, C., Love, G.D., Bottcher, M.E., Twitchett, R.J., Grosjean, E., Summons, R.E., Turgeon, S.C., Dunning, W., Jin, Y., 2005. Photic zone euxinia during the Permian-Triassic superanoxic event. Science 307, 706-709

Hammer, O., Harper, D.A.T., Ryan, P.D., 2001. PAST: palaeontological statistics software package for education and data analysis. Palaeontologia Electronica 4, 1–9.

1861 Häntzschel, W., 1975. Trace fossils and problematica. In: Teichert, C. (ed.), Treatise of
1862 Invertebrate Paleontology (2nd Edition), Part W, Miscellanea, Supp 1. University of
1863 Kansas and Geological Society of America, Lawrence, Kansas, 269 pp.
1864 He, J.W., 1981. Clay minerals in the Changhsingian stratotype section and the basal part
1865 of Yinkeng Formation, with reference to the Permo-Triassic boundary (in Chinese).
1866 Journal of Stratigraphy 5, 197–206
1867 He, J.W., Rui, L., Chai, Z.F., 1987. The latest Permian and earliest Triassic volcanic
1868 activities in the Meishan area of Changxing, Zhejiang. Journal of Stratigraphy 11,
1869 194–199.
1870 He, W., Feng, Q., Gu, S., Jin, Y., 2005. Changxingian (Upper Permian) Radiolarian fauna
1871 from Meishan D section, Changxing, Zhejiang, China, and its possible
1872 paleoecological significance. Journal of Paleontology 79, 209–218.
1873 Hinojosa, J.L., Brown, S.T., Chen, J., DePaolo, D.J., Paytan, A., Shen, S.Z., Payne, J.L.,
1874 2012. Evidence for end-Permian ocean acidification from calcium isotopes in
1875 biogenic apatite. Geology 40, 743-746.
1876 Huang, C.J., Tong, J.N., Hinnov, L., Chen, Z.Q., 2011. Did the great dying of life take
1877 700 ky? Evidence from global astronomical correlation of the Permian-Triassic

boundary interval. Geology 39, 779-782.

Huang, Y.F., Tong, J.N., Fraiser, M.L., Chen, Z.Q., 2014. Extinction patterns among bivalves in South China during the Permian-Triassic crisis. Palaeogeography, Palaeoclimatology, Palaeoecology 399, 78-88.

Hubbard, S.M., Shultz, M.R., 2008. Deep burrows in submarine fan-channel deposits of the Cerro Toro Formation (Cretaceous), Chilean Patagonia: implications for firmground development and colonization in the deep sea. Palaios 23, 223–232.

Jacobsen, N., Twitchett, R.J., Krystyn, L., 2011. Palaeoecological methods for assessing marine ecosystem recovery following the Late Permian mass extinction event. Palaeogeography, Palaeoclimatology, Palaeoecology 308, 200–212.

Jiang, H.S., Lai, X., Luo, G., Aldridge, R., Zhang, K., Wignall, P.B., 2007. Restudy of conodont zonation and evolution across the P/T boundary at Meishan section, Changxing, Zhejiang, China. Global and Planetary Change 55, 39-55.

Jiang, H.S., Aldridge, R.J., Lai, X.L., Sun, Y.D., Luo, G.M., 2008. Observations on the surface microreticulation of platform elements of *Neogondolella* (Conodonta) from the Upper Permian, Meishan, China. Lethaia 41, 263-274.

Jiang, H.S., Lai, X.L., Sun, Y.D., Wignall, P.B., Liu, J., Yan, C., 2014. Permian-Triassic

conodonts from Dajiang (Guizhou, South China) and their implication for the age of microbialite deposition in the aftermath of the end-Permian mass extinction. Journal of Earth Science 25, 413-430.

Jiang, H.S., Lai, X.L., Yan, C.B., Aldridge, R.J., Wignall, P., Sun, Y.D., 2011. Revised conodont zonation and conodont evolution across the Permian-Triassic boundary at the Shangsi section, Guangyuan, Sichuan, SouthChina. Global and Planetary Change, 77, 103-115,

Jiang,Y., Tang,Y.,Dai, S., Zou,X.,Qian,H., Zhou,G., 2006. Pyrites and sulfur isotopic composition near the Permian–Triassic boundary in Meishan. Zhejiang. Acta Geologica Sinica 80, 1202–1207.

Jin, Y., Wang, Y., Wang, W., Shang, Q., Cao, C., Erwin, D.H., 2000. Pattern of marine mass extinction near the Permian-Triassic boundary in South China. Science 289, 432-436.

Joachimski, M.M., Lai, X., Shen, S., Jiang, H., Luo, G., Chen, B., Chen, J., Sun, Y., 2012. Climate warming in the latest Permian and the Permian–Triassic mass extinction. Geology 40, 195–198.

Jost, L., 2006. Entropy and diversity. Oikos 113, 363–375.

1912 Jost, L., 2007. Partitioning diversity into independent alpha and beta components.
1913 Ecology 88, 2427–2439.
1914 Jumars, P.A., Wheatcroft, R.A., 1989. Responses of benthos to changing food quality and
1915 quantity with a focus of deposit feeding and bioturbation. In: Berger, W.H., Smetacek,
1916 V.S., Wefer, G., (eds.), Productivity in the Ocean: Past and Present. Wiley, Chichester,
1917 pp. 235-253.
1918 Kaiho, K., Chen, Z.Q., Miura, Y., Kawahata, H., Kajiwara, Y., Sato, H., 2006b. Close-up
1919 of the end-Permian mass extinction horizon recorded in the Meishan section, South
1920 China: Sedimentary, elemental, and biotic characterization with a negative shift of
1921 sulfate sulfur isotope ratio. Palaeogeography, Palaeoclimatology, Palaeoecology 239,
1922 396-405.
1923 Kaiho, K., Kajiwara, Y., Chen, Z.Q., Gorjan, P., 2006a. A sulfur isotope event at the end
1924 of the Permian. Chemical Geology 235, 33-47
1925 Kaiho, K., Chen, Z.Q., Sawada, K., 2009. Possible causes for a negative shift of stable
1926 carbon isotope ratio before, during, and after the end-Permian mass extinction in
1927 Meishan, South China. Australian Journal of Earth Sciences 56, 799-808.
1928 Kaiho, K., Kajiwara, Y., Nakano, T., Miura, Y., Chen, Z.Q., Shi, G.R., 2001. End-Permian

catastrophe by a bolide impact: evidence of a gigantic release of sulfur from the mantle. Geology 29, 815-818.

Keighley, D.G., Pickeril, P.K., 1994. The ichnogenus *Beaconites* and its distinction from *Ancorichnus* and *Taenidium*. Palaeontology 37, 305-337.

Knaust, D., 1998. Trace fossils and ichnofabrics on the Lower Muschelkalk carbonate ramp (Triassic) of Germany: tool for high-resolution sequence stratigraphy. Geologische Rundschau 87, 21-31.

Knaust, D., 2004. Cambro–Ordovician trace fossils from the SW Norwegian Caledonides. Geological Journal 39, 1–24.

Knoll, A.H., Bambach, R.K., Oayne, J.L., Pruss, S., Fischer, W.W., 2007. Paleophysiology and end-Permian mass extinction. Earth and Planetary Science Letters 256, 295–313.

Korte, C., Kozur, H., Joachimski, M.M., Strauss, H., Veizer, J., Schwark, L., 2004a. Carbon, sulfur, oxygen and strontium isotope records, organic geochemistry and biostratigraphy across the Permian/Triassic boundary in Abadeh, Iran. International Journal of Earth Sciences 93, 565–581

Kosnik, M.A., Wagner, P.J., 2006. Effects of taxon abundance distributions on expected

numbers of sampled taxa. Evolutionary Ecology Research 8, 195–211.

Kozur, H., 2007. Biostratigraphy and event stratigraphy in Iran around the Permian–Triassic Boundary (PTB): Implications for the causes of the PTB biotic crisis. Global and Planetary Change 55, 155–176.

Lea, D.W., Pak, D.K., Spero, H.J., 2000. Climate impact of late quaternary equatorial pacific sea surface temperature variations. Science 289, 1719–1724.

Li, J., Cao, C.Q., Servais, T., Zhu, Y.H., 2004. Later Permian acritarchs from Meishan (SE China) in the context of Permian palaeobiogeography and palaeoecology. Neues Jahrbuch für Geologie und Paläontologie, Monatshefte 7, 427-448.

Li, W.Z., Shen, S.Z., 2008. Lopingian (Late Permian) brachiopods around the Wuchiapingian-Changhsingian boundary at the Meishan sections C and D, Changxing, South China. Geobios 41, 307–320.

Liang H., 2002, End-Permian catastrophic event of marine acidification by hydrated sulfuric acid: Mineralogical evidence from Meishan section of South China: Chinese Science Bulletin 47, 1393-1397.

Liao, Z.T., 1984. New genera and species of Late Permian and earliest Triassic brachiopods from Jiangsu, Zhejiang and Anhui Provinces. Acta Palaeontologica

Sinica 23, 276–285.

Luo, G.M., Lai,X.L., Jiang, H.S., Zhang, K.X., 2006. Size variation of the end Permian conodont *Neogondolella* at Meishan section, Changxing, Zhejiang and its significance. Science in China, Series D 49, 337–347.

Luo, G.M., Lai, X.L., Shi, G.R., Jiang, H.S., Yin, H.F., Xie, S.C., Tong, J.N., Zhang, K.X., He, W.H., Wignall, P.B., 2008. Size variation of conodont elements of the *Hindeodus-Isarciciella* clade during the Permian-Triassic transition in South China and its implication for mass extinction. Palaeogeography, Palaeoclimatology, Palaeoecology 264, 176-187.

Luo, G.M., Huang, J.H., Xie, S.C., Wignall, P.B., Tang, X.Y., Huang, X.Y., Yin, H.F., 2010. Relationships between carbon isotope evolution and variation of microbes during the Permian-Triassic transition at Meishan section, South China. International Journal of Earth Sciences 99, 775-784.

Luo, G.M., Wang, Y.B., Yang, H., Algeo, T.J., Kump, L., Huang, J.H., Xie, S.C., 2011. Stepwise and large-magnitude negative shift in delta C-13 (carb) preceded the main marine mass extinction of the Permian-Triassic crisis interval. Palaeogeography, Palaeoclimatology, Palaeoecology 299, 70-82.

MacEachern, J.A., Raychaudhuri, I., Pemberton, S.G., 1992. Stratigraphic applications of the *Glossifungites* ichnofacies: delineating discontinuities in the rock record. In: Pemberton, S.G. (ed.), Applications of Ichnology to Petroleum Exploration: A Core Workshop: SEPM Core Workshop No. 17, pp. 169–198 Tulsa, USA.

MacEachern, J.A., Bann, K.L., Pemberton, S.G., Gingras,M.K., 2007. The ichnofacies paradigm: high-resolution paleoenvironmental interpretation of the rock record. In: MacEachern, J.A., Bann, K.L., Gingras, M.K., Pemberton, S.G. (eds), Applied Ichnology: SEPM Short Course Notes No. 52, pp. 27–64. Tulsa, USA.

Mei, S.L., Zhang, K.X., Wardlaw, B.R., 1998. A refined succession of Changhsingian and Griesbachian neogondolellid conodonts from the Meishan section, candidate of the Global Stratotype Section and Point of the Permian-Triassic boundary. Palaeogeography, Palaeoclimatology, Palaeoecology 143, 213-226.

Miller, M.F., Smail, S.E., 1997. A semiquantitative method for evaluating bioturbation on bedding planes. Palaios 12, 391–396.

Mundil, R., Metcalfe, I., Ludwig, K.R., Renne, P.R., Oberli, F., Nicoll, R.S., 2001. Timing of the Permian–Triassic biotic crisis: implications from new zircon U/Pb age data (and their limitations). Earth and Planetary Science Letters 187, 131–145.

1997 Mundil, R., Ludwig, K.R.,Metcalfe, I., Renne, P.R., 2004. Age and timing of the Permian
1998 mass extinctions: U/Pb dating of closed-system zircons. Science 305, 1760–1763.
1999 Myrow, P.M., 1995. *Thalassinoides* and the enigma of early Paleozoic open-framework
2000 burrow systems. Palaios 10, 58-74.
2001 Nicoll, R.S., Metcafle, I., Wang, C.Y., 2002. New species of the conodont genus
2002 Hindeodus and conodont biostratigraphy of the Permian–Triassic boundary interval.
2003 Journal of Asian Earth Sciences 20, 609–631.
2004 Olszewski, T.D., 2004. A unified mathematical framework for the measurement of
2005 richness and evenness within and among multiple communities. Oikos 104,
2006 377–378.
2007 Orchard, M.J., Krystyn, L., 1998.Conodonts of the lowermost Triassic of Spiti, and new
2008 zonation based on *Neogondolella* successions. Rivista Italiana di Paleontogia e
2009 Stratigrafia 104, 341–368.
2010 Orchard, M.J., Nassichuk, W.W., Rui, L., 1994. Conodonts from the Lower Griesbachian
2011 *Otoceras latilobatum* bed of Selong, Tibet and the position of the Permian–Triassic
2012 boundary. Canadian Society of Petroleum Geologists, Proceedings of Pangea
2013 Conference, Memoir 17, 823–843.

2014 Payne, J.L., Clapham, M.E., 2012. End-Permian mass extinction in the oceans: An
2015 ancient analog for the twenty-first century? Annual Reviews of Earth and Planetary
2016 Sciences 40, 89–111.
2017 Payne, J.L., Lehrmann, D.J., Wei, J.Y., Orchard, M.J., Schrag, D.P., Knoll, A.H., 2004.
2018 Large perturbations of the carbon cycle during recovery from the end-Permian
2019 extinction. Science 205, 505-509.
2020 Payne, J.L., Lehrmann, D.J., Wei, J., Knoll, A.H., 2006. The pattern and timing of biotic
2021 recovery from the end-Permian extinction on the Great Bank of Guizhou, Guizhou
2022 Province, China. Palaios 21, 63–85.
2023 Payne, J.L., Lehrmann, D.J., Follett, D., Seibel, M., Kump, L.R., Riccardi, A., Altiner, D.,
2024 Sano, H., Wei, J., 2007. Erosional truncation of uppermost Permian shallow-marine
2025 carbonates and implications for Permian–Triassic boundary events. Geological
2026 Society of America, Bulletin 119, 771–784.
2027 Pemberton, S.G., Frey, R.W., 1985. The *Glossifungites* ichnofacies: modern examples
2028 from the Georgia coast, USA. In: Curran, H.A., (ed.), Biogenic Structures: Their Use
2029 in Interpreting Depositional Environments: SEPM Special Publication, 35, pp.
2030 237–259, Tulsa, USA.

Pemberton, S.G., Flach, P.D., Mossop, G.D., 1982. Trace fossils from the Athabasca Oil Sands, Alberta, Canada. Science 217, 825-827.

Pemberton, S.G., MacEachern, J.A., Saunders, T., 2004. Stratigraphic applications of substratespecific ichnofacies: delineating discontinuities in the fossil record. In: McIlroy, D. (ed.), The Application of Ichnology to Palaeoenvironmental and Stratigraphic Analysis: Geological Society of London, Special Publication, 228, 29–62.

Perri, M.C., Farabegoli, E., 2003. Conodonts across the Permian–Triassic boundary in the Southern Alps. Courier Forschungsinstitute Senckenberg 245, 281–313.

Pruss, S.B., Bottjer, D.J., 2004. Early Triassic fossils of the western United States and their implications for prolonged environmental stress from the end-Permian mass extinction. Palaios 19, 551-564.

Reichow, M.K., Pringle, M.S., Al'Mukhamedov, A.I., Allen, M.B., Andreichev, V.L., Buslov, M.M., Davies, C.E., Fedoseev, G.S., Fitton, J.G., Inger, S., Medvedev, A.Y., Mitchell, C., Puchkov, V.N., Safanova, I.Y., Scott, R.A., Saunders, A.D., 2009. The timing and extent of the eruption of the Siberian Traps large igneous province: implications for the end-Permian environmental crisis. Earth and Planetary Sciences

Letters 277, 9–20.

Renne, P.R., Black, M.T., Zheng, Z.C., Richards, M.A., Basu, A.R., 1995. Synchrony and causal relations between Permian–Triassic boundary crisis and Siberian flood volcanism. Science 269, 1413–1416.

Renne, P.R., Mundil, R., Balco, G., Min, K., Ludwig, K.R., 2010. Joint determination of 40K decay constants and 40Ar*/40K for the Fish Canyon sanidine standard, and improved accuracy for 40Ar/39Ar geochronology. Geochimica et Cosmochimica Acta 74, 5349–5367.

Riccardi, A., Arthur,M.A., Kump, L.R., 2006. Sulfur isotopic evidence for chemocline upward excursions during the end-Permian mass extinction. Geochimica et Cosmochimica Acta 70, 5740–5752.

Rindsberg, A.K., Kopaska-Merkel, D.C., 2005. *Treptichnus* and *Arenicolites* from the Steven C. Minkin Paleozoic footprint Site (Langsettian, Alabama, USA). In: Buta, R.J., Rindsberg, A.K., Kopaska-Merkel, D.C., (eds.), Pennsylvanian Footprints in the Black Warrior Basin of Alabama: Monograph, 1. Alabama Paleontological Society, pp. 121–141.

Rui, L., He, J., Chen, C., Wang, Y., 1988. Discovery of fossil animals from the basal clay

of Permian–Triassic boundary in the Meishan area of Changxing, Zhejiang and its significance. Journal of Stratigraphy 12, 48–52.

Savrda, C.E., 1992. Trace fossils and benthic oxygenation. In: Maples, C.G., West, R.R. (eds), Trace Fossils, Short Courses in Paleontology 5. University of Tennessee Press, Knoxvill pp. 172–196.

Savrda, C.E., Bottjer, D.J., 1987. The exaerobic zone, a new oxygen-deficient marine biofacies. Nature 327, 54-56.

Savrda, C.E., Browning, J.V., Krawinkel, H., Hesselbo, S.P., 2001. Firmground ichnofabrics in deep-water sequence stratigraphy, Tertiary clinoform-toe deposits, New Jersey slope. Palaios 16, 294–305.

Seilacher, A. 1967. Bathymetry of trace fossils. Marine Geology 5, 413-428.

Seilacher, A. 1977. Pattern analysis of *Paleodictyon* and related trace fossils. In: Crimes, T.P., Harper, J.C. (eds.), Trace Fossils 2. Geological Journal Special Issue No. 9, 289-334.

Seilacher, A., 2007. Trace Fossil Analysis. Springer, Berlin. 226 pp.

Sephton, M.A., Looy, C.V., Brinkhuis, H., Wignall, P.B., de Leeuw, J.W., Visscher, H., 2005. Catastrophic soil erosion during the end-Permian biotic crisis. Geology 33,

941–944.

Sepkoski Jr., J.J., 1982. A Compendium of Fossil Marine Families: Milwaukee Public Museum Contributions in Biology and Geology, 51, p. 125.

Sepkoski Jr., J.J., 2002. A Compendium of Fossil Marine Animal Genera: Bulletin of American Paleontology 363, 1-563.

Sheldon, N.D., 2006. Abrupt chemical weathering increase across the Permian–Triassic boundary. Palaeogeography, Palaeoclimatology, Palaeoecology 231, 315–321.

Shen, J., Algeo, T.J., Zhou, L., Feng, Q., Yu, J., Ellwood, B., 2012. Volcanic perturbations of the marine environment in South China preceding the latest Permian mass extinction and their biotic effects. Geobiology 10, 82-103.

Shen, S.Z., James L. Crowley, J.L., Wang, Y., Bowring, S.A., Erwin, D.H., Sadler, P.M., Cao, C.Q., Rothman, D.H., Henderson, C.M., Ramezani, J., Zhang, H., Shen, Y.A., Wang, X.D., Wang, W., Mu, L., Li, W.Z., Tang, Y.G., Liu, X.L., Liu, L.J., Zeng, Y., Jiang, Y.F., Jin, Y.G., 2011b. Calibrating the end-Permian mass extinction. Science 9, 1367-1372,

Shen, W.J., Lin, Y.T., Xu, L., Li, J. F., Wu, Y.S., Sun, Y.G., 2007. Pyrite framboids in the Permian-Triassic boundary section at Meishan, China: Evidence for dysoxic

deposition. Palaeogeography, Palaeoclimatology, Palaeoecology 253, 323-331.

Shen, Y.A., Farquhar, J., Zhang, H., Masterson, A., Zhang, T., Wing, B.A., 2011a. Multiple S-isotopic evidence for episodic shoaling of anoxic water during Late Permian mass extinction. Nature Communications 2, 210e.

Sheng, J., Chen, C., Wang, Y., Rui, L., Liao, Z., Bando, Y., Ishii, K., Nakazawa, K., Nakamura, K., 1984. Permian–Triassic boundary in Middle and Eastern Tethys. Journal of Faculty of Science, Hokkaido University 21, 133–181.

Sheng, J.Z., Chen, C.Z., Wang, Y.G., Rui, L., Liao, Z.T., He, J.W., Jiang, N.Y., Wang, C.Y., 1987. New evidence on the Permian and Triassic boundary of Jiangsu, Zhejiang and Anhui. In: Nanjing Institute of Geology and Palaeontology, Academia Sinica (ed.), Stratigraphy and Palaeontology of Systemic Boundaries in China. Permian–Triassic Boundary (1). Nanjing University Press, Nanjing, pp. 1–21

Shi, C., Chen, D., 1987. The Changhsingian ostracodes from Meishan, Changxing, Zhejiang. In: Nanjing Institute of Geology and Palaeontology, Academia Sinica (Ed.), Stratigraphy and Palaeontology of systemic boundaries in China. Permian-Triassic boundary (1). Nanjing University Press, Nanjing, pp. 23-80.

Song, H., Tong, J., Chen, Z.Q., 2009. Two episodes of foraminiferal extinction near the

Permian–Triassic boundary at the Meishan section, South China. Australian Journal of Earth Sciences 56, 765–773.

Song, H., Tong, J., Zhang, K., Wang, Q., Chen, Z.Q., 2007. Foraminiferal survivors from the Permian–Triassic mass extinction in the Meishan section, South China. Palaeoworld 16, 105–119.

Song, H.J., Wignall, P.B., Tong, J.N., Yin, H.F., 2013a. Two pulses of extinction during the Permian-Triassic crisis. Nature Geoscience 6, 52-56.

Song, H.J., Wignall, P.B., Chu, D.L., Tong, J.N., Sun, Y.D., Song, H.Y., He, W.H., Tian, L., 2014. Anoxia/High temperature double whammy during the Permian-Triassic marine crisis and its aftermath. Scientific Reports 4, 4132.

Song, H.Y., Tong, J.N., Algeo, T.J., Horacek, M., Qiu, H.O., Song, H.J., Tian, L., Chen, Z.Q., 2013b. Large vertical $\delta^{13}C$ gradients in Early Triassic seas of the South China craton: Implications for oceanographic changes related to Siberian Traps volcanism. Global and Planetary Change 105, 7–20.

Sun, Y.D., Joachimski, M.M., Wignall, P.B., Yan, C.B., Chen, Y.L., Jiang, H.S., Wang, L., Lai, X.L., 2012. Lethally hot temperatures during the Early Triassic greenhouse. Science 338, 366–370.

Formatted: Font:

2133 Tian, S.F., Chen, Z.Q., Huang, C.J., 2014. Orbital forcing and sea-level changes in the
2134 earliest Triassic of the Meishan section, South China. Journal of Earth Science 25,
2135 64-73.
2136 Tong, J.N., Yang, Y., 1998. Advance in the study of the Lower Triassic conodonts at
2137 Meishan section, Changxing, Zhejiang Province. Chinese Science Bulletin 43,
2138 1350–1353.
2139 Twitchett, R.J., 1999. Palaeoenvironments and faunal recovery after the end-Permian
2140 mass extinction. Palaeogeography, Palaeoclimatology, Palaeoecology 154, 27-37.
2141 Twitchett, R.J., 2006. The palaeoclimatology, palaeoecology and palaeoenvironmental
2142 analysis of mass extinction events. Palaeogeography, Palaeoclimatology,
2143 Palaeoecology 232, 190-213.
2144 Twitchett, R.J., Barras, C.G., 2004. Trace fossils in the aftermath of mass extinction
2145 events. In: McIlroy, D. (Ed.), Application of Ichnology to Palaeoenvironmental and
2146 Stratigraphic Analysis. Geological Society of London, Special Publication 228, pp.
2147 395-415.
2148 Twitchett, R.J., Krystyn, L., Baud, A., Wheeley, J.R., Richoz, S., 2004. Rapid marine
2149 recovery after the end-Permian mass-extinction event in the absence of marine

anoxia. Geology 32, 805-808.

Wang, C., Visscher, H., 2007. Abundance anomalies of aromatic biomarkers in the Permian–Triassic boundary section at Meishan, China—evidence of end-Permian terrestrial ecosystem collapse. Palaeogeography, Palaeoclimatology, Palaeoecology 252, 291–303.

Wang, Y., Sadler, P.M., Shen, S.Z., Erwin, D.H., Zhang, Y.C., Wang, X.D., Wang, W., Crowley, J.L., Henderson, C.M., 2014. Quantifying the process and abruptness of the end-Permian mass extinction. Paleobiology 40, 113-129.

Wignall, P.B., 2007. The end-Permian mass extinction—how bad did it get? Geobiology 5, 303–309.

Wignall, P.B., Hallam, A., 1993. Griesbachian (earliest Triassic) palaeoenvironmental changes in the Salt Range, Pakistan and southeast China and their bearing on the Permo–Triassic mass extinction. Palaeogeography, Palaeoclimatology, Palaeoecology 102, 215-37.

Wignall, P.B., Twitchett, R.J., 2002. Extent, duration and nature of the Permian-Triassic superanoxic event. Geological Society of America, Special Paper 356, 395-413.

Wignall, P.B., Morante, R., Newton, R., 1998. The Permo–Triassic transition in

Spitsbergen; δ^{3}Corg chemostratigraphy, Fe and S geochemistry, facies, fauna and trace fossils. Geological Magazine 135, 47-62.

Wignall, P.B., Newton, R., Brookfield, M.E., 2005. Pyrite framboid evidence for oxygen-poor deposition during the Permian–Triassic crisis in Kashmir. Palaeogeography, Palaeoclimatology, Palaeoecology 216, 183–188.

Wignall, P.B., Kershaw, S., Collin, P.Y., Crasquin-Soleau, S., 2009. Comment: erosional truncation of uppermost Permian shallow-marine carbonates and implications for Permian–Triassic boundary events. Geological Society of America, Bulletin 121, 954–956.

Williams, A., James, M.A., Emig, C.C., Mackay, S., Rhodes, M.C., Cohen, B.L., Gawthrop, A.B., Peck, L.S., Curry, G.B., Ansell, A.D., Cusack, M., Walton, D., Brunton, C.H.C., MacKinnon, D.I., Richardson, J.R., 1997. Treatise on Invertebrate Paleontology Part H, Brachiopoda, Revised, Volume 1: Introduction. The Geological Society of America and The University of Kansas, Boulder, Colorado and Lawrence, Kansas, 539 pp.

Wilson, M.A., Palmer, T.J., 1998. The earliest *Gastrochaenolites* (Early Pennsylvanian, Arkansas, USA): an upper Paleozoic bivalve boring? Journal of Paleontology, 72,

769–772.

Wu, H.C., Zhang, S.H., Hinnov, L.A., Jiang, G.Q., Feng, Q.L., Li, H.Y., Yang, T.S., 2013. Time-calibrated Milankovitch cycles for the Late Permian. Nature Communications 4, 2452.

Xie, S.C., Pancost, R.D., Yin, H.F., Wang, H.M., Evershed, R.P., 2005. Two episodes of microbial change coupled with Permo/Triassic faunal mass extinction. Nature 343, 494-497.

Xie, S., Pancost, R.D., Huang, J., Wignall, P.B., Yu, J., Tang, X., Chen, L., Huang, X., Lai, X., 2007. Changes in the global carbon cycle occurred as two episodes during the Permian–Triassic crisis. Geology 35, 1083–1086.

Xu, D.Y., Yan, Z., 1993. Carbon-isotope iridium event markers near the Permian-Triassic boundary in the Meishan section, Zhejiang Province, China. Palaeogeography, Palaeoclimatology, Palaeoecology 104, 171-176.

Yang, W., Jiang, N., 1981. Sedimentary features and microfacies of the Changhsing Formation and Permian-Triassic boundary. Bulletins of the Nanjing Institute of Geology and Palaeontology, Academia Sinica 2, 113-133.

Yang, Z., Yin, H., Wu, S., Yang, F., Ding, M., Xu, G., 1987. Permian-Triassic boundary

2201 stratigraphy and fauna of South China. Ministry of Geology and Mineral Resources,
2202 People's Republic of China, Geological Memoirs Series 2, Number 6. Geological
2203 Publishing House, Beijing, 379 pp.
2204 Yang, Z., Wu, S., Yin, H., Xu, G., Zhang, K., Bi, X., 1993. Permo-Triassic events of South
2205 China. Geological Publishing House, Beijing, 153 pp.
2206 Yin, H., Ding, M., Zhang, K., Tong, J., Yang, F., Lai, X., 1995. Dongwuan-Indosinian
2207 (Late Permian-Middle Triassic) Ecostratigraphy of the Yangtze Region and its
2208 Margins. Science Press, Beijing, 338 pp.
2209 Yin, H., Zhang, K., Tong, J., Yang, Z., Wu, S., 2001. The Global Stratotype Section and
2210 Point (GSSP) of the Permian-Triassic Boundary. Episodes 24(2), 102-114.
2211 Yin, H., Sweet, W.C., Glenister, B.F., Kotlyar, G., Kozur, H., Newell, N.D., Sheng, J.,
2212 Yang, Z. and Zakharov, Y.D., 1996, Recommendation of the Meishan section as
2213 Global Stratotype Section and Point for basal boundary of Triassic System:
2214 Newsletter on Stratigraphy 34, 81–108.
2215 Yin, H.F., Feng, Q.L., Lai, X.L., Baud, A., Tong, J.N., 2007a. The protracted
2216 Permo-Triassic crisis and multi-episode extinction around the Permian-Triassic
2217 boundary. Global and Planetary Change 55, 1-20.

2218 Yin, H.F., Huang, S.J., Zhang, K.X., Hansen, H.J., Yang, F.Q., Ding, M.H., Bie, X.M.,
2219 1992, The effects of volcanism on the Permo-Triassic mass extinction in South
2220 China, *in* Sweet, W.C., Yang, Z.Y, Dickins, J.M., Yin, H.F. (eds), Permo-Triassic
2221 Events in the Eastern Tethys. Cambridge, UK, Cambridge University Press, p.
2222 169-174.
2223 Yin, H.F., Xie, S., Luo, G., Algeo, T.J., Zhang, K., 2012. Two episodes of environmental
2224 change at the Permian-Triassic boundary of the GSSP section Meishan.
2225 Earth-Science Reviews 115, 163-172.
2226 Yin, H.F., Jiang, H.S., Xia, W.C., Feng, Q.L., Zhang, N., Shen, J., 2014. The end-Permian
2227 regression in South China and its implication on mass extinction. Earth-Science
2228 Reviews 137, 19-33 ~~(in press)~~.
2229 Yuan, D.X., Shen, S.Z., Henderson, C.M., Chen, J., Zhang, H., Feng, H.Z., 2014. Revised
2230 conodont-based integrated high-resolution timescale for the Changhsingian Stage
2231 and end-Permian extinction interval at the Meishan sections, South China. Lithos
2232 204, 220-245~~(in press), doi.10.1016/j.lithos.2014.03.026~~.
2233 Zeebe, R.E., Zachos, J.C., Dickens, G.R., 2009. Carbon dioxide forcing alone insufficient
2234 to explain Palaeocene–Eocene thermal maximum warming. Nature Geoscience 2,

576–580.

Zhang, H., Shen, S.Z., Cao, C.Q., Zheng, Q.F., 2014. Origins of microspherules from the Permian-Triassic boundary event layers in South China. Lithos ~~(in press)~~204, 246-257~~doi.10.1016/j.lithos.2014.02.018~~.

Zhang, K.X., Lai, X.L., Tong, J.N., Jiang, H.S., 2009. Progresses on study of conodont sequence for the GSSP section at Meishan, Changxing, Zhejiang Province, South China. Acta Palaeontologica Sinica 48, 485-495.

Zhang, K.X., Tong, J.N., Shi, G.R., Lai, L.X., Peng, Y.Q., Yu, J.X., He, W., Jin, Y.L., 2007. Early Triassic conodont-palynological biostratigraphy of the Meishan D section in Changxing, Zhejiang Province, South China. Palaeogeography, Palaeoclimatology, Palaeoecology 252, 4–23

Zhang, K.X., Tong, J.N., Yin, H.F., Wu, S.B., 1997. Sequence stratigraphy of the Permian-Triassic boundary section of Changxing, Zhejiang, Southern China. Acta Geologica Sinica 71, 90-103.

Zhang, K.X., Tong, J.N., Hou, G.J., Wu, S.B., Zhu, Y.H., Lin, Q.X., 2005. Regional Geological report, the People's Republic of China (Meishanzhen Map H50E006023, Changxingian Map, H50E006024, Scale:1:50000). University of Geosciences Press,

264 pp., Wuhan, China.

Zhao, J., Sheng, J., Yao, Z., Liang, X., Chen, C., Rui, L., Liao, Z., 1981. The Changhsingian and Permian-Triassic boundary of South China, Bulletin of the Nanjing Institute of Geology and Palaeontology, Academia Sinica 2, 1-95.

Zhao, X.M., Tong, J.N., 2010. Two episodic changes of trace fossils through the Permian-Triassic transition in the Meishan section cores, Zhejiang Province, Science China, Earth Science 40, 1241-1249.

Zheng, Q.F., Cao, C.Q., Zhang, M.Y., 2013. Sedimentary features of the Permian-Triassic boundary sequence of the Meishan section in Changxing County, Zhejiang Province. Science China, Earth Sciences 56, 956-969.

Zhao, L., Chen, Y., Chen, Z.Q., Cao, L., 2013b. Uppermost Permian to Lower Triassic conodont zonation from Three Gorges area, South China. Palaios 28, 523-540.

Zhao, L., Chen, Z.Q., Algeo, T.J., Chen, J., Chen, Y., Tong, J., Gao, S., Zhou, L., Hu, Z., Liu, Y., 2013a. Rare-earth element patterns in conodont albid crowns: Evidence for massive inputs of volcanic ash during the latest Permian biocrisis? Global and Planetary Change 105, 135-151.

Zonneveld, J.-P., Gingras, M.K., Beatty, T.W., 2010. Diverse ichnofossil assemblage

following the P–T mass extinction, Lower Triassic, Alberta and British Columbia, Canada: evidence for shallow marine refugia on the northwestern coast of Pangaea. Palaios 25, 368–392.

Figure captions

Fig. 1. The GSSP for the Permian-Triassic boundary at Meishan, ~~,~~Changxing county, northwestern Zhejiang Province, east China. A, location of the Meishan section. B, close-up of the white volcanic ash bed (Bed 25) in Meishan. C, geopark of the GSSP Meishan showing GSSP position at the Meishan section D. D, the P-Tr boundary beds showing biostratigraphic boundary through the mid-Bed 27 and the mass extinction horizon at the base of Bed 25. E, outcrop of the P-Tr boundary beds and Yinkeng Formation along strike on the Meishan hill from the geopark section.

Fig. 2. Biostratigraphy of the P-Tr transition at the Meishan section with the updated conodont zones and correlations with ammonoid, bivalve, brachiopod and microfloral assemblages from Meishan as well as conodont zones from North Italy, Iran and

Germany, and India. Note that the updated conodont zonation is revised from those documented by Jiang et al. (2007) and Zhang et al. (2009) and our new observations. White arrows indicate that conodont zones extend to horizons below Bed 22 of Meishan and its equivalents.

Fig. 3. P-Tr succession exposed in the GSSP Meishan showing lithology, facies types, depositional environments, stratigraphic distributions of trace fossils, and bioturbation levels. Ichnofabric indices (ii: Droser and Bottjer, 1986) are assessed as 1 to 6, indicating bioturbation from lowest to highest levels. Bedding plane bioturbation index (bpbi) is evaluated based on bedding plane coverage of burrows (Miller and Smail, 1997). Facies symbols: om = offshore mudstone facies, bs = basinal black shale facies, ow = offshore wackestone facies, os = offshore siltstone facies; ew = epeiric sea wackestone facies, HCS = hummocky cross stratification, hb = horizontal bedding. Depositional environment (DE): ns = nearshore, fw = fair-weather wave base, sw = subtidal zone to fair-weather wave base, swb = storm wavebase.

Fig. 4. Lithology and fossils from the exposure of the P-Tr transition in Meishan. A-B, D, field photograph, polished surface and microphotograph showing hummocky cross-stratified (HCS) muddy limestone (Bed 54), upper Yinkeng Formation; pen is 15

cm long; scale bars are 2 cm. C, pale mudstone and calcareous mudstone (Bed 41) showing horizontal stratification, lower Yinkeng Formation; pen is 15 cm long. E, F, I, ammonoid fossils across the P-Tr boundary with large ammonoid shell (E) in Bed 24e of the Changhsing Formation contrasting to small shells (F, I) recorded in the middle and upper Yinkeng Formation; coins are 1.5 cm in diameter; scale bar is 1 cm. G, dark thin-bedded limestone interbedded with bioclastic limestone bands, Bed 24e; pen is 10 cm long. H, irregular contact between Beds 24d and 24e; cross-bedding is pronounced in the uppermost Bed 24d; scale bar is 1 cm. J, vertical burrow of *Balanoglossites* in the upper part of Bed 24d; scale bar is 1.5 cm.

Fig.5. Microfacies and fossil fragment assemblages from Beds 23-~~24~~26, upper Changhsing Formation. A, microphotograph of claystone, Bed 25. B, microphotograph showing horizontal laminae (black arrow) of black shale, Bed 26. C, bioclastic packstone of Bed 23a showing brachiopod (b), crinoid~~s~~ (c), and ostracod~~s~~ (o) fragments. D, ~~Bioclastic~~ bioclastic packstone of Bed 24c showing abundant foraminifer (f), brachiopod (b), crinoid~~s~~ (c), ostracod~~s~~ (o) and other fragments.

Fig. 6. Pie diagrams showing percentage of major components in all rocks sampled from Beds 22-60 in Meishan. Detailed fossil fragment contents (%) of each sample are

tabulated in Table 3. Component symbols: 1 = foraminifers, 2 = ostracods, 3 = crinoids, 4 = echinoids, 5 = brachiopods, 6 = bryozoans, 7 = sponge spicules, 8 = calcareous sponges, 9 = gastropods, 10 = radiolarians, 11 = macroalgae, 12 = micrites, 13 = cavities, 14 = other particles (fecal pellets, peloids, pyrites and undetermined particles).

Fig.7. Microfacies across the boundary between Beds 24e-5 and 24e-6. A, transverse view of one sponge spicule. B-C, cross-section view of sponge spicules. D, microphotograph showing the laminated horizon separating bioclastic layer (Bed 24e-5) from the overlying sponge spicule-rich layer (Bed 24e-6). E, SEM image of one isolated specimen of a sponge spicule. B-C, scale bars are both 50μm; E, Scale bar is 40 μm.

Fig. 8. Microfacies and fossil fragment assemblages from Bed 26b, 8-10 cm above the base of Bed 25. A, microphotograph showing foraminifer (f), bryozoan (bry), echinoid (e), and brachiopod (bra) fragments. ~~A, microphotograph showing froaminifer (f), bryozoan (bry), echinoid (e), and brachiopod (bra) fragments.~~ B, microphotograph showing ostracod (o), echinoid (e), and brachiopod (bra) fragments. C, microphotograph showing brachiopod (bra) and echinoid (e) fragments. D, microphotograph showing bryozoan (bry) and brachiopod (bra) fragments. E, microphotograph showing foraminifer (f) and echinoid (e) fragments. F, microphotograph showing brachiopod (bra) and

2337 foraminifer (f) fragments. G, microphotograph showing foraminifer (f) and echinoid (e)
2338 fragments. H, microphotograph showing bryozoan (bry) and foraminifer (f) fragments. I,
2339 microphotograph showing foraminifer (f) and echinoid (e) fragments. J,
2340 microphotograph showing foraminifer (f) fragments. K, microphotograph showing
2341 bryozoan (bry) and echinoid (e) fragments. L, microphotograph showing foraminifer (f)
2342 and echinoid (e) fragments. All scale bars are all 100 μm.
2343 **Fig. 9**. Polished surface of Bed 27 and its microfacies features. A, polished surface
2344 showing the entire bed is subdivided into four parts (labelled a, b, c, d) by two sets of
2345 pronounced irregular surfaces, in which burrows (red arrows) are commonly present. B,
2346 microphotograph of the basal part of Bed 27a, 11-13 cm above the base of Bed 25,
2347 showing foraminifer (f) and brachiopod (bra) fragments. C, microphotograph of the
2348 upper part of Bed 27a, 13-15 cm above the base of Bed 25, showing foraminifers (f) and
2349 other fossil fragments. D, microphotograph of the lower part of Bed 27b, 15-17 cm above
2350 the base of Bed 25, showing claystone-dominated texture. E, microphotograph of the
2351 upper part of Bed 27b, 18-20 cm above the base of Bed 25, showing echinoid (e) and
2352 other fossil fragments. F, microphotograph of the upper part of Bed 27c, 21-23 cm above
2353 the base of Bed 25, showing abundant foraminifer (f), echinoid (e) and brachiopod (bra)

fragments. G, microphotograph of Bed 27d, 23-28 cm above the base of Bed 25, showing abundant ostracods (o), foraminifers (f), echinoid (e), and other fragments. H, microphotograph of the upper part of Bed 26b, 8-10 cm above the base of Bed 25, showing abundant foraminifer (f) and other fossil fragments.

Fig. 10. Bioclastic packstone to wackestone showing various fossil fragments from Bed 27a, 13-15 cm above the base of Bed 25. A, foraminifer (f). B, brachiopod (bra) and other fragments. C, foraminifer (f), echinoid (e) and other undetermined fragments. D, foraminifer (f). E, foraminifer (f). F, foraminifer (f), brachiopod (b) and other undetermined fragments. G, I-K, foraminifer tests. H, echinoid (e) fragment. Scale bars are all 50 μm.

Fig. 11. Bioclastic packstone and various fossil fragments from Bed 27c, 21-23 cm above the base of Bed 25. A, foraminifer (f) and brachiopod (bra) fragments. B, foraminifer *Frodina permica* test. C, echinoid (e) and brachiopod (b) fragments; D, bryozoan (bry) , foraminifer (f) and other undetermined fragments. E, foraminifer (f) *Nodosinelloides netschajewi* test and echinoid (e) fragments. F, foraminifer test of *Hemigordius* sp. G, brachiopod (bra) fragment. H, bryozoan (bry) fragment. I, foraminifer (f) *Hemigordius* sp. test. J, foraminiferal (f) fragment. K, echinoid (e) and foraminifer (f) fragments. L-M,

2371 echinoid fragments. Scale bars are all 50 μm.

2372 **Fig. 12**. Bioclastic packstone to wackestone showing various fossil fragments from Bed
2373 27d, 23-28 cm above the base of Bed 25. A, foraminifer test of *Nodosinelloides* sp. B,
2374 brachiopod (b), foraminifer (f), and echinoid (e) fragments. C-D, foraminifer tests of
2375 *Nodosinelloides* sp. and *Nodosaria* sp., respectively. E, brachiopod (bra), foraminifer (f),
2376 and other fragments. F, echinoid fragment. G, sponge spicule. H, foraminiferal fragment
2377 of *Tuberitina maljavkini*. I, echinoid fragment. J, brachiopod (bra) and sponge spicule (ss);
2378 K, foraminifer test of *Nodosinelloides* sp. L, foraminifer Nodosinelloides aequiampla and
2379 brachiopod (bra) fragments. M, foraminifer (f) fragment. N, ostracod (o), foraminifer (f),
2380 and echinoid (e) fragments. O, brachiopod (bra) and echinoid (e) fragments; P,
2381 brachiopod (bra) and echinod (e) fragments. B, scale bar is 100 μm; F-G, scale bars are
2382 20μm-; other scale bars are all 50 μm.

2383 **Fig. 13**. Microfacies and fossil fragment assemblage from strata of Bed 29 and above. A,
2384 bioclastic wackestone with ostracod (o) and brachiopod (bra) fragments, Bed 29. B,
2385 bioclastic wackestone with brachiopod (bra) and ostracod (o) fragments, Bed 29. C,
2386 echinoid fragment, Bed 53. D, ostracods test, Bed 52. F, ostracod test, Bed 53. I, K, M,
2387 ostracods tests, Bed 54. N, ostracods test, Bed 55. P-R, ostracod tests, Beds 56, 57 and 58,

2388 respectively. E, foraminifer fragment, Bed 29. J, L, foraminifer fragments, Beds 52 and

2389 53, respectively. G, foraminifer *Nodosaria* sp., Bed 56. H, foraminifer *Nodosaria*

2390 *rostrata* Trifonova, Bed 56. O, micrite containing pyrite particles (black) and tiny tubes

2391 (t), Bed 44. Scale bars are all 50 μm.

2392 **Fig. 14**. Fossil fragment distributions over the P-Tr transition (Beds 22-60) in Meishan.

2393 Vertical axis represents percentage of various fossil fragments in all rock.

2394 **Fig. 15**. Shell beds from the Yinkeng Formation in Meishan. A, *Claraia* concentrations

2395 (white arrows) from Bed 40; scale bar is 1 cm; B, shell concretions of *Claraia griesbachi*

2396 (c) and *Ophiceras* sp. (o) of the *O-P* community from Bed 32; coin is 1.5 cm in diameter;

2397 C, shell concretions of *Claraia griesbachi* from Bed 35; coin is 1.5 cm in diameter; D,

2398 shell concretions of *Claraia wangi* of the *C* community from Bed 40; coin is 1.5 cm in

2399 diameter; E, shell concretions of *Claraia griesbachi* from Bed 36; coin is 1.5 cm in

2400 diameter; F, shell concretions of *Meishanorhynchia* (m), *Lytophiceras* (ly) and

2401 ophiceratid (o) of the *M-L* community from Bed 55; Scale bar is 4 mm.

2402 **Fig. 16**. Trace fossils from the Changhsing Formation of the Meishan section. A, D,

2403 *Thalassinoides* sp. 1 on base of Bed 8; coin is 1.5 cm; B, *Paleophycus* isp. from Bed 9;

2404 scale bar is 1 cm; C, *Balanoglossites triadicus* from Bed 24d; coin is 1.5 cm in diameter;

2405 E, *Taenidium* isp. from upper surface of Bed 24d; coin is 1.5 cm in diameter; F, *Lockeia*

2406 isp. on the upper surface of Bed 9; coin is 1.5 cm in diameter.

2407 **Fig. 17**. Trace fossils from the Changhsing Formation (Beds23-24) continued. A, E,

2408 horizontal burrows of *Planolites* isp. 1 from upper surface of Bed 24e-6; USB is 2 cm

2409 long; B-C, problematica from upper surface of Bed 23; Coins are 1.5 cm in diameter; D,

2410 *Taenidium* isp. from upper surface of Bed 24e; Coin is 1.5 cm in diameter; F,

2411 *Dendrorhaphe* isp. from upper surface of Bed 23; Coin is 1.5 cm in diameter.

2412 **Fig. 18**. Trace fossils from the Yinkeng Formation. A-B, F, *Planolites* from upper

2413 surfaces of Bed 36, 41, and 56, respectively; coins are 1.5 cm, 2 cm and 1.5 cm in

2414 diameter, respectively; C, *Chondrites* isp. on upper surface of Bed 52; Coin is 1.5 cm in

2415 diameter; D-E, *Thalassionoides* isp. 3 from upper surfaces of Bed 53 and 56, respectively;

2416 coins are 1.5 in diameter; G-H, sketch reconstruction and trace of *Treptichnus* isp. on

2417 upper surface of Bed 57; coin is 1.5 cm in diameter.

2418 **Fig. 19**. Polished slabs and sketches showing the successions of trace-fossil assemblages

2419 in Bed 27. A–C, vertical cross section of Bed 27 showing the ichnofabric change from a

2420 firmground ichnocoenoses of *Glossifungites* ichnofacies in the lower to a softground

2421 ichnocoenose in the upper. Note these three sample blocks (A-C) were cut from one

2422 complete sample of Bed 27. D–F, portraits of blocks A–C, respectively. Ar. = *Arenicolites*

2423 isp., Ch. = *Chondrites* isp. 1, Ga. = *Gastrochaenolites* isp., Pa. = *Planolites* isp. 2, Ps. =

2424 *Psilonichnus*; isp., Th. = *Thalassinoides* isp. 2.

2425 **Fig. 20**. Polished surface and its portrait of Bed 27 showing burrow systems in

2426 firmground of the *Glossifungites* ichnofacies and vertical colonization by ichnofaunas on

2427 different substrates. A, polished slab across the entire Bed 27 (from base to top). B, sketch

2428 reconstruction showing ichnofabrics manifested in Fig. 25A. C, cartoon reconstruction

2429 showing the generalized colonization zonation of ichnofaunas. For abbreviations of

2430 ichnotaxon names see caption of Fig. 19.

2431 **Fig. 21**. Trace fossil evolution at Meishan. A, ichnodiversity change throughout the

2432 uppermost Changhsingian to Griesbachian in Meishan. B, burrow size variations (in

2433 mean diameter and maximum diameter) over the P-Tr transition. C, tiering level change

2434 through the P-Tr transition.

2435 **Fig. 22**. Burrow sizes of selected ichnogenera through the P-Tr transition. A, burrow size

2436 variation of *Planolites* through the P-Tr transition. B, burrow size variation of

2437 *Thalassinoides* through the P-Tr transition. C, burrow sizes of both *Dendrorhaphe* and

2438 problematic trace from the upper Changhsing Formation. D, burrow sizes of

2439 *Balanoglossites*, *Taenidium*, *Chondrites*, and *Treptichnus* from the P-Tr transition in

2440 Meishan.

2441 **Fig. 23**. Pyrite framboids and crystals preserved on fossil skeletons and in sediments of

2442 Bed 27. A-C, pyrite crystals (white arrows) on brachiopod shells of *Paryphella*. D-E,

2443 pyrite crystals (white arrows) preserved in sediments and foraminiferal test; scale bars are

2444 40 μm; F-G, pyrite crystals (white arrows) preserved in foraminiferal tests; scale bars are

2445 all 40 μm. H, L, SEM images showing pyrite framboids preserved on brachiopod shells

2446 of Bed 27; I-K, pyrite framboids preserved in sediments of Bed 27; M-N, EDS results

2447 showing mineral composition of framboids of Fig. 23L and Fig. 23J, respectively.

2448 **Fig. 24**. Sizes of pyrite framboids from 17 horizons through the P-Tr transition in

2449 Meishan. MD = mean diameter, SD = standard derivation, N = Number of framboid

2450 grains.

2451 **Fig. 25**. Redox conditions indicated by pyrite framboid sizes through the P-Tr transition

2452 at Meishan. Two SEM images show morphologies of pyrite framboids from Bed 24 (left)

2453 and Bed 39 (right). PTB = Permo-Triassic boundary; PTME = Permo-Triassic mass

2454 extinction.

2455 **Fig. 26**. Composite figure showing exceptionally increased seawater surface temperature,

carbon isotopic excursion, Chemical index of alternation (CIA) and Eu/Eu* profiles, through the P-Tr transition at Meishan. Total organic content (TOC) and Ce/Ce* profiles, framboid size variation, specific and generic richness variations, and community structural changes indicated by true diversity index (Exp (H)) and dominance (D) through the P-Tr transition in Meishan. Note: seawater temperature data after Joachimski et al. (2012) and Sun et al. (2012); CIA value is calculated using published data by Zhang et al. (2005); Carbon isotopic excursion after Burgess et al. (2014); Eu/Eu* and Ce/Ce* values after Zhao et al. (2013a). TOC profile after Yin et al. (2012). Framboid size data from this study. Detailed bioturbation data see Fig. 3; II = Ichnofabric indices; BPBI = Bedding plane bioturbation index. Datum source of burrow diameters sees Fig. 24. More details of fossil fragment contents see Fig. 14. Species and genus richness data after Song et al. (2013a). Community structure data from Chen et al. (2010a).

Table captions

Table 1. Radiometric ages obtained from the P-Tr succession at the GSSP Meishan (in Ma).

2473 Table 2. Key conodont zones with their durations across the PTB in Meishan.

2474 Table 3. Percentage of major components in all rocks sampled from Beds 22-60 in

2475 Meishan.

2476 Table 4. X-ray diffraction (XRD) data of the PTB beds at Meishan (sourced from Liang,

2477 2002).

2478 Table 5. Structural indices of the latest Permian to earliest Triassic shelly communities

2479 from Meishan (Chen et al., 2010a).

2480 Table 6. Major indices showing community structural changes over the P-Tr transition in

2481 Meishan

2482 Table 7. Characteristics of major trace fossils from the uppermost Permian to lowest

2483 Triassic in Meishan

2484

Figure 1

Click here to download high resolution image

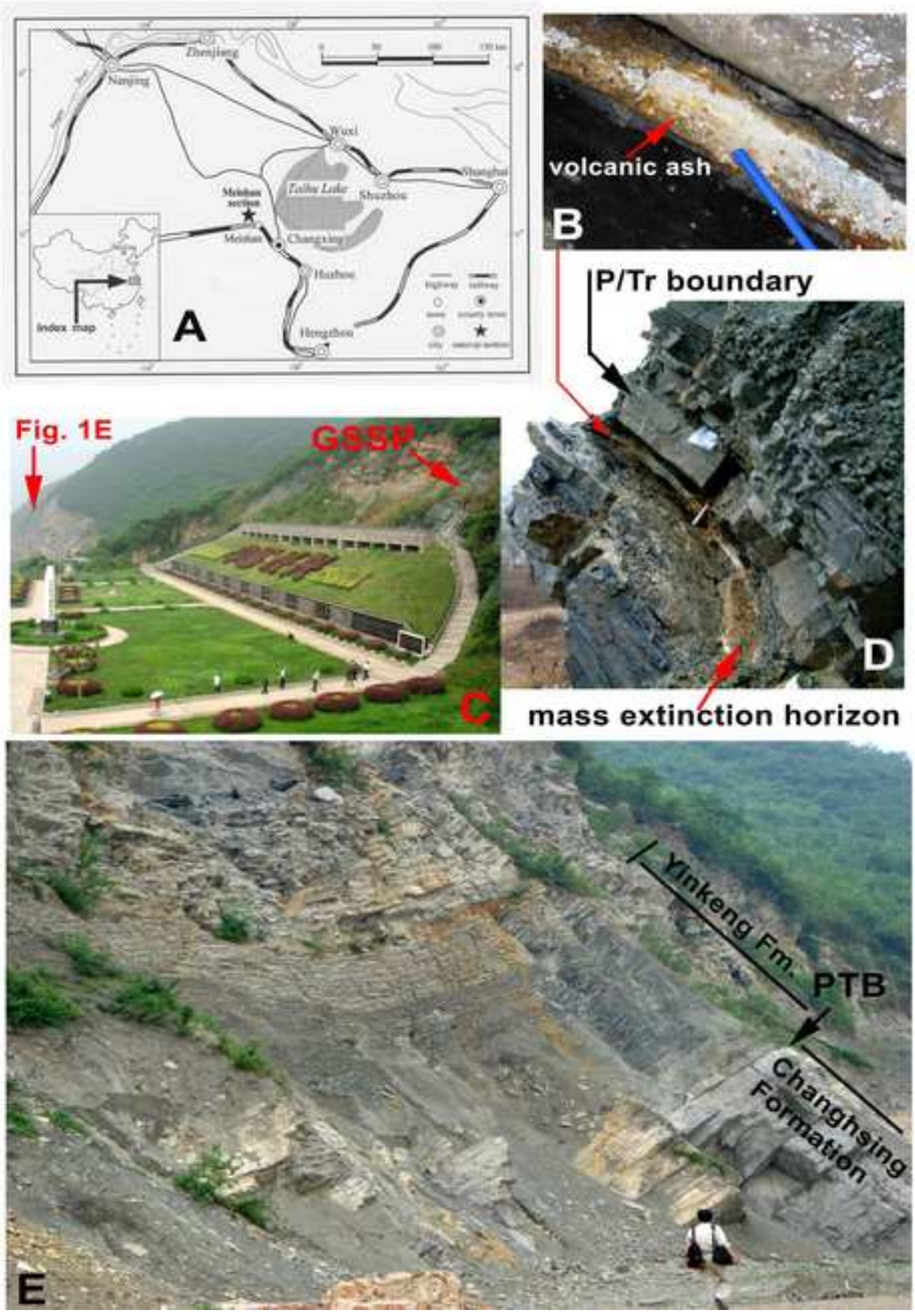

Figure 2

Click here to download high resolution image

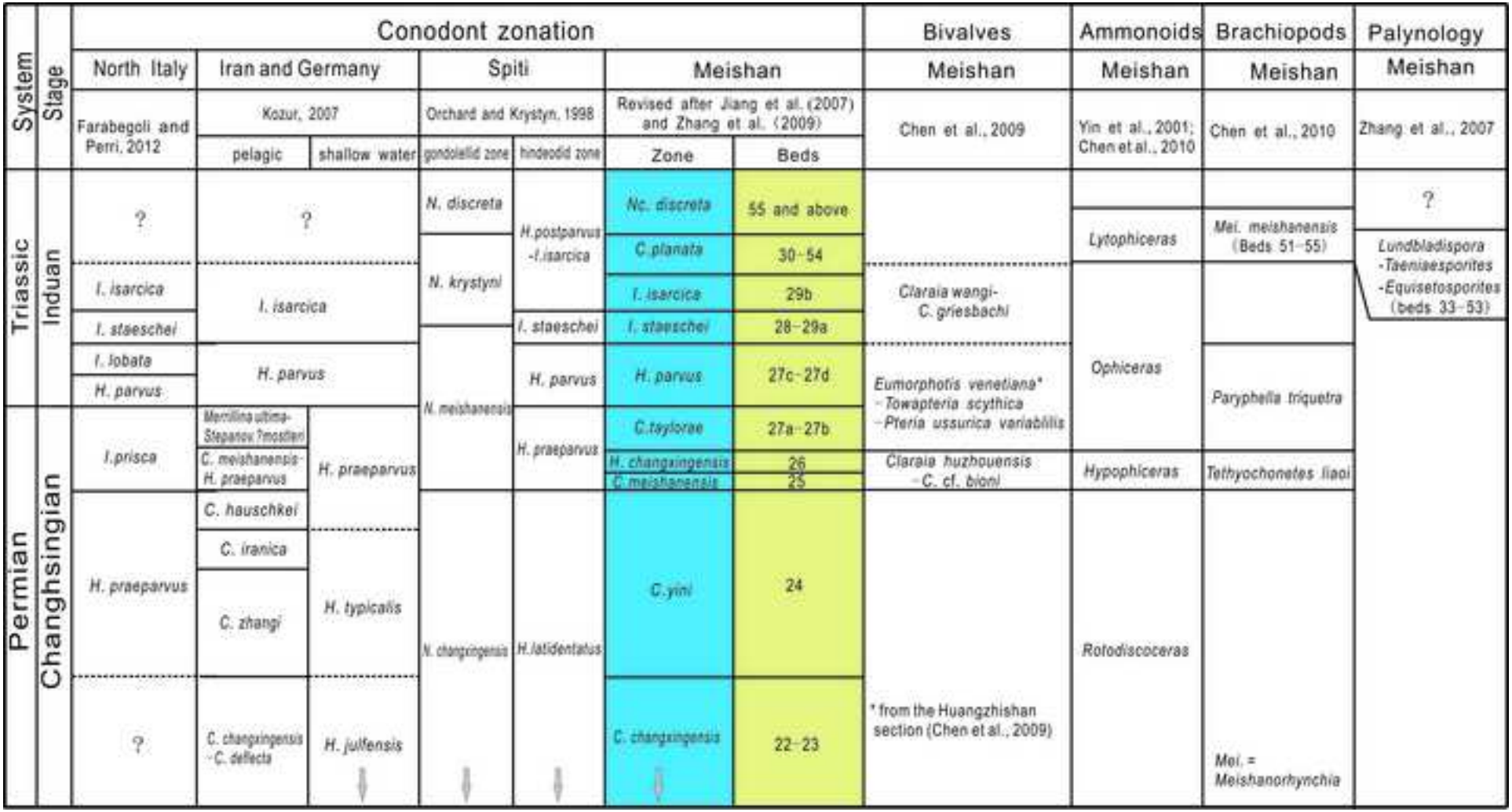

Figure 3

Click here to download high resolution image

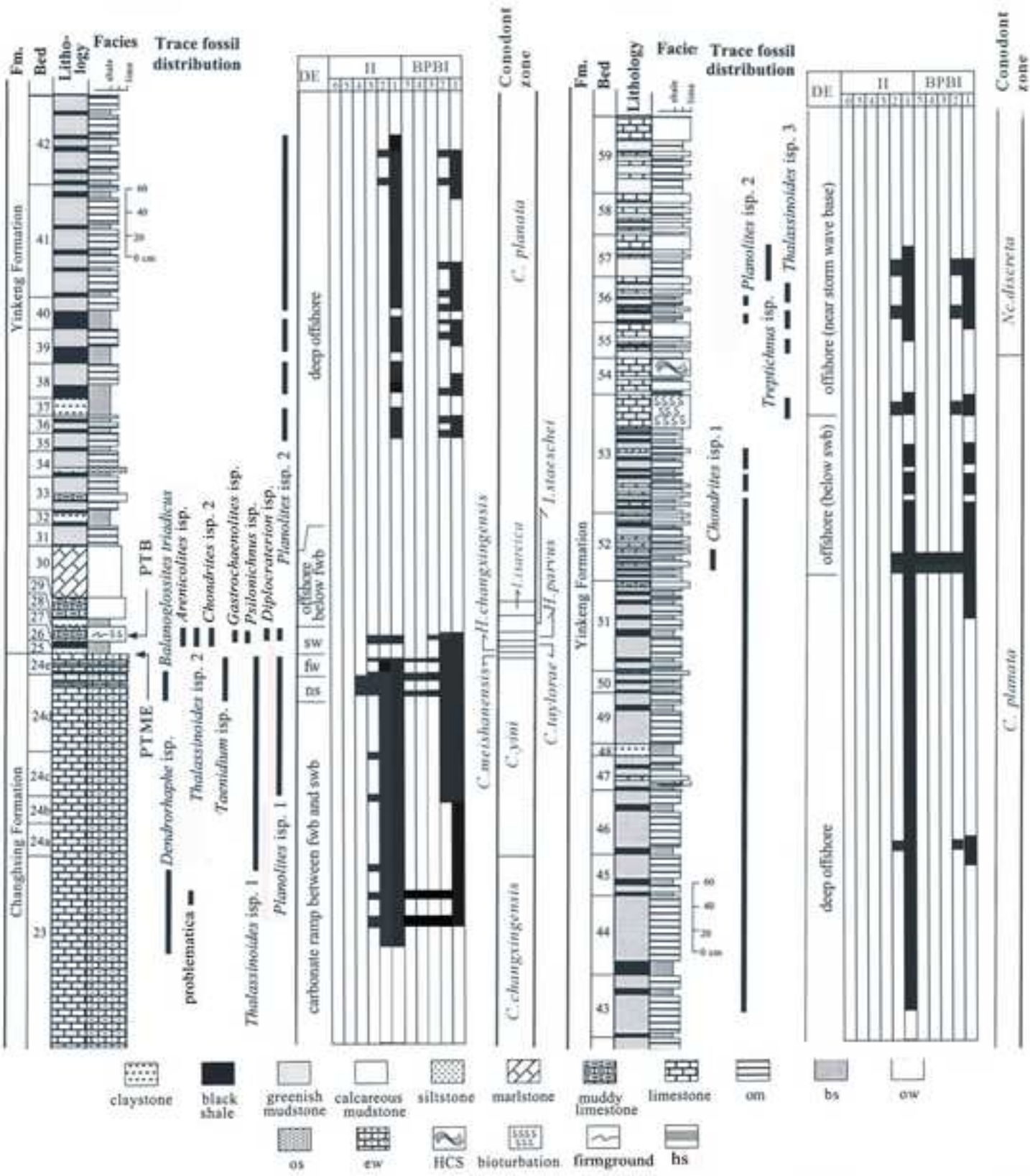

Figure 4

Click here to download high resolution image

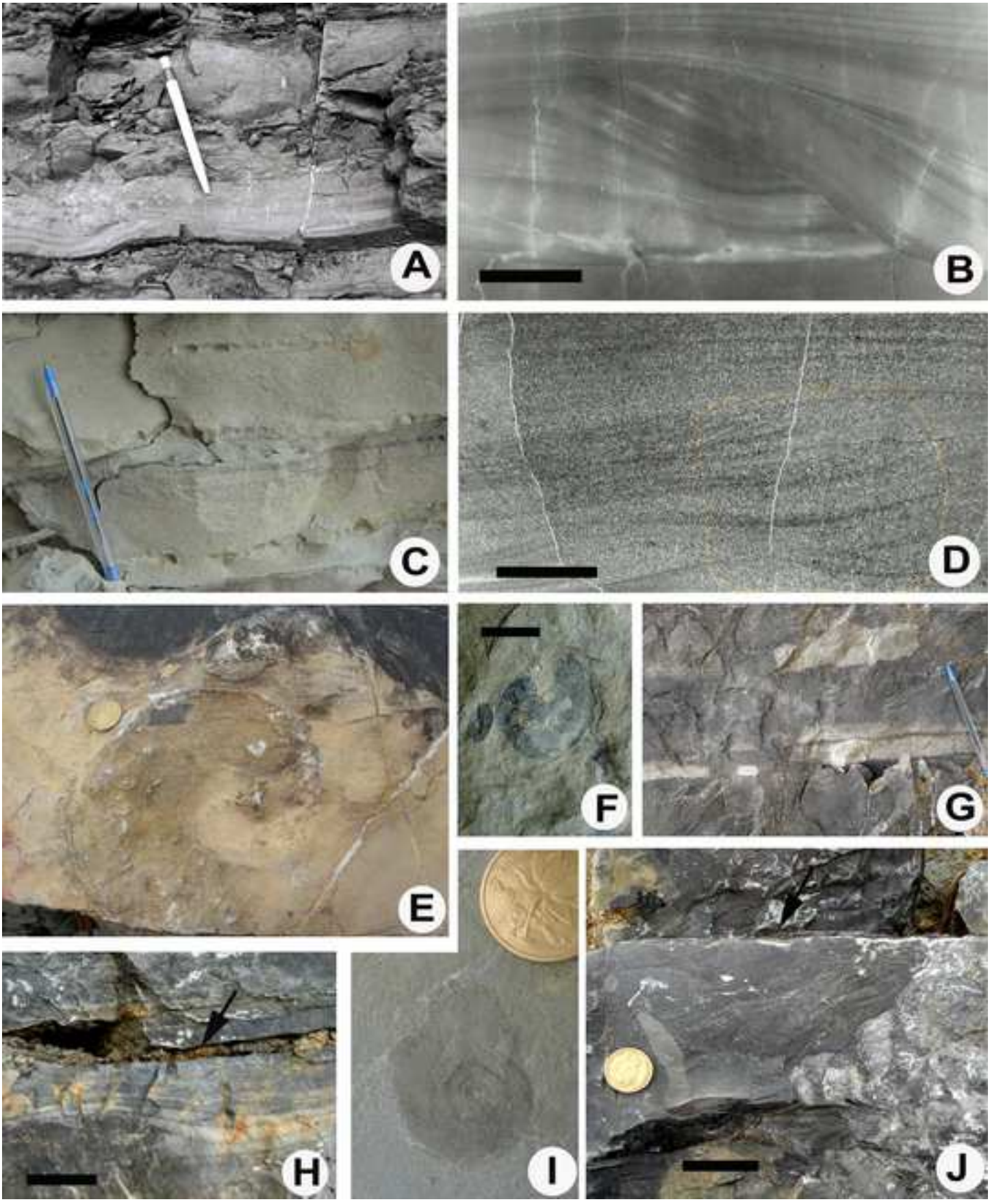

Figure 5

Click here to download high resolution image

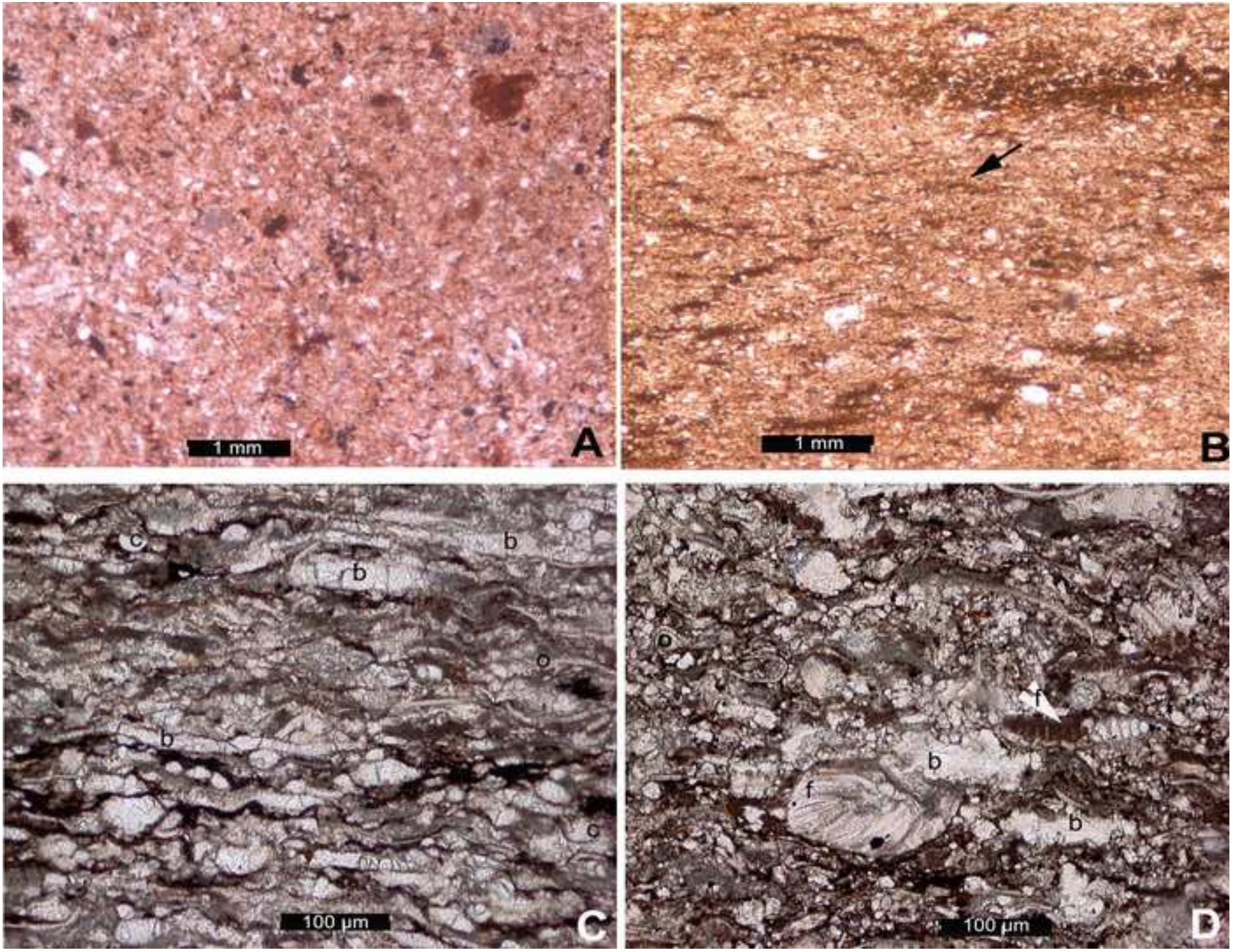

Figure 6

Click here to download high resolution image

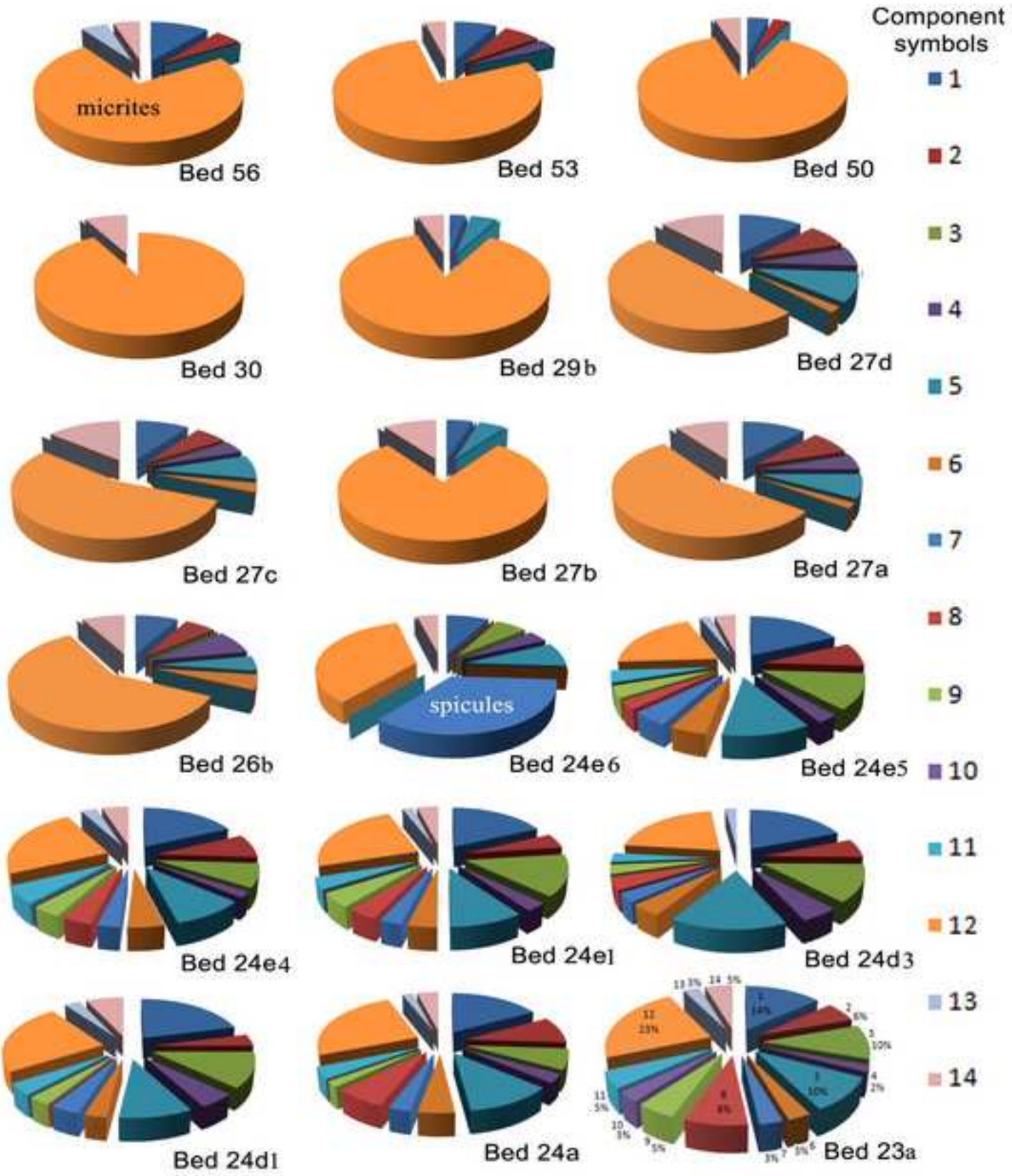

Figure 7

Click here to download high resolution image

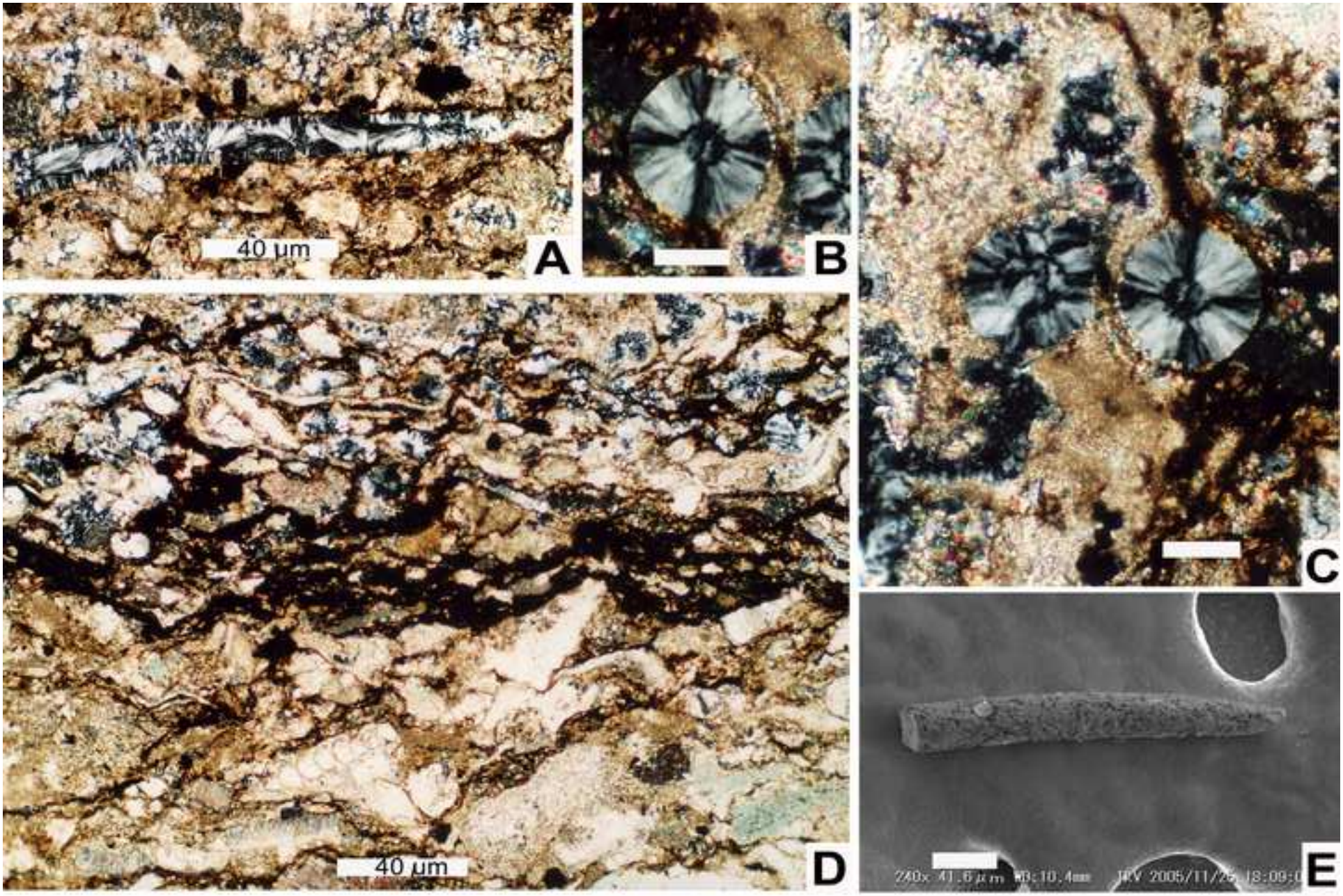

Figure 8

Click here to download high resolution image

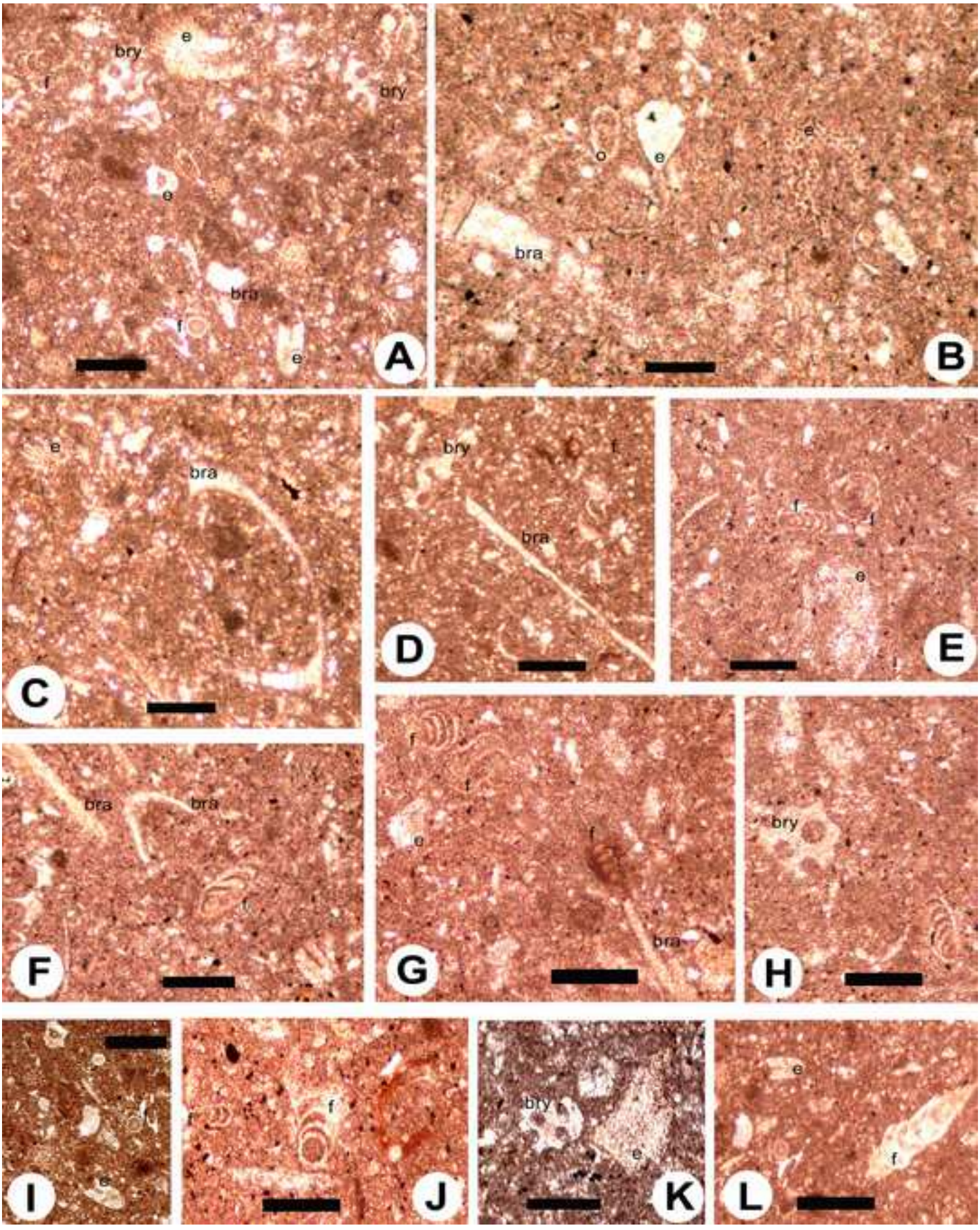

Figure 9
Click here to download high resolution image

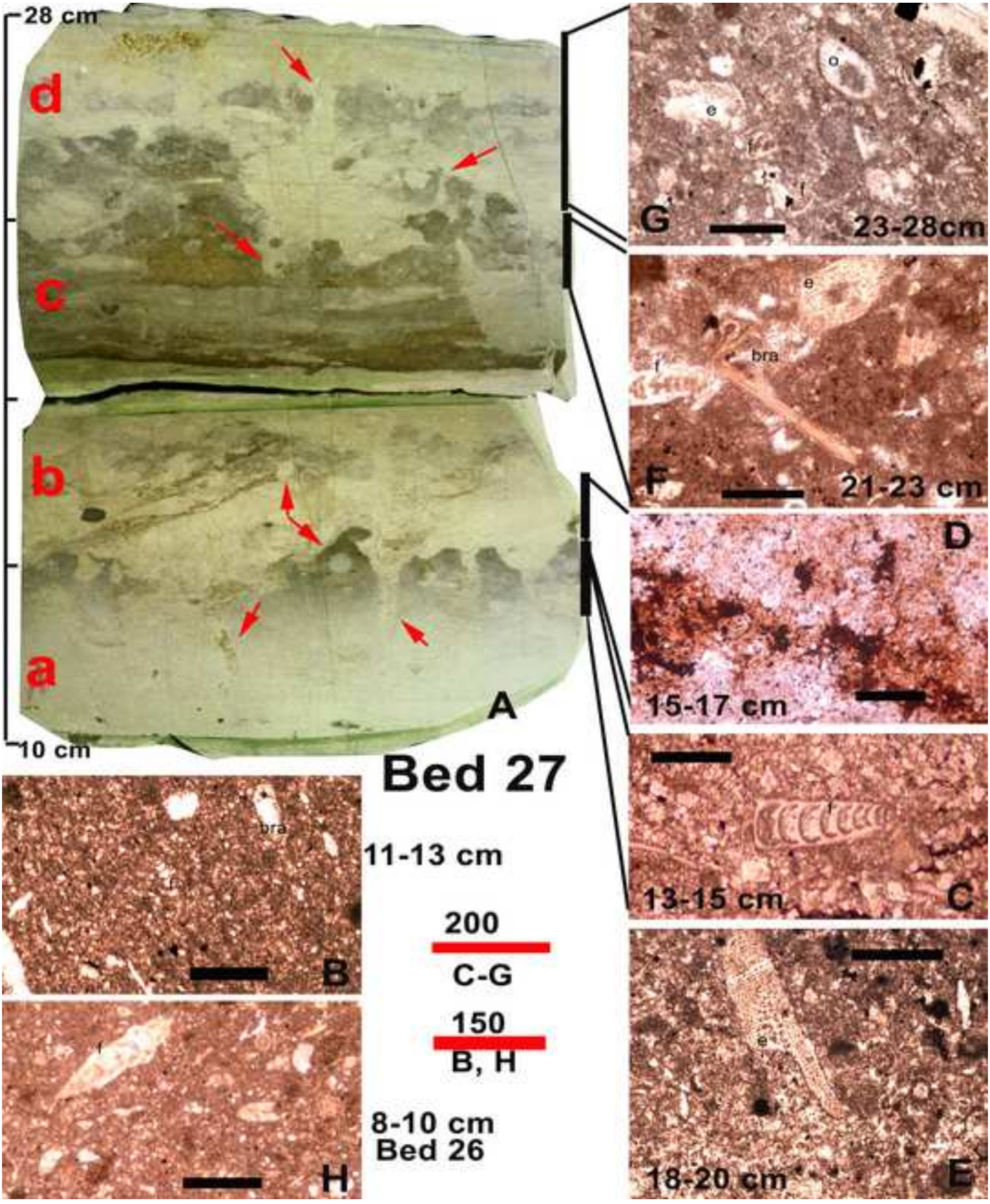

Figure 10

Click here to download high resolution image

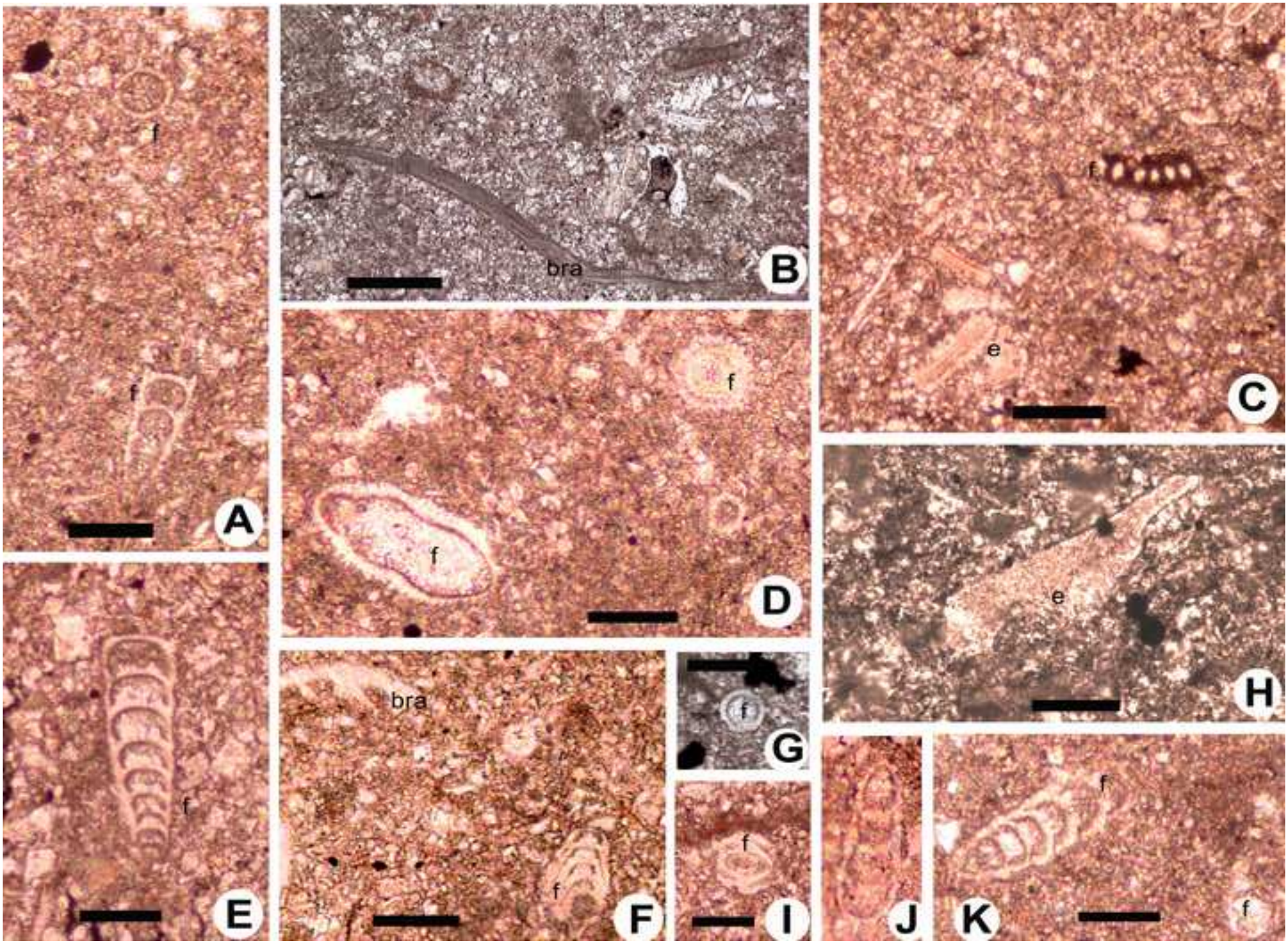

Figure 11

Click here to download high resolution image

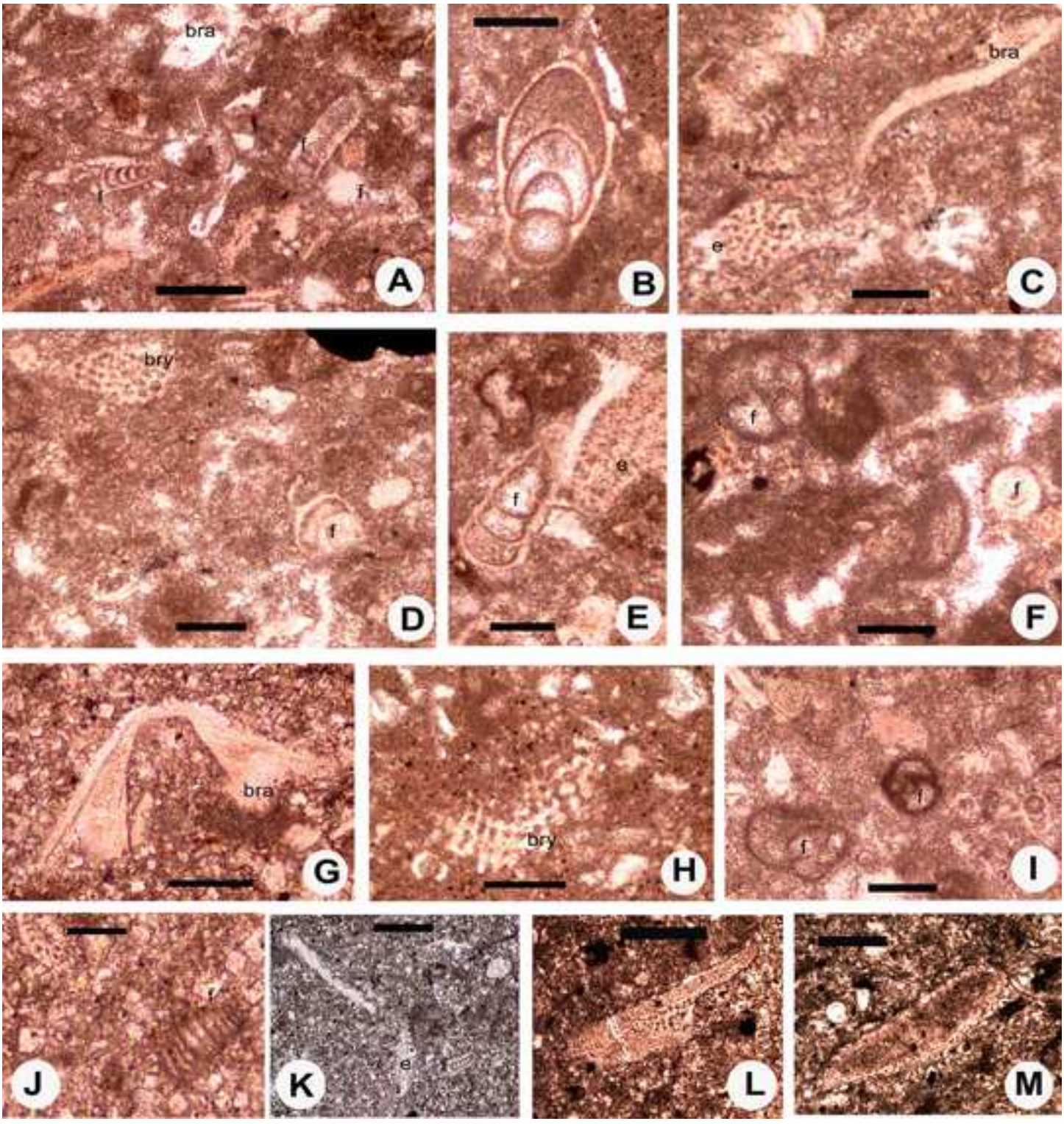

Figure 12

Click here to download high resolution image

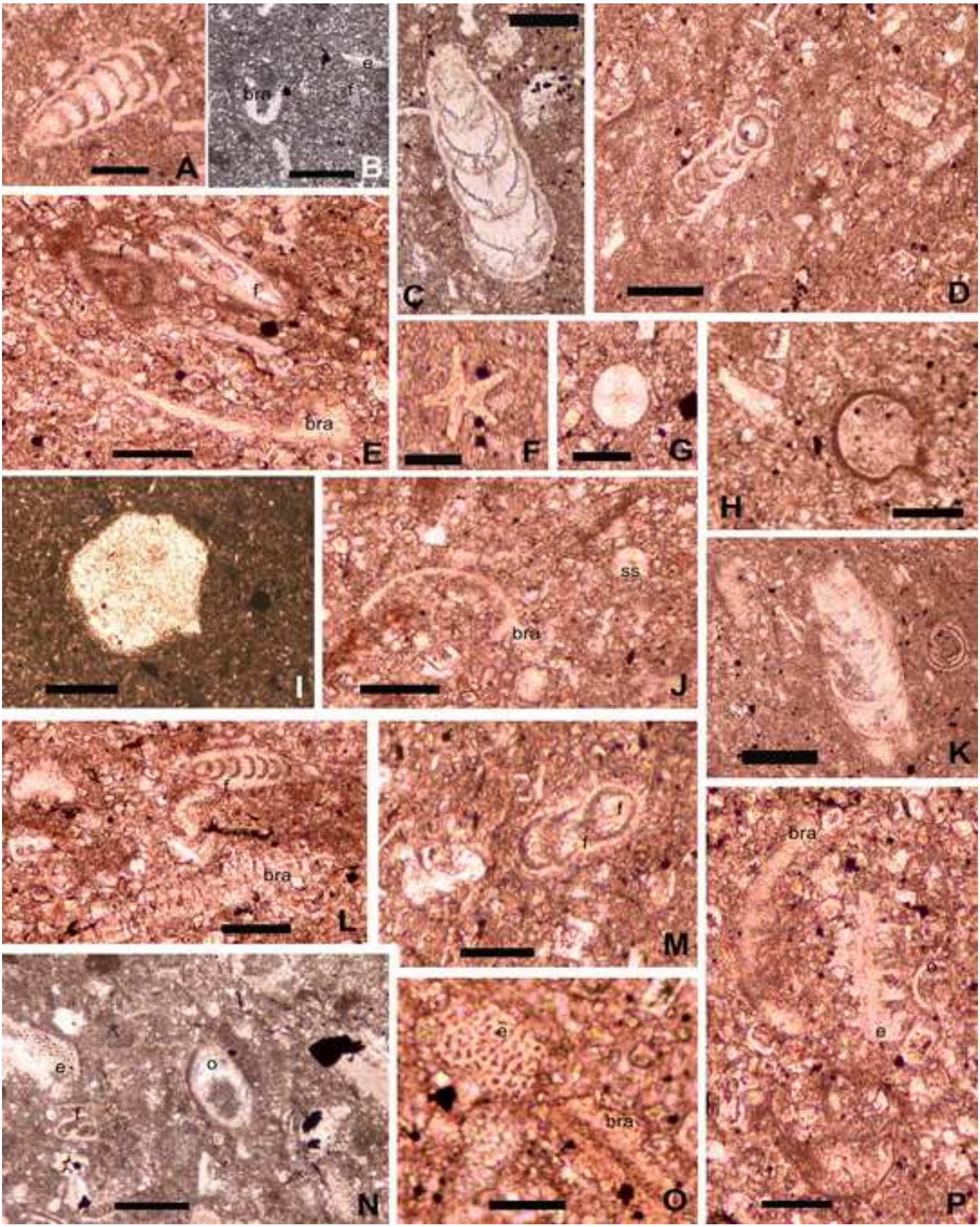

Figure 13

Click here to download high resolution image

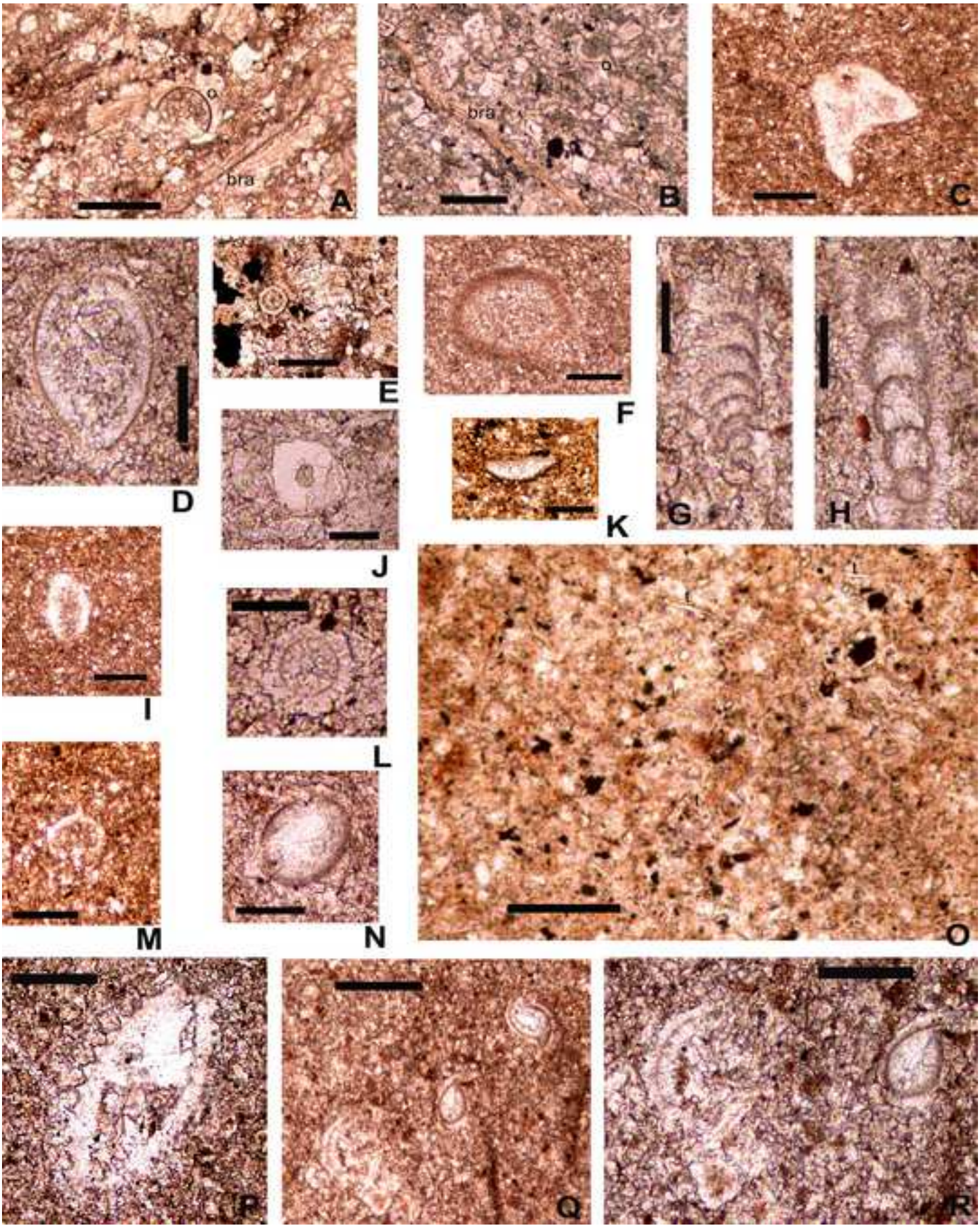

Figure 14

Click here to download high resolution image

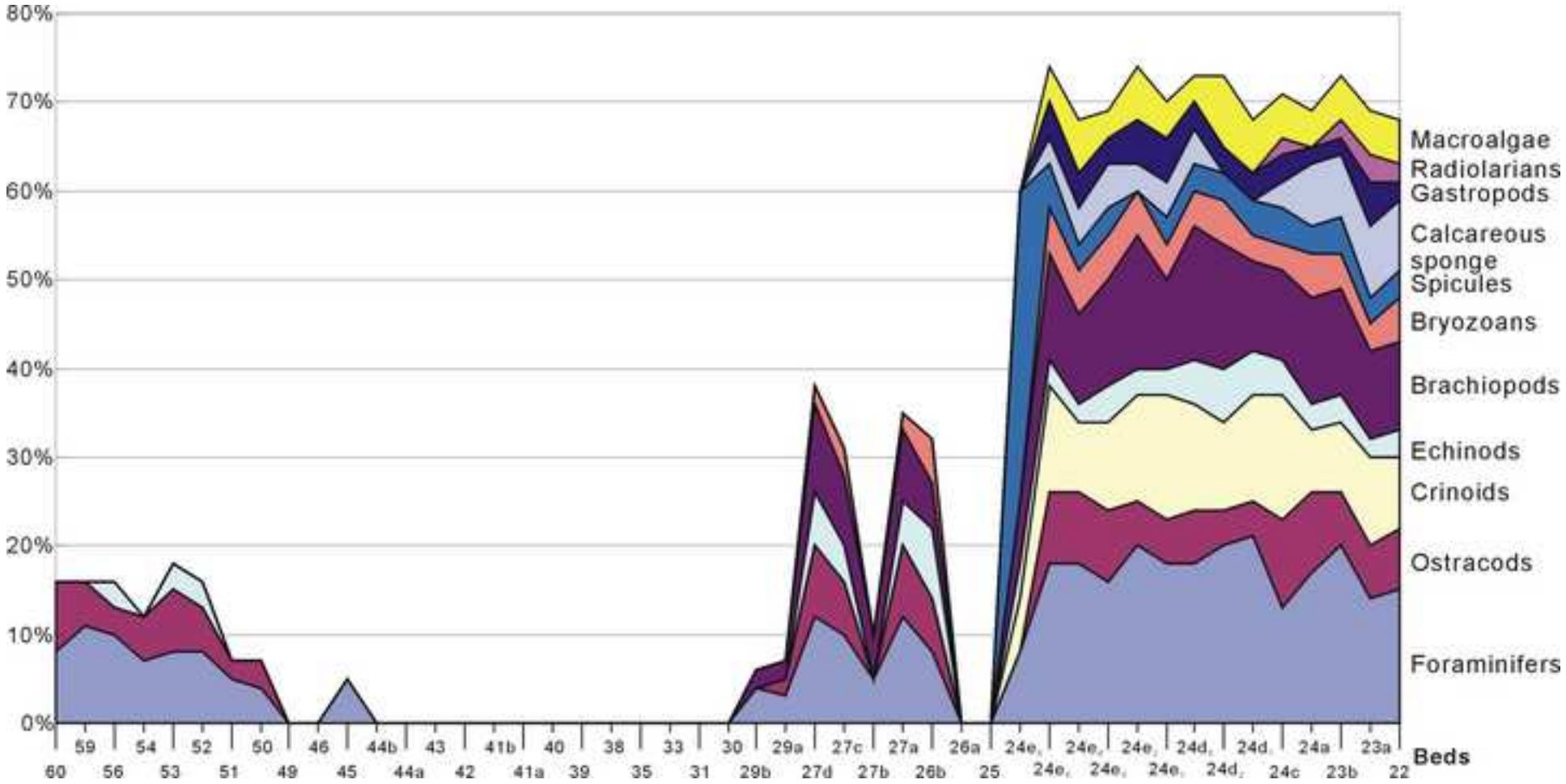

Figure 15

Click here to download high resolution image

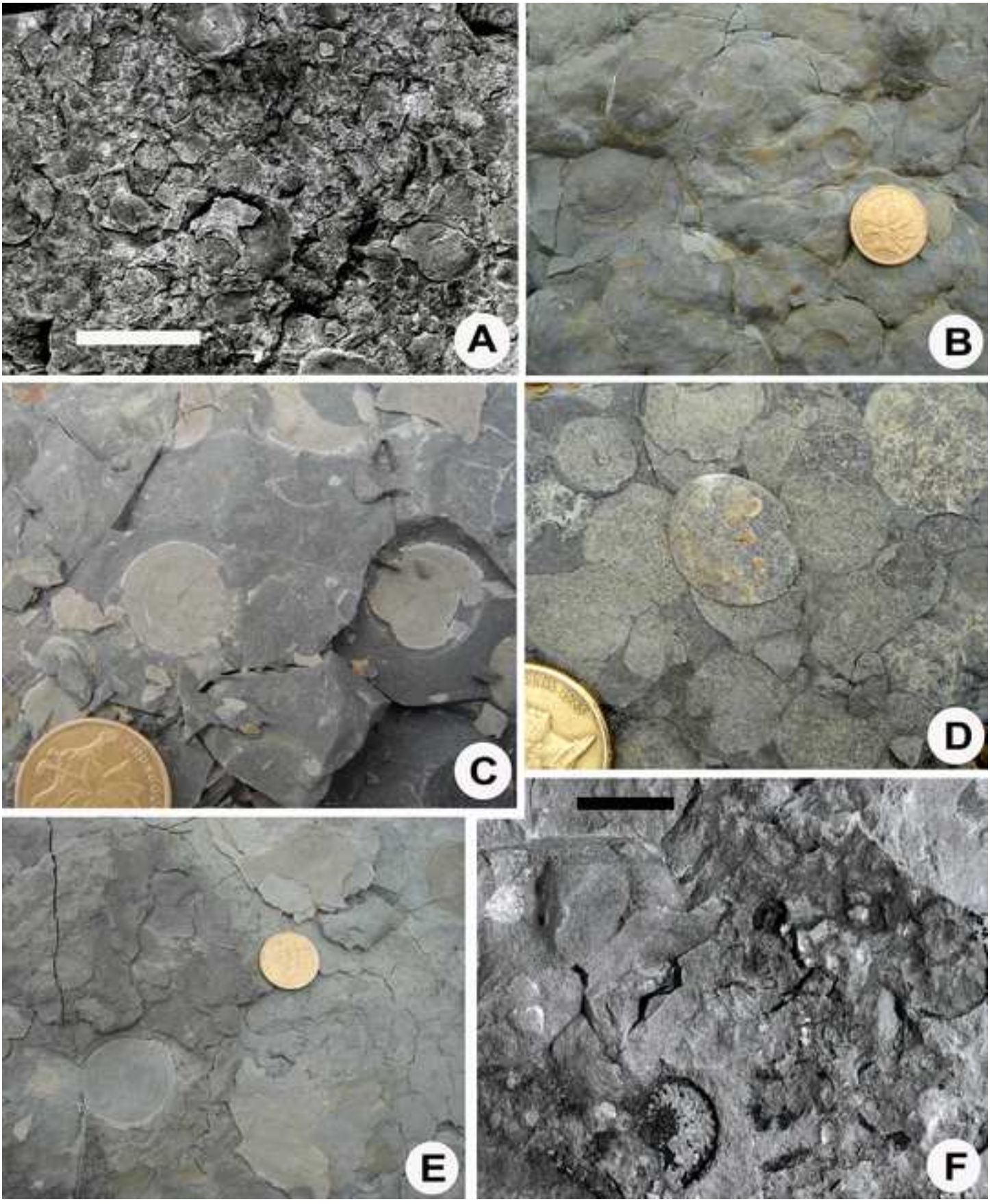

Figure 16

Click here to download high resolution image

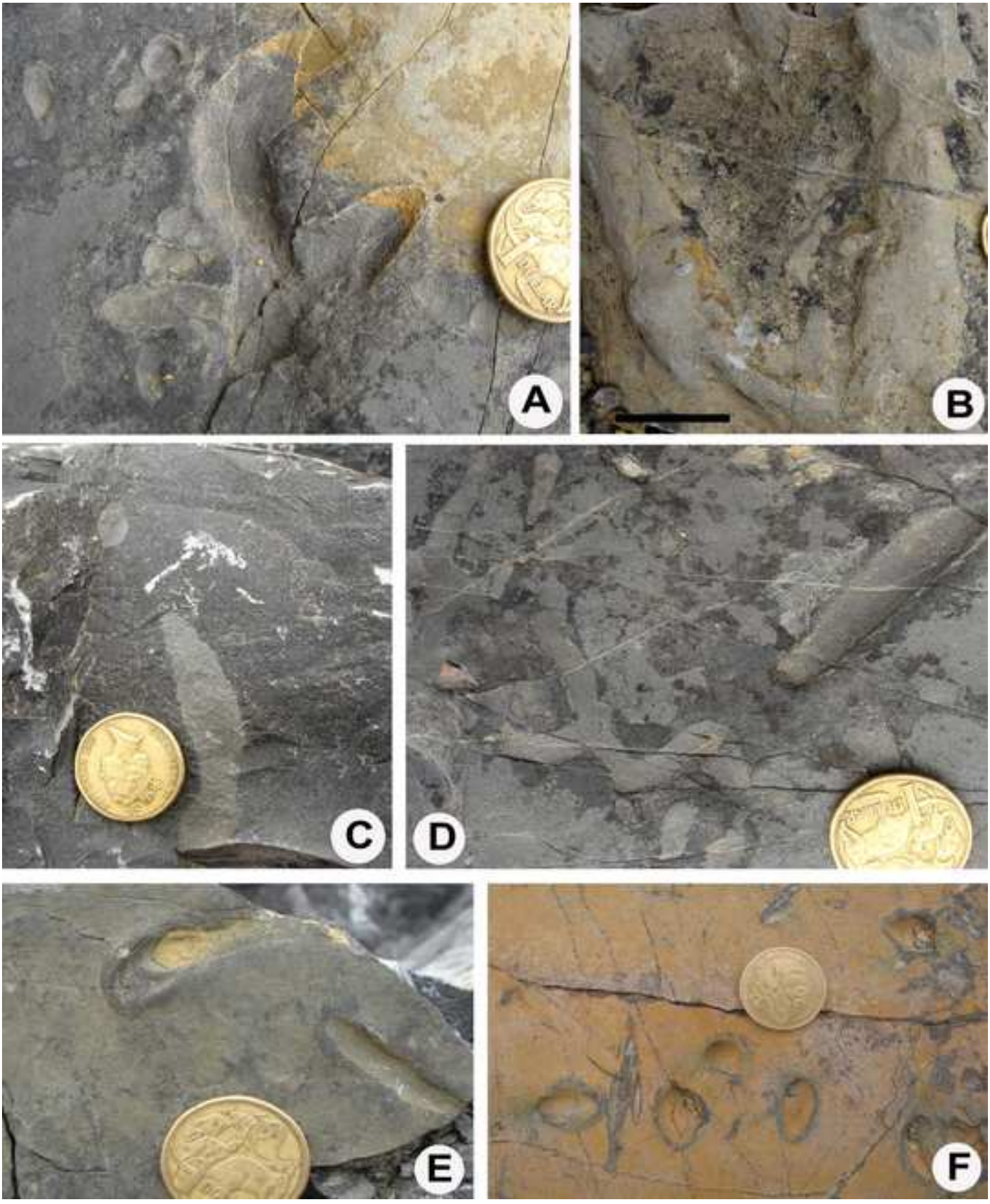

Figure 17
Click here to download high resolution image

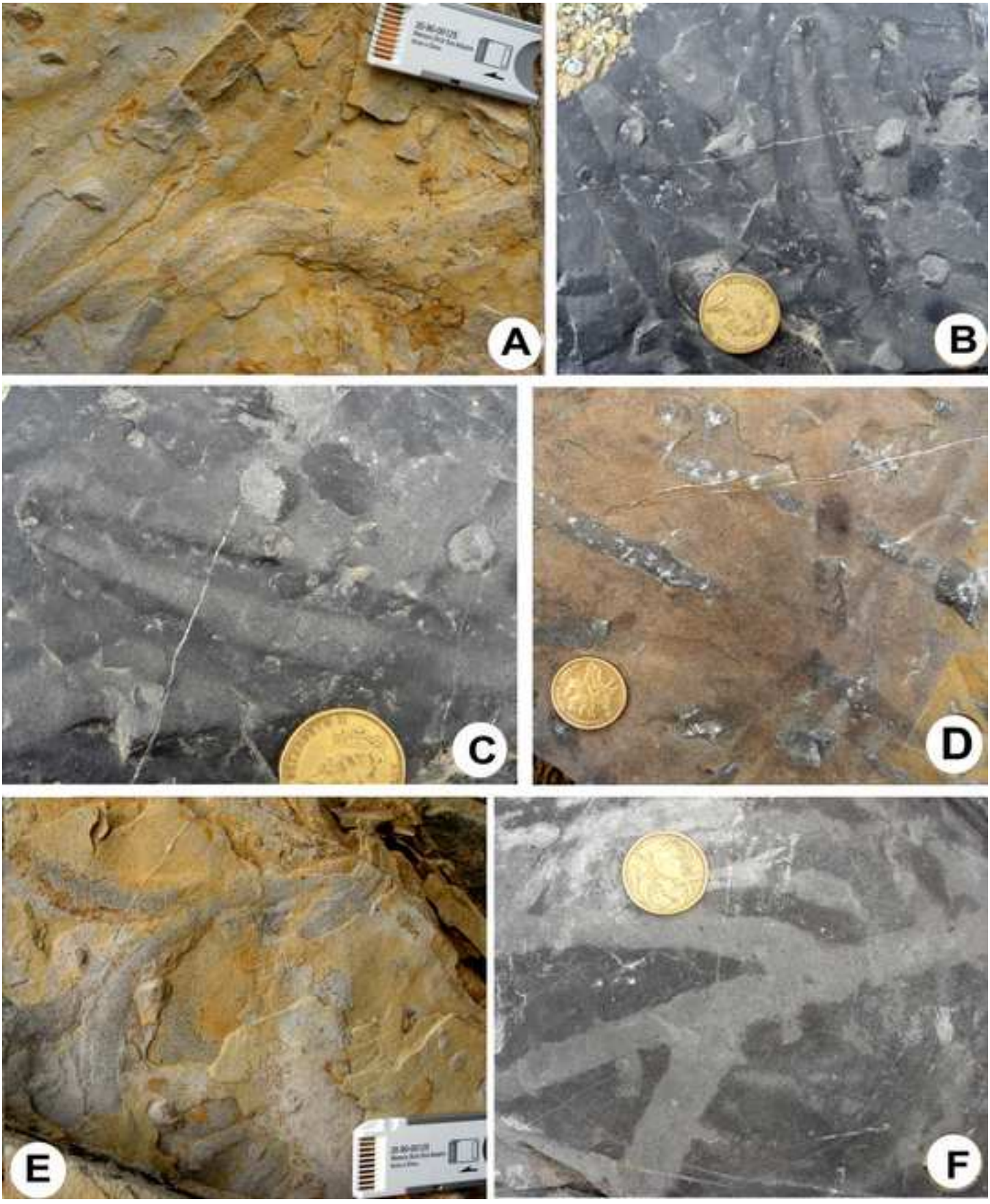

Figure 18

Click here to download high resolution image

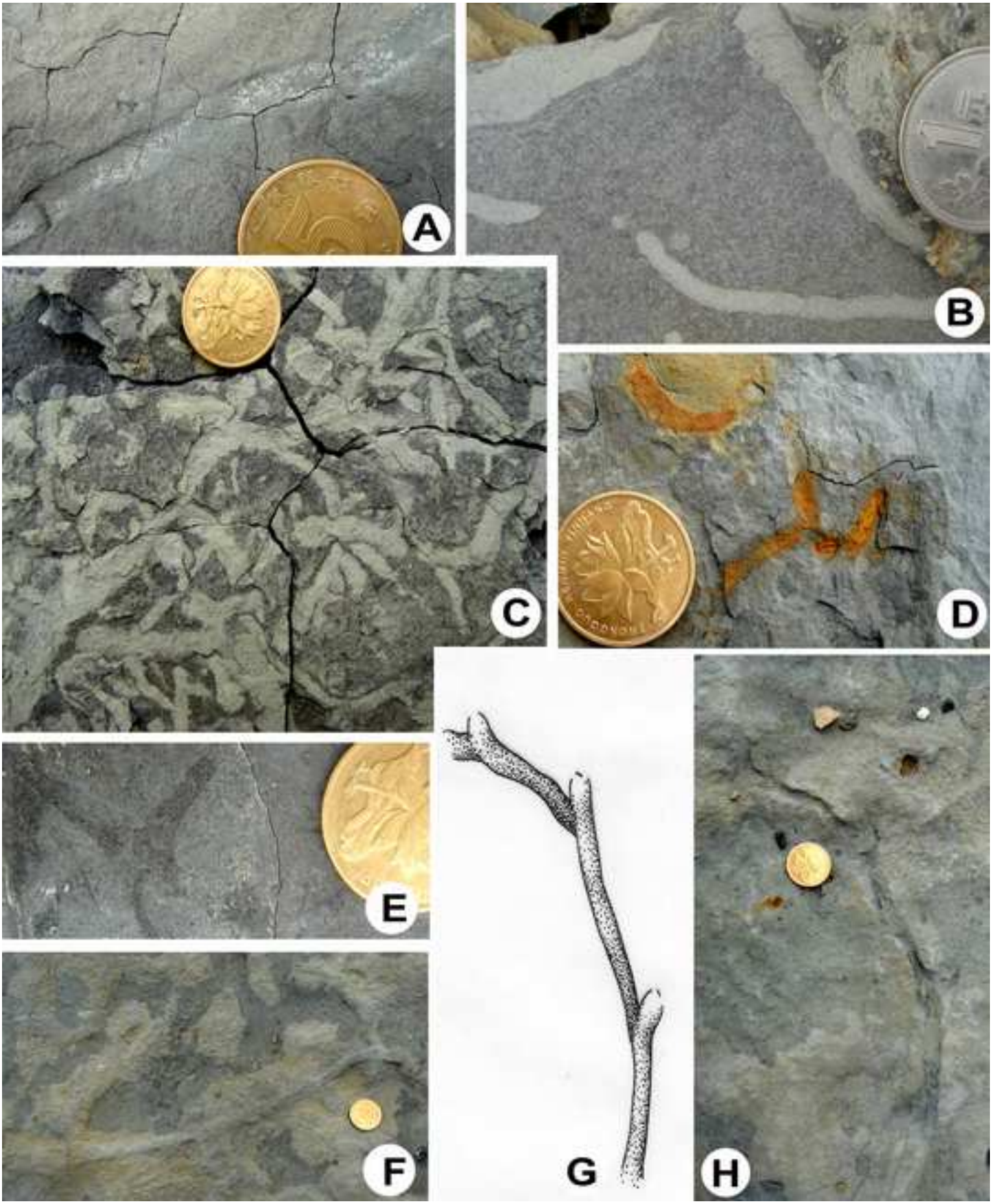

Figure 19
Click here to download high resolution image

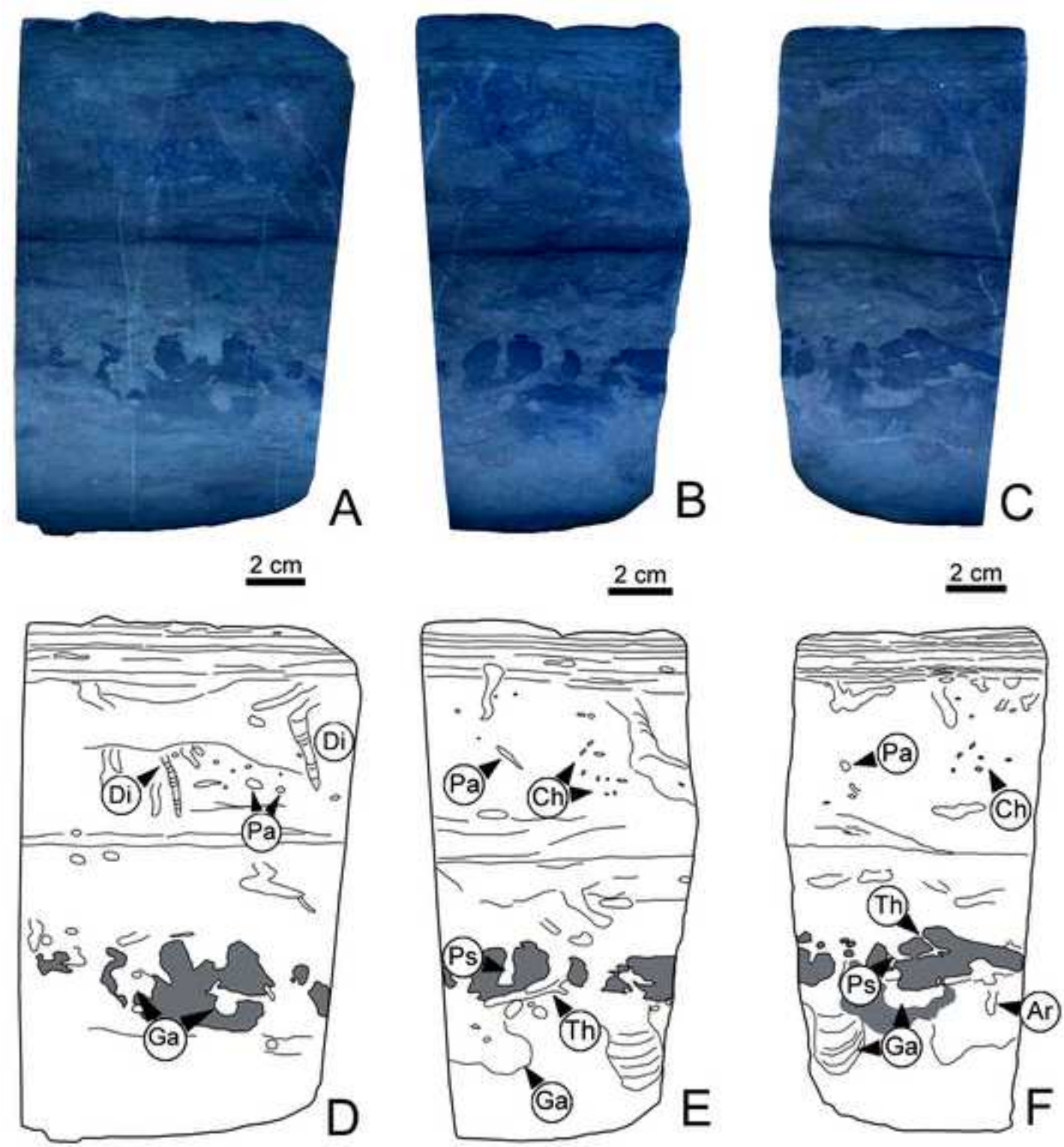

Figure 20

Click here to download high resolution image

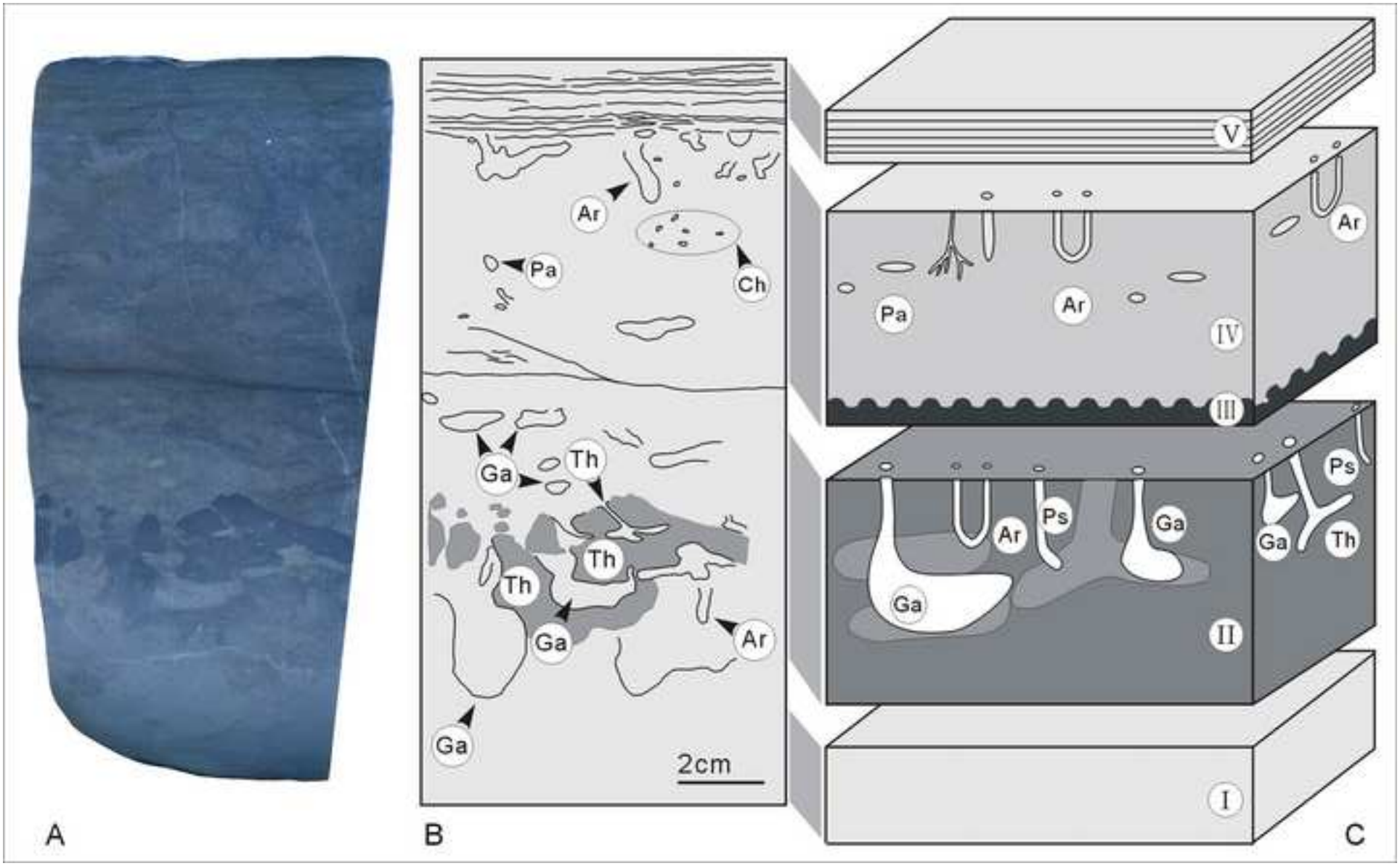

Figure 21
Click here to download high resolution image

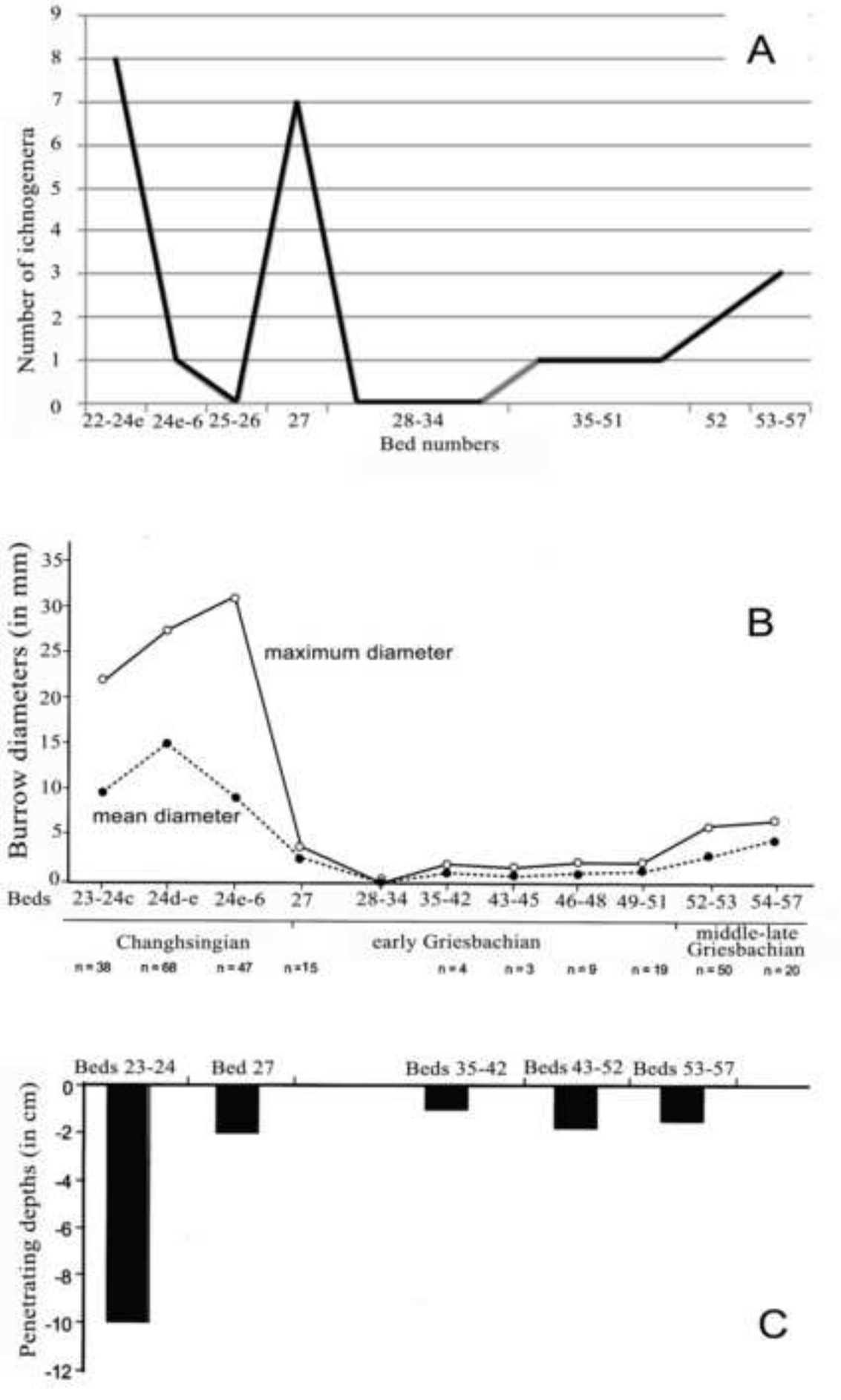

Figure 22

Click here to download high resolution image

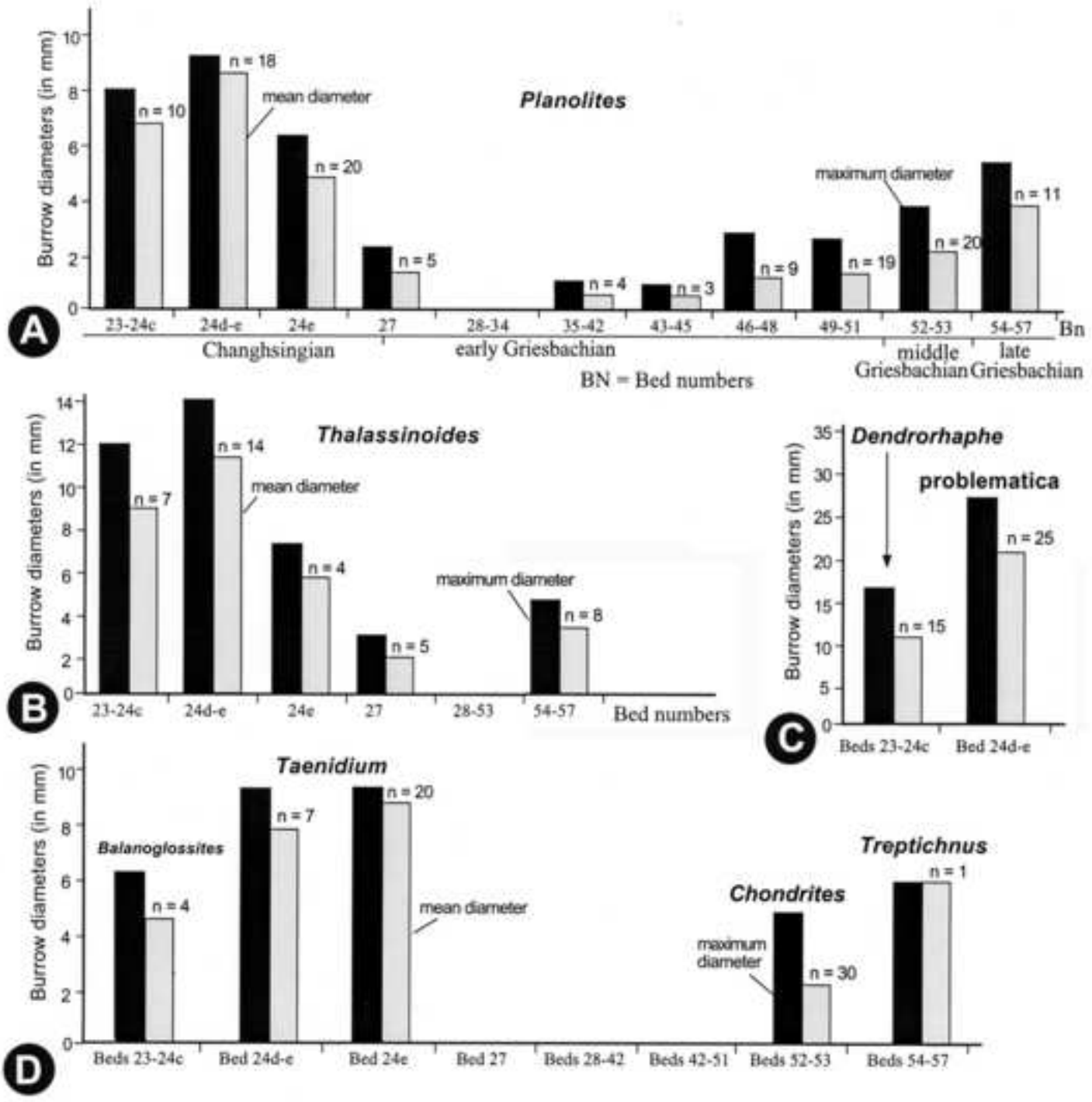

Figure 23

Click here to download high resolution image

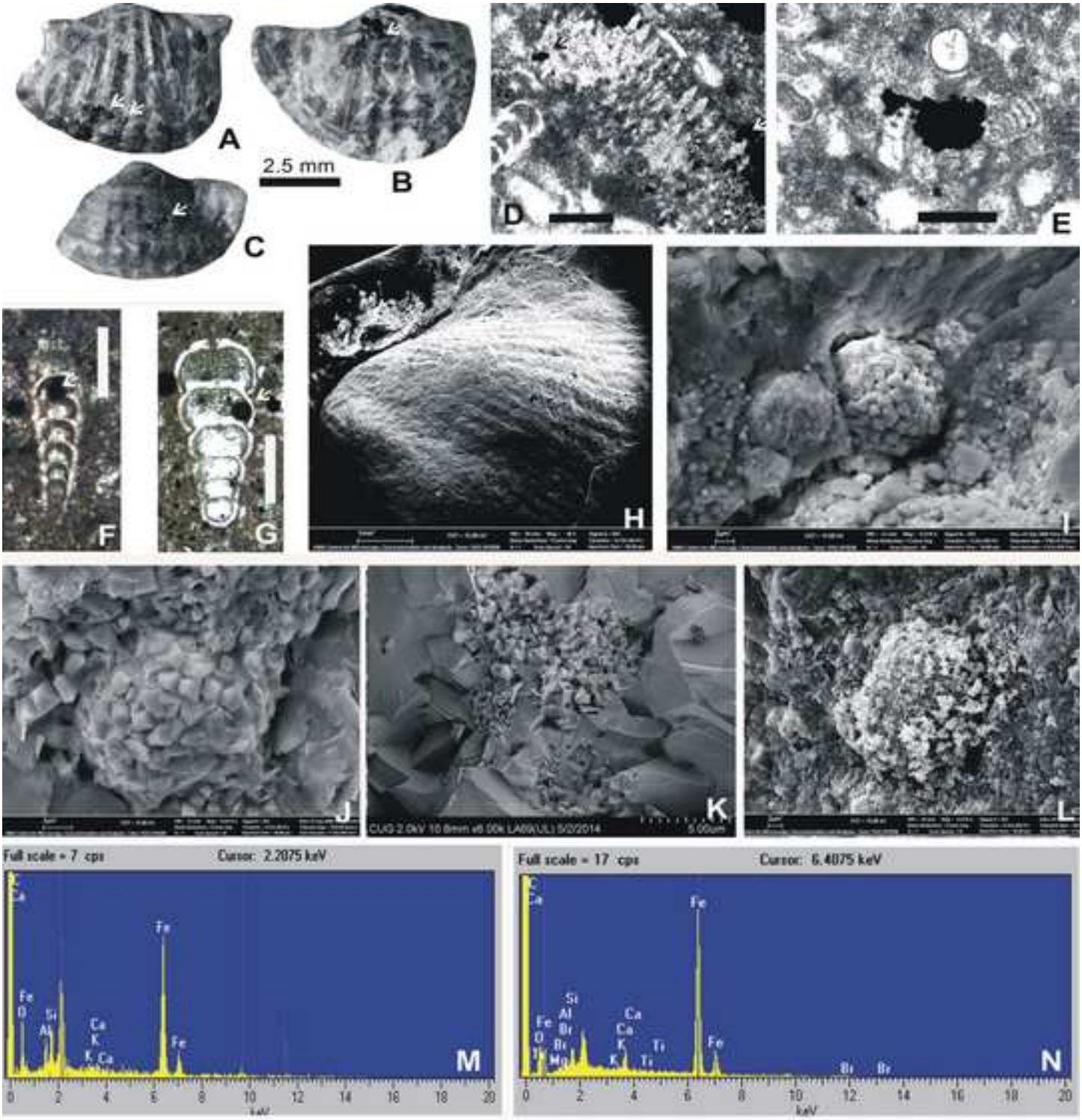

Figure 24

Click here to download high resolution image

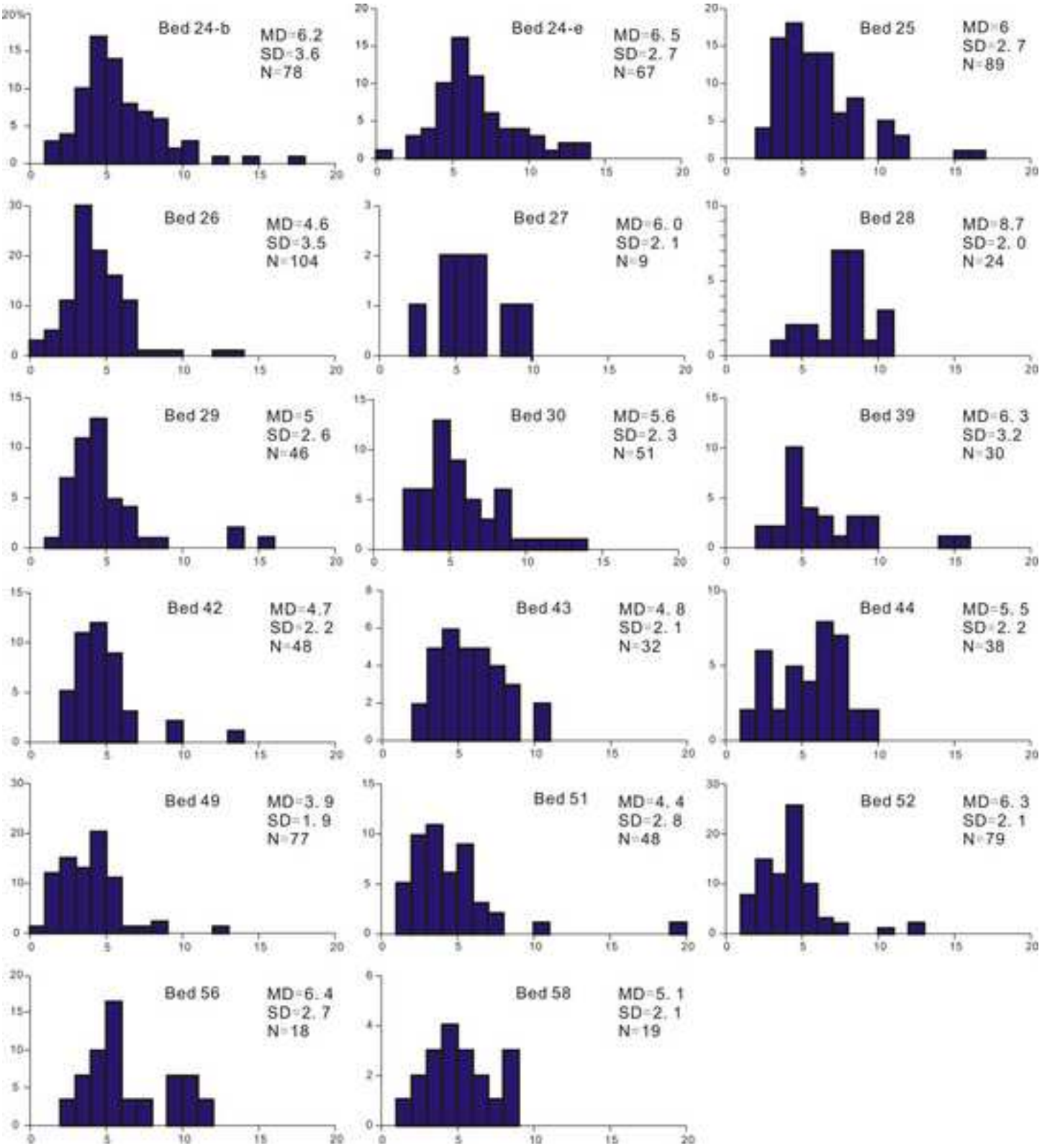

Figure 25

Click here to download high resolution image

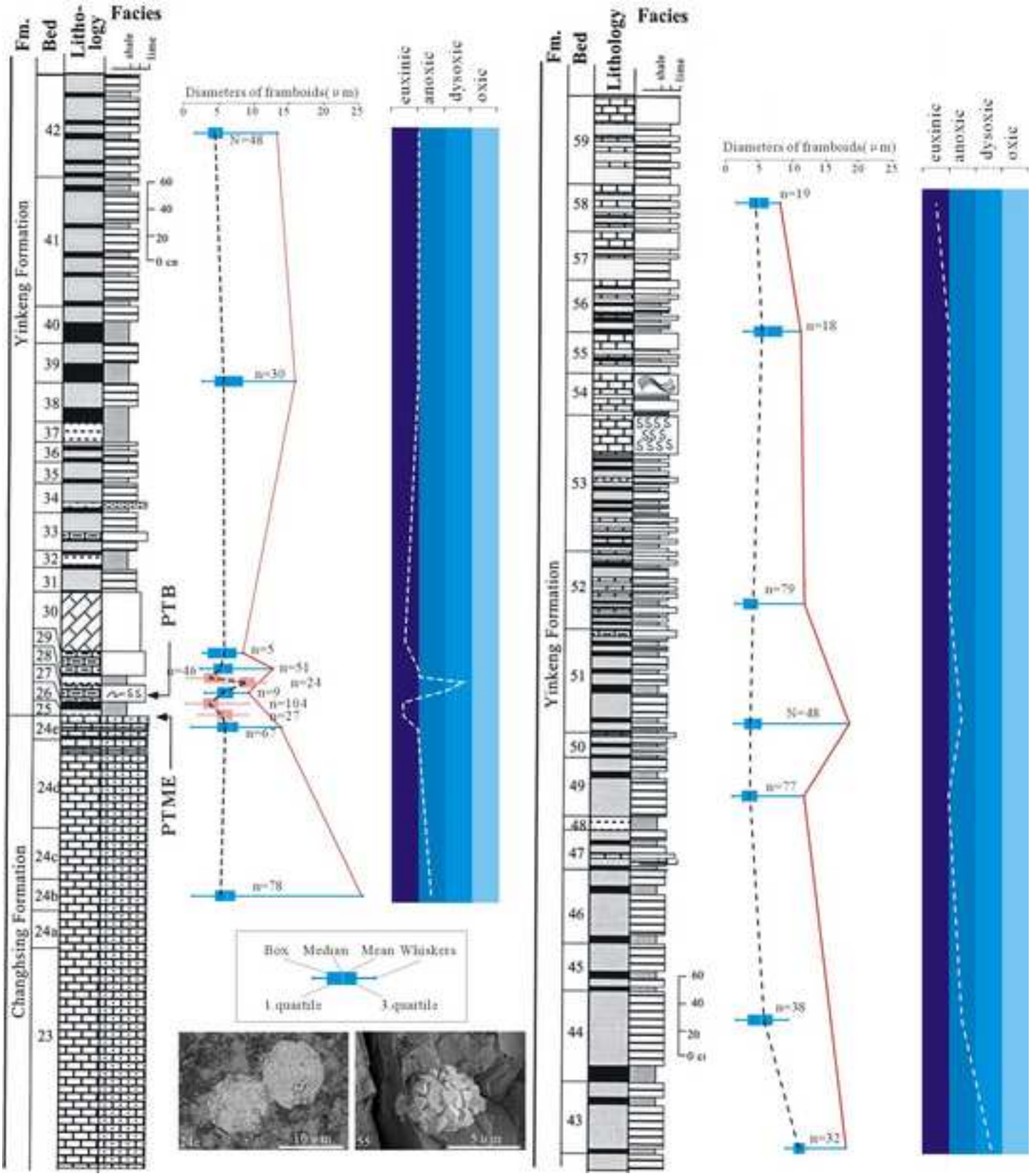

Figure 26

Click here to download high resolution image

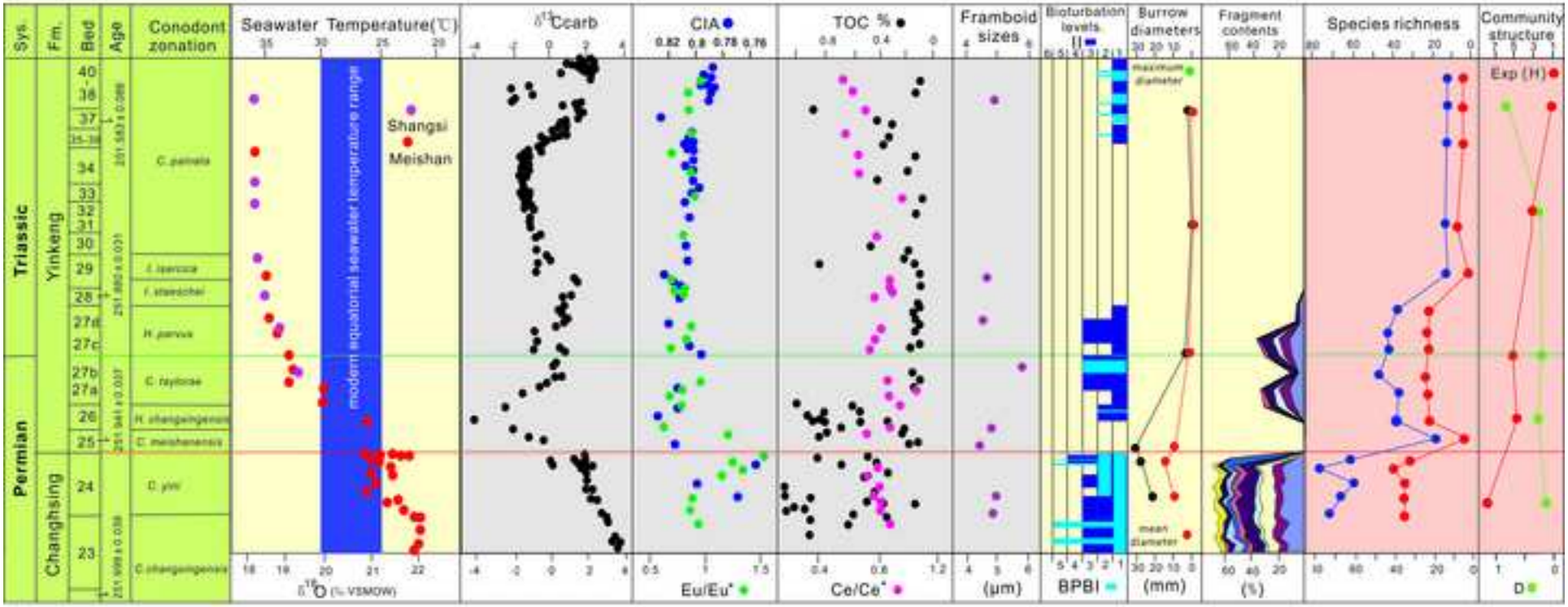

Table 1. Radiometric ages obtained from the P-Tr succession in GSSP Meishan (in Ma)

	Bed 7	Bed 22	Bed 25	Bed 28	Bed 37	Bed 48
Claoue-Long et al., 1991			251.2 ± 3.4 (SHRIMP)			
Renne et al., 1995			249.91 ± 0.15*			
Bowring et al., 1998	253.4 ± 0.2	252.3 ± 0.2	251.4 ± 0.3	250.7 ± 0.3	250.4 ± 0.5	250.2 ± 0.2
Mundil et al., 2001, 2004			252.41 ± 0.41	252.48 ± 0.3		
Reichow et al., 2009				250.98 ± 0.14 *		
Renne et al., 2010			251.63 ± 0.2*			
Shen et al., 2011	253.45 ± 0.08	252.50 ± 0.11	252.28 ± 0.08	252.10 ± 0.06		
Burgess et al., 2014		252.104 ± 0.06	251.941 ± 0.037	251.880 ± 0.031	251.583 ± 0.086	251.495 ± 0.064

* $^{40}Ar/^{39}Ar$ age; others are $^{206}Pb/^{238}U$ ages. Note: Beds 33 and 34 of Bowring et al. (1998), Shen et al. (2011) and Burgess et al. (2014) are equivalent to Beds 37 and 48 of this study, respectively.

Table 2. Key conodont zones with their durations across the PTB in Meishan

Conodont zones	**Stratigraphic ranges**	**Starting dates**	**Duration**
I. isarcica Zone	Bed 29b	251.845 Ma	27 ka
I. staeschei Zone	Beds 28-29a	251.880 Ma	35 ka
H. parvus Zone	Bed 27c-d	251.896 Ma	16 ka
C. taylorae Zone	Bed 27a-b	251.912 Ma	16 ka
H. changxingensis Z.	Bed 26	251.933 Ma	21 ka
C. meishanensis Z.	Bed 25	251.941 Ma	8 ka
C. yini Zone	Bed 24	251.969 Ma	28 ka
C. changxingensis Z.	Beds 22-23	252.104 Ma	135 ka

Table 3

Click here to download Table: Table 3-Fossil fragments.doc

Table 3. Percentage of major components of rocks sampled from Beds 22-60 in Meishan

Beds	Elev.* (cm)	Foram (%)	Ostra. (%)	Crin. (%)	Echin. (%)	Brach. (%)	Bryo. (%)	Spon. (%)	Cal. sp. (%)	Gastr. (%)	Radio. (%)	Algae (%)	Micrites (%)	Cavity (%)	Particles (%)
60	1357～1363	8	8	0	0	0	0	0	0	0	0	0	72	3	9
59	1250～1255	11	5	0	0	0	0	0	0	0	0	0	74	5	5
56	1160～1165	10	3	0	3	0	0	0	0	0	0	0	80	0	4
54	1055～1060	7	5	0	0	0	0	0	0	0	0	0	80	0	8
53	1005～1010	8	7	0	3	0	0	0	0	0	0	0	78	0	4
52	950～955	8	5	0	3	0	0	0	0	0	0	0	77	0	7
51	900～910	5	2	0	0	0	0	0	0	0	0	0	88	0	5
50	850～855	4	3	0	0	0	0	0	0	0	0	0	88	0	5
49	800～810	0	0	0	0	0	0	0	0	0	0	0	90	0	10
46	750～755	0	0	0	0	0	0	0	0	0	0	0	90	0	10
45	700～705	5	0	0	0	0	0	0	0	0	0	0	90	0	5
44b	650～655	0	0	0	0	0	0	0	0	0	0	0	95	0	5
44a	600～605	0	0	0	0	0	0	0	0	0	0	0	95	0	5
43	550～556	0	0	0	0	0	0	0	0	0	0	0	95	0	5
42	500～505	0	0	0	0	0	0	0	0	0	0	0	90	0	10
41b	450～455	0	0	0	0	0	0	0	0	0	0	0	92	0	8
41a	400～405	0	0	0	0	0	0	0	0	0	0	0	92	0	8
40	350～355	0	0	0	0	0	0	0	0	0	0	0	90	0	10
39	300～305	0	0	0	0	0	0	0	0	0	0	0	95	0	5
38	250～255	0	0	0	0	0	0	0	0	0	0	0	90	0	10
35	200～205	0	0	0	0	0	0	0	0	0	0	0	92	0	8
33	160～165	0	0	0	0	0	0	0	0	0	0	0	95	0	5
31	100～110	0	0	0	0	0	0	0	0	0	0	0	90	0	10
30	60～63	0	0	0	0	0	0	0	0	0	0	0	92	0	8
29b	36～39.5	4	0	0	0	2	0	0	0	0	0	0	88	0	6
29a	30～33.5	3	2	0	0	2	0	0	0	0	0	0	88	0	5
27d	23～28	12	8	0	6	10	2	0	0	0	0	0	50	0	12
27c	21～23	10	6	0	4	8	3	0	0	0	0	0	55	0	14
27b	15～17	5	0	0	0	5	0	0	0	0	0	0	80	0	10
27a	13～15	12	8	0	5	8	2	0	0	0	0	0	55	0	10
26b	8～10	8	6	0	8	5	5	0	0	0	0	0	60	0	8
26a	4～6	0	0	0	0	0	0	0	0	0	0	0	0	0	0
25	0.3～2	0	0	0	0	0	0	0	0	0	0	0	0	0	0
24e6	-1～0	8	0	6	4	7	0	35	0	0	0	0	35	0	5
24e5	-2～-1	18	8	12	3	12	5	5	3	4	0	4	20	2	4
24e4	-3～-2	18	8	8	2	10	5	3	4	4	0	6	24	3	5
24e3	-6～-3	16	8	10	4	12	5	3	5	3	0	3	24	2	5
24e2	-9～-6	20	5	12	3	15	5	0	3	5	0	6	20	2	4

24e1	-11～-9	18	5	14	3	10	4	3	4	5	0	4	24	2	4
24d3	-14～-11	18	6	12	5	15	4	3	4	3	0	3	20	2	5
24d2	-20～-15	20	4	10	6	14	5	3	0	3	0	8	18	4	5
24d1	-45～-50	21	4	12	5	10	3	4	0	3	0	6	24	3	5
24c	-60～-55	13	10	14	4	10	3	4	3	3	2	5	22	2	5
24a	-90～-80	17	9	7	3	12	5	3	7	2	0	4	25	2	4
23b	-150～-145	20	6	8	3	12	4	4	7	2	2	5	21	3	3
23a	-205～-200	14	6	10	2	10	3	3	8	5	3	5	23	3	5
22	-255～-250	15	7	8	3	10	5	3	8	2	2	5	22	2	8

*Elev. = Elevation, referring to accumulative distance (in cm) of sampling horizon to the base of Bed 25; minus value indicates sampling horizon below Bed 25.
Component codes: Foram. = foraminifers, Ostra. = ostracods, Crin. = crinoids, Echin. = echinoids, Brach. = brachiopods, Bryo. = bryozoans, Spon. = sponge spicules, Cal. sp. = calcareous sponges, Gastr. = gastropods, Radio. = radiolarians, Algae = macroalgae, Particles = other particles (fecal pellets, peloids, pyrites and undetermined particles).

Table 4.

Beds	Samples	BT. mm	Composition and percentage	Colour	lithology
Bed 29	MD 29	260	calcite 6%, ankerite 62%, silica 15%, illite 5%, kaolinite 2%	grey	marlstone
Bed 28	MD 28	40	calcite 4%, silica 50%, illite 16%, kailinite 22%, orthoclase 5%	white	claystone
Bed 27c-d	MD 27cd	80	calcite 33%, ankerite 38%, silica 23%, illite 4%, kaolinite 2%	grey	marlstone
Bed 27a-b	MD 27ab	80	calcite 30%, ankerite 38%, silica 26%, illite 4%, kaolinite 2%	grey	marlstone
Bed 26	MD 26	60	gypsum 21%, calcite 8%, silica 36%, illite 18%, kaolinite 17%	black	shale
Beds 25-2, 25-3	MD 25	40	gypsum 34%, chlorite 9%, montm 28%, illite 10%, kaolinite 19%	white	claystone
Bed 25-1	MD 25mr	0.3	gypsum 63%, goethite 25%, chlorite 12%	red	
Bed 24e-3	MD 25 my	0.3	gypsum 76%, chlorite 6%, silica 18%	yellow	
Bed 24e-3	MD 25mb	0.3	gypsum 35%, calcite 11%, chlorite 4%, silica 50%	brown	
Beds 24e-2, 24e-1	MD 24e	200	calcite 97%, illite 0.5%, kaolinite 0.5%, silica 2%	black	packstone
Bed 24d	MD 24d	230	calcite 98%, silica 2%	black	packstone

BT. = Bed thickness

Table 5. Structural indices of the latest Permian to earliest Triassic shelly communities from Meishan (Chen et al., 2010a).

CC	Beds	Age	SR	N	H	Exp(H)	D	D'	Δ	E
R–P	24	Changhsingian	9	42	2.029	7.60648	0.1519	1.1791	0.15561	0.8453
T	26	Changhsingian	8	36	1.47	4.34942	0.3673	1.5805	0.37779	0.5439
P–T	27	Griesbachian	7	67	1.565	4.78267	0.2658	1.3620	0.26983	0.6836
C–O	32	Griesbachian	3	125	0.7559	2.12953	0.5233	2.0978	0.52752	0.7098
C	40	Griesbachian	1	129	0	1	1	?	1.00781	1
M–L	53-55	Griesbachian	8	143	1.288	3.62553	0.4379	1.7790	0.44098	0.4531

CC: Community codes; SR: species richness; N: individual number; H: Shannon entropy; Exp (H): standard diversity Shannon index; D: Dominance entropy; D': standard diversity dominance index [1/(1-D)]; Δ: bias-corrected Simpson's evenness [N×D/(N-1)]; E: evenness index (e^H/S).

Table 6. Major indices showing community structural changes over the P-Tr transition in Meishan

Community boundary	Diversity [Exp (H)] changes	D' changes
R–P/T	-43.6%	+34.0%
T/P–T	+10%	-14.1%
P–T/C–O	-55.5%	+54%
C–O/C	-53%	?
C/M–L	+262.6%	?
C–O/M–L	+70%	-15.2%

Exp (H): standard diversity Shannon index; D': standard diversity dominance index [1/(1-D)]; - indicates decrease, while + represents increase

Table 7
Click here to download Table: Table 7-Description of trace fossils.doc

Table 7. Characteristics of major trace fossils from the uppermost Permian to lowest Triassic in Meishan

Ichnotaxa	Beds	Illustr.	Description	Interpretation
Arenicolites isp.	27	Figs. 24-25	U-shaped burrows with unbranched, parallel limbs, 0.5 to 3.0 mm in diameter, perpendicular to bedding plane, and lacking spreite; filled with light-grey, coarse sediments that are distinguished from surrounding dark, fine-grained sediments.	Domichnia with trace-makers of polychaete worms, amphipod and crustaceans (Knaust, 2004; Chen et al., 2011, 2012)
Balanoglossites triadicus	24d	Fig. 20C	Vertical tubes, 14-18 mm wide and 10 cm long, perpendicular to bedding, penetrating to a depth of 5-10 cm; filled with light-coloured sediments distinguished from the surrounding dark sediments.	Produced by polychaete-like or enteropneust worms (Hantzschel, 1975).
Chondrites isp. 1	52	Fig. 25C	Plantlike dendritic system composed of fine, branching, cylindrical ramifying burrows, parallel to bedding plane in compact groups, and filled with yellow, coarsely grained sediments distinct from surrounding dark, fine-grained sediments.	Fodinichnia, feeding structures of sediment-eating animals (Bromley and Ekdale, 1984; Chen et al., 2011).
Chondrites isp. 2	27	Fig. 24-25	Small branching, cylindrical burrows forming plantlike dendritic systems, penetrating into sediments, and filled with light, coarsely grained sediments and distinguished from surrounding dark, fine-grained sediments	Same as above
Dendrorhaphe isp.	23	Fig. 21G	Tree-like trace system comprises a rather straight main axis, along which side branches are mostly perpendicular to the main axis and given off on both sides. Minor branches also give birth to further secondary branches in same way.	Occurring in deep-water or oxygen-deficient niches; feeding structures of sediment-eating animals (Seilacher, 1977)
Diplocraterion isp.	27	Fig. 24	U-shaped burrows with unbranched, parallel limbs, perpendicular to bedding plane, and having spreite; filled with light-grey, coarse sediments that are distinguished from surrounding dark, fine-grained sediments.	Produced by polychaete worms, amphipod and crustaceans (Knaust, 2004)
Gastrochaenolites isp.	27	Figs. 24-25	Irregular, tear-shaped borings filled by light grey sediments in a dark-colored firmground lime mudstone substrate, penetrating down to the firmground layer at a maximum depth of 4 cm.	Produced by various organisms i.e., bivalves, annelids and sipunculans (Benner and Ekdale, 2004)
Lockeia isp.	8-9	Figs. 20F, 21B	Small, almond-shaped oblong structure, 8-18 mm long and 7-12 mm wide, tapering to sharp points at both ends; preserved in either concave impressions on the tops or convex relief on the soles.	Resting impressions of bivalves (Bromley, 1996; Ekdale and Bromley, 2001)
Paleophycus isp.	8-9	Fig. 20B	Branching, slightly curved, cylindrical burrows, 2−7 mm in diameter, with wall typically lined and preserved as positive reliefs on top of bed.	Rrepichnion or domichnion, produced by predaceous or suspension-feeding animals (Gouramis et al., 2003).

Psilonichnus isp.	27	Figs. 24-25	Vertical cylindrical burrows that are inclined with bedding in its distal end.	Trace of ocypodid ghost crabs (Buatois and Mángano, 2011).
Planolites isp. 1	24e	Fig. 23A-F	Simple, unbranched, unornamented, vermiform burrows that are straight and horizontally distributed on bedding tops, with some intersecting the sediment irregularly. Burrows, 3-9 mm in diameters, are occasionally densely packed.	Deposit-feeding activities of polychaetes or worm-like creatures, or feeding burrow of deposit-feeders (Bromley, 1996).
Planolites isp. 2	34-53, 55-56	Fig. 25A-B, F	*S*imple, unbranched, vermiform burrows that, 1-4 mm in diameter, are straight or curving and horizontally distributed on bedding surfaces.	Same as above
Problematic trace	23	Fig. 21A, C-D	Simple, straight, unbranched burrows, 20-27 mm in diameter, with 2-5 mm thick tube wall. Single burrow originates at a small, rounded end and extends distally to form a horn-shaped burrow with an open distal end.	Sharing the same trace-makers with *Planolites*.
Taenidium isp.	24d-e	Figs. 20E, 21E	Cylindrical, straight, unbranching burrows with backfilling structures; Some tubes are horizontal on tops of beds, and others are slightly oblique to bedding planes. Tube diameters are 6-9.5 mm.	Feeding behaviours of worm-like animals (Keighley and Pickerill, 1994).
Thalassinoides isp. 1	23-24 c	Fig. 20A, D	Large Y-shaped, branching, smooth, rounded burrows, 10-14 mm in diameter (Fig. 22), penetrating a depth of < 1 cm into sediment and forming incomplete intricate networks.	Behaviour of cerianthid sea anemones, worms and decapod crustaceans (Myrow, 1995; Bromley, 1996; Ekdale and Bromley, 2003).
Thalassinoides isp. 2	27	Figs. 24-25	Small Y-shaped, branching burrows, 1-2 mm in diameter, penetrating a depth of < 1 cm into sediment, filled with light coarsely grained sediments distinct from surrounding dark, fine-grained sediments.	Same as above
Thalassinoides isp. 3	53-56	Fig. 25D-E	Medium-sized Y-shaped, branching burrows, 3-4.5 mm in diameter, mostly horizontal on tops of beds and filled with dark, organic sediments.	Same as above
Treptichnus isp.	56-57	Fig. 25G-H	Meandering burrow system with one main burrow, 6 mm in width, terminates its growth after bifurcating to give a minor branch on its outer side. The minor branch ceases its growth soon after giving birth to further secondary branch.	Deposit-feeding of worm-like organism in a zigzag or other segmented pattern with older segments abandoned after use (Rindsberg and Kopaska-Merkel, 2005; Seilacher, 2007).

Illustr. = Illustration